Driven and Obstructed Colloids in Random Energy Landscapes

Inauguraldissertation

zur Erlangung des Doktorgrades
der Mathematisch-Naturwissenschaftlichen Fakultät
der Heinrich-Heine-Universität Düsseldorf

vorgelegt von

Christoph Zunke
aus Düsseldorf

Düsseldorf, Oktober 2017

aus dem Institut für experimentelle Physik der kondensierten Materie
der Heinrich-Heine-Universität Düsseldorf

Gedruckt mit der Genehmigung der
Mathematisch-Naturwissenschaftlichen Fakultät der
Heinrich-Heine-Universität Düsseldorf

Berichterstatter:

1. Prof. Dr. Stefan U. Egelhaaf

2. Prof. Dr. Jan K. G. Dhont

3. Prof. Dr. Ralf Metzler

Tag der mündlichen Prüfung: 22.12.2017

Declaration of Originality

This dissertation is the result of my own work and includes nothing which is the outcome of work done in collaboration except as specified in the text. It was prepared considering the "Grundsätze zur Sicherung guter wissenschaftlicher Praxis an der Heinrich-Heine-Universität Düsseldorf". It is not substantially the same as any that I have submitted, or, is being concurrently submitted for a degree or diploma or other qualification at the Heinrich-Heine-Universität or any other University or similar institution except as specified in the text. I further state that no substantial part of my dissertation has already been submitted, or, is being concurrently submitted for any such degree, diploma or other qualification at the Heinrich-Heine-Universität or any other University of similar institution except as specified in the text.

Düsseldorf, 04.10.2017

Christoph Zunke

Abstract

Driven and obstructed motion is often found in the microscopic world, e.g. for diffusion in biological cells and in disordered media, in the motion of microorganisms or in glasses. As these systems are found in nature, their dynamics is often affected by random potentials or forces. In order to investigate underlying processes, it is therefore desirable to mimic these systems in a controlled way. In this work, four different kinds of driving and obstruction in one- and two-dimensional random potentials are experimentally realised by means of colloidal particles, time-dependent laser light fields and a piezo stage.

To create a quasi-two-dimensional system with particles undergoing Brownian motion while being inside random potentials, speckle-patterned light fields are exerted on micrometre-sized polystyrene spheres dispersed in aqueous solutions. The same forces present in an optical tweezers setup result in the particles experiencing a random potential when exposed to the speckle light field. Two different optical setups are used to create either one-dimensional or two-dimensional random light fields. The one-dimensional fields are created by a spatial light modulator, a device capable of time-dependently shaping light in almost arbitrary patterns. The two-dimensional light fields are static and realised by an Engineered Diffuser™ that creates a top-hat beam with an inherent speckle pattern.

Firstly, the short-time diffusion of dilute particle dispersions exposed to one-dimensional random potentials is investigated. Randomly distributed colloids are quenched by a random potential, resulting in a temporary enhancement of the diffusion coefficient before particles relax into the potential minima. Brownian dynamics simulations quantitatively agree with the experimental results.

In a second step, periodically varying one-dimensional random potentials are

exposed to non-interacting colloidal particles. Their diffusion coefficient is enhanced or reduced depending on the length of the period with which the random potential is changed, resulting in a resonance curve-like behaviour. Theoretical calculations and Brownian dynamics simulations are found to quantitatively reproduce the experimental findings.

Subsequently, the dynamics of individual colloidal particles dragged with a constant velocity through a two-dimensional random potential is the focus. Depending on the forces due to the applied drag velocity, distinct regimes differing in their dynamics can be identified. While motion perpendicular to the drag only shows subdiffusion, diffusion coefficients along the drag direction are enhanced by up to more than an order of magnitude. Additionally, first-passage time distributions are found to exhibit kinks.

Ultimately, samples made up of two differently sized colloids are exposed to two-dimensional random light fields. The bigger particles are highly restricted due to the interaction with the light field and thus serve as obstacles. The smaller particles, called tracers, which are almost unaffected by the light, diffuse through the voids created by the obstacles. The obstacle concentration is varied which leads to a tracer dynamics similar to that found for diffusion in a Lorentz gas. When the restriction of the obstacle motion is lifted, the long-time tracer diffusion is diffusive instead of the long-time subdiffusion found when obstacles are restricted.

Zusammenfassung

Getriebene und behinderte Bewegung findet sich oft in der mikroskopischen Welt, z.B. für Diffusion in biologischen Zellen und ungeordneten Medien, bei der Bewegung von Mikroorganismen oder in Gläsern. All diese Systeme kommen natürlich vor und unterliegen daher oft zufälligen Potentialen oder Kräften. Um zu verstehen wie die Prozesse in diesen zufälligen Umgebungen ablaufen, ist es daher wünschenswert, ein kontrolliertes Modellsystem dieser Systeme zu studieren. In dieser Arbeit werden deshalb vier verschiedene Experimente mit getriebener oder behinderter Bewegung mit Hilfe von kolloidalen Teilchen, zeitabhängigen Lichtfeldern und einem Mikroskoptisch mit Piezoantrieb untersucht.

Mikrometer große Polystyrolkugeln in wässrigen Lösungen werden einem Lichtfeld mit zufälligem Fleckenmuster ausgesetzt und erzeugen so ein quasi-zweidimensionales System von Teilchen, die Brown'sche Bewegung vollziehen während sie sich in einem Zufallspotential befinden. Die gleichen Kräfte, die auch in einer optische Pinzette wirken, sind die Ursache dafür, dass die Teilchen ein Potential spüren, wenn sie dem Lichtfeld ausgesetzt sind. Zwei verschiedene optische Aufbauten werden dazu verwendet entweder eindimensionale oder zweidimensionale Zufallspotentiale zu erzeugen. Die eindimensionalen Potentiale werden mit Hilfe eines Spatial Light Modulators realisiert, ein Gerät, das Licht zeitabhängig zu fast beliebigen Mustern formen kann. Die statischen zweidimensionalen Felder werden mit einem Engineered Diffuser™ erzeugt, der einen zylindrischen Strahl mit einem zufälligen Fleckenmuster formt.

Zunächst wird die Kurzzeitdiffusion verdünnter kolloidaler Dispersionen in eindimensionalen zufälligen Potentialen untersucht. Zufällig verteilte Kolloide werden schlagartig einem zufälligen Potential ausgesetzt. Dadurch wird ihr Dif-

fusionskoeffizient zeitweilig erhöht bevor die Teilchen in die Potentialminima relaxieren. Die Ergebnisse von Brownian-Dynamics-Simulationen dieses Experiments stimmen gut mit den experimentellen Ergebnissen überein.

In einem zweiten Schritt werden verdünnte kolloidale Dispersionen einem periodisch variierenden eindimensionalen Potential ausgesetzt. Der Diffusionkoeffizient der Teilchen wird abhängig von der Periodendauer erhöht oder verringert und zeigt somit ein Resonanzverhalten. Theoretische Berechnungen und Brownian-Dynamics-Simulationen stimmen quantitativ mit den Experimenten überein.

Anschließend steht die Dynamik von einzelnen kolloidalen Teilchen im Fokus, die gleichförmig durch eine zufällige zweidimensionale Potentiallandschaft gezogen werden. Abhängig von der Kraft, die durch die gleichförmige Bewegung auf die Teilchen wirkt, zeigt die Teilchenbewegung mehrere Regimes. Während die Teilchendynamik senkrecht zur Zugbewegung subdiffusiv ist, wird der Diffusionskoeffizient entlang der Zugbewegung um bis zu mehr als eine Größenordnung erhöht. Zusätzlich zeigen sich Knicke in den Verteilungen der ersten Durgangszeiten.

Abschließend werden Dispersionen aus zwei verschieden großen kolloidalen Teilchen einem zweidimensionalen Lichtfeld ausgesetzt. Die größeren Teilchen werden durch die Interaktion mit dem Licht stark in ihrer Bewegung eingeschränkt und agieren somit als Hindernisse. Die kleineren Teilchen, auch Tracer genannt, werden kaum durch das Lichtfeld beeinflusst und diffundieren in den Freiräumen zwischen den Hindernissen. Die Variation der Hinderniskonzentration führt zu einer Tracerdynamik, die der für Diffusion in einem Lorentz-Gas ähnelt. Wenn die Einschränkung der Hindernisbewegung aufgehoben wird, verändert sich die Langzeitdynamik der Tracer von subdiffusivem zu diffusivem Verhalten.

Acknowledgements

First of all, I would like to thank Prof. Stefan U. Egelhaaf for giving me the opportunity and constant support throughout the last years. It was always a pleasure to discuss science and to throw around ideas even in the late hours. Your cheerful nature always encouraged me to take that next step and will definitely be missed going further.

Furthermore, I thank Prof. Jan K. G. Dhont and Prof. Ralf Metzler for spending the time and effort to examine this thesis.

Thanks to Florian for proof-reading basically my entire scientific output. Without you, this thesis would be unreadable. Besides that, I am grateful for all the valuable advice and discussions on manuscripts we had—especially in the last months.

Jörg and Richie, this thesis would not have happened without you. Thank you for building the optical setups and showing me how to maintain them. Special thanks go out to Jörg: I will never forget all the long yet amusing chats about how, where and even why to analyse a sample. After all, they seem to have helped us both get there in the end.

Gracias, Manuel, for all the explanations on scattering methods and Mexican colloquial language. What would the world be without some interdisciplinary talk on soft matter physics from time to time, jefe?!

Hab Dank, Christoph, for guiding me through the physics studies. Funny, how a coincidental meeting in a school physics course can end up in something like this.

Thanks a lot, Kevin, for thoroughly proof-reading the whole thesis and making it sound less German. I owe you. Next time, all beer on mir.

In addition, I sincerely say "Thank You!" to all the people with whom I had

the pleasure to work in this soft matter group and foreign groups: Andreas, Arjun, Dana, Debasish, Jan, Juan-Pablo, Martin Schramm, Max, Philipp, Prof. Peter Kern, Ramón, Ronja, and all the others I might have forgotten and who hopefully forgive me.

The acknowledgements would not be complete without thanking all my friends for providing comic relief on the weekends and constantly finding a way to mock me about not being finished with my Ph.D. I am pretty confident you will find other ways, now that it is finally done.

I am very grateful to my whole family for the constant support throughout the last 30 years. Without you, this would not have been possible.

The biggest thanks go out to my wife, Katharina. Your constant encouragement, support and ability to distract me in complicated times were my elixir without which I could not have done this.

"It is a truth very certain that,
when it is not in our power to determine what is true,
we ought to follow what is most probable."

— René Descartes (1596–1650)

Contents

List of Symbols

Symbol	Description	Unit
a_g	Gravitational acceleration on the earth's average surface radius	[m/s^2]
A	Area	[m^2]
A_{FOV}	Area of the field of view	[m^2]
A_H	Hamaker constant: quantifies magnitude of van-der-Waals-interactions	[J]
A_P	Surface area of a particle	[m^2]
$\boldsymbol{A}$	Area vector	[m]
$\mathcal{A}$	Amplitude	[1]
α_D	Anomalous diffusion exponent	[1]
α_2	Non-Gaussian parameter	[1]
α_p	Polarisability	[C m^2/V]
b	Exponent	[1]
$\boldsymbol{B}$	Magnetic field	[T]

Symbol	Description	Unit
$\mathcal{B}$	Complex amplitude	[1]
β_2	Kurtosis	[1]
c	Speed of light	[m/s]
c_0	Electrolyte concentration in the bulk of a liquid	[mol/m^3]
C_j	Microlens cell of an Engineered Diffuser	[a.u.]
C_R	Reflection coefficient	[1]
C_T	Transmission coefficient	[1]
$\mathcal{C}_\mathrm{M}$	Michelson contrast	[1]
$\mathcal{C}_\mathrm{RMS}$	RMS contrast	[1]
d	Dimension	[1]
d_f	Fractal dimension	[1]
d_w	Walk dimension	[1]
d_z	Dynamic exponent	[1]
D	Diffusion coefficient	[m^2/s]
D_0	Diffusion coefficient for free diffusion near a wall	[m^2/s]
D_b	Diffusion coefficient in the bulk	[m^2/s]
D_F	Diffusion coefficient due to Faxén's law	[m^2/s]
D^l	Long-time diffusion coefficient	[m^2/s]
D^s	Short-time diffusion coefficient	[m^2/s]
$\delta[x]$	Dirac delta function of x	[1]

Symbol	Description	Unit
Δ	Representation of a difference	[a.u.]
$\Delta \boldsymbol{r}$	Multidimensional displacement	[m]
Δt	Time step	[s]
Δt_{L}	Trajectory length	[s]
Δt_{min}	Minimum time step in a measurement	[s]
$\Delta x, \Delta y, \Delta z$	Displacement in x-, y-, or z-direction	[m]
e	Elementary charge	[C]
$\hat{\boldsymbol{e}}$	Unit vector	[1]
E	Energy	[J]
E_{U}	Typical energy of a random potential	[J]
$\boldsymbol{E}$	Electric field	[V/m]
e	Euler's number	[1]
ϵ	Permittivity	[As/Vm]
ϵ_0	Vacuum permittivity	[As/Vm]
ϵ_r	Relative permittivity	[1]
η	Viscosity	[Pa s]
f	Intermediate scattering function	[1]
F	Force	[N]
F_{B}	Fluctuating force due to Brownian motion	[N]
F_{E}	External force	[N]

Symbol	Description	Unit
F_g	Gravitational force	[N]
F_G	Gradient force	[N]
F_S	Scattering force	[N]
$\mathcal{F}$	First-passage time distribution	[1/s]
$g(\Delta \boldsymbol{r})$	Pair distribution function	[1/m]
$g(\Delta r)$	Radial distribution function	[1/m]
$\mathcal{G}$	van Hove function	[1/m]
γ	Strain	[1]
γ_1	Skewness	[1]
γ_2	Excess kurtosis	[1]
γ_α	Normalised excess kurtosis	[1]
Γ	Gamma function	[1]
Γ_0	Constant depending on the electrostatic surface potential of a colloidal particle	[1]
h	Distance of particle centre to a wall	[m]
i	Index of summation	[1]
I	Intensity	[W/m^2]
I_P	Intensity altered due to the interaction with a colloidal particle	[W/m^2]
i	Imaginary unit	[1]

Symbol	Description	Unit
j	Index of summation	[1]
J	Particle flux	[mol/(m^{2}s)]
J_g	Particle flux due to gravity	[mol/(m^{2}s)]
k	Magnitude of the wave vector	[1/m]
$\boldsymbol{k}$	Wave vector	[1/m]
k_B	Boltzmann constant	[J/K]
k_r	Radial spring constant / trap stiffness	[N/m]
κ	Inverse Debye length: reciprocal length, in which a screened electric potential of a particle drops to its 1/e part	[1/m]
l_g	Gravitational length, i.e. the characteristic length of the height distribution of a particle ensemble inside the earth's gravitational field	[m]
l_F	Correlation length of forces caused by a potential	[m]
l_U	Correlation length of potential U	[m]
l_ξ	Typical (or correlation) length of a fractal	[m]
λ	Wavelength of light	[m]
m	Mass	[kg]
M	Shape parameter of the gamma distribution	[1]
$\boldsymbol{m}_E$	Electric dipole moment	[C m]
μ	Permeability	[H/m]
μ_0	Vacuum permeability	[H/m]

Symbol	Description	Unit
n	Refractive index	[1]
n_{M}	Refractive index of the dispersion medium	[1]
n_{O}	Density of obstacles in a two-dimensional Lorentz gas	[1/m^2]
$n_{\mathrm{O,c}}$	Critical density of obstacles in a two-dimensional Lorentz gas	[1/m^2]
n_{P}	Refractive index of a particle	[1]
n_{ϱ}	Microscopic particle density	[1]
N	Number	[1]
N_{FOV}	Number of particles in the field of view	[1]
N_x, N_y	Number of pixels in the x- or y-direction	[1]
$\boldsymbol{n}$	Director of a liquid crystal	[1]
ν	Critical exponent	[1]
p	Momentum	[kg m/s]
$\boldsymbol{p}$	Momentum vector	[kg m/s]
P	Power	[W]
P_{L}	Laser power	[W]
$\mathcal{P}$	Probability distribution function	[a. u.]
$\mathcal{P}_{\mathrm{B}}$	Probability distribution function due to Brownian motion	[1/m]
$\mathcal{P}_{\mathrm{FD}}$	Probability distribution function of intensity values for a fully developed speckle field	[m^2/W]
$\mathcal{P}_{\Gamma}$	Gamma distribution of a speckle field	[m^2/W]

Symbol	Description	Unit
ϕ	Cross section	[m^2]
φ_A	Area fraction	[1]
φ_l	Line fraction	[1]
Φ, Θ	Phase	[rad]
Φ_0	Surface potential of a particle	[V]
Ψ	Waiting time distribution	[1/s]
q	Surface shape of a microlens of an Engineered Diffuser	[1]
Q	Efficiency factor	[1]
Q_z	Efficiency factor in axial direction	[1]
Q_{ES}	Electrostriction coefficient	[m^4/C^2]
Q_{PE}	Piezoelectric coefficient	[m/V]
r	Radial distance between to points in space	[m]
$\boldsymbol{r}$	Spatial vector	[m]
R	Radius of a colloidal particle	[m]
R_h	Hydrodynamic radius of a colloidal particle	[m]
Re	Reynolds number	[1]
ϱ	Volumetric mass density	[kg/m^3]
ϱ_M	Volumetric mass density of the dispersion medium	[kg/m^3]
ϱ_N	Particle concentration / density	[mol/m^3]
$\varrho_{N,0}$	Particle density at the bottom of a container	[mol/m^3]
$\varrho_{N,g}$	Particle density defined by gravity	[mol/m^3]
ϱ_P	Polarisation density	[C/m^2]

Symbol	Description	Unit
s	Perimeter	[m]
S	Dynamic structure factor	[1]
$\boldsymbol{S}$	Poynting vector	[W/m^2]
$\mathcal{S}$	Order parameter of a liquid crystal	[1]
σ^2	Variance or squared standard deviation	[a.u.]
$\sigma^2_{\Delta x}$	Variance for displacements in x-direction	[m^2]
$\sigma^2_{\Delta \boldsymbol{r}}$	Variance for displacements in multiple directions	[m^2]
t	Time	[s]
t_B	Brownian time	[s]
t^*_B	Hydrodynamic drag-corrected Brownian time	[s]
t_F	Characteristic time defined by l_F	[s]
$t_\mathcal{O}$	Observation time in a measurement	[s]
T	Absolute temperature	[K]
$\boldsymbol{T}_\mathrm{M}$	Maxwell stress tensor	[Pa]
τ	Period	[s]
$\tau_{\boldsymbol{E}}$	Oscillation period of an electric field	[s]
θ	Angle / azimuthal coordinate	[rad]
u, w	Transformed coordinate	[1/m]
U	Potential	[J]
U_A	Attractive potential	[J]
U_r	Radial potential	[J]

Symbol	Description	Unit
U_R	Repulsive potential	[J]
U_{DLVO}	Potential derived from DLVO-theory	[J]
U_{vdW}	Potential due to van-der-Waals-Forces	[J]
v	Velocity	[m/s]
v_B	Velocity of a Brownian particle due to its environment's temperature	[m/s]
v_D	Drag velocity	[m/s]
v_g	Velocity of a particle due to gravitation	[m/s]
V	Volume	[m^3]
V_P	Volume of a particle	[m^3]
W_P	Weight function for the interaction of a particle with light	[1]
x, y, z	Spatial coordinate	[m]
ξ	Coefficient of friction	[kg/s]
ξ_b	Coefficient of friction in the bulk	[kg/s]
ξ_0	Coefficient of friction near a wall	[kg/s]
Ξ	Ratio of refractive indices	[1]
ζ	Valency of specific species	[1]

I Introduction

Driving and obstruction are two sides of the same coin as both represent an alteration of movement. In everyday life, man-made driving is encountered regularly in any type of motor where it is used to move an object—be it a car, boat or industrial machines. Obstruction, on the other hand, not only slows down motion but can also be utilised to control motion, e.g. when barriers are put up in front of sporting events to guide people to the entrances or breakwaters that protect coastal areas by dissipating the energy of approaching water waves. Furthermore, driven and obstructed motion can be advantageously combined as in turbines where a driven fluid that is obstructed by blades can generate electrical power.

In the natural world, these concepts are found similarly. On a macroscopic level, driven motion is represented by water and air streams spread all over the earth, while in avalanche areas, obstruction by trees can save humans lives. The interplay of driven and obstruction motion can be witnessed when tectonic plate movements take place and possibly result in earthquakes. On a microscopic level, actin and myosin motors exhibit driven motion and thus help contracting muscles [1]. Microorganisms like bacteria often possess motors that drive them towards or away from certain stimuli [2]. In addition, micrometre-sized particles perform Brownian motion when they are dispersed in a medium such as water at non-zero temperature. It is a random motion caused by the bombardment of the particles by the molecules of the dispersion medium resulting in diffusion. Obstructed motion is then encountered for the diffusion of molecules in heterogeneously crowded environments such as cells [3] or for proteins diffusing inside cell membranes [4, 5].

These and similar phenomena concerning driven and obstructed motion on

microscopic length scales are the focus of ongoing research. Several studies on molecular transport [6], the dynamics inside living cells [7], active particles in complex environments [8], the effect of obstruction on the diffusivity of self-propelled particles [9], crystal growth in fluid flow [10], the glass dynamics under shear [11], the effect of active fluctuations on dynamics of particles, motors and DNA-hairpins [12], and transport in heterogeneous media [13] are just a few examples for the large interest that driven and obstructed motion aroused in the last two years.

In order to mimic complex microscopic and even atomic systems found in nature, colloids, i.e. particles in the size range between about 1 nm and 10 μm, are often used as a model system [14–16]. Amongst other applications, colloidal particles were used to determine Avogadro's number [17] or provided insight into friction on a molecular level [18]. Colloidal particles usually consist of silica [19] or plastics, e.g. poly(methyl methacrylate) [20] or polystyrene [21] and are thus easy to handle. Due to their size, their dynamics can be observed in real space by a wide range of microscopy techniques such as bright field [21], dark field [22] or confocal microscopes [23]. Colloids can be very versatile with shapes ranging from spheres to ellipsoids and arbitrary hybrids [24, 25]. In addition, interparticle potentials can be tuned from the very basic hard-sphere potential to soft and patchy interactions [14, 26].

Just like the microscopic components found in nature, colloids perform Brownian motion when dispersed inside a medium at non-zero temperature. This naturally occurring motion can be easily manipulated in an experiment, e.g. driven or obstructed by means of invasive and non-invasive additional potentials. Invasive methods manipulate particles by immediate interactions such as microfluidic flows which drag particles through viscous forces [27], chemical reactions resulting in a directed motion of the colloids [28] or physical obstacles which are fixed to the sample cell and prevent particles from visiting certain regions [29]. Non-invasive methods, on the other hand, manipulate particles without influencing the system as a whole. Examples include the use of the gravitational field of the earth to apply a tilting force on particles with different buoyant masses than

the dispersion medium [29], magnetic fields to apply forces to paramagnetic colloids [30] or electro-magnetic fields, i.e. light, to create potentials dependent on the difference of the refractive index of the particles to that of their surroundings [31]. The disadvantage of invasive methods is usually the lack of flexibility when it comes to changing measurement parameters. While magnetic or light fields can be changed over time without much effort and many side effects, the change of a fluid flow or the exchange of fixed physical obstacles often result in turbulences and the rebuilding of the whole measured system, respectively.

Unlike in many experiments on colloids in external potentials found in the literature [18, 29, 32–34], driving and obstructing potentials are usually not periodic in nature. Even though periodicity often helps understanding basic concepts, e.g. the weather driven by periodic high and low pressure areas, these concepts are often found to be extended by a certain randomness in nature, e.g. the continents altering the otherwise regular distribution of high and low pressure areas around the globe. Similarly, in the microscopic world, randomness plays a crucial role in everyday phenomena. Many examples for motion in random environments can be found in biological matter: a DNA strand resembles a one-dimensional random potential for a protein diffusing on it and thereby facilitates recognition of the right base pair [35], the compartments which diffuse inside a cell move in crowded environments [5] and are thus subject to random forces exerted by neighbouring compartments, or a protein folds according to multidimensional random potential energy landscape where the potential minimum in the random landscape corresponds to the native state of the protein [36]. Random potentials are also found in models describing glasses, where the glass dynamics corresponds to a random walk inside a multidimensional random potential landscape [37]. Furthermore, heterogeneous materials such as rocks exhibit random paths, also called fractals in that context, where fluids can flow [38] which is important to the evolution of the earth's crust [39].

To account for the aspects discussed so far, i.e. driven and obstructed motion, colloidal particles as a model system and non-invasive external potentials, the work described in this thesis focusses on the driven and obstructed dynamics of

colloidal particles in one- and two-dimensional random potential energy landscapes. The landscapes were created by the usage of electro-magnetic waves, i.e. light. The forces exerted on the colloidal particles were the same that are present in optical tweezers [31]. They originated from a difference in refractive indices of the particles and the surrounding medium and could be externally controlled through the light intensity. The colloids had a different density than the medium they were dispersed in and thus formed a two-dimensional layer. In addition, the colloidal particle samples were dilute in most experiments discussed in this thesis and hence particle-particle interactions were not important for the most part. In order to evoke driven motion, time-dependent one-dimensional random potentials and a piezo stage moving the entire sample cell were used. Obstructed motion was caused by adding a second particle species that was restricted in its motion and thus these particle acted as obstacles.

This thesis is split into several chapters in order to successively increase the complexity of the discussed topics. In Chapter II, the thesis starts with addressing the basic physical phenomena necessary to understand the ensuing chapters. The terms soft matter and colloids are defined, before interactions of colloidal particles and their Brownian motion is discussed. Subsequently, optical forces, a pivotal element to most experiments presented in this thesis, are characterised. The expansion of optical tweezers to multidimensional light fields by devices such as a spatial light modulator or an Engineered Diffuser™ is explained in detail while a short excursion to piezoelectricity concludes the chapter.

After the physical phenomena crucial for the later presented experiments have been introduced, Chapter III concentrates on the experimental application of these phenomena. In the work described in this thesis, two different setups were used—one for creating one-dimensional random potentials and another one for random potentials in two dimensions. Both of these setups are explained and the light fields they produce are characterised. The dynamics of colloidal particles was captured by video microscopy in real space. Therefore, common pitfalls concerning this method are addressed and solutions are provided. As the quantification of driven and obstructed dynamics of colloidal particles is the focus,

statistical quantities used throughout this thesis such as variance and excess kurtosis are elaborated on and their characteristics are exemplarily discussed.

Once all the necessary theory and tools have been introduced, Chapter IV deals with the short-time diffusion of single particles in a one-dimensional random energy landscape. The colloids were randomly distributed before they were quenched by the sudden exertion of the random potential. The reaction to this quench manifested in driven particle motion and is primarily studied by means of the diffusion coefficient. The experimental results are compared to a theory and simulations developed by Hartmut Löwen and Michael Schmiedeberg.

The same one-dimensional random potential is focussed on in Chapter V but instead of quenching the single particles once and analysing their reaction, the colloids were quenched periodically and were thus continuously driven while the length of the period was subject to change. The experimental results are again compared to simulations conducted by Michael Schmiedeberg and to the results obtained in Chapter IV. Furthermore, several quantities in addition to the diffusion coefficient are studied to gain insight into the mechanisms related to the dynamics of the periodically driven colloids.

In Chapter VI, driven dynamics of single particles in two-dimensional random potentials are in focus. With the aid of a microscope stage actuated by a piezo, colloids are uniformly dragged with varying forces through random potentials of two different strengths. The motions along the dragging force and perpendicular to it are analysed separately. Several quantities such as the mean, the variance, the skewness and the excess kurtosis of the particle displacements are studied to be able to discern various regimes in the particle dynamics. In addition, first-passage times are computed to further understand the mechanisms leading to these regimes.

Chapter VII concerns obstructed motion of single particles in random potentials. Instead of using only one particle species like in all the previous chapters, colloids with two different sizes were used simultaneously and exerted to the two-dimensional random potential also used in Chapter VI. Larger colloids reacted more strongly to the external potential and were thus more restricted in their mo-

tion. They acted as obstacles with the smaller particles, also called tracers, diffusing around them. Depending on the concentration of the larger particles, a labyrinth-like system similar to a fractal evolved. The dynamics of such a system is studied for different obstacle concentrations. Furthermore, the restriction of the obstacle motion can be tuned by means of the external potential. The effect of the degree of obstacle restriction on the dynamics of the tracers is analysed for two different obstacle concentrations.

This thesis closes with Chapter VIII, where a short summary of all the presented results is found.

II Physical Phenomena

Theoretical concepts are the basis of every experiment. To understand and interpret an experiment, it is crucial to have an overview of the phenomena involved. Therefore, this chapter is dedicated to a brief look into physical phenomena, which ar indispensable for this thesis, namely colloidal particles and their dynamics and interactions, which influence the aforementioned: optical forces and piezoelectricity.

1 Soft Matter and Colloids

As all experiments described in this thesis were conducted with colloidal particles (also called colloids), it is helpful to get to understand the soft matter world to which they belong. Soft matter physics belongs to the wider field of condensed matter physics and is defined by the size range of the objects involved, which lies between 1 nm and 10 µm (Fig. II.1). This size range is often referred to as mesoscopic [40], meaning objects' sizes lie between that of microscopic objects (atoms and molecules) and macroscopic objects (visible to the human eye).[1] The lower boundary is big enough for atomic forces, quantum physics, and chemical details to become unimportant [41, 42]. It also allows the treatment of the medium in which the mesoscopic objects can be dispersed (e.g. water) as being continuous [41, 42]. The upper boundary is such that the energies with which the soft matter objects are bound and distorted are comparable with thermal energy. As a result, Brownian motion, the omnipresent phenomenon in this thesis, can be

[1] Soft matter physics should not be confused with mesoscopic physics. This field also takes its name from the term mesoscopic, but its focus is small electric circuits and is highly quantum physics related—in contrast to soft matter physics.

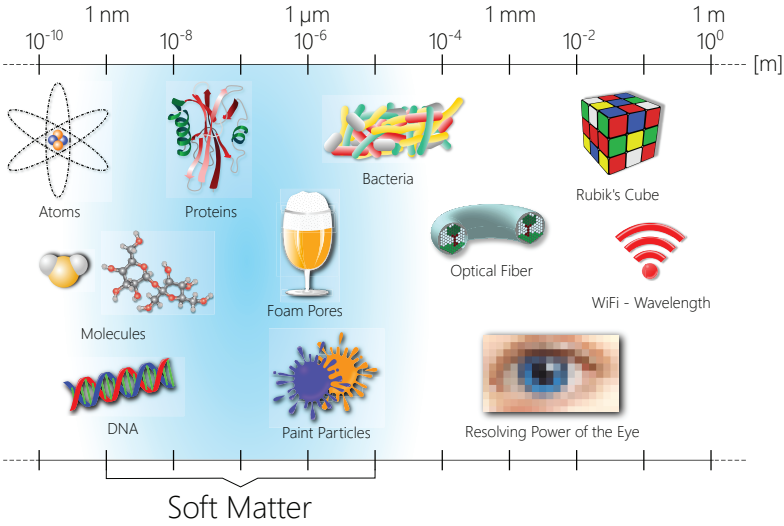

Figure II.1: Length scales of things encountered on a daily basis in comparison to soft matter. Images taken from and based on [43–50].

found throughout soft matter. These low energies are also the reason that soft matter materials flow or can be sheared when they are exposed to sufficiently high forces and can thus be considered soft. Three-dimensional atomic long-range order found in a crystalline solid usually prevents solid-state materials from behaving in that way. The lack thereof distinguishes soft matter from a solid [40].

From these criteria it can be easily inferred that soft matter is encountered very often in day-to-day life. A lot of foodstuffs can be thought of as soft matter [42] and several other materials, such as proteins, foam and paint, exist in the range of the soft matter length scale (Fig. II.1). To get a better overview, soft matter physics is usually divided into the branches colloidal particles, polymers, surfactants, liquid crystals, and active media [41, 51, 52] (Fig. II.2):

– Defining the word colloid or colloidal particles is not an easy task. Etymologically, colloid comes from Greek and means glue-like. It originates

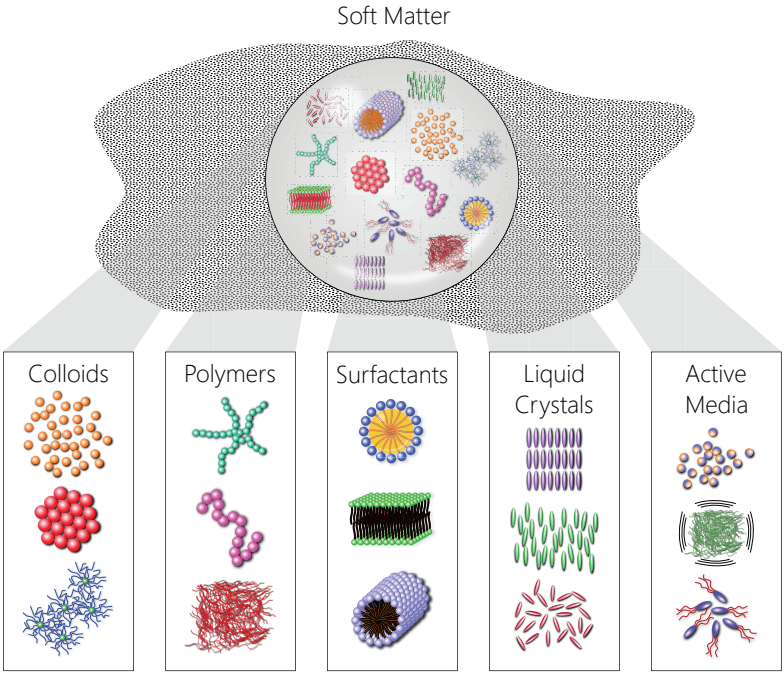

Figure II.2: Branches of soft matter physics: colloids, small particles immersed in a medium; polymer chains made from monomers that are responsible for plastics and rubbers; surfactants, amphiphilic compounds that can lower the surface tension; liquid crystals, rodlike particles able to influence light; active media, particles and networks that are self-propelled.

from gelatinous polymer colloids, which were described by Thomas Graham in 1860 [53]. From this it can be already seen that single fields in soft matter physics, namely colloids and polymers, and especially colloid science, are not restricted by well defined conditions. It has even been stated that every definition of the field of colloids could lead to unnecessary restrictions [54]. Is is nevertheless generally agreed that colloids exist in the size range of 1 nm to 10 µm [42, 53, 55]. Colloids and soft matter in gen-

eral are defined similarly, i.e. the same size range. Therefore, it is not surprising that colloids and soft matter are often used as synonyms. In this thesis, a distinction between colloids and soft matter in general is made. Colloids are usually found in colloidal dispersions. As the word suggests it is different from a normal solution. A colloidal dispersion consists of a discontinuous, dispersed phase, the colloids, and a continuous phase, the dispersion medium [53, 54]. This kind of mixture is often found in real life, e.g. in body fluids and food. Hence there is a whole branch of industry engaged in colloid science [40, 42, 53, 55, 56].

– As seen in Fig. II.2, polymers, which comes from Greek and means many pieces, are chainlike molecules made up of monomers. The monomers, i.e. single pieces, can be anything from amino acids in proteins (Fig. II.1) to single units in rubber, e.g. for tyres. Polymers can consist of tens of millions of monomers [51]. These monomers are usually bound together with covalent bonds that are much stronger than their physical counterparts and therefore bind the monomers on larger time scales than physical bonds would.[2] Polymers can be found as string-like, star-like or gel networks (Fig. II.2) [40, 42]. Due to their versatile shape and composition, polymers are indispensable in modern life. They are the building blocks of rubbers, plastics, films, glues, textiles, biomaterials, and life itself [40, 42, 51].

– The word surfactant is a contraction of "surface active agent" and describes amphiphiles which contain both hydrophilic (water-loving) and hydrophobic (water-hating) materials [40]. They are usually made up of a hydrophilic head group and a hydrophobic tail and thus preferentially adsorb at interfaces and surfaces. Depending on the external influences they face, they can form diverse structures, such as micelles, bilayers, or vesicles (Fig. II.2). These structures are caused by their individual parts seeking to avoid a specific aspect of an environment. For example, when surfactants are dis-

[2] That is one of the reasons why it takes so long for plastic bags to degrade.

solved in water they form micelles in order to shield their hydrophobic parts and minimise any energetically unfavourable contact with water. This behaviour is advantageously used in our everyday life, e.g. when we wash ourselves. Soap is made up of surfactants: when we wash ourselves with water only, the usually hydrophobic dirt will not be solubilised. By adding soap, the dirt will be enclosed by the surfactants and can easily be rinsed off by water due to the now hydrophilic outer shell of the encapsulated dirt.

– The term liquid crystal would usually be an oxymoron, as matter can either be liquid or crystalline but not both at the same time. Liquid crystals however, exhibit both states. Typically, they consist of rod-like or plate-like molecules that are liquid but arranged in a crystalline manner. Some of the phases formed by liquid crystals are shown in Fig. II.2 in a decreasingly ordered fashion. They can either form a crystal, a smectic liquid crystal (not shown), a nematic liquid crystal, or an isotropic liquid. The most common is the nematic phase. With the aid of an electric field, the optical properties of this phase can be changed easily. Therefore, they are widely used in display devices, such as monitors or digital watches [42, 51].

– Active media is a relatively new field in soft matter physics [57–59]. It includes phenomena such as active Brownian motion, in which a particle takes up energy from its environment and converts it into directed motion [60]. For example, Janus particles—colloids that are covered on one side with e.g. gold—can be exposed to laser light that makes them move in a specific direction. Furthermore, active gels play an important role in biology. When a cell divides, its cytoskeletal filaments, an active gel consisting of actin and myosin motors, convert energy into motion [61]. In Fig. II.2, typical microswimmers can be seen underneath the Janus particles and the active gels. They also belong to active media as they can, similar to Janus particles, carry out directed motion due to chemotaxis—motion affected by chemicals in the microswimmers' environment. All these phenomena fuel expectations in drug delivery science as they might help convey medication to the right place inside the human body on a

nanoscale level [62].

1.1 Colloidal Particles

As the work described in this thesis focusses on colloids in particular, this section is designed to give further insight into their properties. In the previous section, it was mentioned that colloidal dispersions consist of two phases: the dispersed phase, more precisely the colloidal particles, and the dispersion medium, which is a continuous phase. The term continuous phase usually refers to a phase that can be thought of as having no boundaries and whose constituent components are in general much smaller than those of the dispersed medium. To better illustrate this matter, Fig. II.3 and the enclosed table show several everyday examples. One very common example is milk, whereby the dispersion medium is water and the dispersed phase consists of liquid oil droplets in the above-mentioned size range. These droplets form a boundary layer with the surrounding water and are therefore discontinuous. It is also due to these droplets that milk appears to be white. The scattering of light by oil droplets gives milk its characteristic look. Milk is an example of a liquid phase dispersed in a liquid phase. Consequently, the dynamics of this system can be rather complicated. This thesis focusses on a simpler realisation of a colloidal dispersion, namely plastic particles dispersed in water. Thus the following considerations and explanations concentrate on this kind of solid-liquid dispersion.

One thing all colloidal dispersions have in common is their size range (see Fig. II.1). This leads to a large surface area-to-volume ratio of the dispersed phase in the dispersion medium. This ratio leads to far-reaching implications for the behaviour of those systems. Due to the high surface area, surface chemistry plays a very important role [40, 54, 55, 63, 64]. As a result, changing the concentration of the colloidal particles can lead to changes of the surface tension of the dispersion [65]. Besides the concentration of the dispersed phase, other defining parameters are the interactions of particles among themselves and between particles and medium. The former range from very basic concepts like the hard-sphere potential to rather complicated ones like externally tunable sizes and at-

tractions [66, 67]. The latter is the well-known Brownian motion, a random walk carried out by colloidal particles due to their collisions with molecules of the dispersion medium. As both are of interest for this thesis, the following sections deal with them in more detail.

1.2 Inter-Particle Interactions

The inter-particle interactions, i.e. the way a particle reacts to the presence of an additional particle, largely determine how stable a colloidal dispersion is. If the potential of the dispersed particles were purely attractive, all particles would aggregate in one point in space and form a particle block in a time span defined by the magnitude of the potential. If the potential were purely repulsive, however, the particles would move apart endlessly.[3] In neither scenario can the dispersion ever reach equilibrium. Therefore, a balance of attractive and repulsive forces is needed to reach an equilibrium state, i.e. to stabilise the colloidal dispersion.

First, a closer look is taken at attractive forces. Two colloidal particles with the same radius, R, dispersed in a medium such as water are considered. These two particles will attract each other due to the van der Waals forces. This attraction originates from the dipole-dipole interaction of the atoms in each particle. As there are many dipoles in each particle, the r^{-6}-dependence, which is characteristic for the van der Waals potential U_{vdW} between two atoms separated by a distance r, becomes[4]

$$U_{\mathrm{vdW}} = -\frac{A_{\mathrm{H}} R}{12(r-2R)}. \tag{II.1}$$

The Hamaker constant, A_{H}, defines the strength of the interaction depending on the particles' and dispersion medium's material. Usually, A_{H} is in the range of several $k_{\mathrm{B}}T$, where k_{B} is the Boltzmann constant and T the absolute temperature. The distance r is defined as the distance between the particle centres. This inherent attractive force between particles has to be compensated by a repulsive

[3] If the colloidal dispersion were inside a finite container, purely repulsive forces would be sufficient to reach equilibrium.

[4] This equation is only obtained when using Derjaguin's approximation assuming the separation of the particles' surfaces to be smaller than the particles' radii [51].

Dispersed Phase	Dispersion Medium	Name	Example
Liquid	Gas	Liquid aerosol	Fog, liquid sprays
Solid	Gas	Solid aerosol	Smoke
Gas	Liquid	Foam	Foams and froths
Liquid	Liquid	Emulsion	Milk, mayonnaise
Solid	Liquid	Sol, colloidal dispersion, paste (high solid content)	Silver iodide in phographic film, paints, toothpaste
Gas	Solid	Solid foam	Polyurethane foam, expended polystyrene
Liquid	Solid	Solid emulsion	Tarmac, ice cream
Solid	Solid	Solid suspension	Opal, pearl, pigmented plastic

Figure II.3: Examples of colloidal dispersions: the upper figure shows examples of three of the most common day-to-day life colloids, namely smoke, paint and milk (from left to right). The lower table gives an overview on the possible kinds of colloidal dispersions and their day-to-day life counterparts. Images taken from [68–70] and table from [40].

force for a colloidal dispersion to be stable. Generally there are two well-known strategies to accomplish this task [51], namely via electrostatic or entropic inter-

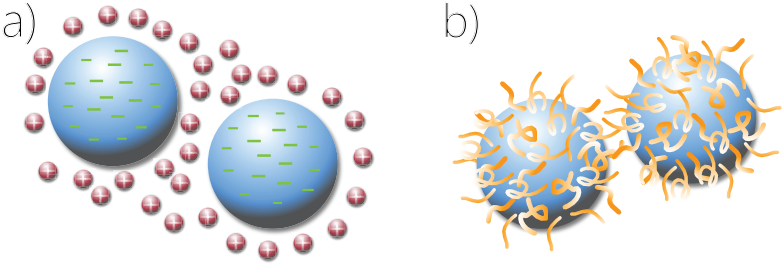

Figure II.4: The two widely known ways of stabilising a colloidal dispersion: a) Charge-stabilisation through surface charges on particles that can be tuned by the amount of counterions in the dispersion medium. In the shown example colloidal particles (blue) are charged negatively. The counterions (red) are therefore positively charged. b) Steric stabilisation through grafted polymers on colloidal particles' surfaces. When polymers (orange) put on colloids (blue) overlap, their mobility is restricted. That causes the particles to repel each other.

actions (Fig. II.4). The former arise by introducing surface charges on the particles. These charges will cause like-charged particles to repel each other. The range of the repulsion can be tuned by the amount of counterions in the surrounding medium. Adding salt to a dispersion of colloidal particles in water will reduce the range of the repulsion for example. This stabilisation method does not work for high salt concentrations and is difficult to apply for organic solvents however [51]. These environments require entropic interactions to stabilise the dispersion. Such interactions can be generated by grafting polymers onto the particle surfaces. Whenever colloids with those polymers approach each other, the mobility of the grafted polymers decreases. This lowers the entropy and, in turn, increases the free energy causing the particles to repel each other [40]. In the work described by this thesis exclusively charge-stabilised colloids have been used. Therefore, this type of stabilisation will be concentrated on going further. Choosing charge-stabilisation leads to an inter-particle potential that can be described by the so-called Derjaguin-Landau-Verwey-Overbeek (DLVO) theory. The DLVO potential, U_{DLVO}, is given by a sum of an attractive and a repulsive

part [40]:

$$U_{\mathrm{DLVO}} = U_{\mathrm{R}} + U_{\mathrm{A}}\,, \tag{II.2}$$

where U_{R} is the repulsive and U_{A} the attractive part. The latter is represented by the van der Waals potential. To define the repulsive part, two spherical colloidal particles with radius R are assumed to be in an electrolyte of bulk concentration c_0. These conditions together with further approximations[5] and Eq. II.1 lead to

$$U_{\mathrm{DLVO}} = \frac{64\pi R k_{\mathrm{B}} T c_0 \Gamma_0^2}{\kappa^2} \exp\{-\kappa(r-2R)\} - \frac{A_{\mathrm{H}} R}{12(r-2R)} \tag{II.3}$$

where

$$\Gamma_0^2 = \frac{\exp\{\zeta e \Phi_0/(2k_{\mathrm{B}}T)\} - 1}{\exp\{\zeta e \Phi_0/(2k_{\mathrm{B}}T)\} + 1} = \tanh\left(\frac{\zeta e \Phi_0}{2k_{\mathrm{B}}T}\right)\,. \tag{II.4}$$

The Debye length, κ^{-1}, describes the distance over which the surface potential of a particle, Φ_0, drops to $1/\mathrm{e}$ of its original value, where $\mathrm{e} = \exp\{1\}$, and is thus a good measure for the range of the repulsive electrostatic potential. The more counterions present in the surrounding medium, the smaller the Debye length and the shorter the range over which the electrostatic repulsion is felt by another particle. To calculate κ and also Γ_0, the valency of the counterion species, ζ, as well as the elementary charge, e, are needed. A typical potential shape reflecting Eq. II.3 and therefore a good description for charge-stabilised particles in an electrolyte is shown in Fig. II.5 a). For very close distances, $r \gtrsim 2R$, the DLVO potential (green line) becomes infinitely high as the particles cannot overlap. When the distance becomes larger, the potential drops below zero as the attractive van der Waals forces (purple line) are felt more strongly than the electrostatic repulsion (red line). For larger distances, the repulsive force dominates. The repulsive electrostatic potential strongly depends on the amount of counterions in the surrounding electrolyte. Similarly, the attractive van der Waals potential can be modified by choosing specific materials for particles and medium. Thus the shape of the DLVO potential can be changed according to the experimenter's needs. If proper conditions are chosen, charge-stabilised colloidal par-

[5] The mentioned approximations can be found in Ref. [40].

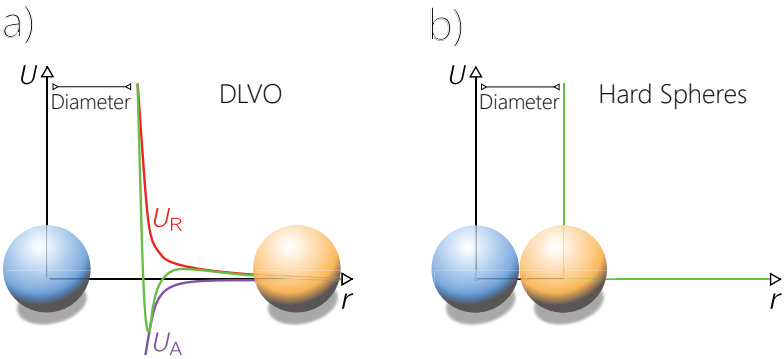

Figure II.5: Two possible interaction potentials of a colloidal dispersion: a) The attractive van der Waals potential inversely proportional to r (purple line) and a repulsive electrostatic force (red line) add up to the DLVO potential (green line). b) Particles do not feel each other until their surfaces touch and they cannot overlap (green line). This potential is referred to as the hard-sphere potential.

ticles can behave similarly to hard spheres with their quite simple interaction potential (Fig. II.5 b)). This potential does not show any dependencies on r except for $r = 2R$. As particles cannot overlap, the potential rises to infinity at that point. Colloidal interaction potentials can often be approximated by the hard sphere case when conducting experiments [71, 72], especially when particle concentrations are very low and therefore distances between particles are so large that interaction forces tend to vanish.

1.3 Brownian Motion—With and Without Drift

In the previous Sec. II.1.2, the focus was the interactions between the colloidal particles themselves. This section focusses on the interactions between colloidal particles and the surrounding medium. To this end, a single spherical colloidal particle dispersed in water is considered. Gravity should not be taken into account for now and additionally this particle does not react chemically with the dispersion medium in any way. It can however interact with the water physically.

If the absolute temperature T is not equal to zero, water molecules can be thought of as a heat bath and will conduct thermal motion. This thermal motion will cause the molecules to move randomly. The higher the temperature is the more thermal energy the molecules have and therefore the faster the molecules move. As the molecules move, they bump into the colloidal particle transferring their energy and causing it to move in a random fashion itself as seen on the left-hand side of Fig. II.6. The resulting random walk of the particle is termed Brownian motion as the botanist Robert Brown was one of the first to describe it in 1828 [73]. However, Albert Einstein in 1905 [74] and Paul Langevin in 1908 [75] were the first to construct theories describing it. Throughout this section, this motion will be mainly described in only one dimension, which is referred to as the x-direction. The formulae and explanations stated below can be generalised to all three dimensions. In general, every colloidal object with a mass, m, exposed to a heat bath will undergo Brownian motion. According to the equipartition theorem, an object's mean kinetic energy in one dimension reads [76]

$$\frac{1}{2}m\langle v_{\mathrm{B},x}^2\rangle = \frac{1}{2}k_{\mathrm{B}}T \quad \Leftrightarrow \quad \sqrt{\langle v_{\mathrm{B},x}^2\rangle} = \sqrt{\frac{k_{\mathrm{B}}T}{m}}\,. \tag{II.5}$$

The object's root mean square velocity, $\sqrt{\langle v_{\mathrm{B}}^2\rangle}$, is inversely proportional to its mass. Therefore, Brownian motion is not observable for macroscopic objects.

To describe Brownian motion in a more quantitative way, an ensemble of colloidal particles rather than a single particle is considered in the following [41, 74, 76]. The basis of the description is Anton Fick's diffusion equations. Fick's first law of diffusion relates a gradient in a space- and time-dependent distribution of particles, $\varrho_N(x,t)$, also referred to as particle concentration or density, to a particle flux, $J_x(x,t)$, using the diffusion coefficient, D, via

$$J_x(x,t) = -D\frac{\partial\,\varrho_N(x,t)}{\partial x}\,, \tag{II.6}$$

where t denotes time. From Eq. II.6, it can be seen that the higher the particle concentration gradient is, the bigger the flux in the opposite direction.

In this regard, the diffusion coefficient D is a factor describing the relation between concentration gradient and flux. To quantify this relation, one can think of the non-interacting particle distribution in water inside a sealed container—this time being exposed to gravity in the z-direction. In thermal equilibrium, the particle density, $\varrho_{N,\mathrm{g}}(z)$, dependent on the height z can be written as

$$\varrho_{N,\mathrm{g}}(z) = \varrho_{N,0} \exp\left\{-\frac{F_\mathrm{g} z}{k_\mathrm{B} T}\right\} \tag{II.7}$$

with $\varrho_{N,0}$ being the concentration at the bottom of the container and F_g being the gravitational force. Inside the container, there are two fluxes that balance each other as the container is in an equilibrium state. Firstly, there is a flux, J_g, due to F_g acting on the particles. The gravitational force leads to a velocity of the particles via $v_\mathrm{g} = F_\mathrm{g}/\xi$, where ξ is the coefficient of friction depending on the particle shape and size. Therefore, the resulting flux reads

$$J_\mathrm{g}(z) = \varrho_{N,\mathrm{g}}(z) v_\mathrm{g} = \varrho_{N,\mathrm{g}}(z) \frac{F_\mathrm{g}}{\xi} . \tag{II.8}$$

As already mentioned, $J_\mathrm{g}(z)$ is counterbalanced by a second flux. This flux is due to diffusion and was introduced in Eq. II.6. In equilibrium, both fluxes yield

$$J_\mathrm{g}(z) = J_z(z) \quad \Leftrightarrow \quad \varrho_{N,\mathrm{g}}(z) \frac{F_\mathrm{g}}{\xi} = -D \frac{\partial \varrho_{N,\mathrm{g}}(z)}{\partial z} = D \frac{F_\mathrm{g}}{k_\mathrm{B} T} \varrho_{N,\mathrm{g}}(z) . \tag{II.9}$$

Here Eq. II.7 was used together with the fact that thermal equilibrium cancels out the time dependence in Eq. II.6. The balance of both fluxes in Eq. II.9 then leads to the Stokes-Einstein relation and thereby to the quantification of the diffusion coefficient,

$$D = \frac{k_\mathrm{B} T}{\xi} \quad \overset{\xi=\xi_\mathrm{b}}{\Longrightarrow} \quad D_\mathrm{b} = \frac{k_\mathrm{B} T}{6\pi\eta R_\mathrm{h}} , \tag{II.10}$$

where a friction coefficient determined by Stokes $\xi_\mathrm{b} = 6\pi\eta R_\mathrm{h}$ for a spherical particle with the hydrodynamic radius, R_h,[6] in the bulk of a medium with viscosity

[6] For a hard sphere, $R_\mathrm{h} = R$.

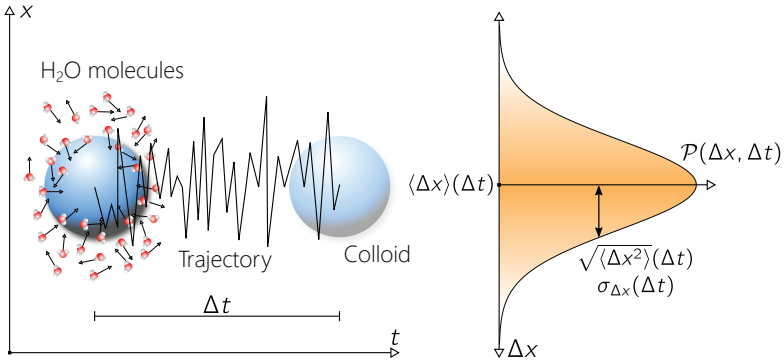

Figure II.6: Brownian motion shown in one dimension x. Due to collisions with water molecules, the colloidal particle performs a random walk. A one-dimensional time-dependent schematic trajectory with time length Δt is shown on the left-hand side (black line). The resulting histogram of displacements Δx is shown on the right in orange and typically resembles a Gaussian function. For pure Brownian motion, the mean displacement $\langle \Delta x \rangle$ vanishes and therefore the mean square displacement, here defined as the second moment about zero $\langle \Delta x^2 \rangle$ equals the variance of displacements $\sigma^2_{\Delta x}$.

η is assumed [51].[7] From Eq. II.10 it is apparent that the diffusion increases with increasing temperature of the surrounding medium or decreasing size of particles.

Now that the diffusion coefficient has been derived, the gravitation is again omitted. From the continuity equation and Eq. II.6, one arrives at Fick's second law of diffusion, which reads[8]

$$\frac{\partial \varrho_N(x,t)}{\partial t} = D \frac{\partial^2 \varrho_N(x,t)}{\partial x^2}. \tag{II.11}$$

It establishes a connection between the time and space dependence of the particle

[7] This equation for the coefficient of friction is only valid for very small Reynolds numbers $Re \ll 1$.
[8] It is assumed that the diffusion coefficient is position-independent, i.e. $D(x) = D$.

distribution and can be solved by a Gaussian function:

$$\varrho_N(x,t) = \frac{1}{\sqrt{4\pi Dt}}\exp\left\{-\frac{x^2}{4Dt}\right\}. \tag{II.12}$$

Instead of considering a particle distribution, $\varrho_N(x,t)$, one can also think of the distribution of displacements of a single Brownian particle. The corresponding probability density function (PDF), $\mathcal{P}(\Delta x, \Delta t)$,[9] can be derived with the same argument and will be similar to Eq. II.12. On the left-hand side of Fig. II.6, The trajectory of a single particle for a time interval, Δt, is depicted. In an experiment, the measured quantities are not necessarily absolute but rather time intervals Δt and spatial displacements Δx, which additionally are not continuous as they are assumed to be here. Still, a measured probability density function can be often described by a continuous function, which can be written, similarly to Eq. II.12, as

$$\mathcal{P}_\mathrm{B}(\Delta x, \Delta t) = \frac{1}{\sqrt{4\pi D\Delta t}}\exp\left\{-\frac{\Delta x^2}{4D\Delta t}\right\}, \tag{II.13}$$

where the index B denotes Brownian motion. Eq. II.13 describes the self-part of the van-Hove function, i.e. the continuous probability distribution function calculated from discrete values measured in an experiment, which will be explained in more detail in Sec. III.4.1 [78, 79]. Figure II.6 indicates what $\mathcal{P}(\Delta x, \Delta t)$ looks like for a typical trajectory given on its left-hand side: For a random walk with no preferred direction the first moment, $\langle \Delta x \rangle$, its mean, vanishes. Angle brackets refer to an average of the PDF over time or ensembles. The second moment,

[9] The term probability density function is used to describe a continuous probability distribution function, since the term probability distribution function is quite general. In some sources a discrete PDF is called probability mass function whereas a continuous PDF is called probability density function [77]. In this thesis, naturally all described measurements produce discrete data as there are no continuous data in an actual experiment and its postprocessing. However, continuous probability distribution functions can be calculated from discrete measurement values by binning data and assigning a probability density to them. Continuous functions like the Gaussian function can then often well describe discrete data obtained in the work described in this thesis. Therefore, all the probability distribution functions used in this thesis are continuous ones and can also be called probability density functions. They are referred to as PDF or $\mathcal{P}$ mostly. It is never used for cumulative probabilities. These are called cumulative distribution functions here.

$\langle \Delta x^2 \rangle(\Delta t)$, of a Gaussian determines how broad it is and can be determined to be

$$\langle \Delta x^2 \rangle(\Delta t) = 2D\Delta t\,. \tag{II.14}$$

It increases linearly in time and thus indicates, together with Eq. II.13, a broadening of the distribution due to Brownian motion. As displacements along different dimensions are independent for Brownian motion, the second moment, $\langle \Delta \boldsymbol{r}^2 \rangle(\Delta t)$, in d dimensions reads [42]

$$\langle \Delta \boldsymbol{r}^2 \rangle(\Delta t) = 2dD\Delta t\,, \tag{II.15}$$

where $\boldsymbol{r}$ represents a d-dimensional vector. The second moment of PDFs of the particle displacements is often called the mean square displacement (MSD). The MSD is the first non-vanishing moment for pure Brownian motion and thus is often calculated to quantify the particle dynamics. As can be seen in Fig. II.6 the vanishing first moment is tantamount to the second moment being equal to the variance of the PDF, $\sigma^2_{\Delta x}(\Delta t)$, since

$$\sigma^2_{\Delta x}(\Delta t) = \langle \Delta x^2 \rangle - \langle \Delta x \rangle^2 \tag{II.16}$$

and thus

$$\sigma^2_{\Delta x}(\Delta t) = 2D\Delta t \quad \text{or} \quad \sigma^2_{\Delta \boldsymbol{r}}(\Delta t) = 2dD\Delta t\,. \tag{II.17}$$

If there is a preferred direction for the random walk of the particle, things look slightly different. The higher probability to take a step in the preferred direction leads to the particle drifting that way sooner or later. To get a better idea of the issue, a particle undergoing Brownian motion in one dimension is considered once more. This time a constant drag force, F_D, is added. The constant force is proportional to a drag velocity, v_D, and can be expressed as

$$F_\mathrm{D} = \xi\, v_\mathrm{D} \tag{II.18}$$

with ξ being the friction coefficient of the surrounding medium, in this case wa-

ter. Due to the constant force, Fick's first law (Eq. II.6) changes to[10]

$$\begin{aligned} J_{\mathrm{D}}(\Delta x, \Delta t) &= -D\frac{\partial \mathcal{P}_{\mathrm{D}}(\Delta x, \Delta t)}{\partial \Delta x} + v_{\mathrm{D}}\mathcal{P}_{\mathrm{D}}(\Delta x, \Delta t) \\ &= -D\frac{\partial \mathcal{P}_{\mathrm{D}}(\Delta x, \Delta t)}{\partial \Delta x} + \frac{F_{\mathrm{D}}}{\xi}\mathcal{P}_{\mathrm{D}}(\Delta x, \Delta t)\,, \end{aligned} \tag{II.19}$$

where the index D stands for drift. Together with the continuity equation, Eq. II.19 can be written as[11]

$$\frac{\partial \mathcal{P}_{\mathrm{D}}(\Delta x, \Delta t)}{\partial \Delta t} = D\frac{\partial}{\partial \Delta x}\left[\frac{\partial}{\partial \Delta x} - \frac{F_{\mathrm{D}}}{k_{\mathrm{B}}T}\right]\mathcal{P}_{\mathrm{D}}(\Delta x, \Delta t)\,. \tag{II.20}$$

The solution of this differential equation is slightly different to Eq. II.13:

$$\mathcal{P}_{\mathrm{D}}(\Delta x, \Delta t) = \frac{1}{\sqrt{4\pi D\Delta t}}\exp\left\{-\frac{(\Delta x - v_{\mathrm{D}}\Delta t)^2}{4D\Delta t}\right\}. \tag{II.21}$$

The behaviour of $\mathcal{P}_{\mathrm{D}}(\Delta x, \Delta t)$ for different time intervals Δt can be seen in Fig. II.7. As can be seen there, the PDF of Brownian particles being dragged by a force F_{D} is not centred about zero as was the case with Eq. II.13, but about its non-vanishing first moment $\langle \Delta x \rangle(\Delta t) = v_{\mathrm{D}}\Delta t$. On the left-hand side, $\langle \Delta x \rangle(\Delta t_1) = 0$ and thus $\mathcal{P}_{\mathrm{D}}(\Delta x, \Delta t_1)$ is very similar to the distribution shown in Fig. II.6. On the right-hand side, the same function is found for a longer time interval. Instead of a Gaussian broadening with time at $\Delta x = 0$, the PDF broadens while its mean additionally increases with $v_{\mathrm{D}}\Delta t$. Thus the second moment $\langle \Delta x^2 \rangle_{\mathrm{D}}(\Delta t_2)$ is not equal to the variance $\sigma_{\Delta x}(\Delta t_2)$ but is larger by $v_{\mathrm{D}}^2\Delta t^2$. The variance itself still follows Eq. II.17, whereas $\langle \Delta x^2 \rangle(\Delta t)$ does not. More details on the second moment and variance are given in Sec. III.4.3.

[10] As noted before, instead of a particle density $\varrho_N(x, t)$ one can use the PDF for a single particle, $\mathcal{P}(\Delta x, \Delta t)$, which is done here.

[11] It is assumed that the diffusion coefficient is position-independent, i.e. $D(x) = D$.

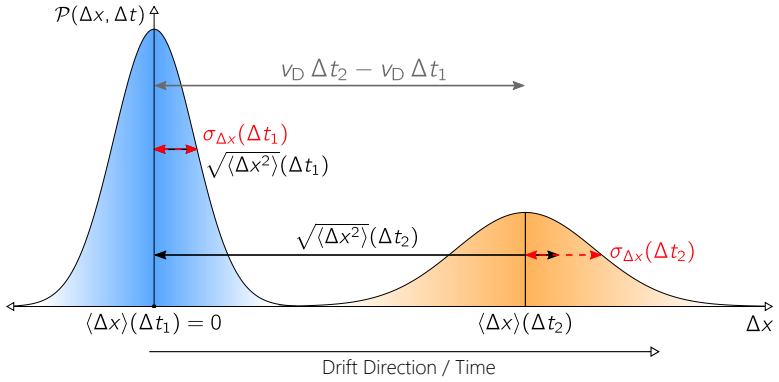

Figure II.7: Histograms of displacements Δx for time Δt_1 and at a later time Δt_2 for particles being exposed to Brownian motion and a drag velocity, v_D, are shown. At $\Delta t = \Delta t_1$, the first moment $\langle \Delta x \rangle$ vanishes. Thus the second moment and the variance are equal. That changes when the first moment changes over time with $v_D \Delta t$ due to the drift. Then there can be a significant difference between $\langle \Delta x^2 \rangle$ and $\sigma^2_{\Delta x}$.

1.4 Models of Anomalous Diffusion

Now that the theory of Brownian motion has been introduced, several models of anomalous diffusion will be described, i.e. when the particle dynamics does not follow Eq. II.17 but [5, 80–82]

$$\sigma^2_{\Delta x}(\Delta t) = 2D\Delta t^{\alpha_D} \quad \text{or} \quad \sigma^2_{\Delta \boldsymbol{r}}(\Delta t) = 2bD\Delta t^{\alpha_D}\,. \tag{II.22}$$

The anomalous diffusion exponent, $\alpha_D(\Delta t)$, quantifies how strongly the dynamics deviates from Brownian motion. When $\alpha_D = 1$, Eq. II.17 is recovered. Thus, $\alpha_D \neq 1$ indicates anomalous diffusion of particles. For $\alpha_D < 1$, the variance grows slower than expected for Brownian motion. Particle behaviour is called subdiffusive. When $\alpha_D > 1$, particles spread faster than expected. They are said to be superdiffusive.

One of the most common models is the continuous time random walk (CTRW), which was introduced by Montroll and Weiss in 1965 [83] and is often used to

describe diffusion in biological samples [82, 84, 85]. Brownian motion can be described by a particle undergoing steps at a constant rate with a constant length in a random direction [86, 87]. A CTRW is similar to Brownian motion but the time at which a particle moves, the waiting time, Δt_W, and the step length, Δx_S, are random [82, 88]. Both, Δt_W and Δx_S, are drawn from PDFs, $\Psi(\Delta t_W)$ and $\mathcal{P}(\Delta x_S)$ respectively, so that every new pair is independent of the pair chosen for the previous step [88]. When the mean waiting time, $\langle \Delta t_W \rangle$, and second moment of the step length, $\langle \Delta x_S^2 \rangle$, are finite, Brownian motion is found for $\Delta t \to \infty$. When $\Psi(\Delta t_W) \propto \Delta t_W^{-1-\alpha_D}$ and $0 < \alpha_D < 1$, the mean waiting time tends to infinity. As a result, particle motion becomes subdiffusive and Eq. II.22 is found for long times [5, 86, 88]. Additionally, due to the long time tail in $\Psi(\Delta t_W)$, the system evolves in time and is said to be ageing [82, 86, 88]. A superdiffusive case of the CTRW is the Lévy flight. Instead of $\langle \Delta t_W \rangle$, the second moment of Δx_S is infinite [88]. This happens when $\mathcal{P}(\Delta x_S) \propto \Delta x_S^{-1-b}$ and $0 < b < 2$. As a result, a series of small displacements is interrupted by large ones leading to a diverging MSD [88]. For situations where the concept of Lévy flights—the instantaneous particle movement independent of the step length—is considered unphysical, the Lévy walk model can be used instead [89]. It couples Δt_W and Δx_S and leads to finite MSDs [88].

A different, yet not less commonly used [85, 90] model, is fractional Brownian motion (FBM) introduced by Mandelbrot and van Ness in 1968 [91]. It can be defined by the covariance

$$\langle \Delta x(\Delta t_1) \Delta x(\Delta t_2) \rangle \propto \Delta t_1^{\alpha_D} + \Delta t_2^{\alpha_D} - |\Delta t_1 - \Delta t_2|^{\alpha_D}\,, \tag{II.23}$$

which reduces to Eq. II.22 for $\Delta t_1 = \Delta t_2$. For $\alpha_D < 1$, displacements are negatively correlated corresponding to chaotic behaviour with trajectories being curlier than for Brownian motion [92, 93]. When $\alpha_D > 1$, displacements are positively correlated. Particle trajectories have a higher persistence and are smoother than for Brownian motion. Both scenarios yield anomalous diffusion following Eq. II.22 for long times. Fractional Brownian motion can be thought of as a description of one particle in a many-particle system [94] and thus is used as a model

for diffusion in viscoelastic environments [82, 85], single-file diffusion [85, 95][12] and conformations of polymer chains [93]. In practice, it is often compared to CTRW [85, 97], where an essential difference between the two models is ageing of the system, which is asymptotically found for CTRW but only transiently for FBM [88, 94, 98].

A third widely used model related to anomalous diffusion is obstructed motion or diffusion in a fractal [5, 82, 88, 99]. In models like CTRW and FBM, motion is implicitly assumed to take place in a homogeneous medium, since waiting times in CTRW and correlations of displacements are not bound to certain positions in space [5]. In contrast to this, obstructed motion explicitly describes the particle dynamics in a spatially heterogeneous medium, where motion is affected by, e.g., obstacles or labyrinthine environments [5, 82]. Obstacle concentration plays a crucial role in whether and when subdiffusive motion is found. For low obstacle concentrations, particles show only transient subdiffusivity, whereas for high concentrations, particle motion is restricted to a finite region resulting in a constant $\sigma^2_{\Delta \boldsymbol{r}}$ for $\Delta t \to \infty$. In between these two extreme cases, subdiffusive motion following Eq. II.22 is found for long times. The value of α_D is then defined by the dimensionality of the system and characteristics of the used model [5]. An experimental realisation of obstructed motion is presented in Sec. VII and the concept of fractals and diffusion are discussed in more detail.

Besides these three models, there are several other models found in the literature, such as scaled Brownian motion, where the diffusion coefficient is dependent on time [82, 88]. For $D(\Delta t) \propto \Delta t^{\alpha_\mathrm{D}-1}$ and $0 < \alpha_\mathrm{D} < 2$, particle displacements can be described by Eq. II.22. Thus sub- and superdiffusion can be found for scaled Brownian motion [88]. When D is independent of time but depends on position $\boldsymbol{r}$, particle motion is referred to as a heterogeneous diffusion process [88]. Particles accumulate in low diffusivity regions and show similar characteristics as in a CTRW [88]. However, heterogeneous diffusion processes are different from CTRW as they do not exhibit the renewal process after each step that is integral to the latter, but exhibit a static distribution of diffusivity values.

[12] Single-file diffusion is, e.g., found for hard sphere-like particles diffusing in a narrow channel [96]. It results in $\sigma^2_{\Delta x} \propto \Delta t^{1/2}$ for $\Delta t \to \infty$.

Depending on the space dependency assumed for $D(\boldsymbol{r})$, either sub- or superdiffusive motion can be found [88, 100, 101]. Additionally, anomalous diffusion can depend on the spatial direction in which they are probed.

2 Optical Forces and Landscapes

Interactions between light[13] shaped to a specific pattern and matter, namely a transfer of momentum from the former to the latter constitute an integral part of the work described in this thesis. They are responsible for the anomalous colloidal dynamics described later. Therefore, the following sections deal with these interactions, where they stem from, and the shaping of light to non-trivial patterns.

In everyday life, a change of momentum caused by light is rarely encountered. It is well known that sunlight can heat up a car over a longer period of time or that it can be converted to electrical energy with the help of a solar panel. Light setting a car into motion has not yet been observed, even though it can contain a high amount of energy. The reason is that the momentum flux of light is connected to its energy flux by the speed of light, c [31, 102]:

$$\frac{\mathrm{d}p}{\mathrm{d}t} = \frac{n\frac{\mathrm{d}E}{\mathrm{d}t}}{c} \quad \Leftrightarrow \quad F = \frac{nP}{c}, \tag{II.24}$$

where p is the momentum, E the wave energy, P the power, F the resulting force and n the refractive index of the medium in which the light travels. So even if an electromagnetic wave hits an object and all the power is converted to force, the resulting force is about eight orders of magnitude lower than the power of the wave. For practical reasons, an efficiency factor, Q, is introduced. The force then reads $F = QnP/c$ and can be measured in units of nP/c. The factor Q is a dimensionless quantity describing the ratio of power converted to force and is usually around 0.1–0.2 [103]. From eq. II.24, it is known that high powers and

[13] As in all the experiments described in this thesis, the used electromagnetic waves have wavelengths in the visible range, light and electromagnetic waves are used as synonyms here.

a high sensitivity to momentum changes are needed in order to observe optical forces. Arthur Ashkin noticed that these conditions were met with the help of a then newly invented laser and a highly focussing microscope objective together with colloidal particles immersed in water [102, 104]. In 1970, he was the first to describe manipulating the motion of a particle with light [104]. Later, in 1986, Ashkin et al. [105] were able to trap a colloidal particle inside a laser beam in all three spatial directions—the optical tweezers were born. Steven Chu, one of the coauthors of Ref. [105], went on to refine the technique Ashkin first applied and was able to not only trap colloidal particles like Ashkin but to cool atoms [106, 107]. Subsequently Chu, together with Claude Cohen-Tannoudji and William D. Phillips, received the Nobel Prize in 1997 for their developments of methods to cool and trap atoms with laser light [108]. In this thesis, trapping of colloidal particles rather than atoms is central. Therefore, the matter with which the light interacts will always be assumed to be a colloidal particle in the following chapters.

2.1 Theory of Optical Forces: Optical Tweezers

To understand the theory of optical forces, it is useful to consider the simplest situation, namely optical tweezers. They are made up of one strongly focussed laser beam that is brought into contact with an object in the colloidal size range (cf. Fig. II.8 a)). Optical tweezers are able to exert forces on this small object and thus hold it at a specific position. When changing the focal position of the beam, the object is dragged with the beam—just like one would grab the object with tweezers. Here, the object is assumed to be a spherical colloidal particle with radius R and refractive index n_P immersed in a medium with refractive index n_M.

As stated in Sec. II.2, Ashkin was the first to manipulate particle movement with the help of laser light [104]. He did so by shining a laser beam on particles. The particles were forced to move in the propagation direction of the beam until they reached the end of the sample cell and were pressed against its walls. The optical force responsible for the particles moving in direction of the beam is called radiation pressure or scattering force F_S and can intuitively be explained by the

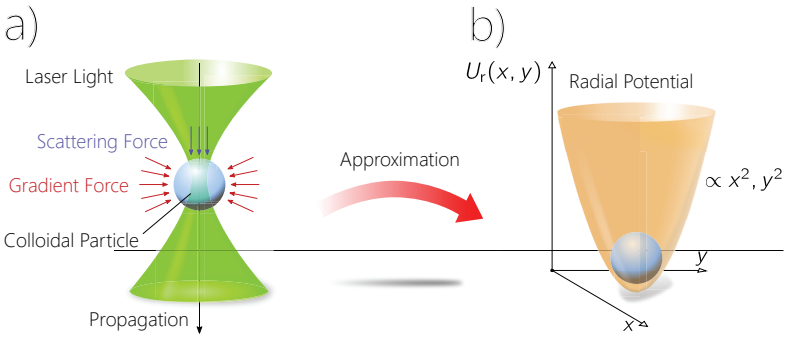

Figure II.8: Classical optical tweezers and their approximation by a harmonic oscillator potential. a) When applying a tightly focussed beam on a colloidal particle, scattering and gradient forces act on the particle trapping it inside the focus. b) For small displacements from its equilibrium position, the particle can be treated as if it was inside a harmonic oscillator with a radial potential $U_r(x, y) \propto x^2$ and y^2 [109]. Image inspired by [110].

momentum carried by light. The transfer of momentum from light to particles due to absorption or scattering results in a force in the propagation direction of light [102], as can be seen in Fig. II.8 a). Later Ashkin managed to manipulate particles in all three spatial directions [105]. This discovery can be ascribed to a second force that is present when light interacts with matter: the gradient force, F_G. Its qualitative explanation is not as easy as that for the scattering force but can also be made in terms of momenta [102]. The momentum of a beam of light largely depends on its degree of collimation. Only the components parallel to the beam axis contribute to the momentum of the beam. The more the beam is focused the smaller the total momentum. Therefore, every change in the convergence of the beam leads to a transfer in momentum $p \propto k$, where k is the wave vector. Depending on the refractive index of a particle, n_P, in comparison to that of the surrounding medium, n_M, it can act as a converging or diverging lens.

Figure II.9 a) shows a particle acting as a converging lens, since n_P is larger than n_M. On the left-hand side of Fig. II.9 a), a focussed beam is converged even

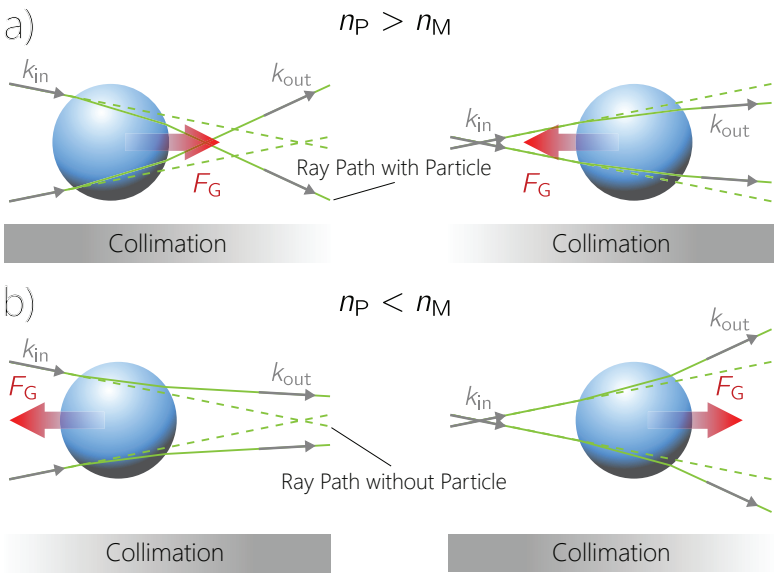

Figure II.9: The gradient force, F_G, explained with the change of photon momentum $p \propto k$, where k represents the wave vector. The ray paths with the particle being present are represented by solid green lines whereas the paths that would be valid without an interaction with a particle is drawn in dotted green lines. When hitting the particle, the total momentum of the beam is changed as its degree of collimation is changed indicated by the grey bars. If the particle causes the beam to be less collimated, the particle will be pushed towards the direction of propagation (top left and bottom right). The opposite happens if the beam is more collimated after it has hit the particles (Fig. II.9, top right and bottom left). Thus particles with a refractive index $n_P > n_M$ are pushed towards the focal spot of a beam, whereas particles with $n_P < n_M$ are pushed away from it. Figure idea taken from [102].

more strongly. The beam (solid green lines) is less collimated than it would be if it did not hit the particle (dotted green lines) which is indicated by a lighter grey colour in the collimation bar. This results in a gradient force F_G in the direction of propagation of the ray. On the right-hand side, the same situation is shown, but the particle is situated behind the focal spot of the beam and causes it to be more highly collimated afterwards. The outcome is a gradient force in the oppo-

site direction. In both cases, the particle is dragged towards the focal spot of the beam.

Figure II.9 b) shows a particle acting as a diverging lens. There the originally focussed beam is defocused by the particle causing it to be more collimated afterwards (Fig. II.9 b), left). Hence, F_G points conversely to the propagation direction of the beam. The opposite is the case when the same particle is situated behind a focal spot. Then the gradient force points in the propagation direction of the beam. Thus, when $n_P < n_M$, particles are pushed away from the focal spot.[14] The same argument holds for the lateral directions: particles with $n_P > n_M$ are drawn towards the focal spot of a beam and particles with $n_P < n_M$ are pushed away from it. Thus the gradient force is decisive for trapping a particle inside an optical beam. The interplay of F_S and F_G then leads to the actual potential a particle feels inside the focal spot of optical tweezers and defines its ability to trap a particle. To constantly trap a particle, F_G has to be larger than F_S. Otherwise the particle is not trapped but only pushed in the propagation direction of the beam. To quantify the effective forces, one usually draws on the efficiency factor Q [111–113] and approximates the radial trapping potential originating from the scattering and gradient forces with that of a common spring or a two-dimensional harmonic oscillator $U_r(x, y)$ (Fig. II.8 b)) [103, 109, 114].[15] From that potential, one can then draw the radial spring constant k_r, also called the trap stiffness, and the related force $F_r = -k_r \Delta r$ [102, 113, 115]. As this is an approximation, it only holds for small displacements Δr from the equilibrium position of the trap [109]. Nevertheless, it is widely used to characterise the ability of the optical tweezers to trap a particle [109, 113, 116]. When used in biological environments, k_r is typically around 5×10^{-5} N/m [31]. Taking into consideration that a typical biological sample moves in the micrometre-to-nanometre-range, forces usually vary around the order of piconewtons and are therefore large enough to strongly restrict the movement of a particle. They counteract the Brownian motion and

[14] In this thesis n_P is always larger than n_M. Still, all the explanations and equations established in this section are valid for both cases.

[15] Only the radial potential is considered here since particles are only trapped in radial directions and therefore the axial potential is not relevant to the rest of this thesis.

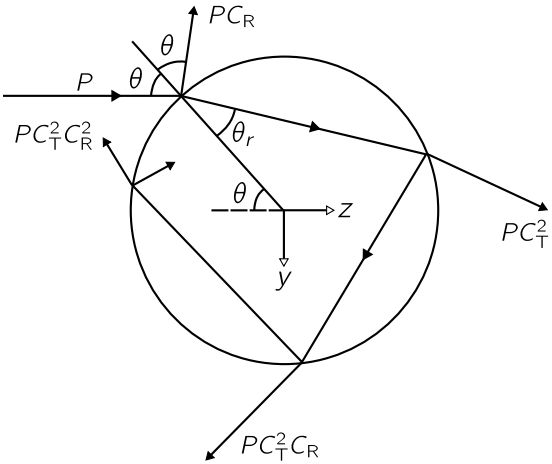

Figure II.10: Descriptive drawing of Ashkin's assumptions when calculating the optical forces in the ray optics regime. Figure redrawn from [118].

cause the particle to move as if it were in a harmonic potential (Fig. II.8 b)) [103].

To calculate the gradient and scattering forces exactly, there are two approaches that concur with two limiting cases [102]. The first approach is the calculation of the momentum flux towards a particle using the so-called ray optics regime, where the particle radius, R, is much larger than the wavelength of the incident light, λ. The second approach is to calculate the force per unit volume with the so-called Rayleigh scattering regime where $R \ll \lambda$ holds.

Roosen and Ashkin were the first to calculate the forces for the first case, the ray optics regime [117, 118]. Ashkin assumed a dielectric spherical particle being hit by a light beam of power P (Fig. II.10). The particle was assumed to have an transmission coefficient, C_T, and a reflection coefficient, C_R. Angles θ and θ_r are the angles of incidence and its counterpart on the inside of the particle, respectively. Summing up all the reflected and refracted rays hitting the outside and

inside of the surface of the particle leads to the following equations [118]:

$$F_S = \frac{n_M P}{c}\left\{1 + C_R\cos(2\theta) - \frac{C_T^2[\cos(2\theta - 2\theta_r) + C_R\cos(2\theta)]}{1 + C_R^2 + 2C_R\cos(2\theta_r)}\right\}$$
$$F_G = \frac{n_M P}{c}\left\{C_R\sin(2\theta) - \frac{C_T^2[\sin(2\theta - 2\theta_r) + C_R\sin(2\theta)]}{1 + C_R^2 + 2C_R\cos(2\theta_r)}\right\}. \tag{II.25}$$

In the literature, there are several results for the ray optics regime. Nieminen et al. used the same approach and derived the multidimensional momentum delivered to the particle, $\Delta\boldsymbol{p}$ [102]:

$$\Delta\boldsymbol{p} = \int_{t_1}^{t_2}\int_{A_P} \boldsymbol{T}_M \,\mathrm{d}\boldsymbol{A}\,\mathrm{d}t + \epsilon\mu\int_{V_P}\boldsymbol{S}(t_1)\,\mathrm{d}V - \epsilon\mu\int_{V_P}\boldsymbol{S}(t_2)\,\mathrm{d}V \tag{II.26}$$

whereby t_1 and t_2 are times during which the electromagnetic field of the beam changes, $\boldsymbol{T}_M$ is the Maxwell stress tensor, $\boldsymbol{S}$ is the Poynting vector, ϵ is the permittivity and μ the permeability of the particle, A_P is the surface area and V_P the volume of the particle.

The second approach relies on calculating the force per unit volume. The light waves hitting the particle are assumed to be time-harmonic. Additionally, the Rayleigh approximation is used, so that the particle is assumed to be so small that the electric field of the incident light is constant inside the whole particle volume. Therefore, one can treat the whole particle as one dipole with an electric dipole moment, $\boldsymbol{m}_E$, and start with the Lorentz force on a dipole [102, 119, 120]:

$$\boldsymbol{F}_L(\boldsymbol{r},t) = [\boldsymbol{m}_E(\boldsymbol{r},t)\cdot\nabla]\boldsymbol{E}(\boldsymbol{r},t) + \frac{d\,\boldsymbol{m}_E(\boldsymbol{r},t)}{dt}\times\boldsymbol{B}(\boldsymbol{r},t)\,, \tag{II.27}$$

where $\boldsymbol{r}$ is a spatial vector, and $\boldsymbol{E}$ and $\boldsymbol{B}$ are the space- and time-dependent electric and magnetic field in which the dipole is situated. Together with the relation of the dipole moment to the electric field $\boldsymbol{m}_E = \alpha_p\boldsymbol{E}$, where α_p is the polarisability of the particle, and the vector identity $(\boldsymbol{E}\,\nabla)\boldsymbol{E} = \nabla(\boldsymbol{E}^2)/2 - \boldsymbol{E}\times(\nabla\times\boldsymbol{E})$, Eq. II.27

reads [102, 119, 120]:

$$\boldsymbol{F}_{\mathrm{L}}(\boldsymbol{r},t) = \alpha_p \cdot \left[\nabla\left(\frac{1}{2}\boldsymbol{E}(\boldsymbol{r},t)^2\right) + \frac{d}{dt}\left(\boldsymbol{E}(\boldsymbol{r},t)\times\boldsymbol{B}(\boldsymbol{r},t)\right)\right], \tag{II.28}$$

since $\nabla \times \boldsymbol{E} = 0$. The polarisability of a sphere can be computed as [120, 121]:

$$\alpha_p = 4\pi\epsilon_0 n_{\mathrm{M}}^2 \left(\frac{\Xi^2-1}{\Xi^2+2}\right) R^3, \tag{II.29}$$

with the vacuum permittivity ϵ_0 and $\Xi = n_{\mathrm{P}}/n_{\mathrm{M}}$. To calculate the force on the particle for not only a specific point in time t, but for all times, Eq. II.28 is averaged over time for its first and second term on the right-hand side separately.

Considering the first term on the right-hand side of Eq. II.28, integration of the time-harmonic electric field over an oscillation period $\tau_{\boldsymbol{E}}$ yields:

$$\langle \boldsymbol{E}(\boldsymbol{r},t)^2\rangle_{\tau_{\boldsymbol{E}}} = \frac{1}{2}|\boldsymbol{E}(\boldsymbol{r})|^2, \tag{II.30}$$

where $\langle\,\cdot\,\rangle_{\tau_{\boldsymbol{E}}}$ denotes the average over a period $\tau_{\boldsymbol{E}}$. Inserting the intensity of a beam, $I(\boldsymbol{r}) = |\boldsymbol{E}(\boldsymbol{r})^2|$, the left part of Eq. II.28 can be identified as the previously introduced gradient force [102, 120]:

$$\boldsymbol{F}_{\mathrm{G}}(\boldsymbol{r}) = \frac{2\pi n_{\mathrm{M}}}{c}\left(\frac{\Xi^2-1}{\Xi^2+2}\right) R^3\,\nabla I(\boldsymbol{r}). \tag{II.31}$$

It is proportional to the volume of a particle, i.e. R^3, and to the gradient of the intensity of the incident light—hence the name gradient force.

Consequently, the second part on the right-hand side of Eq. II.28 represents the scattering force that is dependent on the Poynting vector, $\boldsymbol{S} = \boldsymbol{E}\times\boldsymbol{B}/\mu_0$, with the vacuum permeability, μ_0. After averaging over time, the scattering force reads [120, 122]:

$$\boldsymbol{F}_{\mathrm{S}}(\boldsymbol{r}) = \frac{\phi_{\mathrm{pr}}\langle \boldsymbol{S}(\boldsymbol{r},t)\rangle_t}{c/n_{\mathrm{M}}} = \left(\frac{n_{\mathrm{M}}}{c}\right)\phi_{\mathrm{pr}}\, I(\boldsymbol{r})\,\hat{\boldsymbol{e}}_z. \tag{II.32}$$

Here, $\hat{\boldsymbol{e}}_z$ represents the unit vector in the propagation direction of the beam and ϕ_{pr} the cross section of the particle on which radiation pressure acts [120]. As the particle is assumed to be very small compared to the wavelength of incident light, it scatters isotropically and therefore ϕ_{pr} corresponds to the scattering cross section ϕ_{S} [120, 122]:

$$\phi_{\mathrm{pr}} = \phi_{\mathrm{S}} = \frac{8}{3}\pi(kR)^4 R^2 \left(\frac{\Xi^2 - 1}{\Xi^2 + 2}\right)^2 , \tag{II.33}$$

where $k = 2\pi n_{\mathrm{M}}/\lambda$. Inserting Eq. II.33 into Eq. II.32 then yields [105]:

$$\boldsymbol{F}_{\mathrm{S}}(\boldsymbol{r}) = \frac{128\pi^5 n_{\mathrm{M}}}{3\lambda^4 c}\left(\frac{\Xi^2 - 1}{\Xi^2 + 2}\right)^2 R^6\, I(\boldsymbol{r})\, \hat{\boldsymbol{e}}_z\,. \tag{II.34}$$

When comparing the gradient force, Eq. II.31, to the scattering force, Eq. II.34, there are three prominent aspects. Firstly, the gradient force is proportional to the gradient of the beam intensity, whereas the scattering force is proportional to the intensity itself. Secondly, the direction in which the gradient force acts is again defined by the electric field gradient. The scattering force is, however, always directed towards the propagation direction of the beam. And lastly, the gradient force scales with the volume of a particle, whereas the scattering force scales with the square of it. That means a material that cannot be trapped at a certain particle size might be trapped when the particle becomes smaller [102]. A common example for such a mechanism is that of gold nanoparticles which cannot be trapped in three dimensions for radii $R \approx \lambda$ [123], but are trapped when the particles become smaller [124, 125]. As these particles also undergo Brownian motion, not only the combination of F_{G} and F_{S} but also their ratio to the random bombardment of the surrounding medium is important for successfully trapping them [102].

Both limits—the ray optics regime for $R \gg \lambda$ and the Rayleigh regime for $R \ll \lambda$—yield analytical results that give insight into the behaviour of forces inside an optical trap. Many experiments in soft matter are however conducted with particles in the micrometre range and lasers around the visible range [21,

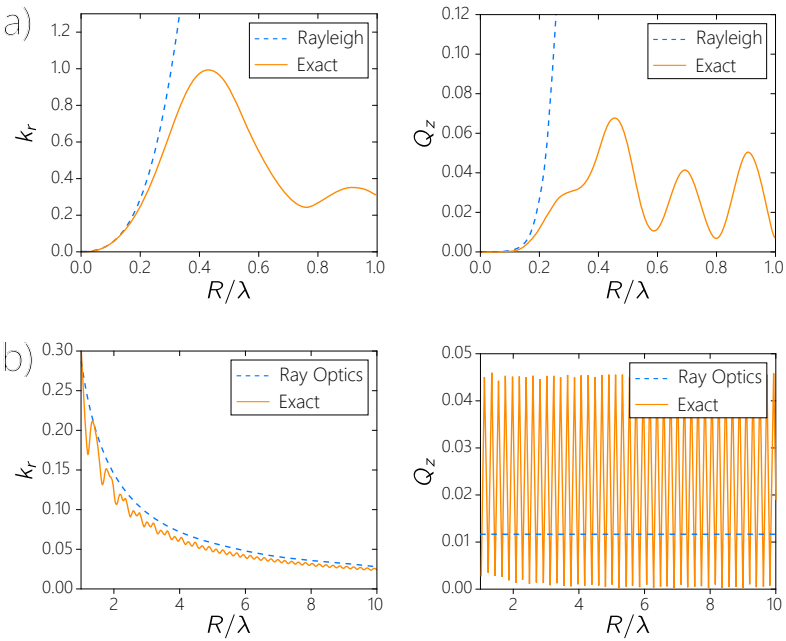

Figure II.11: Comparison of results obtained by Nieminen et al. with the ray optics and Rayleigh approximation for optical forces depending on the particle radius R. a) The Rayleigh approximation only delivers sensible results for particles with $R \ll \lambda$. b) The ray optics approximation shows useful values for k_r for the whole particle size range (left). Figures redrawn from [102].

104, 126]. There, $R \approx \lambda$ holds and neither limit is applicable. For this situation, there is no single approximation, so that the generalised Lorenz-Mie theory has to be applied [127–130]. Nieminen et al. [102] did so and compared their precise results for the trap stiffness, k_r, and the scattering force, $F_S \propto Q_z$[16], to both aforementioned limits. In Fig. II.11 a), the Rayleigh approximation is compared to the exact result for several particle sizes normalised by the wavelength. They found

[16] As the propagation direction of the beam is assumed to be the z-direction in Ref. [102] and the only varying parameter is the efficiency parameter Q (see Sec. II.2), Q_z is considered here instead of the scattering force, F_S.

that the Rayleigh approximation only delivers reliable results for k_r and Q_z when the particle radius, R, is smaller than 0.1 λ. This corroborates the assumption that R has to be much smaller than λ for the equations to hold. In Fig. II.11 b), the same comparison is shown between the ray optics approximation and the exact result. The results of the ray optics approximation agree with the precise results for the whole particle size range. They do not show any oscillations, but that can be an advantage in practice, since these oscillations stem from interference in perfectly spherical particles, which are not available in a real experiment [102]. To sum up, the ray optics rather than the Rayleigh approximation is a good method, both qualitatively and quantitatively, to explain optical forces and therefore can be used when they play a role in this thesis.

2.2 Optical Landscapes

Now that the forces acting on a dielectric colloidal particle due to its interaction with light have been introduced these forces can be expanded to one-, two-, or three-dimensional force fields. In Fig. II.12, examples of optical landscapes in each spatial dimension and their corresponding potentials are shown. Optical tweezers can be thought of as a zero-dimensional optical or force field as the resulting harmonic oscillator potential does virtually not show an extension in any spatial direction. To create a one-dimensional optical landscape, a ring can be shaped from a conventional beam coming from e.g. a laser. Compared to straight lines, a ring has the advantage of having periodic boundary conditions. A light ring or lines can be created by, for example, using holographic [21, 131], scanning optical tweezers [132, 133], or multiple optical traps [134]. The component perpendicular to these potentials usually behaves like optical tweezers limiting the particle in its perpendicular movement. The parallel component depends on the method with which it was created. Scanning optical tweezers often result in channel-like potentials with no spatial dependency [132]. Multiple or holographic optical traps can however create periodic [21, 134] or random fields [131]. The latter is shown in Fig. II.12 and will be discussed more precisely in a later section, since it is integral to the work described in this thesis. In the

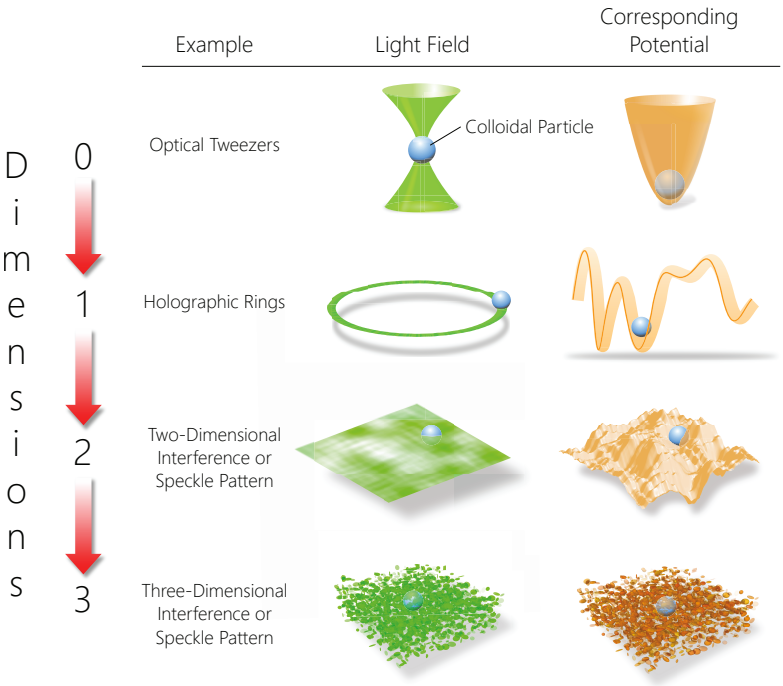

Figure II.12: Multi-dimensional optical fields (green) and their corresponding potentials (orange) caused by the interaction of light and matter. Optical tweezers can be approximated by the potential of a harmonic oscillator (cf. Fig. II.8) and can be thought of as a zero-dimensional potential as it does not extend in any direction. A ring, created by holographic optical tweezers, corresponds to a one-dimensional potential with periodic boundary conditions. The potential's shape largely depends on the method creating the optical ring. Two- or three-dimensional light fields can be created by interference of light or speckle fields due to scattering. These fields result in a two- or three-dimensional potential landscape for the colloidal particle.

same manner, two- and three-dimensional light fields can be created (Fig. II.12, bottom). Spatial light modulators [135], optical fibres [136], interference [137], diffusers [138], and scattering [139] can be effective means to manipulate Gaussian beams from a laser to form multi-dimensional optical landscapes. In the

same way as in the one-dimensional case, the method defines whether the resulting field is periodic (interference or diffusers) or random (spatial light modulators, optical fibres, diffusers, and scattering). The interaction of the above mentioned fields with a colloidal particle then leads to a specific potential to which a colloid is exposed (Fig. II.12, right column).

In order to find the intensity a particle feels, $I_\mathrm{P}(x,y,z)$, and thereby the resulting potential, $U(x,y,z)$, a convolution of the optical field with a particle weight function, $W_\mathrm{P}(x,y,z)$, can be conducted [138]. In two dimensions, it reads:

$$\begin{aligned} U(x,y) \mathrel{\widehat{=}} I_\mathrm{P}(x,y) &= I(x,y) * W_\mathrm{P}(x,y) \\ &= \int_{-\infty}^{\infty} I(x,y)\, W_\mathrm{P}(x-\Delta x, y-\Delta y)\, \mathrm{d}\Delta x\, \mathrm{d}\Delta y \\ &\overset{\text{discrete}}{=} \sum_{k=-\infty}^{\infty} \sum_{l=-\infty}^{\infty} I(x,y)\, W_\mathrm{P}(x-k, y-l)\,. \end{aligned} \tag{II.35}$$

The convolution mimics the interaction of the particle with an intensity $I(x,y)$. Therefore, $W_\mathrm{P}(x,y)$ represents the volume interacting with light. For a spherical particle, it can be calculated as [138]:

$$W_\mathrm{P}(x,y) = \begin{cases} \frac{1}{R}\sqrt{R^2 - x^2 - y^2} & \text{for} \quad \sqrt{x^2+y^2} \leq R \\ 0 & \text{for} \quad \sqrt{x^2+y^2} > R\,. \end{cases} \tag{II.36}$$

The resulting potential, $U(x,y)$, can then be treated as if a pointlike particle interacted with it. In Fig. II.13 a three-dimensional visualisation of a two-dimensional $W_\mathrm{P}(x,y)$ for a spherical particle and its application according to Eq. II.35 is shown. When $U(x,y)$ is calculated, the intensity, $I(x,y)$, is mostly smeared out by convolution with $W_\mathrm{P}(x,y)$. However, as a multi-dimensional potential emerges from the total light intensity incident on a finite sized colloidal particle, the optical forces present can mutually compensate or amplify. The interaction of a particle volume $W_\mathrm{P}(x,y)$ with a light field $I(x,y)$ can therefore not only lead to a potential $U(x,y)$ that corresponds to a smeared out $I(x,y)$ but also to an altered

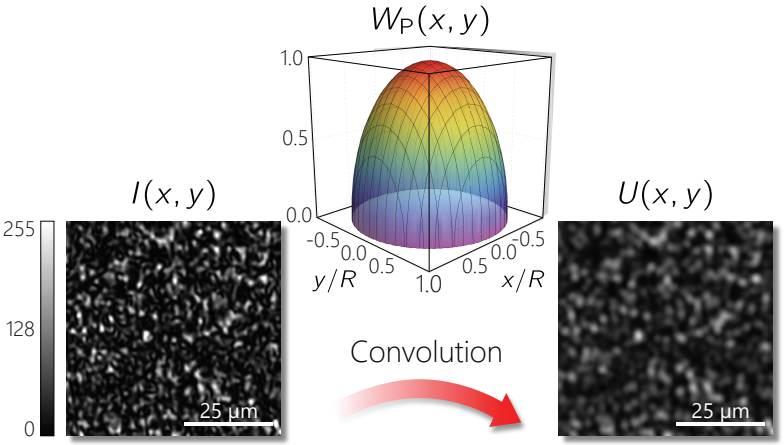

Figure II.13: To mimic the interaction between light and colloids, the optical landscape with intensity $I(x, y)$ incident on a colloidal particle (left) can be convolved with a weight function $W_P(x, y)$ for a spherical particle (middle). As a result the potential $U(x, y)$ a spherical particle would feel due to the interaction with $I(x, y)$ is acquired.

one. This leads to rather unintuitive consequences where a relatively large particle can be trapped in between two intensity minima, since this is energetically more favourable [137]. Whether the interaction of a particle with light leads to a smeared out potential or an altered one, depends on the particle size amongst other properties, namely $W_P(x, y)$.

2.3 Spatial Light Modulators

A spatial light modulator (SLM) is a transmissive or reflective device that can—according to a given input—spatially modulate an electromagnetic wave, e.g. light. The modulation can be one-, two-, or three-dimensional. As mentioned in Sec. II.2.2, SLMs can be used to create multi-dimensional optical fields that in turn represent potential landscapes when interacting with, for example, a colloidal particle.

In the work described in this thesis, an SLM was used to create one-dimensional potentials. Therefore, it is important to consider such light modulating devices and the holograms that are needed to make use of it in greater detail. In general, there are two ways an SLM can receive an input signal: an electrically addressed SLM and an optically addressed SLM [140–142]. While an electrically addressed SLM converts an electrical signal coming for example from a computer to spatial modulation, an optically addressed SLM uses a so-called write beam to change the configuration of the SLM so that it modulates a second beam, the read beam, interacting with the SLM. In addition to the input, the method with which the SLM manipulates the light can also differ [140–142]:

- One of the most commonly used methods that is also used in the work described in this thesis is the manipulation with a liquid crystal. The device can either be reflective or transmissive and is addressed electrically or optically. Depending on the input signal, the liquid crystals turn and modulate the phase or amplitude of light. The same technique is used in liquid crystal displays that are widely used for TVs and computer monitors.

- An array of many small mirrors is called a digital mirror device (DMD) and can be used to manipulate light by reflecting it in different directions. Each mirror can be addressed individually and can be turned $\pm 12°$ between an off- and an on-state to reflect only the parts of the beam that are wanted [143].

- By making use of the acousto-optic effect, acousto-optic deflectors (AODs) can deflect light in one direction. By applying sound waves to a crystal, e.g. TeO_2, the refractive index of the material is changed so that a beam travelling through it is deflected. To deflect light in two spatial directions or even create acousto-optic lenses, two or more AODs can be combined [144].

- The Pockels or Kerr effect can be used by applying an electric field to specific crystals. These crystals change their refractive index linearly (Pockels) or with the square (Kerr) of the applied electric field. The device making

use of these phenomena is called an electro-optic modulator (EOM) and can either be used to modulate the phase or the amplitude of a beam.

– In the same manner in which an EOM depends on the applied electric field, a magneto-optic modulator (MOM) depends on the applied magnetic field. It makes use of the Faraday effect where the polarisation of an electromagnetic wave can be turned depending on the magnetic field applied.

2.3.1 Functionality of a Liquid Crystal SLM

As mentioned in Sec. II.2.3, the SLM used in the work described in this thesis manipulates light with the use of liquid crystals (LC). Technically, the term liquid crystal is an oxymoron. Matter can usually be either liquid or crystalline but not both at the same time. In 1888 an Austrian botanist, Friedrich Reinitzer, studied liquid cholesteryl benzoate (Fig. II.14) in a mesophase, which later turned out to be birefringent. He heated it up and noticed that it first turned cloudy and viscous before becoming isotropic and clear. Hence, it was liquid but showed features of a crystal—thus liquid crystals were discovered [145].

LCs macroscopically behave like a fluid, but their microscopic structure has features of a crystal [146]. Hence, they display anisotropy in many physical quantities, such as refractive index, viscosity, and electrical conductivity. This behaviour stems from the fact that LCs are made up of elongated molecules that have large dipole moments. The preferential direction in which the semi-major axes of the molecules point is called the director, $\boldsymbol{n}$. By applying an external electric field, $\boldsymbol{n}$ can be changed due to the large dipole moments involved. To characterise the deviation of the LC from $\boldsymbol{n}$, an order parameter $\mathcal{S} = \frac{1}{2}\langle 3\cos^2(\theta) - 1\rangle$ is introduced, where θ is the angle between a molecule and the director $\boldsymbol{n}$, as depicted in Fig. II.14, and $\langle \ldots \rangle$ denotes the spatial and temporal average over all molecules [146]. In this regard, an order parameter $\mathcal{S} = 1$ denotes all molecules being parallel, whereas $\mathcal{S} = 0$ is found in an isotropic LC with no order. As stated above, LCs often show anisotropy in the refractive index and are therefore birefringent and can influence an electromagnetic wave, e.g. visible light.

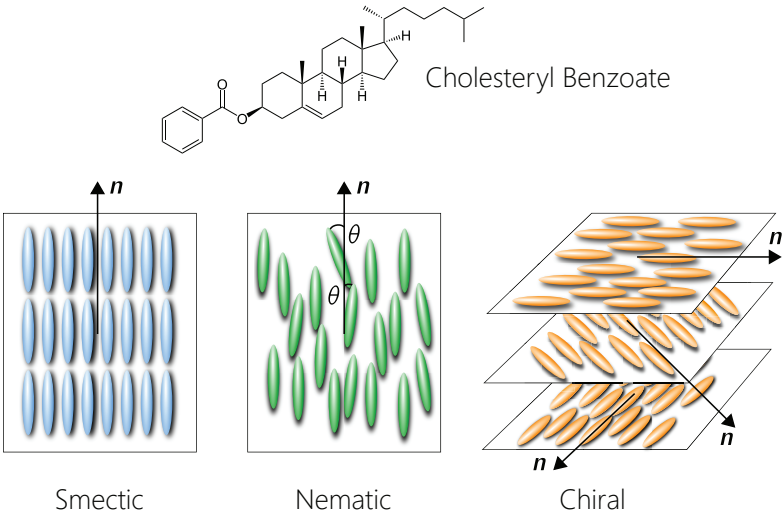

Figure II.14: The first liquid crystalline substance ever observed, cholesteryl benzoate, and three common phases found in liquid crystals: smectic, nematic, and chiral. The smectic phase shows the highest order parameter and is very similar to a crystal. The nematic phase has high long-range directional order, but no positional order of the centres of mass of the molecules. In the chiral phase a liquid crystal can be split up into layers where the director of each layer is rotated by a certain angle compared to the neighbouring layers.

Liquid crystalline phases are usually split into three different types: the smectic, nematic, and chiral phases (Fig. II.14). The smectic phase is closest to a solid crystal. The molecules do not have fixed positions but can be moved inside a layer. This is contrary to a solid crystal where not only the orientation but also the positions are fixed [146]. The nematic phase is less ordered than the smectic and has an order parameter $S \lesssim 1$, so that most of the molecules are oriented in the direction of $\boldsymbol{n}$ [146]. Therefore, it has long-range directional order but the centre of mass positions of the molecules are not ordered. The chiral phase has different layers, where the director of each layer is rotated by an angle relative to the neighbouring layers. As a consequence, $\boldsymbol{n}$ of a chiral LC forms a helix [146].

The nematic, especially the twisted-nematic, LC is mostly used when it comes

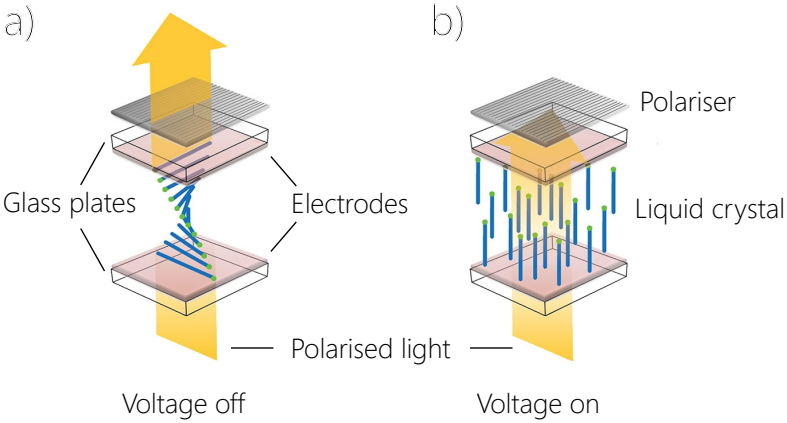

Figure II.15: Schematic of a twisted-nematic cell. In a) no voltage is applied to the cell. Therefore, the polarisation is rotated by 90° and an optional polariser in the end would pass all of the light. In b) an electric field is applied so that the LC molecules align with it. As a result the phase of the incident light beam is not affected and thus the light is blocked by the optional polariser. Image taken from [147].

to SLMs [148]. Twisted-nematic LCs (TNLC) originated in 1971 [149] and are slightly different to the nematic phase shown in Fig. II.14. Instead of all molecules being aligned in one direction, the molecules and director in a TNLC cell are—as the name suggests—twisted by around 90° between two glass plates, as depicted in Fig. II.15 a).[17] As a result, the polarisation of light entering the cell is turned by 90° in the same manner in which the molecules themselves are turned. In addition to the two glass plates forming the twisted-nematic cell, two transparent electrodes surround the LC. An electric field can be applied with these. The stronger the electric field, the more the molecules are tilted in its direction. Due to this tilt, the phase of the entering light is not affected as much as it is without any electric field. When all molecules are aligned with the electric field, the phase is not changed at all as shown in Fig. II.15 b). Thus the resulting phase shift can be controlled by the voltage applied to the electrodes. Figure II.15 additionally

[17] These cells are also called Schadt-Helfrich cells.

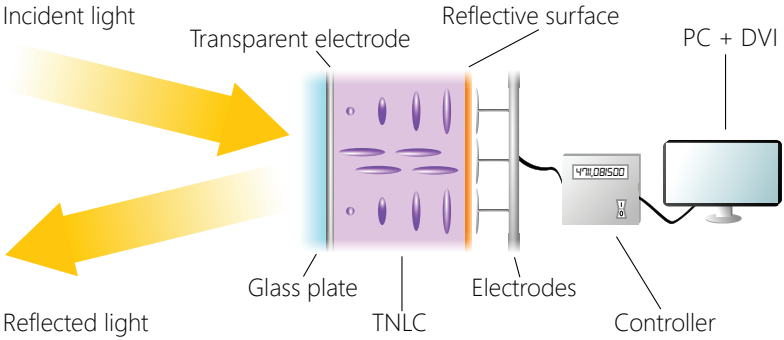

Figure II.16: Schematic of a twisted-nematic liquid crystal spatial light modulator (TNLC SLM). Image adapted from [150].

shows how the amplitude of light can be controlled with a twisted-nematic cell: by introducing a polariser that is rotated by 90° relative to the polarisation of light entering the cell.[18] When no voltage is applied to the electrodes the polarisation is rotated by 90° and the polariser will pass all of the light (Fig. II.15 a)). When an electric field is applied and all the molecules are tilted, the polariser will block all of the unaffected light (Fig. II.15b)).

An SLM is supposed to modulate light spatially. For that reason, it is not made up of one but a matrix of TNLC cells that are mostly produced in the liquid crystal on silicon (LCoS) structure [150]. Figure II.16 shows a fraction of a matrix of a TNLC SLM built with an LCoS procedure. The LC is sandwiched by two alignment layers (not shown in Fig. II.16) and put on a silicon waver that was additionally coated with a reflective layer to be able to reflect incoming light. Behind the reflective layer is a CMOS (complementary metal oxide semiconductor) with electrodes that can be addressed individually. A transparent electrode, which complements the electrodes behind the LC, is put on top of it. To seal the matrix, a glass plate covers the whole structure. As there are no polarisers in-

[18] A polariser in front of the cell can be introduced as well, so that the polarisation of light entering it is well-defined.

volved (cf. Fig. II.15), the layout in Fig. II.16 can only modulate the phase. To address the electrodes, a controller together with a DVI connection and a PC is used. A so-called hologram—often a bitmap—is sent to the SLM, in which each pixel corresponds to an individually addressed electrode in the SLM. The grey level of each pixel then represents the amount of phase shift. When in use, incident light enters the structure and is modulated by the LC, reflected by the backplane and again goes through the LC before it exits the SLM. Depending on the input given via a DVI connection, every single pixel in the SLM can modulate incident light individually. When there is no input given, incoming light is not affected by the TNLC—the SLM acts like a mirror.

2.3.2 Using a Liquid Crystal SLM

In the previous section, holograms were introduced as the input for an SLM in order to modulate the phase of an incident light beam. As only a phase modulating SLM is used for the work outlined in this thesis, this type will be focussed on. When manipulating the phase to create a certain light pattern, a setup similar to the one shown in Fig. II.17 is usually used. A narrow beam, e.g. coming from a laser, is first sent through a beam expander to be able to use as much area of the SLM as possible. The expanded beam subsequently hits the SLM, is modulated and reflected. This modulation takes place in the Fourier plane. Next, the modulated beam goes through a positive lens and is thus Fourier transformed to the image plane, where it forms the so-called target—a pattern such as the rings seen in Fig. II.17. Accordingly, manipulating light with a LC SLM is a diffraction method and exhibits all the advantages and drawbacks that go with it. On the one hand, an LC SLM can basically create any one-, two- or three-dimensional pattern that can be thought of. On the other hand, these patterns suffer from phenomena known for any kind of diffraction, such as multiple diffraction orders.

The hologram, also called a kinoform, has to contain the phase information needed to form the target pattern in the image plane. Positive lenses generally act as Fourier transformers [151]. Therefore, the link between phase information in the plane of the SLM and the targeted pattern is a Fourier transform. In

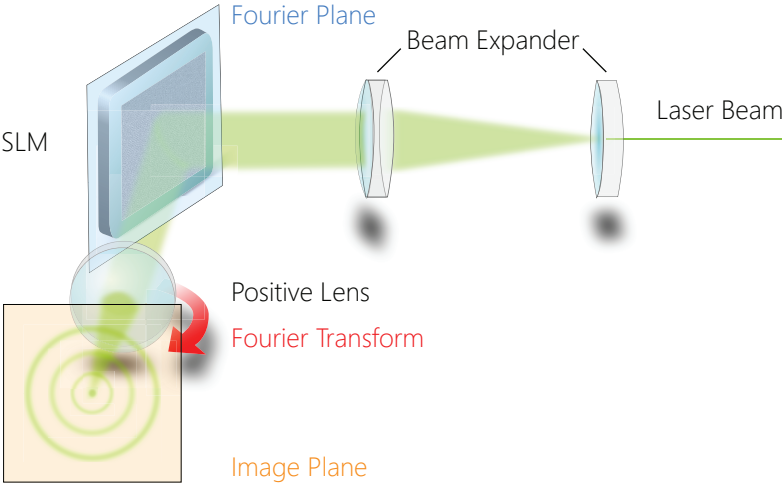

Figure II.17: Schematic of an experimental setup of an SLM and the corresponding optical planes. A laser beam is expanded and then modulated in the Fourier plane by an SLM. After that, a lens transforms the beam to the image plane and hence creates the intended light pattern, e.g. rings.

1971, Gerchberg and Saxton published an algorithm that tackles the problem of finding the adequate phase information by transforming between the SLM plane and the image plane (Fig. II.18) [152]. Its basic idea is presented in Fig. II.18. It is an iterative algorithm that finds the required kinoform within N_f iterations, until the calculated result is sufficiently close to the target. In the beginning, a random phase image, $\Phi^{(0)}$, the amplitude of the light beam incident on the SLM, $\mathcal{A}_\mathrm{S}$, usually a Gaussian beam, and a target image, $\mathcal{A}_\mathrm{T}$, that should be created in the image plane (cf. Fig. II.17) are needed. The random phase image is adjusted with each algorithm iteration i and is eventually returned as a kinoform $\mathcal{A}_\mathrm{K}$. At first, the random phase $\Phi^{(0)}$ is combined with $\mathcal{A}_\mathrm{S}$ to get the complex amplitude $\mathcal{B}_1^{(0)}$ in the SLM plane. $\mathcal{B}_1^{(0)}$ is Fourier transformed ($\mathcal{F}$ in Fig. II.18) into the image plane to obtain $\mathcal{B}_2^{(0)}$. From $\mathcal{B}_2^{(0)}$, the image $\mathcal{A}_{\mathcal{B}_2}$ can be calculated and compared to the targeted image $\mathcal{A}_\mathrm{T}$. The discrepancy between both images should

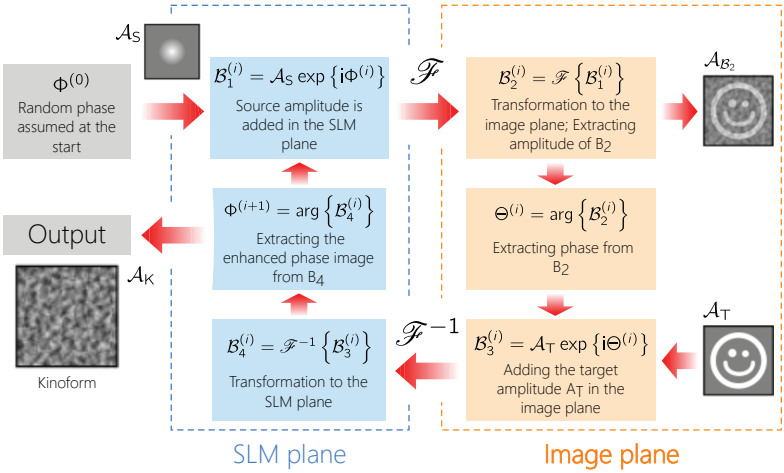

Figure II.18: Schematic of the Gerchberg-Saxton algorithm. A random phase serves as a starting point (top left). This phase and the source amplitude are used as an input and then transformed to the image plane to create a preliminary target image (top right). The preliminary image is compared to the actual target image (bottom right) and transformed back to the SLM plane to extract a phase. When the preliminary target image is reasonably close to the actual target image, the algorithm is stopped and the final phase extracted. The final phase image is called the kinoform. Image adapted from [153, 154].

be as small as possible after all iterations N_f. As a next step, the phase $\Theta^{(0)}$ is extracted and combined with the targeted image $\mathcal{A}_T$ to obtain $\mathcal{B}_3^{(0)}$. Afterwards, the complex amplitude $\mathcal{B}_3^{(0)}$ is inversely Fourier transformed to $\mathcal{B}_4^{(0)}$ in the SLM plane ($\mathcal{F}^{-1}$ in Fig. II.18). The phase $\Phi^{(1)}$ can thus be extracted. It should be one iteration step closer to the final kinoform than the starting phase $\Phi^{(0)}$. After N_f iterations the final phase image $\Phi^{(N_f+1)}$ can be passed to the SLM as the kinoform $\mathcal{A}_K$. When $\mathcal{A}_K$ is used as the phase image in the SLM, the modulated light beam should create a pattern that is very close to $\mathcal{A}_T$ when focused by a positive lens (Fig. II.17). As the whole procedure is based on a phase modulation, the formed pattern ideally shows several diffraction orders with the first order being the most pronounced. This however also means that there is a zeroth order and

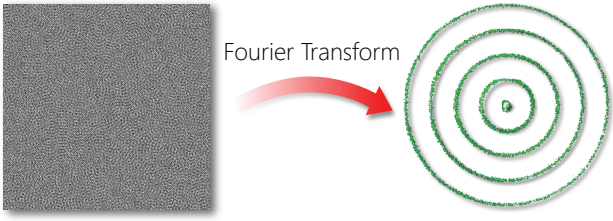

Figure II.19: Example of an actual kinoform and the corresponding light pattern in the image plane. A light beam is modulated by an SLM that was fed the kinoform shown on the left-hand side. Fourier transforming that light beam in optics with a positive lens leads to the pattern on the right-hand side. It shows four rings as the first-order diffraction maximum and the zeroth order in the middle.

higher orders formed behind the positive lens. Figure II.19 shows an example of a kinoform and the resulting pattern. The kinoform is Fourier transformed by a lens and creates four rings as the first order maximum. The dot in the middle is the zeroth order of the diffracted beam whose appearance cannot be easily avoided. Higher diffraction orders lie around the first, further away from the zeroth order in the middle but are not shown in Fig. II.19.

2.4 Engineered Diffusers

The term diffuser derives from the Latin word diffundere meaning to spread something. A diffuser is therefore something that spreads some kind of matter or physical magnitude—be it water, air, heat or, as described in this thesis, light. In optics, diffusers are usually used to homogenise light, e.g. in microscopes. Their purpose is to shape light in a specific way with the aid of a combination of several scattering, diffraction or refraction centres [155]. To do so, there are two types of diffusers: random and deterministic [156]. Random diffusers cannot be constructed in the same manner twice. Even though two random diffusers can show exactly the same shaping capabilities, their single scattering centres are not controlled individually. Only the statistics for all diffusers delivering equal

shapes are the same [156]. This also means that the area of a diffuser hit by incoming light is not relevant as long as the beam is big enough to cover a sufficient amount of scattering centres. Therefore, random diffusers are mostly not susceptible to small defects in the scattering centres or varying incoming light intensities. Common examples for random diffusers are surface diffusers, such as ground glass, volume diffusers, such as milk glass, or holographic diffusers that are made from homogenising diffusers and films similar to holograms [156–159]. In contrast to random diffusers, deterministic diffusers can be reproduced identically as often as wanted. Their production involves algorithms that determine the spatial position of each phase element. A spatially varying photoresist layer on a glass substrate is responsible for changing the phase of the light as it propagates through [160]. As a result, the position of an incident light beam as well as the intactness of each scattering centre is of larger concern than it is with random diffusers. Diffractive diffusers (DD) are a common example for deterministic diffusers, which can be computer-generated with the use of Fourier transforms [159, 160]. In principle, DDs can produce arbitrarily shaped light beams and are therefore superior to random diffusers introduced above. Similar to an SLM described in Sec. II.2.3.2 and shown in Fig. II.19, DDs not only create the calculated light pattern, which corresponds to the first diffractive order, but also a zeroth and higher orders. These orders are often unwanted and can corrupt the pattern or light field created by a DD.

A third kind of diffuser combining random and deterministic attributes are Engineered Diffusers™ (ED) by RCP Photonics Inc. [162]. Instead of having diffractive or scattering centres, an ED consists of an array of microlenses and thus shows refractive behaviour (Fig. II.20). The refractive nature of an ED ensures that there are no such things as zero or higher order patterns as there are with DDs. Compared to DDs, having relief depths of around the order of a wavelength of light, EDs show a much bigger relief depth (Fig. II.20, bottom right)—since diffraction relies on feature size, whereas refraction concentrates on slope angles [156]. This higher relief depth puts higher demand on the manufacturing process [163]. Microlenses can be made of polymer on a glass substrate, as de-

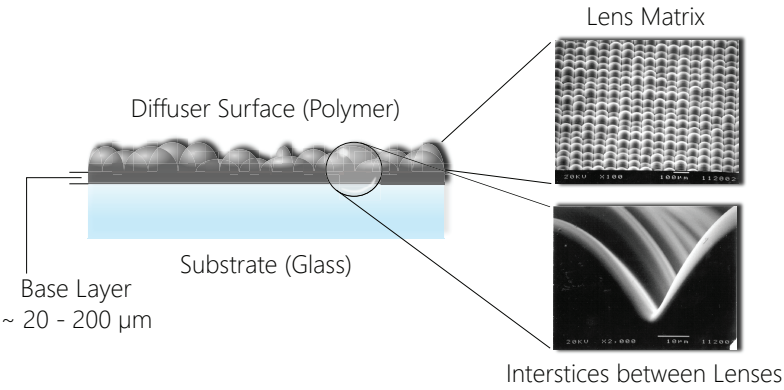

Figure II.20: Schematic of an Engineered Diffuser™. It consists of a substrate, in this thesis glass, a base layer of polymer that is between 20 and 200 µm thick and the diffuser surface that is made of polymer as well and corresponds to a matrix of small lenses. On the right-hand side an actual picture taken with a scanning electron microscope shows the appearance of this matrix. Below that there is an scanning electron microscope picture of the interstitial areas of adjacent lenses illustrating the sag existent in lens matrices. Left-hand side adapted from [161], right-hand side taken from [156].

picted in Fig. II.20, embossed in polymer, made out of films, or etched in fused silica [162]. The polymer-on-glass version of EDs is depicted in Fig. II.20. It consists of a glass substrate that is covered by a polymer base layer with a thickness of between 20 and 200 microns. On top of this base layer, the actual microlenses—also made from polymer—can be found. To produce these structures, a photoresist technique is used [163]. To be able to shape a light beam, all the microlenses have to exhibit an individually predetermined shape and positioning inside the array. Both can be determined by taking into account that the light pattern generated by the ED, $\mathcal{B}_{\mathrm{ED}}$, is connected to the relief structure of the diffuser by a Fourier

transform [151, 164]:

$$\mathcal{B}_{\mathrm{ED}}(u,w) = \frac{\exp\{\mathrm{i}kz\}}{\mathrm{i}\lambda z} \sum_j \int_{C_j} \int \exp\Big\{\mathrm{i}k[n(\lambda)-1]q_j(x,y) - \mathrm{i}\frac{2\pi}{\lambda z}(xu+yw)\Big\}\,\mathrm{d}x\mathrm{d}y\,, \tag{II.37}$$

where u and w are transformed coordinates, $k = 2\pi/\lambda$, the wave vector, and n is the index of refraction of the incident beam of wavelength λ. The coordinates x and y represent points on the ED and i is the imaginary unit. The integration over the whole ED is split up into a sum of integrals over small cells, C_j, with each cell representing a microlens [164]. The local surface shape of each lens, q_j, can be individual, so that in general $q_i \neq q_j$ for $i \neq j$ [164].[19]

A predetermined microlens array represents a deterministic diffusor. To homogenise the intensity inside the created light pattern, the microlenses are randomised according to probability density functions that work together with the beam shaping requirements [155, 156, 164]. In practice, one feature of the microlenses is often randomised by a uniform distribution as it is the easiest to handle [164]. As several features of the lenses are usually coupled, e.g. sag and radius of curvature, the probability density function for the second feature is a result of the randomisation of that of the first. This can be seen in Fig. II.21 where in a) the radius of curvature of the lenses is randomised by a uniform distribution. The resulting distribution for the sag is on the other hand skewed to the right. In Fig. II.21 b) the opposite is the case: when the sag is randomised by a uniform distribution, the distribution of the curvature is skewed. The result of both randomisations is depicted in Fig. II.21 c). There, the uniform randomisation of the curvature leads to stronger tails in the intensity pattern. This is due to the skewed distribution of the sag leading to larger angles of refraction [164]. Depending on the requirements for the intensity pattern, an appropriate randomisation distribution can then be found by adjusting the distributions accordingly [155, 156,

[19] Of course, there are additional constrains to the calculation of an ED which can be read about in the patent specification of Morris et al. [164].

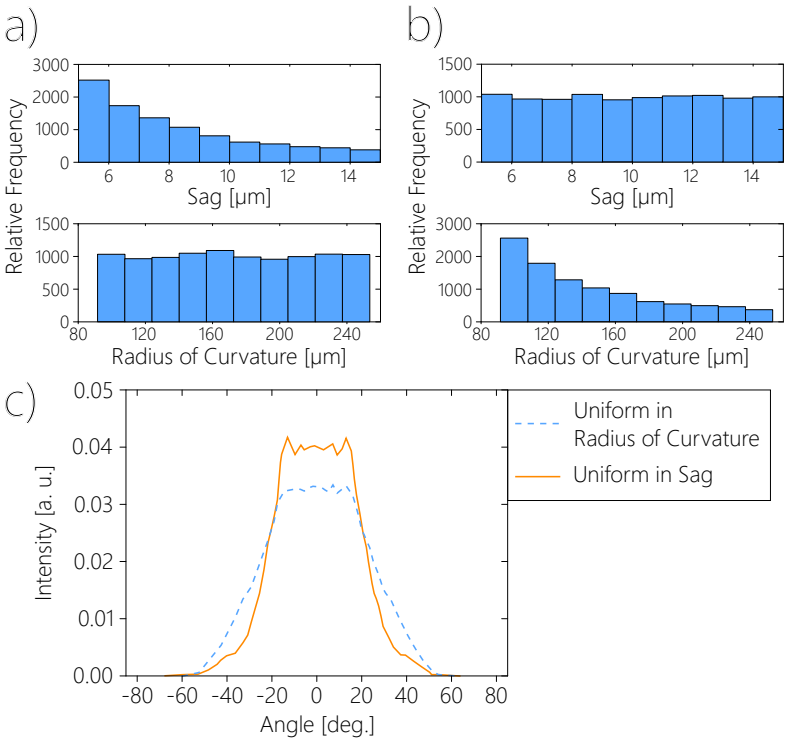

Figure II.21: Example of randomising microlenses from the patent specification of Morris et al. [164]. a) The distributions for the case where the radius of curvature of the lenses was randomised by a uniform distribution. The sag distribution is the result of the coupling between sag and curvature. b) The sag is randomised by a uniform distribution. Again, the other distribution results from coupling between sag and curvature. c) The intensities of an ED for the two different ways of randomising are shown. Image redrawn from [164].

164].

There are several ways of implementing an ED into the beam path when used inside an optical setup [165]. They all require a collimated source, e.g. a laser. When a non-collimated light source is used, the light pattern can be smeared out. Additionally, the microlenses of the ED should point towards the incident light

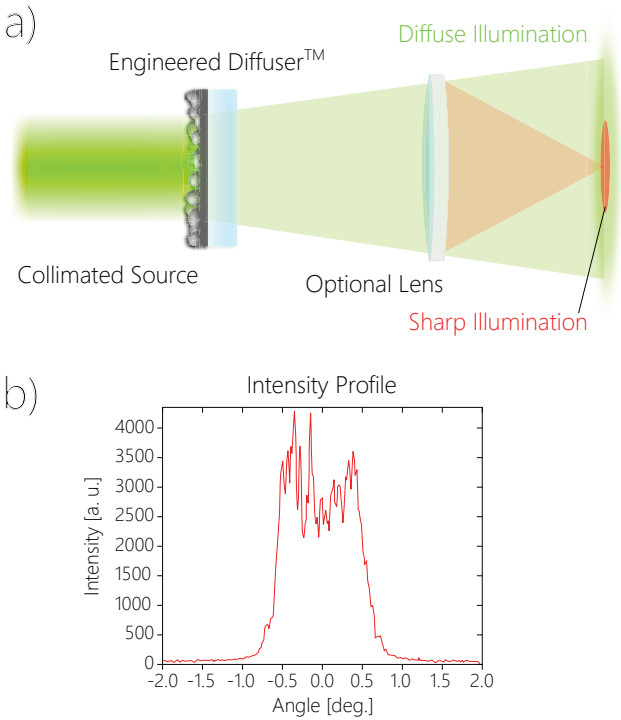

Figure II.22: Schematic of the functionality of an Engineered Diffuser™. a) A collimated light source, e.g. a laser beam, hits a diffuser and is refracted at its lens matrix. The refraction results in a slightly diverging beam that forms a predetermined diffuse shape. Introducing an additional positive lens to the beam path results in the same shape, however, this time a sharp illumination is delivered. b) An actual intensity profile of the Engineered diffuser used in the work described in this thesis. a) adapted from [165], b) redrawn from [161].

beam (Fig. II.22) [161, 165]. A collimated source hitting the patterned surface of an ED is then diffused to form a specific pattern as depicted for a flat-top field in Fig. II.22. The bigger the collimated source is before the ED, the better the uniformity of the field is after it. When there is no additional optical element in the beam path, the resulting pattern is diffuse (Fig. II.22, green path) [165]. This is the

simplest configuration but is often impractical, as a bigger collimated source not only yields higher uniformity but also stronger blur. When introducing a lens in front of or behind the ED, the pattern is focussed at the focal plane of the lens and appears sharp, independent of the size of the source (Fig. II.22, red path). Thus, a uniform and simultaneously sharp pattern can be created [165]. High collimation often involves high coherency—like in a laser. When used with a coherent light source, EDs often show an artefact: As each microlens can be treated as a point source, a pattern formed by an ED is also an interference pattern of several coherent light sources. Consequently, coherent light leads to—sometimes unwanted—speckles in the formed light pattern [161]. Instead of achieving a flat-top pattern, the use of an ED together with a laser yields an intensity pattern similar to that depicted in Fig. II.22 b). The speckle formation depends on the area and the position hit by the light source. The bigger the area the source hits, the smaller the speckles are [138]. Moreover, every ensemble of microlenses has a specific random speckle pattern. Thus, changing the position of a light source on a diffuser results in a statistically equivalent yet different random speckle pattern [138].

3 Piezoelectricity

In some parts of the work described in this thesis, a drift is imposed on colloidal particles to study their dynamics when subjected to external potentials such as optical fields, while being dragged through them. There are various ways of imposing drifts on colloidal particles, be it gravity [29, 166], shear [167, 168], tilted optical potentials [33, 169], flow of a dispersion medium [27, 136, 170], or movement of the sample itself [134, 171]. The latter can be realised easily by means of translation stages driven by piezoelectric elements.

The word piezo is Greek and means to squeeze. A piezoelectric element changes dimensions when subjected to an electric field. This is called the converse piezoelectric effect.[20] In general, this behaviour is not special as all materials show

[20] The normal piezoelectric effect can be observed when a piezoelectric element is subjected to an ex-

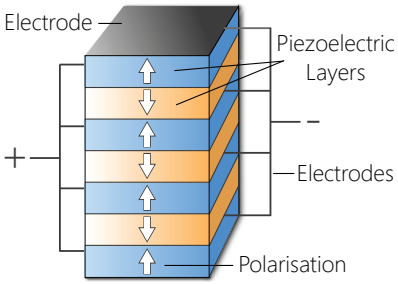

Figure II.23: Schematic of a layered piezo structure used in an actuator. To be able to obtain larger deformations, alternating polarised piezoelectric layers with electrodes in between are layered. Colours are for clarification. Adapted from [173, 174].

what is called electrostriction [172]. For materials with a relative permittivity, ϵ_r, the polarisation density is proportional to the applied electric field $|\boldsymbol{E}|$ yielding a strain $\gamma \propto |\boldsymbol{E}|^2$ [172]. In contrast to electrostriction, the converse piezoelectric effect has a linear dependence on the applied field $|\boldsymbol{E}|$ and is therefore dependent on its direction:

$$\gamma = Q_{\mathrm{PE}} |\boldsymbol{E}| \tag{II.38}$$

where Q_{PE} is the piezoelectric coefficient.[21] Compared to electrostriction, piezoelectric effects are significantly stronger [172] and are therefore more often used as actuators. These effects are strongly related to electric dipole moments inside a crystal. Piezoelectric materials have a crystal unit cell with a non-vanishing polarisation. An applied external electric field then enhances or decreases the distance between single atoms inside a unit cell and therefore the polarisation.

In practice, two of the most important piezoelectric materials are barium titanate and lead zirconate-titanate, often called PZT [172]. To build an actuator utilised in a microscope stage to move a sample, not only a single piezoelectric

ternal stress. This results in an altered internal polarisation density and thus an electric field, thus explaining the origin of the word piezo. This phenomenon is widely used in electronic lighters to ignite the gas.

[21] Q_{PE} is actually a tensor as it connects multidimensional magnitudes like strain γ and electric field $\boldsymbol{E}$.

crystal is used, but rather layers of several crystals to amplify the effect, as depicted in Fig. II.23 b) [172, 173]. Adjacent layers show an alternating polarisation with electrodes sandwiching them. Thus, deformation of a single piezoelectric crystal can be multiplied by the amount of alternating crystals [173]. Implemented in an actual microscope stage, a piezoelectric material is then controlled by feedback circuits and sensors that ensure precise movement [173, 175].

III Materials and Methods

After introducing the most relevant physical phenomena encountered in this thesis in the previous chapter, this chapter deals with the preparation, execution, and analysis of the experiments.

1 Colloidal Suspensions and Samples

All measurements were conducted with a system of spherical colloidal particles inside a sample cell made from glass. In most cases, the colloids have a diameter of $2R = 2.8\,\mu m$ and are made from polystyrene with sulfate functional groups on their surfaces to make them negatively charged (Sulfate Latex 8 % w/v, diameter 2.8 µm, polydispersity 3.2 %, Molecular Probes Inc.) leading to charge-stabilisation (cf. Sec. II.1.2). Depending on the used experimental setup (see Sec. III.2), either purified water (Purelab Flex, ELGA LabWater, electrical resistivity $18.2 \cdot 10^4\,\Omega m$) or deionised heavy water (Deuterium oxide 99.9 %, Deutero GmbH) served as a dispersion medium. The heavy water was deionised with ion exchange resin (Amberlite®, Carl Roth GmbH + Co. KG), so that aggregation of particles and sticking of particles to cell walls were reduced to a minimum. Interparticle interactions are considered to be hard-sphere like throughout this thesis (cf. Sec. II.1.2). At a standard lab temperature $T = 293.15 \pm 1\,K \hat{=} 20 \pm 1°C$, the polystyrene particles have a refractive index, $n_P = 1.59$, whereas both dispersion media exhibit $n_M = 1.33$. From Sec. II.2.1, it is known that colloids with $n_P > n_M$ are attracted by high light intensities. Consequently, all systems studied exhibit this behaviour. The density of the colloids at $T = 293.15\,K$, $\varrho_P = 1.055\,g/cm^3$, lies between that of water, $\varrho_H = 0.999\,g/cm^3$, and heavy water, $\varrho_D = 1.107\,g/cm^3$.

Hence, whether particles swim or sediment when subjected to gravity inside a sample cell depends on the dispersion medium. To quantify this behaviour, the gravitational length as derived from Eq. II.7 can be calculated:

$$l_g = \frac{k_B T}{\frac{4}{3}\pi R^3 \Delta\varrho\, a_g} \tag{III.1}$$

where $\Delta\varrho$ is the difference in density between the dispersed phase and dispersion medium and a_g is the gravitational acceleration on the averaged surface radius of the earth. The gravitational length represents the distance from the bottom or to top of the sample cell to the point in space where the particle concentration, ϱ_N, drops to its 1/e-part. For H_2O and D_2O, the gravitational lengths are $l_{g,H} = 0.64$ µm and $l_{g,D} = -0.69$ µm, respectively. Hence, for both configurations, particles only have a small tendency to diffuse in the third dimension once they are equilibrated at the bottom or top of the sample cell and are assumed to behave like a (quasi-) two-dimensional layer.

Besides l_g, the diffusion coefficient of the particles, D, and the friction coefficient, ξ, are of interest in a colloidal system. As the viscosities of both fluids are slightly different, $\eta_H = 1.00 \times 10^{-3}$ Pa s for water and $\eta_D = 1.25 \times 10^{-3}$ Pa s for heavy water at 20°C [176], their diffusive behaviour also differs. With the aid of Eq. II.10, the bulk diffusion coefficient, D_b, of a colloidal particle diffusing in water can be determined to be $D_{b,H} = 0.15$ µm²/s and $D_{b,D} = 0.12$ µm²/s in heavy water. The polystyrene particles used here sediment or cream and consequently diffuse close to the wall of a sample cell, which alters the particle diffusion. O. Hilding Faxén obtained a correction term for a sphere diffusing parallel to a flat

wall to make up for this discrepancy [177, 178]:[1]

$$D_{\mathrm{F}} = \left[1 - \frac{9}{16}\left(\frac{R}{h}\right) + \frac{1}{8}\left(\frac{R}{h}\right)^3 - \frac{45}{256}\left(\frac{R}{h}\right)^4 - \frac{1}{16}\left(\frac{R}{h}\right)^5 + \mathcal{O}\left(\frac{R}{h}\right)^6\right] D_{\mathrm{b}}\,. \tag{III.2}$$

The modified diffusion coefficient, D_{F}, depends on the distance between the centre of the particle and the wall, h, and is always smaller or equal to the bulk diffusion coefficient D_{b}. Often, only the first order approximation is used [178]:

$$D_{\mathrm{F}} = \left[1 - \frac{9}{16}\left(\frac{R}{h}\right) + \mathcal{O}\left(\frac{R}{h}\right)^3\right] D_{\mathrm{b}}\,. \tag{III.3}$$

Together with Eq. II.10, Faxén's term can also be interpreted as an increase of friction:

$$\xi_{\mathrm{F}} = \frac{\xi_{\mathrm{b}}}{1 - \frac{9}{16}\left(\frac{R}{h}\right) + \mathcal{O}\left(\frac{R}{h}\right)^3}\,. \tag{III.4}$$

The bulk coefficients of friction for both fluids, given $R = R_h$, are calculated to $\xi_{\mathrm{b,H}} = 2.6 \times 10^{-8}$ kg/s and $\xi_{\mathrm{b,D}} = 3.3 \times 10^{-8}$ kg/s. The corrected friction coefficients that are felt by particles close to a wall can either be computed provided h is known or determined by measuring the diffusion coefficient of freely diffusing particles near a wall, D_0 (cf. Eq.II.10 and II.15). All the relevant properties of the colloidal systems used in this thesis, including the friction coefficients determined from the diffusion coefficient, can be found in Tab. III.1. The coefficients D_0 and ξ_0 are a factor of $\lesssim 2$ smaller and larger than their calculated counterparts, respectively. Together with Eq. III.3, this leads to heights, h, of 2.4 µm and 1.6 µm for H_2O and D_2O, respectively. Hence, the distance h in the experiments is less than double the radius R, i.e. the particles are close to the sample cell walls.

In order to observe the colloidal systems with microscopes, a well-defined sam-

[1] There is also a correction term for particles diffusing perpendicular to a flat wall. As this thesis only deals with one- and two-dimensional diffusion parallel to a cell wall, this term will not be considered.

Property	Symbol	Value in H_2O	Value in D_2O
Coefficient of friction, bulk, calculated	ξ_b	2.6×10^{-8} kg/s	3.3×10^{-8} kg/s
Coefficient of friction, measured	ξ_0	4.0×10^{-8} kg/s	6.6×10^{-8} kg/s
Density difference	$\Delta\varrho$	0.056 g/cm^3	– 0.052 g/cm^3
Diffusion coefficient, bulk, calculated	D_b	0.15 µm^2/s	0.12 µm^2/s
Diffusion coefficient, measured	D_0	0.10 µm^2/s	0.06 µm^2/s
Gravitational length	l_g	0.64 µm	– 0.69 µm
Particle radius	R	1.4 µm	1.4 µm
Refractive index of the particles	n_P	1.59	1.59
Refractive index of the medium	n_M	1.33	1.33
Viscosity	η	1.00×10^{-3} Pa s	1.25×10^{-3} Pa s

Table III.1: Properties of colloidal particles dispersed in H_2O and D_2O at $T = 293.15$°C.

ple cell is needed. A protocol how to reproducibly construct them is given in Fig. III.1. First, a microscope slide, two coverslips used as spacers and one coverslip used as a cover (all VWR International GmbH) are sonicated in a 2 % Hellmanex II solution (Hellma GmbH & Co. KG) at around 60°C for ten minutes, rinsed with purified water (Purelab Flex, ELGA LabWater), sonicated in purified water at around 20°C for ten minutes, rinsed again with purified water and then dried in air. As depicted in Fig. III.1 a), a microscope slide is used as a base when constructing the sample cell, on top of which two spacers, either with a thickness of 85–130 µm (No. 0) or 160–190 µm (No. 1.5), are glued with UV-curing optical adhesive (Norland Optical Adhesive 61 (NOA 61), Norland Products Inc.) by allowing it to cure for two minutes inside a UV curing chamber (ELC-500 UV Curing Chamber, Electro-Lite Corp.). Only a very small amount of glue should be used when merging coverlips and microscope slide as too much glue will cause the cell to be askew and increase its height. Subsequently, a third coverslip with thickness No. 1.5 is glued on top of the two spacers with NOA 61 to cover the previously created recess on the microscope slide and obtain a capillary (Fig. III.1 b)). The thickness of the third coverslip should not be changed as it interacts with microscope objectives that require certain thicknesses—mostly No. 1.5. The glued capillary is cured thoroughly for ten minutes inside the oven and left for several days to let the glue bind to the glass completely [179]. After that, a sample dispersion is produced by diluting the colloidal stock solution provided by the manufacturer to a certain area fraction φ_A, defined as

$$\varphi_A = \frac{N_{\mathrm{FOV}}\,\pi R^2}{A_{\mathrm{FOV}}} \tag{III.5}$$

with N_{FOV} being the amount of particles in the field of view and A_{FOV} the area of the field of view. With $\varphi_A < 10$ %, particle-particle interactions should be reduced to a minimum while still having enough particles in the field of view of the microscope to obtain good statistics [180, 181]. The produced dispersion is then filled into the capillary with a pipette. Capillary forces ensure the dispersion is sucked into the sample cell and no bubbles are formed (Fig. III.1 c)). The sample

cell is finally sealed with NOA 61 to prevent evaporation and flow when used afterwards. When sealing the sample with glue, it is advisable to use an excess of glue to cover the open ends (Fig. III.1 d)). That way small inaccuracies in producing the capillary that might have entailed some leaks are compensated and additionally the glue bulge, once cured, acts as a bumper for the cover slip and makes sure it is not easily scratched. The glue is finally cured for 3×3 minutes to make sure the sample does not get too hot inside the curing chamber.

2 Experimental Setups

Two setups are used to create light fields similar to those described in Sec. II.2.2 containing a microscope to observe colloidal samples. They differ in their main optical components and in the direction in which the created light field hits the particles. The first setup exploits a spatial light modulator, detailed in Sec. II.2.3, to shape light into a one-dimensional pattern. The second setup uses an Engineered Diffuser™, described in Sec. II.2.4, creating two-dimensional light fields.

2.1 Spatial Light Modulator Setup

From Sec. II.2.3 it is known that a spatial light modulator (SLM) can theoretically create arbitrary light patterns. In the work described in this thesis, it is used to create one-dimensional light fields. The optical setup, used components, and the optical pathway, as well as a photo of the actual setup are shown in Figs. III.2 and III.3, respectively. It was built by Richard Hanes [182] and then modified slightly [131].

2.1.1 Beam Path of the SLM Setup

Like many optical setups, the starting point of that depicted in Fig. III.2 is a laser (Ventus 532-1500, Laser Quantum Ltd.). This diode-pumped solid-state laser emits light with a wavelength $\lambda = 532\,\text{nm}$ and a maximum power of 1500 mW. The emitted light hits two waveplates (WP), the first of which is a $\lambda/2$-plate and

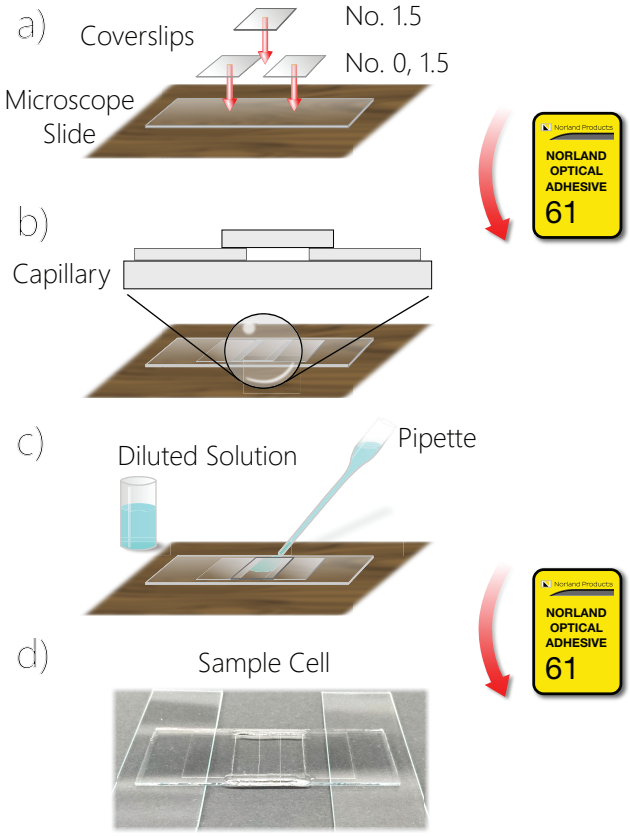

Figure III.1: Preparation of a typical sample used in this work. a) Two coverslips, either of height No. 0 or No. 1.5, are glued on a microscope slide using UV-curing optical adhesive. b) To create a complete capillary, a coverslip of thickness No. 1.5 is glued on top of the two other cover slips. c) Afterwards the capillary is filled with a sample solution using a pipette. d) To seal the filled capillary UV-glue is again used. Brand logo taken from [179].

polarises the light linearly (WP1). After that, a $\lambda/4$-plate (WP2) creates elliptically polarised light, since this polarisation was shown to improve the ability of the SLM's to encode kinoforms [131, 183]. The light is reflected by mirror M1 (all

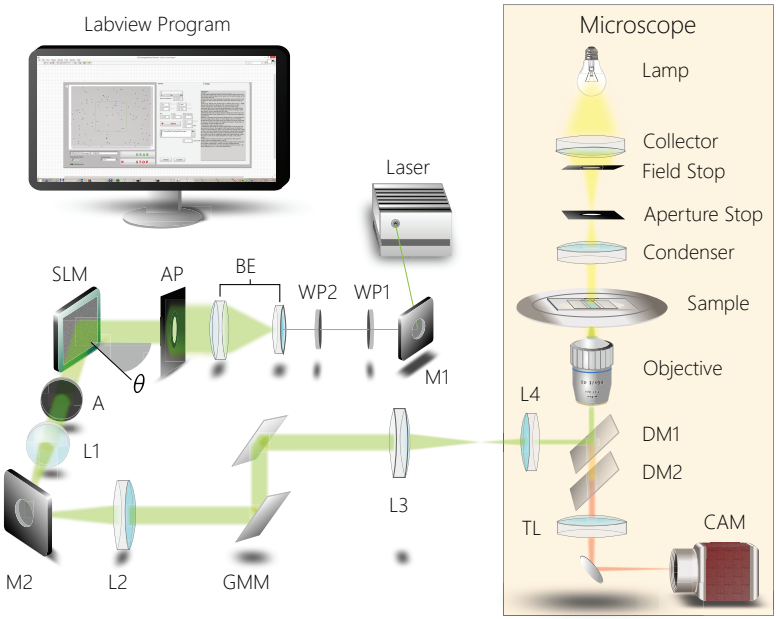

Figure III.2: Setup using a spatial light modulator to create one-dimensional light fields. The components inside the orange rectangle are inside a microscope or its beam path. A beam emitted by a laser is widened (BE) and directed onto an SLM. The resulting phase pattern is transformed into a light field in real space by a lens (L1) and can be moved inside the sample through two galvanometer-mounted mirrors (GMM). The beam is coupled into a microscope and hits the sample from the bottom, in the opposite direction of gravitation. A camera (CAM) is flanged to the microscope to record micrographs of the sample. The other abbreviations are given in the main text.

mirrors from Thorlabs, Inc.) and goes through a beam expander (BE) consisting of a negative and a positive lens (all lenses from Edmund Optics GmbH) that expands the beam diameter to 14 mm. The BE ensures that a subsequent aperture (AP) is filled by the beam and the longest edge of the SLM—situated behind the AP—can be fully illuminated when the AP is completely open. The size of the AP defines the amount of light hitting the SLM and can therefore be integral to

the properties of light fields created with it. The beam hits the SLM (LCR-2500, HOLOEYE Photonics AG) with an angle of incidence of $\theta = 22.5°$. This angle enables the SLM to give the full 2π phase shift [182], which has to be taken into account when calculating the kinoforms described in Sec. II.2.3.2. After the spatial light modulation has taken place at the SLM, the beam is directed through an analyser (A) that, together with the waveplates WP1 and WP2, optimise the efficiency of the first order diffraction of the SLM [183, 184].

The remainder of the setup is exclusively for directing and focussing the beam in the sample plane and controlling its position. Lens L1, positioned after the analyser, transforms modulated light to real space. Close to mirror M2, there is a plane conjugate to the sample plane showing an image of the light field felt by the particles inside the sample when a screen is put in the beam path. Together with lens L2, lens L1 acts as a telescope decreasing the beam diameter to 8 mm. This smaller beam then enters a galvanometer-mounted mirror structure (GMM, Quantum Scan 30, Nutfield Technology, Inc.) made up of two mirrors, each of them being able to rotate around a spatial axis, also depicted at the top of Fig. III.3. The GMMs enable two-dimensional in-plane translation of the light field inside the sample cell and are controlled by LabView (National Instruments Corp.) [182]. The beam is then sent through a second telescope (L3 and L4) to decrease the beam diameter to 6.4 mm to overfill the back aperture of the microscope objective and is fed into the back port of the microscope as can be seen from the side view in Fig. III.3. Inside the microscope (Eclipse TE2000-U, Nikon Corp.), a dichroic mirror (DM1, z532dcrb, Chroma Technology Corp.) directs the beam to a microscope objective (CFI Plan APO VC Oil 60×, Nikon Corp.) that focusses the beam inside a sample that lies on the microscope stage so that colloidal particles feel it in real space.

The light enters the sample from the bottom, so that the gravitational acceleration is in the opposite direction to that of the propagation of light and therefore the scattering force. In this setup, samples with D_2O as dispersion medium were used (cf. Sec. III.1). As a result, buoyancy and scattering force point in the same direction. The objective not only focusses the laser but also acts as an imaging

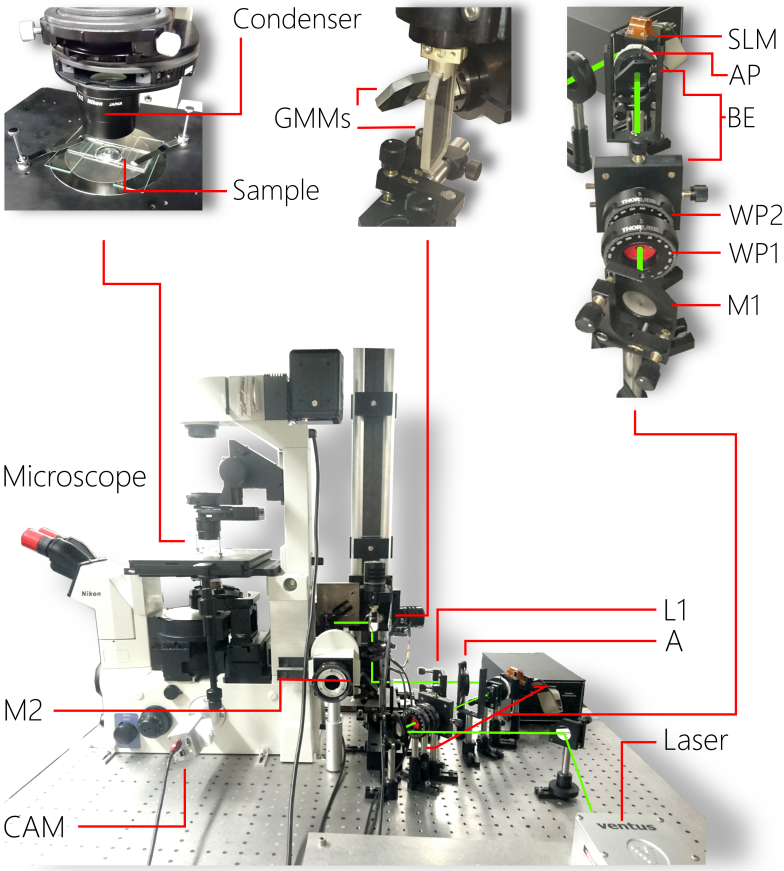

Figure III.3: Photograph of the spatial light modulator setup (schematic shown in Fig. III.2). The drawn green line shows the beam path. Lenses L2 and L3, and all the components housed inside the microscope are not marked. Certain parts of the setup are magnified in the top part of the figure. Abbreviations are given in the main text.

lens for the microscope. Focal spots of the laser light and imaging are chosen to be the same. As can be seen in Figs. III.2 and III.3, the customary bright-field mi-

croscope used here has a CMOS-camera (CAM, PL-B742F, PixeLINK) attached to it on to which the imaged sample is focussed with the implemented tube-lens (TL). The camera, together with the GMMs, is controlled by an external LabView software and captures sequences of images in the JPEG format with a pixel pitch of 0.111 µm/px that can be analysed further [182]. This procedure is called video microscopy and is detailed in Sec. III.3. When the beam is focussed by the objective, there is always light reflected by the surface of the sample cell that mixes with the imaging light and causes the camera to be overexposed (cf. Fig. III.2). To prevent damage to the camera and ensure a high image quality but at the same time be able to observe laser light scattered by particles[2], a second dichroic mirror (DM2, NT69-901, Edmund Optics GmbH) is introduced. Since both dichroic mirrors, DM1 and DM2, filter green light, the images taken by the camera have a prominent red cast. Additionally, stray light manifests itself as green halos around particles. In measurement situations, the laser is turned on at least one hour before a measurement to warm up the laser and setup components.

2.1.2 Creating a Light Pattern: Concentric Rings

The SLM setup is designed to create one-dimensional light fields. From Sec. II.2.3.2, it is known that an LC SLM is used as a diffractive device to create arbitrary light patterns. To calculate kinoforms that can be displayed on an SLM to obtain those patterns, the Gerchberg-Saxton algorithm can be used. In practice however, creating a light pattern usually involves additional steps, which largely depend on the optical setup used. This section deals with the practical aspects of creating a light field using the example of a concentric ring pattern, which will be used later in this thesis.

In Fig. III.4, a step-by-step creation of four concentric rings is shown. First the desired pattern, $\mathcal{A}_{\mathrm{T}}^{\mathrm{ds}}$, has to be drawn as a 768×768 px^2 8-bit-bitmap. Bitmaps are utilised throughout the process as they are lossless. The used size and bit depth are defined by the attributes of the employed SLM. The desired pattern in this case is shown in the bottom left corner of Fig. III.4 and consists of four completely

[2] This will be important in Secs. IV and V.

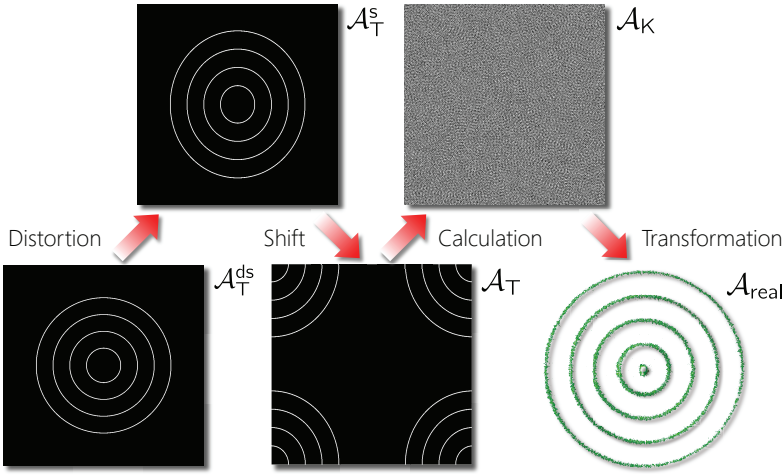

Figure III.4: Illustration of how to create a light field made up of concentric rings with a grey level of 255. The desired pattern, $\mathcal{A}_T^{ds}$, is created first. To compensate for the angle of incidence, θ, and create a light pattern that is centred about the zeroth order, $\mathcal{A}_T^{ds}$ is distorted to get $\mathcal{A}_T^s$ and then shifted. The resulting pattern, $\mathcal{A}_T$, can be transformed with the Gerchberg-Saxon algorithm to obtain $\mathcal{A}_K$, which, in turn, creates $\mathcal{A}_{real}$ when put on the SLM.

circular rings with a grey level of 255 on a black background corresponding to a grey level of 0. The grey level defines how bright the pattern will be when it is formed by the SLM, with 0 representing black and therefore no light and 255 representing white and thus the full intensity provided by the laser, where the intensity is shared by all pixels with finite grey levels. Since light hits the SLM with $\theta = 22.5°$, a perfectly circular ring used as an input for the Gerchberg-Saxton algorithm creates distorted rings in the final light pattern inside the sample, $\mathcal{A}_{real}$. To compensate for this effect, $\mathcal{A}_T^{ds}$ has to be distorted beforehand, namely by the factor $\cos(\theta) = \cos(22.5°) = 0.92$ to create $\mathcal{A}_T^s$ as shown in the top left corner of Fig. III.4. After $\mathcal{A}_T^{ds}$ has been distorted, it is shifted by half its size in both directions. The resulting pattern, $\mathcal{A}_T$, is used to calculate a kinoform $\mathcal{A}_K$ as described

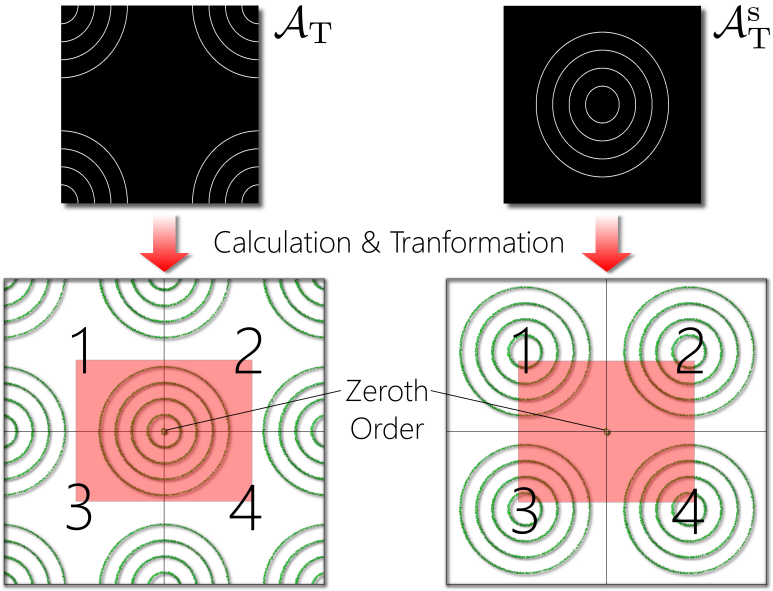

Figure III.5: Schematic of the light field creation inside a sample. The red rectangle corresponds to the field of view. The four single first orders of diffraction are numbered consecutively and surround the zeroth order. To create a pattern that is centred about the zeroth order, the desired pattern has to be shifted beforehand resulting in $\mathcal{A}_\mathrm{T}$ (left). The pattern $\mathcal{A}_\mathrm{T}^\mathrm{s}$ is not shifted and therefore results in four ring-like light fields that are arranged around the zeroth order (right). When the field of view is aligned with the zeroth order, none of the concentric rings is captured entirely.

in Sec. II.2.3.2 and Fig. II.18. Eventually, the SLM setup transforms $\mathcal{A}_\mathrm{K}$ to an actual light field inside the sample plane $\mathcal{A}_\mathrm{real}$ as shown in Fig. II.19.

The shift introduced to create $\mathcal{A}_\mathrm{T}$ is necessary in order to centre $\mathcal{A}_\mathrm{real}$ about the zeroth order of diffraction of the SLM. Figure III.5 shows that $\mathcal{A}_\mathrm{real}$ is actually made up of four first orders (numbered from 1 to 4) that are evenly distributed around a central laser spot that represents the zeroth order. In practice, the central spot is put in the centre of the field of view (FOV) to use it as a distinctive point when analysing the experiment. The FOV is represented by a red rectangle in

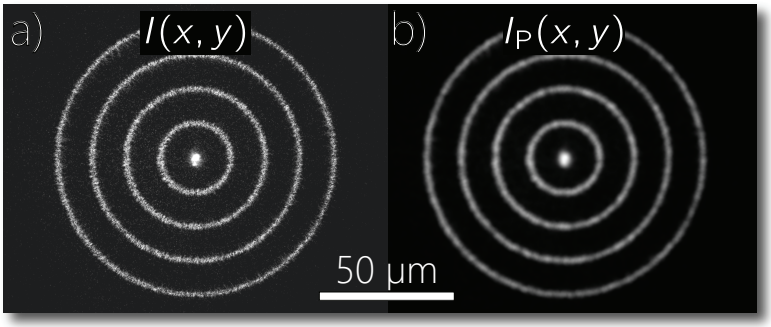

Figure III.6: Concentric rings created by the SLM setup. a) Micrograph of the intensity pattern $I(x, y)$ b) Intensity given in a) convolved with $W_P(x, y)$ of a particle with $R = 1.4$ µm to obtain $I_P(x, y)$.

Fig. III.5. In order to centre a desired light pattern, e.g. concentric rings, about this spot, $\mathcal{A}_T$ has to be shifted beforehand. That way the shifted first orders create a centred pattern as shown on the left-hand side of Fig. III.5. If $\mathcal{A}_T^s$ is used as an input for the Gerchberg-Saxton algorithm, the rings will not be centred about the zeroth order but arranged around it (Fig. III.5, right). In this case the concentric rings could still be used as a light field to manipulate colloids. As the light intensity is highest close to the central spot, the intensity of the rings would be lower and the zeroth order could not be used as an anchor point for the following analysis of the experiment.

2.1.3 Characterisation of Light Fields Created by the SLM Setup

Now that the beam path and the creation of a light field have been introduced, the characteristics of a light field created by the SLM setup are investigated further. This section is mainly based on [131, 135, 185] and describes properties of concentric rings described in the previous section as this is the only light field with which this setup was used.

In Figs. III.4, III.5, and III.6 a), concentric rings created by the SLM setup pho-

tographed in the sample plane are shown. They are not completely uniform but show an inherent pattern, i.e., even though $\mathcal{A}_\mathrm{T}$ only contains rings consisting of grey level 255 everywhere, the light field created in the sample plane shows random fluctuations in intensity—also called speckles [138, 186]. These fluctuations stem from the fact that any SLM has a finite amount of pixels, which themselves have a finite size [135]: the Gerchberg-Saxton algorithm does not correct for these practical constraints. Consequently, the resulting intensity distribution, $\mathcal{A}_\mathrm{real}$, represents the target $\mathcal{A}_\mathrm{T}$ as intended, but inside this pattern it tends to have speckles. Every different random phase, $\Phi^{(0)}$, results in a different random speckle pattern (cf. Fig. II.18). The average size of these speckles depends on the area of the SLM responsible for creating $\mathcal{A}_\mathrm{real}$: the larger a beam hitting an SLM and thus the more pixels participating, the smaller the average speckle size. In the work described in this thesis, the size of the beam hitting the SLM was not changed.

From Sec. II.2.2, it is known that a potential $U(x, y)$ felt by a particle in a light field can be mimicked by convolving the intensity $I(x, y)$ with a particle weight function $W_\mathrm{P}(x, y)$. This is shown in Fig. III.6 b) for the particle size discussed in this thesis, $R = 1.4\,\mu\mathrm{m}$, and $I(x, y)$ shown in Fig. III.6 a). The former shows characteristic smearing out of the light field mentioned in Sec. II.2.2. In the radial direction, the rings show a narrow intensity peak. As the refractive index of the particles is higher than that of the dispersion medium, this leads to a narrow potential minimum similar to the one shown for optical tweezers in Sec. II.2.2. Consequently, a particle is trapped in the radial direction and experiences a potential $U_r(r) = k_r r^2$ [182]. To get a better idea of what intensity $I(s)$ and felt intensity $I_\mathrm{P}(s)$—and thus the potential $U(s)$—look like in the azimuthal direction, parts of $I(s)$ and $I_\mathrm{P}(s)$ are shown in Fig. III.7 a). Intensities along $s = r_\mathrm{R}\theta$ of the outer ring in Fig. III.6 are given in grey levels and shown as blue lines, where r_R represents the radius of the ring and θ the azimuthal angle. Distributions on the right-hand side, shown as blue columns, were obtained by taking into account the whole ring, not just the parts shown here, and fitted with a Gaussian function represented by the orange lines. It is apparent that $I_\mathrm{P}(s)$ shows a coarser struc-

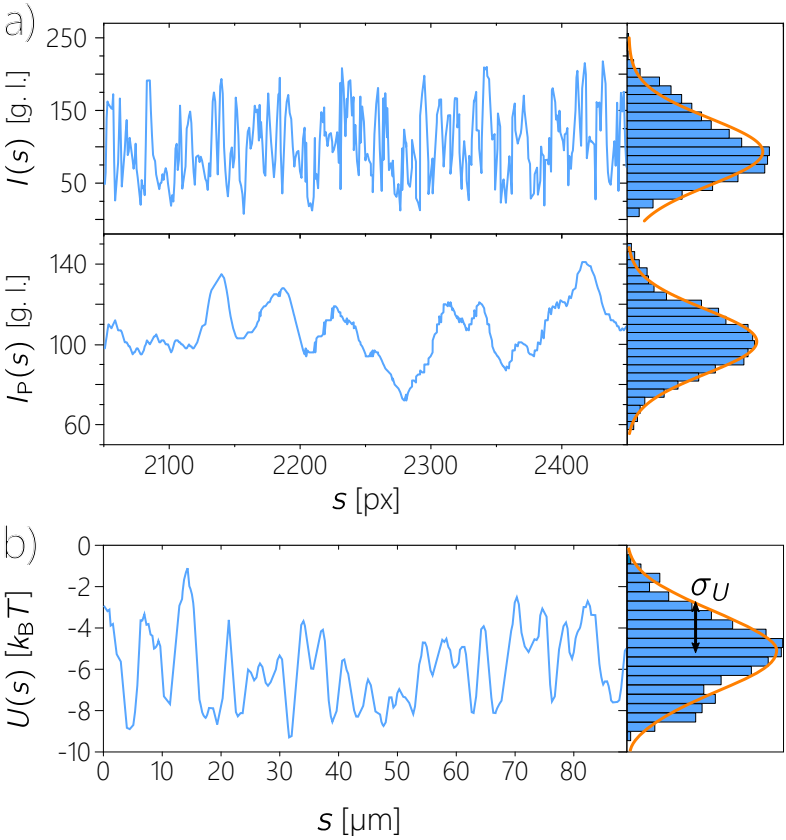

Figure III.7: Intensity and potential in the azimuthal direction of a ring shown in Fig. III.6. a) Intensity $I(s)$ given in grey levels obtained from the outer ring in Fig. III.6 a) shows a relatively short correlation length. The resulting distribution (blue bars) is fitted by a Gaussian function (orange line). Intensity $I_P(s)$ obtained from the outer ring in Fig. III.6 b), given in grey levels, shows a larger correlation length than $I(s)$. The distribution is fitted by a Gaussian function. b) Potential $U(s)$ redrawn from [131]. It was obtained through Boltzmann statistics by measuring particle residence probabilities inside a light field similar to that in Fig. III.6.

ture compared with $I(s)$, which is equivalent to a larger correlation length, l_U. In Ref. [131], the correlation length was defined as the distance at which the spatial autocorrelation of the azimuthal intensity or potential drops to its 1/e-part. The light field used in the work described in this thesis was examined and $l_U \approx 0.2\,R$ for $I(s)$ and $l_U \approx R$ for $I_\mathrm{P}(s)$ were found. These values are in good agreement with the observations made in Fig. III.7 a), where $R = 1.4$ µm corresponds to 13 px.

Furthermore, the intensity distributions of $I(s)$, $\mathcal{P}(I)$, differs from that of $I_\mathrm{P}(s)$, $\mathcal{P}(I_\mathrm{P})$. While $I(s)$ shows a skewed distribution with a tail at higher intensities, $\mathcal{P}(I_\mathrm{P})$ fits well to a Gaussian function. The skewness in $\mathcal{P}(I)$ is common for speckle intensities and can be described by a gamma distribution [135, 186]. Once $I(x, y)$ is convolved with $W_\mathrm{P}(x, x)$, the resulting $\mathcal{P}(I_\mathrm{P})$ shows a Gaussian shape. In Ref. [131], the actual potential arising from the interaction of $I(s)$ given in Fig. III.7 a) with a particle with $R = 1.4$ µm was obtained through Boltzmann statistics by measuring particle residence probabilities. The result is redrawn in Fig. III.7 b). It shows a negative potential $U(s)$ as particles used in the work described in this thesis are attracted by high laser intensities (cf. Sec. III.1). When compared to $I_\mathrm{P}(s)$, $U(s)$ shows the same correlation length, $l_U = R$. Additionally, $\mathcal{P}(U)$ given on the right-hand side of Fig. III.7 b) shows Gaussian behaviour similar to $\mathcal{P}(I_\mathrm{P})$. Both comparisons confirm the statement made in Eq. II.35, namely that $I_\mathrm{P}(x, y)$ resembles $U(x, y)$. The standard deviation, σ_U, of potential, $U(s)$, can be thought of as the roughness of the potential. When increasing the output power of the laser, P_L, the roughness of potential $U(s)$ and the depth of potential $U_r(r)$ increase as well. It was found that both, σ_U and k_r, exhibit a linear dependence on P_L [182].

In summary, the SLM setup creates light fields resulting in attractive one-dimensional random potential landscapes with $l_U = R$, whose distributions can be described by a Gaussian function with a standard deviation, σ_U, that can be adjusted by laser power P_L.

2.2 Diffuser Setup

In contrast to the setup described in Sec. III.2.1, the diffuser setup is used to create two-dimensional light fields. In particular, it is used to realize a flat two-dimensional speckle field (cf. Fig. II.12). The crucial component to achieve this, is an Engineered Diffuser™ (ED) introduced in Sec. II.2.4. The setup was built by Jörg Bewerunge [138]. Its components and optical pathway, as well as a photo of the actual setup can be seen in Figs. III.8 and III.9, respectively.

2.2.1 Beam Path of the Diffuser Setup

Similar to the SLM setup, the diffuser setup contains a diode-pumped solid-state laser emitting light with a wavelength $\lambda = 532$ nm (Opus 532, Laser Quantum Ltd.). Compared to the other laser, it is more powerful with a maximum power of 2600 mW. First, two mirrors (M1, M2, all mirrors from Thorlabs, Inc.) direct the laser light towards a beam expander with a variable magnification (1× –8×) and divergence correction (BE, S6EXZ5076/121, Sill Optics GmbH & Co. KG) as shown in Fig. III.8. In the experiments conducted in the work described in this thesis, the BE is set to 6×. Exiting the BE, laser light passes an aperture (AP1) and hits an Engineered Diffuser (ED, Engineered Diffuser™ EDC-1-07108-A 1R, RPC Photonics, Inc.). This diffuser shapes a top hat beam from the Gaussian beam coming from the laser. As mentioned in Sec. II.2.4 and [161], a coherent light source, just like the laser used here, leads to speckles in the pattern created by an ED. The size of these speckles—or the uniformity of the created pattern—is controlled by the area of light hitting an ED. In this setup, speckles inside the flat light field are desired. Together with the variable magnification of the BE, these speckles can be additionally tuned. Bigger beam areas lead to smaller speckle sizes or higher uniformity. Throughout the work described in this thesis, the size was not tuned but kept constant. Besides tunability of size, the speckles can also be rotated. A rotation mount (RM, PR50CC, Newport Corp.) housing the ED can conduct rotations with the axis parallel to the beam path and as a consequence rotate speckles inside the sample plane. The ED used for this work has a divergence angle of 1° and to compensate, a telescope made up

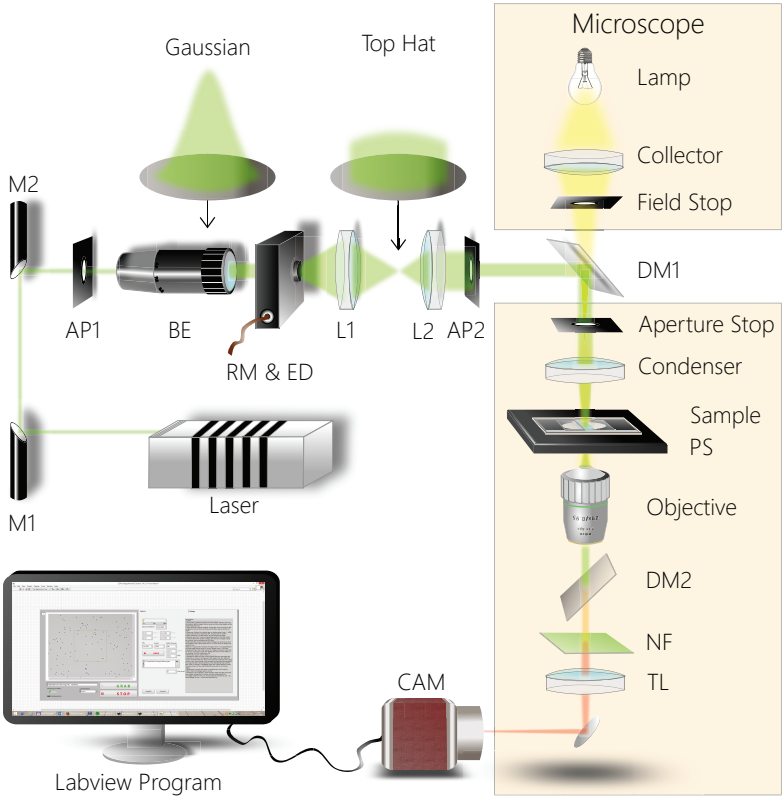

Figure III.8: Setup using an Engineered Diffuser™ (ED) to create two-dimensional light fields. The components inside the orange rectangle are inside a microscope or its beam path. A beam emitted by a laser is widened (BE) and directed onto an ED situated inside a rotation mount (RM). The resulting top hat pattern is focussed (L1, L2, Condenser), coupled into a microscope with a dichroic mirror (DM1) and hits the sample from the top, in the same direction as gravity. The sample cell is housed in a piezo stage to be able to be moved laterally. A camera (CAM) is flanged to the microscope recording micrographs of the sample. Abbreviations are given in the main text.

of lenses L1 (1" DCX 75, Edmund Optics GmbH) and L2 (2" PCX 75, Thorlabs, Inc.) is positioned behind the rotation mount. Next, the beam passes a sec-

ond aperture (AP2) and is coupled into the illumination path of the microscope (Eclipse Ti-U, Nikon Corp.) with a dichroic mirror (DM1, NT69-901, Edmund Optics GmbH). From there, it is directed through the aperture stop (AS), onto the condenser (TI-C-LWD, Nikon Corp.) and coincides with the microscopes illumination path. The condenser is positioned in a way that the laser beam is focussed inside the sample plane. Therefore, Köhler illumination is not necessarily achieved, but computer-assisted identification of colloidal particles is still possible (cf. Sec.III.3).

In contrast to the SLM setup, laser light enters the sample cell from the top and is thus parallel to gravitational forces. H_2O is the dispersion medium leading to gravitation and scattering forces again acting in the same direction. An additional piezo stage (PS, Nano-BioS300, Mad City Labs Inc.) was introduced to be able to move the sample cell in a controlled, well-defined manner perpendicular to the direction of propagation of the beam. It is actuated externally by a PC with a LabView program and features a housing for sample cells (cf. Sec. III.1, Fig. III.9). After the laser beam and light of the illumination path of the microscope pass through the sample, it is collected by the microscope objective (CFI S Plan Fluor ELWD 20×, Nikon Corp.). Laser light is filtered out by a second dichroic mirror (DM2, NT69-901, Edmund Optics GmbH) and a notch filter (NF, z532nf, Chroma Technology Corp.) underneath the objective for similar reasons given in Sec. III.2.1.1, namely to prevent damage of the camera and ensure high image quality.[3] Light that has not been filtered out is used for imaging the sample and hits a monochrome CMOS-camera (CAM, Mako U-130B, Allied Vision Technologies GmbH). This camera is controlled by an external LabView program similar to that used in the SLM setup and effectively records videos by saving sequences of images in the JPEG format resulting in a pixel pitch of 0.241 μm/px. Additionally, the LabView program controls the piezo stage and relates images to the corresponding stage positions. As with the SLM setup, the laser is turned on at least one hour prior to a measurement to warm up the laser and setup components.

[3] Unlike in the SLM setup, all stray light is filtered out in the diffuser setup.

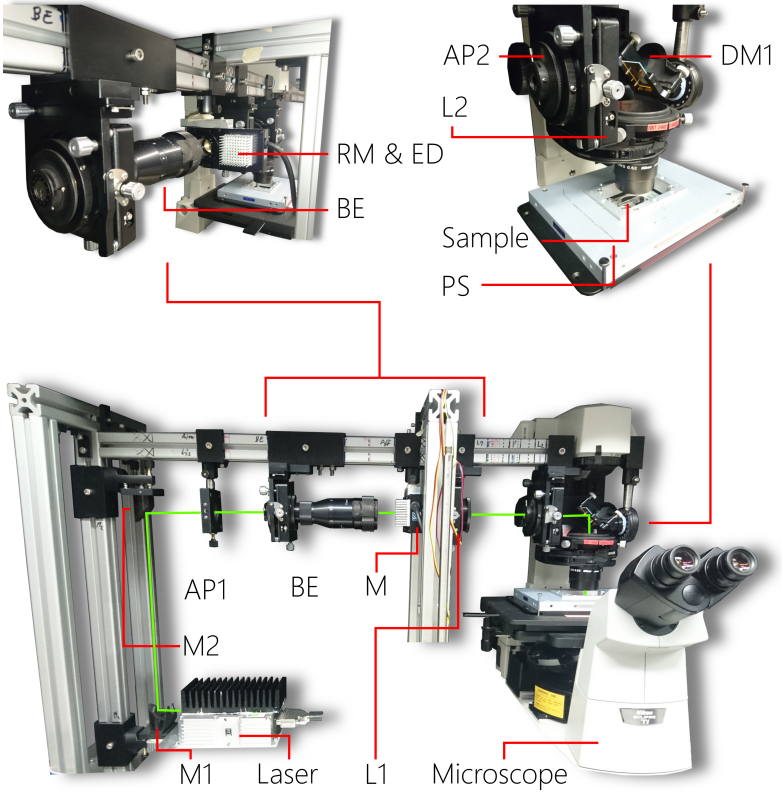

Figure III.9: Photograph of the diffuser setup, the schematic of which was shown in Fig. III.8. The green line shows the beam path. Not all components housed inside the microscope are marked due to space constraints. To get a better view of certain parts of the setup, they are magnified in the top part of the figure. Abbreviations are given in the main text.

2.2.2 Characterisation of Light Fields Created by the Diffuser Setup

As in Sec. III.2.1.3, the properties of a light field created by an ED are addressed here. A thorough investigation of these properties can be found in Refs. [138,

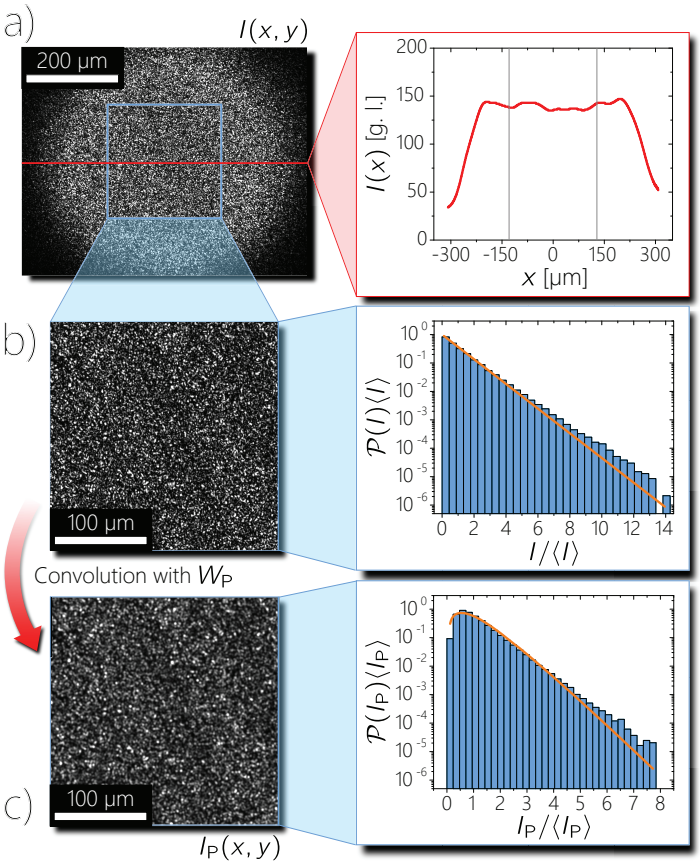

Figure III.10: Intensities and distributions of the light field created by the diffuser setup. a) Entire intensity pattern $I(x,y)$ created with the aid of the ED. The FOV is denoted by the blue square and the grey horizontal lines on the right-hand side, respectively. The profile along the red solid line reveals its overall flatness in the central part. b) The intensity in the FOV and its distribution (blue columns) fitted by an exponential decay (solid orange line). c) The intensity from b) convolved with $W_P(x,y)$ to obtain $I_P(x,y)$. The resulting distribution (blue columns) can be approximated by a gamma distribution (solid orange line).

187], which serve as a base for the analysis.[4] In Fig. III.10 a), a greyscale image of the flat top field created by the diffuser setup can be found. The one-dimensional smoothed intensity, $I(x)$, resolved in grey levels, is plotted for the path along the red line in the image. It shows that the light field exhibits an intensity which is mostly constant in the central region. This central region, marked by vertical grey lines in the plot on the right-hand side, is the FOV and observed when conducting measurements. It has a size of 1024 × 1024 px, or 247 × 247 µm^2, and is shown in more detail in Fig. III.10 b). On short length scales, the light field exhibits a speckle pattern stemming from the random features in an engineered diffuser (cf. Sec. II.2.4). The normalised probability density function (PDF) of the intensity on the right-hand side of Fig. III.10 b), shown in blue columns, reveals that the speckle pattern is similar but not equal to that created by the SLM setup. In the diffuser setup, the pattern is close to a fully developed speckle, where random amplitudes and phases of light creating it are uniformly distributed [186]. The intensity distribution then follows:

$$\mathcal{P}_{\mathrm{FD}}(I) = \frac{1}{\langle I \rangle} \exp\left\{ \frac{I}{\langle I \rangle} \right\}, \tag{III.6}$$

where $\langle I \rangle$ denotes the mean intensity of the speckle field [138, 186]. This exponential decay corresponds to a straight line with slope -1 in the normalised PDF given here and is denoted by the solid orange line. The correlation length—defined as in Sec. III.2.1.3—is about 0.8 R and thus higher than in the SLM setup. The intensity that a point-like particle would feel, $I_{\mathrm{P}}(x, y)$, is again calculated by convolving $I(x, y)$ with the weight function, $W_{\mathrm{P}}(x, y)$ for particles with R = 1.4 µm and can be seen in Fig. III.10 c). The intensity shows the characteristic smeared out features with an enlarged correlation length, l_U = 1.3 R. The corresponding PDF is shown in blue columns on the right-hand side. The convolution of $I(x, y)$ with $W_{\mathrm{P}}(x, y)$ corresponds to a weighted sum of random variables [188], distributed as shown in Fig. III.10 c). To what extent these random variables are correlated depends on the correlation length of $I(x, y)$ together with

[4] The situation described with 'BE 6×' corresponds to the situation described in this thesis.

$W_\mathrm{P}(x,y)$. A sum of completely independent exponentially distributed variables has a PDF that follows a gamma distribution [77, 189]:

$$\mathcal{P}_\Gamma(I_\mathrm{P}) = \frac{1}{\Gamma(M)} \left(\frac{M}{\langle I_\mathrm{P}\rangle}\right)^M I_\mathrm{P}^{M-1} \exp\left\{-\frac{M}{\langle I_\mathrm{P}\rangle} I_\mathrm{P}\right\}, \tag{III.7}$$

where M is the shape parameter. It corresponds to the number of independent speckles within $W_\mathrm{P}(x,y)$ [188] and lies between 1 and 25 for the diffuser setup [138]. M depends on the area of laser light hitting the ED—thereby determining the size, or correlation length, of speckles—and the size of $W_\mathrm{P}(x,y)$. The smaller the correlation length and the larger $W_\mathrm{P}(x,y)$, the more speckles are summed over when convolving $I(x,y)$ and $W_\mathrm{P}(x,y)$, which leads to a higher M. In Fig. III.10 c), $\mathcal{P}(I_\mathrm{P})\langle I_\mathrm{P}\rangle$ is approximated by a gamma distribution with $M = 2.2$ denoted by the solid orange line.

Similarly to Sec. III.2.1.3, the actual potential felt by colloidal particles $U(x,y)$ could be determined through Boltzmann statistics by measuring particle residence probabilities. In one-dimensional potentials, this approach is unproblematic: there are only two possible directions for a particle to move and thus in the long run a particle will explore even the highest potential maxima. In two-dimensional potentials, the possibilities to circumvent the highest maxima are numerous. The probability of single particles exploring the whole two-dimensional potential in realistic sample observation times, $t_\mathcal{O}$, is much lower than in one dimension. Thus, in the work described in this thesis, no measured potential $U(x,y)$ could be obtained by Boltzmann statistics. However, from Sec. III.2.1.3, it is known that $U(x,y)$ can be approximated by $I_\mathrm{P}(x,y)$. Therefore, the $I_\mathrm{P}(x,y)$ presented in Fig. III.10 c) is used as a substitute for $U(x,y)$. From Sec. III.2.1.3 and Ref. [182], it can be inferred that the roughness, or standard deviation, of the two-dimensional potential created by the diffuser setup, σ_U, can be controlled in the same manner with which it was controlled in the SLM setup, namely by the output power of the laser P_L. Here again, there is a linear behaviour between P_L and σ_U [190].

The diffuser setup consequently produces a two-dimensional random poten-

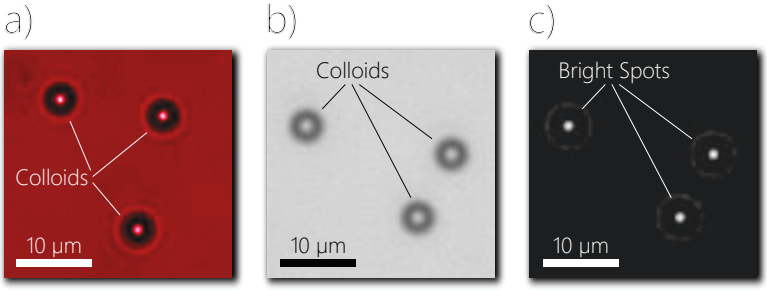

Figure III.11: Examples of photos taken by both setups. a) In the SLM setup the contrast is optimised by Köhler illumination. Central spots of particles appear bright while the background shows a red cast, due to the filters used (cf. Sec. III.2.1.1. b) The colloidal particles appear as dark grey rings on a light grey background in the diffuser setup. The contrast in this picture is not optimal as Köhler illumination is not achieved (cf. Sec. III.2.2). c) When the photo in a) is convolved with a boxcar and a Gaussian function, the particle centres appear as bright spots on a dark background.

tial landscape with correlation length, $l_U = 1.3\,R$ that is gamma distributed, showing a tail for strong potential minima, since particles used in the work described in this thesis are attracted by high intensities (cf. Secs. II.2.1 and III.1). As with the SLM setup, the standard deviation of the potential, σ_U, can be linearly controlled by P_L.

3 Video Microscopy

In Sec. III.2, the two setups used throughout this thesis were introduced. Both setups comprise cameras, which, together with a PC and appropriate LabView programs, enable one to take and save a time-lapse series of photos of a colloidal sample illuminated by a microscope. The rate with which photos are taken is referred to as frames per second (FPS), where 1/FPS corresponds to the minimum time step in a measurement, Δt_min. An example of a photo taken with the SLM setup is given in Fig. III.11 a). The colloidal particles in the field of view (FOV) appear as sharp black rings with white centres. When a setup with lower contrast

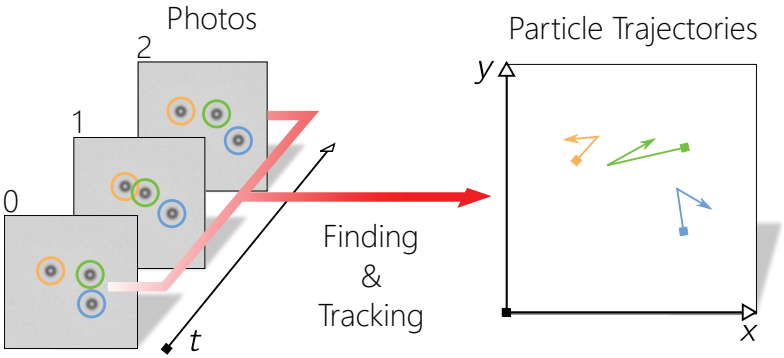

Figure III.12: Schematic of finding and tracking colloidal particles in photos taken during an experiment. Photos 0, 1, and 2 are taken at consecutive points in time t. Three particles are found in each photo. After tracking three different—orange, green, and blue—trajectories are built from particle coordinates.

is used, e.g. the diffuser setup, particles appear as dark grey rings on a light grey background (Fig. III.11 b)). Due to the lack of Köhler illumination in the diffuser setup, the contrast of the photo is only mediocre. In a typical measurement conducted in the course of the work described in this thesis, several thousands of these photos were taken with a constant frame rate and saved as JPEG files. This procedure is called video microscopy.

To make use of the photos taken during a measurement, particles in the FOV have to be first found, i.e. the coordinates of every single particle in each photo have to be extracted. In order to do so, a the features of a photo have to be analysed and categorised to find features that correspond to actual particles. Subsequently, the coordinates of each particle found in the single images have to be linked for the whole measurement to form a trajectory. This process is called particle tracking and is schematically illustrated in Fig. III.12. Photos 0, 1, and 2 contain three particles each and were taken at consecutive points in time t (Fig. III.12, left). For every particle—orange, green, and blue—the x- and y-coordinates are extracted and linked, so that trajectories are built and can be plotted in coordinate space

(Fig. III.12, right). Thereby, each point of a trajectory corresponds to a point in time. Once each particle in the FOV has been identified and a trajectory created, the complete output of the experiment has been gathered. The trajectories can then be used to calculate quantities such as the mean square displacement to quantify the particle dynamics (cf. Sec. III.4.3).

3.1 Computer-Based Analysis in Video Microscopy

In the work described in this thesis, finding, tracking, and the subsequent calculations were done with the aid of the programming language IDL (IDL, Harris Corp.). The routines to find and track particles were described by John Crocker and David G. Grier [191] and are provided on their webpage [192]. Similar routines, all based on [191], can be found for MATLAB [193] or Python [194] amongst others. There is an extensive tutorial on how to use these routines in detail in Ref. [192]. Thus only an overview of the used routines is given here.

To find particles, a photo similar to that shown in Fig. III.11 b) is convolved with a two-dimensional boxcar and a Gaussian function to reduce long-wavelength and random noise, respectively. The resulting image is depicted in Fig. III.11 c). It has a dark background with bright spots. Subsequently, coordinates of centroid, brightness corresponding to the summarised grey value, radius of gyration, and eccentricity are calculated for each bright spot. With these size and shape parameters, bright spots with non-appropriate characteristics can be sorted out, so that only actual particles are recognised as such. The coordinates of the centroids of the bright spots then serve as particle coordinates throughout the rest of the analysis. When all particles are found, their coordinates are linked together for every photo. Each photo corresponds to a point in time or—equivalently—to a time step. The length of the minimum time step a video microscopy measurement can resolve is calculated to $\Delta t_{\mathrm{min}} = 1/\mathrm{FPS}$. To link particle coordinates, the same particle has to be found in two consecutive photos and recognised as such. In order to do so, a probability estimate is conducted. From Sec. II.1.3 it is known that the probability for a Brownian particle to move a two-dimensional displacement, $\Delta \boldsymbol{r}$, is given according to Eq. II.13. Therefore, the probability for

x-Coordinate	y-Coordinate	Brightness	Radius of Gyration	Eccentricity	Time Step	Particle ID
252.9870962	503.7923083	223.9429932	2.565870047	0.01544979960	130.0000000	1.000000000
253.7773368	503.3156932	239.4149933	2.825119972	0.06271880120	131.0000000	1.000000000
254.4479127	504.5318970	183.3029938	2.433660030	0.01330349967	132.0000000	1.000000000
254.3160192	504.1545715	205.9230042	2.696949959	0.03494049981	133.0000000	1.000000000
496.7355850	145.9571681	230.4179993	2.797859907	0.03012749925	0.0000000000	2.000000000
497.0715988	145.7591088	241.0010071	2.609230042	0.02340099961	1.000000000	2.000000000
497.7286221	146.0864243	229.5290070	2.801980019	0.006444999948	2.000000000	2.000000000
496.6216003	145.2894259	237.1699982	2.836519957	0.02354370058	3.000000000	2.000000000

Figure III.13: Snippet of a table obtained by using a tracking routine in IDL. The red line marks a change in particle ID.

N_{FOV} particles in the field of view each making an individual step $\Delta\boldsymbol{r}_i$ reads [191]:

$$\prod_{i=1}^{N_{\mathrm{FOV}}} \mathcal{P}(\Delta\boldsymbol{r}_i, \Delta t) = \frac{1}{\sqrt{8\pi D\Delta t}} \exp\left\{ -\sum_{i=1}^{N_{\mathrm{FOV}}} \frac{\Delta\boldsymbol{r}_i^2}{8D\Delta t} \right\}. \tag{III.8}$$

To find the most likely links between particles, $\prod_{i=1}^{N_{\mathrm{FOV}}} \mathcal{P}(\Delta\boldsymbol{r}_i, \Delta t)$ has to be maximised. This corresponds to a minimisation of $\sum_{i=1}^{N_{\mathrm{FOV}}} \Delta\boldsymbol{r}_i^2$ as Eq. III.8 has its maximum when the exponent vanishes. The routines provided by Crocker et al. [191, 192] follow this idea by calculating all possible displacements between all available particles, $\Delta\boldsymbol{r}_i$, and finding the minimum. The particles are then assigned with an identification number (ID, last column in Fig. III.13), and thereby trajectory, according to the likeliest displacements. To save computational time, a maximal possible magnitude of displacement, Δr_{max}, is defined that a particle can move in one time step. Particles not having a counterpart being at a distance smaller than Δr_{max} in the previous photo are then considered to be newly introduced to the measurement and get a new ID.

A typical result of the tracking routine can be seen in Fig. III.13. It is a snippet of a table containing information about all the particles in a measurement. The first two columns contain the x- and y-coordinates. The last two contain the time step and the particle ID. Columns in between contain particle specific information gathered from the finding process: brightness, radius of gyration, and eccentricity. Rows of the table are sorted according to particle ID and time step. The end of each trajectory can be recognised by a change in particle ID and is

marked by the horizontal red line in Fig. III.13. The length of a trajectory, $\Delta t_{\mathrm{L},i}$, is individual for each particle i and can be calculated by subtracting the first time step of a trajectory $t_{\mathrm{first},i}$ from the last one $t_{\mathrm{last},i}$, where time steps are given as integer numbers in the next to last column in Fig. III.13. For each measurement, a table similar to that shown in Fig. III.13 is obtained. It is used to calculate the statistical quantities introduced in Sec. III.4.

3.2 Challenges and Optimisation of Video Microscopy

In practice, the only information gained from video microscopy are the images taken by a camera flanged to a microscope. Particle trajectories formed by computer software and the ensuing calculation of dynamical quantities belong to the analysis of a measurement and cannot make up for mistakes made when conducting experiments [195]. Problems range from images with low contrast to particles that move too fast. Therefore, great care should be taken when capturing photos of a sample. In the following, an overview of problems arising in video microscopy is given. It is certainly not complete, yet covers most of the challenges encountered in the course of the work described in this thesis.

3.2.1 Difficulties with Particle Finding

Finding particles with the routines described in Sec. III.3.1 can be straightforward—provided the quality of the taken images is sufficient. In this context, sufficient means as good as the experimental circumstances allow. In practice—such as in the setups used in the work described in this thesis—there are usually constraints that lower the highest possible image quality, e.g. the lack of Köhler illumination in the diffuser setup. Thus, it is important that the following problems are avoided, if possible.

One of the most important properties of an image from which a particle should be located is its contrast, $\mathcal{C}$. There are several ways of defining $\mathcal{C}$. Here, we will

focus on the Michelson $\mathcal{C}_{\mathrm{M}}$ [196] and RMS contrast $\mathcal{C}_{\mathrm{RMS}}$[5]. They read:

$$\mathcal{C}_{\mathrm{M}} = \frac{I_{\max} - I_{\min}}{I_{\max} + I_{\min}} \quad \text{and} \quad \mathcal{C}_{\mathrm{RMS}} = \sqrt{\frac{1}{N_x N_y} \sum_{i=1}^{N_x} \sum_{j=1}^{N_y} \left(I_{ij} - \langle I \rangle \right)^2}, \tag{III.9}$$

where $I_{\max}$ and $I_{\min}$ refer to the maximum and minimum grey levels of an analysed image, respectively, N_x and N_y the amount of pixels in x- and y-direction, respectively, I_{ij} a grey level specified by the summation indices for each pixel in the x- and y-direction and $\langle I \rangle$ the mean grey level of the entire image. Both definitions are a measure for the range of grey levels used by an image. The broader a histogram of the grey levels of an image, the higher are $\mathcal{C}_{\mathrm{M}}$ and $\mathcal{C}_{\mathrm{RMS}}$. In video microscopy, contrast can be gained by several methods depending on the setup used. When a confocal microscope is used, contrast can be defined by the fluorescence of the particles and can be changed by adjusting the gain and offset of the photon collector device [195]. In a bright-field microscope, contrast is generated by differences in refractive indices and in absorption. The difference between particle and surrounding medium has to be as high as possible to generate the highest contrast. It can then be adjusted by focus and brightness of the lamp. The former is depicted in Fig. III.14. Three images of colloidal particles with different focal planes are shown with each having their own histogram. The two peaks in the histograms represent the grey values of background and particles. When using video microscopy, the focal spot with the highest contrast, i.e. highest value for $\mathcal{C}_{\mathrm{M}}$ and $\mathcal{C}_{\mathrm{RMS}}$, should be chosen. In practice, this corresponds to the broadest histogram and at the same time the largest distance between the peaks. This is shown in the lower row of Fig. III.14, recognisable by the image, histogram and given values for contrasts. Besides the focal spot, the brightness of the microscope lamp is important. It should be adjusted so that histograms do not saturate at either end of the greyscale. That way, the dynamic range of a setup is optimally used. As a side effect, the highest contrast corresponds to particles appearing as

[5] The definition for $\mathcal{C}_{\mathrm{RMS}}$ is rather reminiscent of the root mean square deviation, also known as root mean square error or standard deviation. Still, the contrast is referred to as RMS, as the common definition for an RMS value would not make sense in this context.

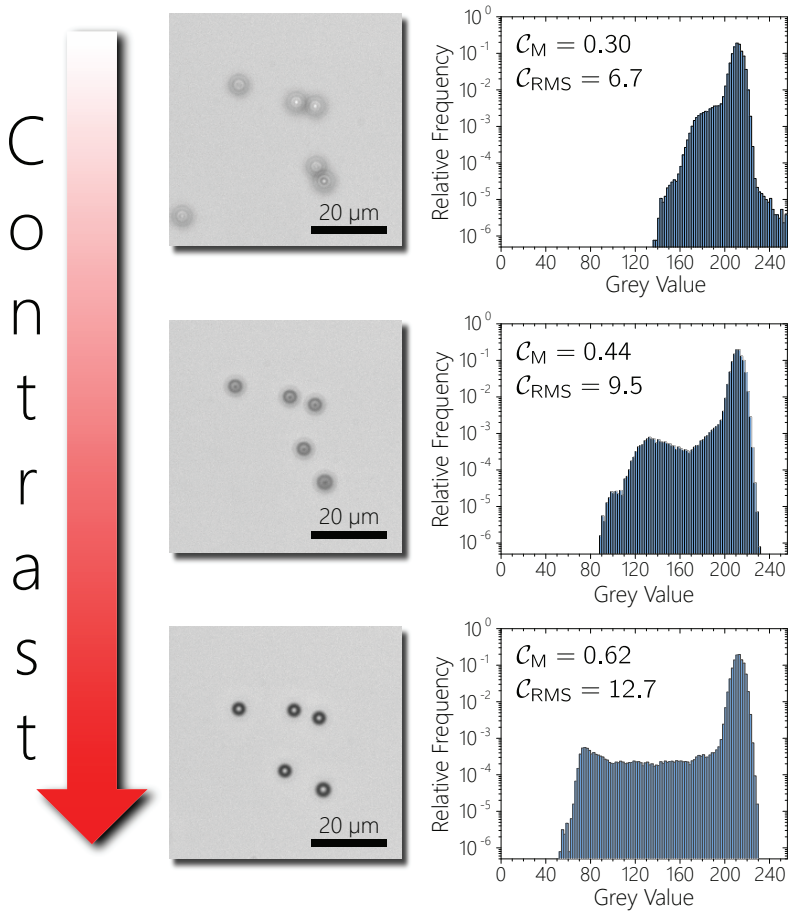

Figure III.14: The same sample observed in different focal planes. From top to bottom the focal plane is changed resulting in images with higher contrast. The histograms on the right-hand side quantify this impression as higher contrast leads to broader histograms and higher values for $\mathcal{C}_M$ and $\mathcal{C}_{RMS}$.

dark rings with a bright centre. As described in Sec. III.3.1, this is exactly the appearance particles should have in order to be found properly. Therefore, in video microscopy, optimum contrast is equivalent to optimum appearance of particles and vice versa.

Sometimes even a high contrast image does not lead to particles looking like dark rings with bright centres, especially when the colloids are very small compared to the FOV and camera resolution. In these cases, particles appear as dark blobs. The finding routines described in Sec. III.3.1 no longer work as there are no bright dots to analyse. The easiest remedy is increasing the magnification of the microscope. A different objective can be introduced to a setup quickly and often leads to more easily findable particles. If objectives cannot be exchanged for some reason, the acquired images can also be inverted in colour space. Light backgrounds will then be dark and dark blob-like particles light, looking similar to the image shown in Fig. III.11 c). Inversion of images however can cause additional problems when particles are close to each other. Then light blobs can touch or overlap and two particles will not be recognised as such, but appear to be one elongated colloid. Thus adjusting the magnification is always preferred when issues with particle size occur.

Another difficulty when using video microscopy can be the image background. Ideally, it is plain and does not show any structure or colour gradients. In reality though, backgrounds can be non-ideal as depicted in the centre of Fig. III.15. In this case, the notch filter inside the diffuser setup is not strong enough. As a result, not only particles (blue circles), but also the light field is imaged and shows features similar to particles. Consequently, particle finding is more difficult and leads to falsely found particles shown as red circles. On the left-hand side of Fig. III.15, the same sample is illuminated more strongly. This leads to poorer contrast, but, due to camera saturation, the background is uniform providing better results in finding particles, although the same parameters were used as in the central image. On the right-hand side, a stronger filter is used inside the setup. It filters out all the laser light and creates a grey uniform background while providing high contrast. As a result, all particles are found correctly. This config-

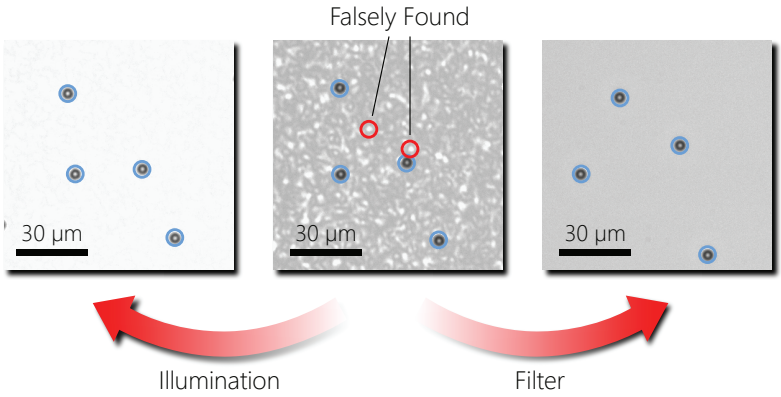

Figure III.15: The same sample with different backgrounds. In the middle, a light field creates a background leading to falsely found particles (red circles). When illuminating the sample more intensively or introducing a stronger filter, the background becomes uniform and particles can be found correctly.

uration would give optimum results in an experiment as the contrast is superior to a more strongly illuminated image.

Besides contrast, particle size and background, particle concentration can be a factor that has to be taken into account when trying to find all particles in the FOV. In very dilute samples, colloids seldom touch and thus do not create problems in finding them. In highly concentrated samples, particles can form aggregates with diversely sized voids in them, as depicted on the left-hand side of Fig. III.16. It shows an experiment conducted with the diffuser setup, where colloids with two different sizes were mixed. As can be seen, larger particles are concentrated more highly than smaller ones. When voids, apparent in Fig. III.16, are completely surrounded by particles and reach the particle size, then these spaces appear to be particles themselves: they have a dark perimeter—created by actual colloids—and a light centre—due to the light background—as can be seen on the right-hand side of Fig. III.16. As a result, voids can be falsely regarded as particles by particle finding routines. There is no easy way of circumventing this difficulty.

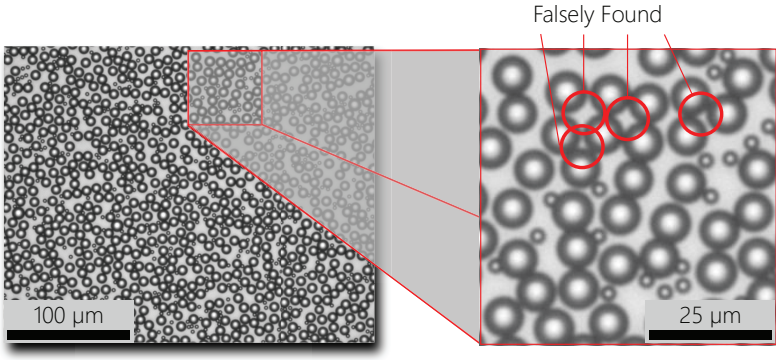

Figure III.16: Highly concentrated sample observed with diffuser setup. Higher concentrations can lead to voids looking similar to actual particles. As a result, voids are falsely identified as particles. Red circles in a 4× magnified detail on the right-hand side illustrate this difficulty.

High contrast images can prevent this problem as high contrast leads to particle centres being brighter than the background. In lower contrast images, careful choice of the right parameter ranges for particle characteristics such as brightness, radius of gyration, and eccentricity, can help minimising falsely found particles. Completely eliminating them can sometimes be impossible, however, as voids can look very similar to actual colloids—even to the human eye. Due to the dynamic nature of experiments conducted in the work described in this thesis void sizes and shapes are not static but change constantly. In practice, that means falsely found particles will pop up and disappear through the course of an experiment. Voids erroneously detected as colloids therefore usually only have short trajectories and can be excluded from analysis in a way that their effect on the final result is as small as possible.

Even if all these problems are solved or minimised and it seems all particles are found correctly, there will be an additional pitfall in the finding process as described in Ref. [192]: particle coordinates can be quantised, i.e. the coordinates of each particle are rounded to the nearest integer pixel value and do not show

sub-integer precision as they should. To check for that error, a histogram of the first decimal number of all the particle coordinates is made. If that histogram shows a uniform distribution, no quantisation exists. If it is peaked at zero and one, coordinates are quantised and finding routines have to be rerun with different input parameters.

In addition to the difficulties encountered with photos themselves, the acquisition process can influence the data analysis. Images are usually supposed to be saved with a constant rate. In practice, this is not always the case, since particularly high FPS can push hardware to its limits resulting in—sometimes random—delays in the acquisition. Successive frames may then have varying time gaps between them. If these are treated as being evenly spaced, this can lead to corrupted results in further analysis. When the particle dynamics—especially on small time scales—deviates from expectation, a varying image acquisition rate can be the cause. In such a case, a smaller amount of FPS or a proper camera-computer-tandem usually improves the situation.

3.3 Difficulties with Particle Tracking

Difficulties in particle tracking are not as evident as in particle finding but can be just as challenging. Compared to finding, tracking does not depend on the image quality itself but on acquisition rates that have to match the particle dynamics.

The tracking routine described in Sec. III.3.1 links coordinates by minimising the distance between all available coordinates in successive frames. Closest coordinates in two consecutive frames are thus assumed to represent the same particles. Hence, the displacement of each particle within 1/FPS, $\Delta r_i(\Delta t_{\min})$, should be equal to or smaller than half of the distance of this particle to its nearest neighbour, Δr_{ij}. When $\Delta r_i(\Delta t_{\min}) \leq \Delta r_{ij}/2$, the particle found at $\Delta t + \Delta t_{\min}$ which is closest to the position of a particle at Δt is always the same particle as depicted in Fig. III.17 a). There, real displacements of particles 1 and 2, $\Delta r_{1,\mathrm{r}}(\Delta t_{\min})$ and $\Delta r_{2,\mathrm{r}}(\Delta t_{\min})$, correspond to displacements calculated by the track routine $\Delta r_{1,\mathrm{t}}(\Delta t_{\min})$ and $\Delta r_{2,\mathrm{t}}(\Delta t_{\min})$, respectively. IDs stay the same as the blue particle is number 1 before and after a time step elapses. What happens when particles go

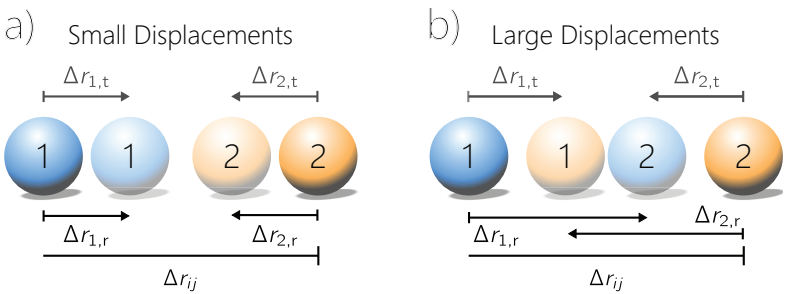

Figure III.17: Particle IDs depending on displacements Δr_i. Both sides show the situation for displacements within a minimum time step Δt_{min}. On the left-hand side $\Delta r_{i,\text{r}}$ are smaller than half the distance of a particle to its nearest neighbour, Δr_{ij}. No ID swapping occurs. On the right-hand side, real particle displacements $\Delta r_{i,\text{r}}$ are larger than half the distance. Thus ID 1 and 2 are swapped and displacements calculated by the track routine $\Delta r_{i,\text{t}}$ are different from the real ones.

further than $\Delta r_{ij}/2$ in one time step can be seen in Fig. III.17 b): two colloids approaching each other can have their IDs swapped as the particle with the closest coordinate in the next frame is not necessarily the same particle. As colloid 2 is closer to colloid 1 after Δt_{min}, the tracking routine assigns ID 1 to particle 2 and vice versa. As a result, displacements appear to be shorter and therefore colloids are calculated to be slower than they actually are. To be tracked correctly, particle displacements have to obey:

$$\Delta r_i(\Delta t_{\text{min}}) \leq \Delta r_{\text{max}} \leq \frac{\Delta r_{ij}}{2}\,, \tag{III.10}$$

where Δr_{max} is the maximum displacement allowed by the tracking routine introduced in Sec. III.3.1. For very high concentrations, almost all particles touch each other and Δr_{ij} can be equated to the particle diameter $2R$.

Equation III.10 also means that, independent of the actual dynamics and particle concentration in an experiment, the way the track routine assigns IDs limits the speed with which particles can move. Any colloids showing displacements

$\Delta r_i(\Delta t_{\min}) > \Delta r_{ij}/2$ will likely be assigned wrong IDs by the tracking routine at some point during a measurement. Consequently, these particles will be artificially slowed down in the long run. As $\Delta r_i(\Delta t_{\min})$ is a statistical quantity, i.e. not the same for every time step, particles will not be slowed down immediately. There is always a chance that no ID swapping occurs even though on average $\Delta r_i(\Delta t_{\min}) > \Delta r_{ij}/2$, but this chance gets smaller with longer measurements, i.e. a larger number of sampled time steps. Thus Eq. III.10 should not be taken as a strict rule but as a guideline: to avoid difficulties in tracking and possible hidden bias in the final data, $\Delta r_i(\Delta t_{\min}) \leq \Delta r_{ij}/2$ should be satisfied if possible. For colloids in strong flow fields, this condition often cannot be satisfied. In order to still be able to track particles, additional routines subtracting flow from coordinates can be introduced [170]. With such methods, tracking is still possible, even though displacements are larger than half of the nearest neighbour distance.

Another challenge connected to $\Delta r_i(\Delta t_{\min})$ is finding the right input parameters for tracking—in particular $\Delta r_{\max}$. In Sec. III.3.1 it was mentioned that not all possible displacements are calculated for two consecutive frames. To save computational time this calculation is limited to particle pairs that are closer than $\Delta r_{\max}$. The process of finding the right $\Delta r_{\max}$ is described in Ref. [192]. At first, a maximum distance is guessed and the tracking routine is conducted. If the histogram of $\Delta r_i(\Delta t_{\min})$[6] for the whole measurement decays to zero before it reaches $\Delta r_{\max}$, a value big enough was chosen. If the value was to small, the histogram still has a relatively high finite value at its tails. In order to save computational time, $\Delta r_{\max}$ should be as small as possible and definitely smaller than $\Delta r_{ij}/2$ as stated in the previous paragraph.

In addition to $\Delta r_{\max}$, the tracking routine can be fed with a minimum trajectory length and a memory feature. From Sec. III.3.2.1 it is known that falsely found particles can be the source of short tracks. In order to neglect these when analysing the data further, a minimum trajectory length can be used to get rid of very short trajectories. The memory feature can account for particles that were lost and reappear in the course of an experiment. This can easily happen at the

[6] This histogram should resemble a Gaussian function when non-interacting Brownian particles were measured.

edges of the FOV and when particles go out of focus for a short period of time. In these cases, use of the memory feature can lead to longer trajectories and more information in further data analysis. However, using this feature can cause problems since it is not known what happened to the particle when it went out of focus or the FOV. By using the memory option, particles lost for some time are assumed to behave similar to those found in the FOV, which is not necessarily a given. Therefore, in the work described in this thesis, the memory feature was not used.

4 Quanitifying Colloidal Dynamics

After measurements have been conducted and particles found and tracked, all information related to these measurements is readily available. Interpreting individual particle trajectories alone is often not very informative since they represent isolated samples. Instead, (histograms of) displacements and their moments, such as mean, variance, skewness and kurtosis are calculated to gain insight into the particle dynamics. They can quantify, e.g., speed (variance) or tendency (mean, skewness) of particle motion or clarify whether observed colloids are Brownian or not (kurtosis).

To get a better understanding of the introduced quantities, the concept of an underlying physical process defining particle trajectories and thus their displacements and moments that is used throughout [77] is discussed in this section. Probability density functions and other quantities of the process are referred to with a hat: $\widehat{\mathcal{P}}$. They represent the model that leads to displacements observed in a measurement. They are fixed and characteristic for a specific experiment. In practice, they are not known exactly because an infinite number of samples would have to be analysed to obtain them [77]. Quantities used in earlier sections, such as mean and variance, were introduced from a theoretical point of view. In that case there is no distinction between process and measured quantities. Since a real measurement only comprises a finite FOV and number of trajectories and can falsify results depending on the measurement procedure used, the best an experimentalist can do is to calculate expected values of aforementioned quantities using an estimate of $\widehat{\mathcal{P}}$ and obtain as many (independent) samples as possible. Thus the difference between expected value and actual (unknown) value of each quantity can be reduced to a minimum. Additionally, moments will be estimated to save computational time. Hence most of the quantities described in this section will be estimators.

4.1 The van Hove Function

The fundamental quantity underlying all other quantities describing the colloidal dynamics in this thesis is the probability density function $\widehat{\mathcal{P}}(\Delta\boldsymbol{r}, \Delta t)$ of particle displacements for a specific time difference $t - t_0 = \Delta t$ between the absolute time t and a starting time t_0 introduced in Sec. II.1.3.[7] For non-interacting Brownian particles it is a Gaussian with its variance proportional to time t. In an experiment, $\widehat{\mathcal{P}}(\Delta\boldsymbol{r}, \Delta t)$ is not known but defined by the process made up of particle behaviour and measurement as explained above. Therefore, $\widehat{\mathcal{P}}$ has to be estimated. To this end, the van Hove function $\mathcal{G}(\Delta\boldsymbol{r}, \Delta t)$ is utilised. It was introduced by Léon van Hove in 1954 [197] and for a system made up of N_P particles, it reads [197–199]:

$$\mathcal{G}(\Delta\boldsymbol{r}, \Delta t) = \frac{1}{N_\mathrm{P}} \left\langle \sum_{i=1}^{N_\mathrm{P}} \sum_{j=1}^{N_\mathrm{P}} \delta[\Delta\boldsymbol{r} - (\boldsymbol{r}_j(t_0 + \Delta t) - \boldsymbol{r}_i(t_0))] \right\rangle , \tag{III.11}$$

where $\delta[\cdot]$ represents the Dirac delta function. The average indicated by the angle brackets refers to an ensemble average over initial conditions that is equivalent to a time average over different starting times t_0 for very long observation times, $t_\mathcal{O}$, or often similar trajectory lengths, Δt_L, when the observed sample is ergodic [88, 190, 198, 200, 201]. In this context the microscopic particle density, $n_\varrho(\boldsymbol{r}, t)$, reads [198]

$$n_\varrho(\boldsymbol{r}, t) = \sum_{i=1}^{N_\mathrm{P}} \delta[\boldsymbol{r} - \boldsymbol{r}_i(t)] , \tag{III.12}$$

where the Dirac delta function represents the local density of a single particle. Density $n_\varrho(\boldsymbol{r}, t)$ should not be confused with the $\varrho_N(\boldsymbol{r}, t)$ introduced in Sec. II.1.3, since $n_\varrho(\boldsymbol{r}, t)$ represents a microscopic quantity, whereas $\varrho_N(\boldsymbol{r}, t)$ is macroscopic, coarse-grained. Under certain conditions, both densities can however behave similarly (see below). Together with Eq. III.12 and by integration over volume, $\mathcal{G}(\Delta\boldsymbol{r}, \Delta t)$ can be rearranged to a density correlation function in time [197, 198,

[7] It was introduced as $\mathcal{P}$, a theoretical quantity, for which $\widehat{\mathcal{P}} = \mathcal{P}$ holds.

202]:

$$\begin{aligned}\mathcal{G}(\boldsymbol{r}', \Delta\boldsymbol{r}, \Delta t) &= \frac{1}{N_\mathrm{P}} \left\langle \int \sum_{i=1}^{N_\mathrm{P}} \sum_{j=1}^{N_\mathrm{P}} \delta[\boldsymbol{r}' + \Delta\boldsymbol{r} - \boldsymbol{r}_j(\Delta t + t_0)] \right. \\ &\qquad \left. \times \delta[\boldsymbol{r}' - \boldsymbol{r}_i(t_0))] \, \mathrm{d}\boldsymbol{r}' \right\rangle \qquad \text{(III.13)} \\ &= \frac{1}{N_\mathrm{P}} \left\langle \int n_\varrho(\boldsymbol{r}' + \Delta\boldsymbol{r}, t_0 + \Delta t) \, n_\varrho(\boldsymbol{r}', t_0) \, \mathrm{d}\boldsymbol{r}' \right\rangle \\ &= \frac{1}{N_\mathrm{P}} \langle n_\varrho(\boldsymbol{r}' + \Delta\boldsymbol{r}, t_0 + \Delta t) \, n_\varrho(\boldsymbol{r}', t_0) \rangle \, .\end{aligned}$$

The van Hove function consequently shows how well correlated a density is with itself depending on the time passed, Δt, and the distance, $\Delta\boldsymbol{r}$. The starting time, t_0, and space coordinate, $\boldsymbol{r}'$, can be chosen to be zero [203]. The van Hove function is not only of great importance in real space, as shown in Eqs. III.11 and III.13, but also in Fourier space. When Fourier transformed in space $\mathcal{G}(\Delta\boldsymbol{r}, \Delta t)$ corresponds to the intermediate scattering function [198, 204]:

$$f(\boldsymbol{k}, \Delta t) = \int \mathcal{G}(\Delta\boldsymbol{r}, \Delta t) \exp\{-\mathrm{i}\boldsymbol{k}\Delta\boldsymbol{r}\} \, \mathrm{d}\Delta\boldsymbol{r} = \langle \exp\{-\mathrm{i}\boldsymbol{k}\Delta\boldsymbol{r}\} \rangle \, , \qquad \text{(III.14)}$$

which also happens to be the so-called characteristic function of $\Delta\boldsymbol{r}$ [5, 205]. This function can be deduced from correlated intensities measured in a scattering experiment [206]. Fourier transforming the intermediate scattering function in time leads to the dynamic structure factor [198, 204]:

$$S(\boldsymbol{k}, \omega) = \int f(\boldsymbol{k}, \Delta t) \exp\{-\mathrm{i}\omega\Delta t\} \, \mathrm{d}\Delta t \qquad \text{(III.15)}$$

which contains information on the spatial arrangement of scattering particles and its time evolution [206]. In the form of $f(\boldsymbol{k}, \Delta t)$, the van Hove function is consequently an integral part of scattering measurements.

Due to the two sums in Eq. III.11, $\mathcal{G}(\Delta\boldsymbol{r}, \Delta t)$ can be split in two parts:

$$\mathcal{G}(\Delta\boldsymbol{r}, \Delta t) = \mathcal{G}_\mathrm{s}(\Delta\boldsymbol{r}, \Delta t) + \mathcal{G}_\mathrm{d}(\Delta\boldsymbol{r}, \Delta t)\,, \tag{III.16}$$

the self part of the van Hove function:

$$\mathcal{G}_\mathrm{s}(\Delta\boldsymbol{r}, \Delta t) = \frac{1}{N_\mathrm{P}} \left\langle \sum_{i=1}^{N_\mathrm{P}} \delta[\Delta\boldsymbol{r} - (\boldsymbol{r}_i(t_0 + \Delta t) - \boldsymbol{r}_i(t_0))] \right\rangle \tag{III.17}$$

and its distinct part:

$$\mathcal{G}_\mathrm{d}(\Delta\boldsymbol{r}, \Delta t) = \frac{1}{N_\mathrm{P}} \left\langle \sum_{i=1}^{N_\mathrm{P}} \sum_{\substack{j=1 \\ j\neq i}}^{N_\mathrm{P}} \delta[\Delta\boldsymbol{r} - (\boldsymbol{r}_j(t_0+\Delta t) - \boldsymbol{r}_i(t_0))] \right\rangle . \tag{III.18}$$

Generally speaking, $\mathcal{G}(\Delta\boldsymbol{r}, \Delta t)\,\mathrm{d}\Delta\boldsymbol{r}$ is the probability that any particle j is found displaced at a region $\mathrm{d}\Delta\boldsymbol{r}$ around $\Delta\boldsymbol{r}$ at time $t_0 + \Delta t$ given that any particle i was at a region $\mathrm{d}\Delta\boldsymbol{r}$ around the origin at time t_0 [198, 204].[8] The self part $\mathcal{G}_\mathrm{s}(\Delta\boldsymbol{r}, \Delta t)$ consequently represents the probability of the same particle being at the origin at t_0 and then displaced by $\Delta\boldsymbol{r}$ at $t_0 + \Delta t$, whereas the distinct part shows how likely it is for a particle j being at $\Delta\boldsymbol{r}$ at time $t_0 + \Delta t$ given that a different particle i was at the origin at t_0. When $\Delta t = 0$, none of the particles are displaced compared to their original position and hence $\mathcal{G}_\mathrm{s}(\Delta\boldsymbol{r}, 0) = \delta[\Delta\boldsymbol{r}]$. The distinct part is then represented by the pair distribution function $g(\Delta\boldsymbol{r})$, namely $\mathcal{G}_\mathrm{d}(\Delta\boldsymbol{r}, 0) = (N_\mathrm{P}/V)\, g(\Delta\boldsymbol{r})$ with the volume, V, in which N_P particles are found. When the system is isotropic, $g(\Delta\boldsymbol{r}) = g(\Delta r)$, where $g(\Delta r)$ is called radial distribution function and $g(\Delta r)\mathrm{d}\Delta r$ is the probability to find a different particle at radius Δr given that another particle is situated at the origin.

A part of $\mathcal{G}(\Delta\boldsymbol{r}, \Delta t)$ is used to estimate $\widehat{\mathcal{P}}(\Delta\boldsymbol{r}, \Delta t)$ in order to calculate several quantities describing the particle dynamics. This part can be identified as the self part. It was stated that $\varrho_N(\boldsymbol{r}, t) \neq n_\varrho(\boldsymbol{r}, t)$ and therefore $\mathcal{G}_\mathrm{s}(\Delta\boldsymbol{r}, \Delta t)$ should not necessarily behave like $\mathcal{P}_\mathrm{B}(\Delta\boldsymbol{r}, \Delta t)$ for Brownian motion, where $\varrho_N(\boldsymbol{r}, t)$ was

[8] The origin mentioned here is defined by $\boldsymbol{r}'$ and can be chosen to be zero.

used. This is, however, only true for very short times. For long times compared to the velocity and positional correlation time—or thermal fluctuations at long wavelengths and low frequencies— a displacement $\Delta\boldsymbol{r}$ conducted in time Δt is made up of many smaller displacements conducted in smaller time steps. According to the central limit theorem the sums of these small displacements should obey a Gaussian distribution [77, 204]. Thus the self part of the van Hove function obeys Fick's second law of diffusion [79, 198, 204]

$$\frac{\partial\, \mathcal{G}_\mathrm{s}(\Delta\boldsymbol{r}, \Delta t)}{\partial \Delta t} = D\, \nabla^2 \mathcal{G}_\mathrm{s}(\Delta\boldsymbol{r}, \Delta t) \tag{III.19}$$

with the same solution for pure Brownian motion in two dimensions as for $\mathcal{P}(\Delta\boldsymbol{r}, \Delta t)$ [198, 199, 204]:

$$\mathcal{G}_{\mathrm{s,B}}(\Delta\boldsymbol{r}, \Delta t) = \frac{1}{\sqrt{8\pi D \Delta t}} \exp\left\{-\frac{\Delta\boldsymbol{r}^2}{8D\Delta t}\right\} = \mathcal{P}_\mathrm{B}(\Delta\boldsymbol{r}, \Delta t)\,. \tag{III.20}$$

In order to calculate $\mathcal{G}_\mathrm{s}(\Delta\boldsymbol{r}, \Delta t)$ in a video microscopy experiment, particle displacements are calculated for each particle, i, for all discrete starting times, t_0, and all repeat measurements, j, and normalised by the total number of samples, N_S. Thus $\mathcal{G}_\mathrm{s}(\Delta\boldsymbol{r}, \Delta t)$ contains the ensemble of all discrete displacements conducted within Δt. It represents a measured probability density function that behaves like a Gaussian function for Brownian particles. Hence the equal sign on the left-hand side in Eq. III.20 signifies "behaves like" for a $\mathcal{G}_\mathrm{s}(\Delta\boldsymbol{r}, \Delta t)$ drawn from empirical data.

The formula to calculate $\mathcal{G}_\mathrm{s}(\Delta\boldsymbol{r}, \Delta t)$ in a video microscopy experiment then reads

$$\mathcal{G}_\mathrm{s}(\Delta\boldsymbol{r}, \Delta t) = \frac{1}{N_\mathrm{S}} \left(\sum_{j=1}^{N_\mathrm{M}} \sum_{i=1}^{N_{\mathrm{P},j}} \sum_{t_0}^{N_{\Delta t,i}} \delta[\Delta\boldsymbol{r} - (\boldsymbol{r}_{ji}(t_0 + \Delta t) - \boldsymbol{r}_{ji}(t_0))] \right), \tag{III.21}$$

where

$$N_{\mathrm{S}}(\Delta t) = \sum_{j=1}^{N_{\mathrm{M}}} \sum_{i=1}^{N_{\mathrm{P},j}(\Delta t)} N_{\Delta t,i}(\Delta t_{\mathrm{L},i}, \Delta t, \Delta t_{\mathrm{min}}) \,. \tag{III.22}$$

In this case, $N_{\Delta t,i} = (\Delta t_{\mathrm{L},i} - \Delta t + \Delta t_{\mathrm{min}})/\Delta t_{\mathrm{min}}$ is an integer amount of a variable time step, Δt, that fits into a trajectory length $\Delta t_{\mathrm{L},i}$ taking into account the minimum time step Δt_{min} of the video microscopy setup. The trajectory length $\Delta t_{\mathrm{L},i}$ introduced in Sec. III.3.1 depends on each particle i and is defined by $\Delta t_{\mathrm{L},i} = t_{\mathrm{last},i} - t_{\mathrm{first},i}$, where $t_{\mathrm{first},i}$ and $t_{\mathrm{last},i}$ are the first and last time steps of a trajectory i in absolute time, t, respectively. N_{M} is the amount of measurements conducted—equivalent to ensembles with different initial conditions—and $N_{\mathrm{P},j}(\Delta t)$ the number of particles for each measurement j depending on Δt, as particles can enter and leave the FOV. Whether each summation and which summation is conducted at all when using Eq III.21, largely depends on the experiment and has to be considered before analysis (see Sec. III.4.6). A typical result for a self part of a van Hove function of Brownian and non-Brownian particles in video microscopy can be seen as blue columns in Fig. III.18. The upper part shows $\mathcal{G}_{\mathrm{s}}(\Delta x)$ for Brownian particles being subject to a constant drag velocity of $v_{\mathrm{D}} = 0.9\,\mu\mathrm{m/s}$ in x-direction for $\Delta t = 10$ s. A Gaussian PDF, depicted in orange, fits well to $\mathcal{G}_{\mathrm{s}}(\Delta x)$. It has a mean (light grey long-dashed line) of $\langle \Delta x \rangle = v_{\mathrm{D}} \Delta t = 9\,\mu\mathrm{m}$ in accordance with Sec. II.1.3. In the lower part, a static potential was added to the experiment resulting in particles being non-Brownian. The corresponding probability density function cannot be fitted by a Gaussian PDF. In further analysis, quantities like variance, skewness and kurtosis can be calculated from $\mathcal{G}_{\mathrm{s}}(\Delta x, \Delta t)$—or equivalently estimated from the ensemble of all the displacements—rendering it the cornerstone of quantification of the colloidal dynamics.

4.2 Mean—Drift—Transport

The mean particle displacement within a specific amount of time Δt has already been mentioned. It is equivalent to the first moment about zero and reads

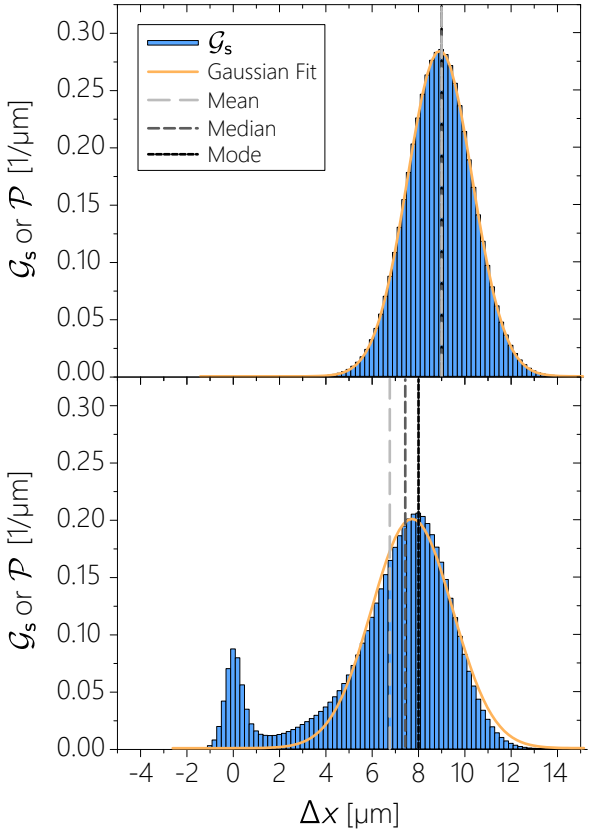

Figure III.18: Self Part of the van Hove function for Brownian and non-Brownian particles subject to a drift $v_D = 0.9$ µm/s for $\Delta t = 10$ s. In the upper part $\mathcal{G}_s(\Delta x)$ for Brownian particles is fitted well by a Gaussian function (orange line). In the lower part an external potential was added in the experiment. As a result particles are non-Brownian and the Gaussian function does not fit anymore. Mean (light grey long-dashed line), median (dark grey dashed line), and mode (black short-dashed line) are marked in both probability density functions.

in one dimension:

$$\widehat{\langle \Delta x \rangle}(\Delta t) = \int_{-\infty}^{\infty} \Delta x \, \widehat{\mathcal{P}}(\Delta x, \Delta t) \, \mathrm{d}\Delta x \,. \tag{III.23}$$

In an actual experiment, $\widehat{\mathcal{P}}(\Delta x, \Delta t)$ is estimated by $\mathcal{G}_\mathrm{s}(\Delta x, \Delta t)$ and not known. Obtaining $\mathcal{G}_\mathrm{s}(\Delta x, \Delta t)$ for each Δx and Δt can be time consuming. As explained in the introduction of Sec. III.4, estimated quantities are used for that reason. The estimator of the mean reads

$$\langle \Delta x \rangle(\Delta t) = \frac{1}{N_\mathrm{S}} \sum_{i=1}^{N_\mathrm{S}} \Delta x_i(\Delta t) \,, \tag{III.24}$$

where i is summed over all displacements calculated according to Eq. III.21. This formula is used when any given $\langle \Delta x \rangle(\Delta t)$ is calculated with the aid of IDL. There is a difference between the mean, which is caused by physical processes in a system, $\widehat{\langle \Delta x \rangle}(\Delta t)$, and the mean that is measured, $\langle \Delta x \rangle(\Delta t)$. The former is desired by every experimentalist, but the latter is that which is obtained. The goal is to obtain a $\langle \Delta x \rangle(\Delta t)$ that is as close to $\widehat{\langle \Delta x \rangle}(\Delta t)$ as possible.

For pure Brownian motion, $\mathcal{G}_\mathrm{s}(\Delta x, \Delta t)$ follows Eq. II.13 and thus $\langle \Delta x \rangle(\Delta t) = 0$. A vanishing mean implies that there is no preferred direction in particle displacements. Consequently, a finite $\langle \Delta x \rangle(\Delta t)$ indicates that there is a preferred direction, also called drift. In some experiments, drift is not wanted, e.g., when it arises from an unstable microscope stage or light source, and therefore is deliberately excluded from data in postprocessing [170, 207–209]. From Sec. II.1.3 it is known that, for Brownian motion with a constant drag velocity v_D, the particle dynamics and therefore $\mathcal{G}_\mathrm{s}(\Delta x, \Delta t)$ follows Eq. II.21 and $\langle \Delta x \rangle(\Delta t) = v_\mathrm{D} \Delta t$. When all particles are subject to the same constant v_D, the mean can be subtracted from displacements Δx to obtain the particle dynamics without drift. In the upper part of Fig. III.18, $\langle \Delta x \rangle(\Delta t) = 9$ µm could be subtracted from all displacements. The result would be a $\mathcal{G}_\mathrm{s}(\Delta x, \Delta t)$ centred about zero revealing pure Brownian motion. When v_D is time- or particle-dependent, this simplification cannot be done as easily. Depending on the types of samples N_S is made up of—

different particles i, different starting times t_0, or both—subtraction of $\langle\Delta x\rangle(\Delta t)$ from displacements would not account for changes in time and particle, because $\langle\Delta x\rangle(\Delta t)$ would not apply for all particles similarly. Due to a space-dependent external potential, the PDF in the lower part of Fig. III.18, for example, shows $\langle\Delta x\rangle(\Delta t) = 6.8$ µm although all particles were subject to the same constant positive drag velocity as in the upper part. Subtracting that value from all displacements alike would result in particles represented by the left peak showing highly negative displacements though being subject to a positive v_D. Physically this would not make sense even if particles were subject to an additional external potential and therefore should not be done in this case. Instead of using diffusing particles to correct for drift, several sources use fixed markers inside their samples to measure their mean displacement and correct for it [208, 210]. That way, drift is measured independently from particle motion and consequently provides better results when subtracted.

Besides being an indicator for biased motion and means to correct for it in postprocessing, $\langle\Delta x\rangle(\Delta t)$ can also be interpreted as transport, flux, or velocity when divided by time t [211–214]. When colloidal particles are subject to external forces their reaction can be quantified by finding their mean displacement—for example when colloidal diffusion is rectified by a ratchet potential [211]. Depending on the alternating frequency of a ratchet, particles tend to move along a ratchet with different speeds. Mean displacements are the means of choice to quantify that behaviour.

In this regard, it can sometimes be more telling when the median or mode are used instead of the mean. The median (dark grey dashed line in Fig. III.18), also called the 50th percentile, splits a distribution into two parts, such that each part represents 50 % of the whole area under the distribution curve. The mode (black short-dashed line in Fig. III.18) is an input value at which a distribution takes its maximum. For symmetric distributions, all three quantities are equal as can be seen in the top part of Fig. III.18. When a PDF is asymmetric like in the lower part of the figure, the median and mode are less affected by long tails as the mean. Therefore, they are sometimes more representative for a majority of particles in

an experiment.

4.3 Variance—Mean Square Displacement—Diffusion

The most frequently used quantity related to colloidal dynamics is probably the second moment. The second moment about zero is referred to as the mean square displacement (MSD) and was already introduced in Sec. II.1.3. In one dimension it reads:

$$\widehat{\langle \Delta x^2 \rangle}(\Delta t) = \int_{-\infty}^{\infty} \Delta x^2 \, \widehat{\mathcal{P}}(\Delta x, \Delta t) \, \mathrm{d}\Delta x \tag{III.25}$$

following the definition of the first moment about zero in Eq. III.23. Second or higher moments can also be defined about the mean—unlike the first moment. The second moment about the mean is called variance and is generally defined as:

$$\begin{aligned}
\sigma^2_{\Delta x}(\Delta t) &= \int_{-\infty}^{\infty} (\Delta x - \langle \Delta x \rangle)^2 \, \mathcal{P}(\Delta x, \Delta t) \, \mathrm{d}\Delta x \\
&= \langle (\Delta x - \langle \Delta x \rangle)^2 \rangle \\
&= \langle (\Delta x^2 - 2\Delta x \langle \Delta x \rangle + \langle \Delta x \rangle^2) \rangle \\
&= \langle \Delta x^2 \rangle - 2\langle \Delta x \rangle^2 + \langle \Delta x \rangle^2 \\
&= \langle \Delta x^2 \rangle - \langle \Delta x \rangle^2 \qquad \Leftrightarrow \\
\langle \Delta x^2 \rangle(\Delta t) &= \sigma^2_{\Delta x} + \langle \Delta x \rangle^2
\end{aligned} \tag{III.26}$$

just as shown in Sec. II.1.3.[9] The Δt dependence was not given explicitly on the right-hand side for convenience.[10] Equation III.26 is valid as long as the first and

[9] The hats on the quantities referring to them as process quantities and not measured ones are omitted here as the relationship is generally valid.

[10] The following equations also depend on Δt on both sides. However, for clarity reasons, stating that explicitly is often limited to the left-hand side.

second moments are computed using the same average. It can be seen that the broadness of a distribution about the origin defined by the square root of the second moment, $\sqrt{\langle \Delta x^2 \rangle}(\Delta t)$, is related to the broadness about the mean defined by the square root of the variance, called standard deviation $\sigma_{\Delta x}(\Delta t)$, via a Pythagorean addition with the mean $\langle \Delta x \rangle(\Delta t)$ (cf. Fig. II.7).

The estimator of the variance used when $\widehat{\mathcal{P}}(\Delta x, \Delta t)$ is not known is given by:

$$\sigma^2_{\Delta x}(\Delta t) = \frac{1}{N_S} \sum_{i=1}^{N_S} (\Delta x_i - \langle \Delta x \rangle)^2 . \tag{III.27}$$

This is the plug-in estimator of variance and is slightly biased [77]. Due to the fact that $\langle \Delta x \rangle(\Delta t)$ also represents an estimator calculated with the same data with which the estimator of the variance is computed, the deviations from this mean tend to be too small. Therefore, the plug-in estimator of variance is biased to low values [77]. To account for that there is the standard, unbiased estimator:

$$\sigma^2_{\Delta x}(\Delta t) = \frac{1}{N_S - 1} \sum_{i=1}^{N_S} (\Delta x_i - \langle \Delta x \rangle)^2 . \tag{III.28}$$

For large N_S both estimators give similar values. As the unbiased estimator also gives reliable results for small N_S, it was used throughout the work described in this thesis. When applied in computers, Eq. III.28 can cause problems due to roundoff errors [215]. Therefore, when the variance was estimated in the work described in this thesis, the corrected two-pass algorithm was used [215–217]. It is called two-pass because all samples have to be analysed twice, first $\langle \Delta x \rangle(\Delta t)$ has to be calculated, then $\sigma^2_{\Delta x}(\Delta t)$ is obtained. The corrected version of that al-

gorithm reads [216]:

$$\sigma^2_{\Delta x}(\Delta t) = \frac{1}{N_\mathrm{S} - 1} \left\{ \sum_{i=1}^{N_\mathrm{S}} (\Delta x_i - \langle \Delta x \rangle)^2 - \frac{1}{N_\mathrm{S}} \left[\sum_{i=1}^{N_\mathrm{S}} (\Delta x_i - \langle \Delta x \rangle) \right]^2 \right\} . \tag{III.29}$$

The first part of the right-hand side represents Eq. III.28. The following term calculates the mean deviation of single displacements from the mean. It would be zero if computer calculations were perfect. In practice it serves as a correction for roundoff errors of the first term [215, 216].

The reason the variance is chosen over the pure second moment when discussing the particle dynamics in this thesis can be given with the aid of Fig. II.7 and III.19. When there is no drift in particle displacements, i.e. $\langle \Delta x \rangle(\Delta t) = 0$ for all time steps Δt, then there is no difference between $\langle \Delta x^2 \rangle(\Delta t)$ and $\sigma^2_{\Delta x}(\Delta t)$ as can be seen on the left-hand side of Fig. II.7. So whenever no drift is expected in an experiment, any of those quantities can be chosen. However in this thesis, there are experiments where drift is expected. In these experiments, $\langle \Delta x \rangle(\Delta t)$ changes over the course of time Δt (cf. Fig. II.7). Since the MSD is a moment about zero, the length $\sqrt{\langle \Delta x^2 \rangle}(\Delta t)$ is affected by the mean and width of a distribution alike and neither represents drift nor diffusion but lies in between. The larger of the latter defines $\langle \Delta x^2 \rangle(\Delta t)$ as depicted in Fig. III.19. There, variance, MSD, and squared mean are given for the experiment represented by the lower part of Fig. III.18: Particles are dragged through an external potential by a drag velocity, $v_\mathrm{D}(\Delta t)$. MSD (orange circles) and squared mean (green triangles) mostly fall on top of each other, showing that the MSD is dominated by drift in that measurement. The diffusive part of the particle dynamics, represented by the width of the distribution shown in the lower part of Fig. III.18 cannot be analysed by $\langle \Delta x^2 \rangle(\Delta t)$ in this case, as drift disguises diffusion. When considering the variance, standard deviation $\sigma_{\Delta x}(\Delta t)$ can be thought of as representing half the width

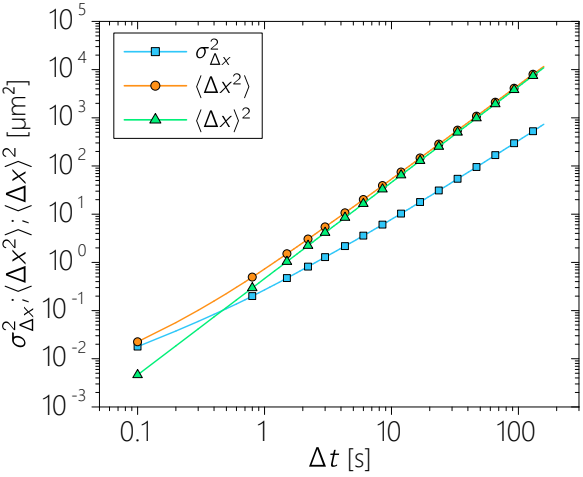

Figure III.19: Time-dependent variance, $\sigma^2_{\Delta x}(\Delta t)$, MSD, $\langle \Delta x^2 \rangle(\Delta t)$, and squared mean, $\langle \Delta x \rangle^2(\Delta t)$ of the experiment introduced in Fig. III.18: Particles being dragged with v_D through an external potential.

of a distribution, as shown in Fig. II.7.[11] The variance depicted by blue squares in Fig. III.19 shows values an order of magnitude lower than $\langle \Delta x^2 \rangle(\Delta t)$ and reveals a trend that was not apparent in the MSD. Thus $\langle \Delta x \rangle(\Delta t)$ and $\sigma^2_{\Delta x}(\Delta t)$ can be looked at separately to be able to interpret drift and diffusion individually.

The reason the variance—or second moment when $\langle \Delta x \rangle(\Delta t) = 0$—serves as the main parameter when it comes to diffusion is the fact that it is the first non-vanishing moment for pure Brownian motion. Its interpretation is nevertheless not very intuitive. Chebyshev's inequality is the only universal way of interpreting it:

$$\Pr\{ \Delta x \in [\langle \Delta x \rangle - j\,\sigma_{\Delta x},\ \langle \Delta x \rangle + j\,\sigma_{\Delta x}] \} > 1 - \frac{1}{j^2}\,, \tag{III.30}$$

[11] Of course, the actual interpretation of $\sigma_{\Delta x}(\Delta t)$ is different from being half of the width of a distribution. As in this thesis there are distributions similar to Gaussian functions for the most part, this statement however mostly gives a good indication.

where $\Pr\{\cdot\}$ stands for "the probability of". It states that at least $100(1-1/j^2)$ % of data will be within $\pm j\,\sigma$ of the mean and is true for any distribution [77]. For a Gaussian function $j = 1$, 2, and 3 represent 68 %, 95 %, and 99.7 %, respectively. From Sec. II.1.3 it is known that $\sigma^2_{\Delta x}(\Delta t)$ follows Eq. II.17 for Brownian motion with and without constant drift. The correct interpretation of this equation is that 68 % of particle displacements lie within $\langle \Delta x \rangle(\Delta t) \pm \sqrt{2D\Delta t}$ for one-dimensional Brownian motion. There are non-vanishing quantities that are much easier to interpret, such as the mean absolute deviation (MAD), which represents the average distance data are away from the mean and is defined as

$$\widehat{\mathrm{MAD}}(\Delta x)(\Delta t) = \int_{-\infty}^{\infty} |\Delta x - \widehat{\langle \Delta x \rangle}|\ \widehat{\mathcal{P}}(\Delta x, \Delta t)\, \mathrm{d}\Delta x\,. \tag{III.31}$$

The major advantage of using variance instead of a more interpretable MAD is the fact that it is a natural parameter of the Gaussian distribution function $\mathcal{P}_{\mathrm{Gauss}}$—the most important distribution in this thesis and arguably the most famous in statistics [77]:

$$\mathcal{P}_{\mathrm{Gauss}}(\Delta x, \langle \Delta x \rangle, \sigma_{\Delta x}) = \frac{1}{\sqrt{2\pi\sigma^2_{\Delta x}}} \exp\left\{ -\frac{(\Delta x - \langle \Delta x \rangle)^2}{2\,\sigma^2_{\Delta x}} \right\}. \tag{III.32}$$

Thus the variance (or second moment) and several associated quantities are used in this thesis and in most other sources dealing with the colloidal dynamics.

One of these associated quantities is the diffusion coefficient $D(\Delta t)$. From Eq. II.17 it is known that for pure Brownian motion

$$\sigma^2_{\Delta x}(\Delta t) = 2D\Delta t \quad \text{or} \quad \sigma^2_{\Delta \boldsymbol{r}}(\Delta t) = 2dD\Delta t\,, \tag{II.17}$$

where D is constant for all Δt. In a measurement, however, the diffusion coefficient might depend on Δt, i.e. $D = D(\Delta t)$. To calculate it, the first derivative of Eq. II.17 is taken:

$$D(\Delta t) = \frac{1}{2} \frac{\partial\ \sigma^2_{\Delta x}(\Delta t)}{\partial \Delta t} \quad \text{or} \quad D(\Delta t) = \frac{1}{2b} \frac{\partial\ \sigma^2_{\Delta \boldsymbol{r}}(\Delta t)}{\partial \Delta t}\,. \tag{III.33}$$

For discrete data—the only kind of data available in this thesis—taking the derivative translates to a finite difference quotient taken symmetrically:

$$D(\Delta t) = \frac{1}{2}\frac{\sigma^2_{\Delta \boldsymbol{r}}(\Delta t + \Delta t_{\mathrm{min}}) - \sigma^2_{\Delta \boldsymbol{r}}(\Delta t - \Delta t_{\mathrm{min}})}{2\,\Delta t_{\mathrm{min}}}\,. \tag{III.34}$$

When $\sigma^2_{\Delta \boldsymbol{r}}(\Delta t)$ tends to be noisy, e.g. when only few samples N_{S} are available, Eq. III.34 amplifies the noise possibly leading to unusable data [218, 219]. To circumvent that problem, there are two options adopted in this thesis. One option is the application of a smoothing filter to $\sigma^2_{\Delta \boldsymbol{r}}(\Delta t)$ prior to taking the finite difference quotient. In this thesis, the "locally weighted scatterplot smoothing" (Lowess) implemented in Origin (OriginLab Corp.) is used [220]. It is said to be useful to detect trends in otherwise noisy data and is thus well-suited. Another option is the calculation of the diffusion coefficient via:

$$\overline{D}(\Delta t) = \frac{1}{2}\frac{\sigma^2_{\Delta x}(\Delta t)}{\Delta t} \quad \text{or} \quad \overline{D}(\Delta t) = \frac{1}{2d}\frac{\sigma^2_{\Delta \boldsymbol{r}}(\Delta t)}{\Delta t}\,, \tag{III.35}$$

even when it is not constant for all Δt. Equation III.35 yields smoother results, especially for large Δt, when $\sigma^2_{\Delta \boldsymbol{r}}(\Delta t)$ often tends to become noisy. Thus the quotient in Eq. III.35 is sometimes preferred over Eq. III.33, even though, strictly speaking, it does not properly represent the diffusion coefficient. Figure III.20 shows $D(\Delta t)$ derived for three different situations in one dimension: pure Brownian motion $D_{\mathrm{B}}(\Delta t)$, Brownian motion in an external potential $D_{\mathrm{B\text{-}P}}(\Delta t)$, and Brownian motion in an external potential with additional drift $D_{\mathrm{B\text{-}P\text{-}D}}(\Delta t)$. Distributions of the first and last situation for $\Delta t = 10$ s are depicted in Fig. III.18. From displacements for all Δt, variances have been calculated. From these variances, $D(\Delta t)$ is derived according to Eq. III.35. For pure Brownian motion, $\sigma^2_{\Delta x}(\Delta t)$ is a straight line with slope $D_{\mathrm{B}}(\Delta t)$. Hence $D_{\mathrm{B}}(\Delta t)$ is a constant, depicted by blue squares in Fig. III.20. The external potential in the experiment slows down diffusion. As a result, the self part of the van Hove function gets broader more slowly than $\propto \Delta t$ and $D_{\mathrm{B\text{-}P}}(\Delta t)$ (orange circles) drops from a value around $D_{\mathrm{B}}(\Delta t)$ to a lower one. When drift is added, $\mathcal{G}_{\mathrm{s}}(\Delta x, \Delta t)$ broadens faster than $\propto \Delta t$. The re-

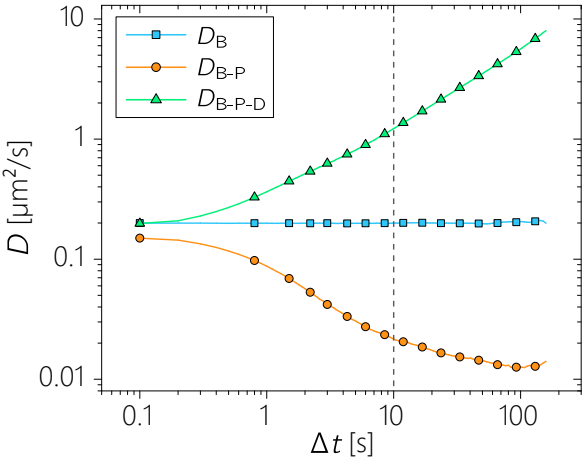

Figure III.20: Time-dependent diffusion coefficients for three different situations: pure Brownian motion, $D_{\mathrm{B}}(\Delta t)$, Brownian motion in an external potential, $D_{\mathrm{B\text{-}P}}(\Delta t)$, and Brownian motion in an external potential with additional drift, $D_{\mathrm{B\text{-}P\text{-}D}}(\Delta t)$. $D_{\mathrm{B}}(\Delta t)$ and $D_{\mathrm{B\text{-}P\text{-}D}}(\Delta t)$ are obtained from distributions shown in Fig. III.18. There, the self part of the van Hove function was shown for $\Delta t = 10$ s marked as the grey dashed line here.

sulting variance is shown as blue squares in Fig. III.19. Taking the first derivative of this variance yields an increasing $D_{\mathrm{B\text{-}P\text{-}D}}(\Delta t)$ (green triangles) as can be seen in Fig. III.20. Particles showing faster Brownian motion—usually the ones with a lower radius (cf. Eq. II.10)—exhibit a higher diffusion coefficient. Thus $D(\Delta t)$ represents the rate of diffusion when Brownian particles are examined. When the function that $\mathcal{G}_{\mathrm{s}}(\Delta x, \Delta t)$ follows is not known, $D(\Delta t)$ should be interpreted as the rate with which $\mathcal{G}_{\mathrm{s}}(\Delta x, \Delta t)$ broadens—assuming that the broadening is proportional to Δt—rather than a rate of diffusion. A change of $D(\Delta t)$ over the course of an experiment then indicates a deviation from this proportionality.

To properly quantify a deviation of $\sigma^2_{\Delta \boldsymbol{r}}(\Delta t)$ from the Δt proportionality valid for Brownian motion, an additional parameter, the anomalous diffusion exponent, α_{D}, introduced in Sec. II.1.4 is used. It allows $\sigma^2_{\Delta \boldsymbol{r}}(\Delta t)$ to not be strictly

proportional to Δt,[12]

$$\sigma^2_{\Delta x}(\Delta t) = 2D\Delta t^{\alpha_D} \quad \text{or} \quad \sigma^2_{\Delta \boldsymbol{r}}(\Delta t) = 2dD\Delta t^{\alpha_D}\,, \tag{II.22}$$

and can be derived by taking the first logarithmic derivative of $\sigma^2_{\Delta \boldsymbol{r}}(\Delta t)$ (or $\sigma^2_{\Delta x}(\Delta t)$) in time:

$$\alpha_D(\Delta t) = \frac{\partial \log\left(\sigma^2_{\Delta \boldsymbol{r}}(\Delta t)\right)}{\partial \log(\Delta t)}\,, \tag{III.36}$$

where $\log(\,\cdot\,)$ denotes the logarithm to base 10.[13] Like the diffusion coefficient, $D(\Delta t)$, $\alpha_D(\Delta t)$ is obtained by conducting a derivative. As a result it also tends to become noisy. Again, the Lowess filter in Origin Ref. [220] can be used prior to applying Eq. III.36. However, there is no second option similar to Eq. III.35, since that could lead to a zero or negative values in the denominator, yielding unphysical results. Fig. III.21 shows $\alpha_D(\Delta t)$ for the same three situations for which $D(\Delta t)$ is depicted in Fig. III.20: pure Brownian motion, $\alpha_{D,B}(\Delta t)$ (blue squares), Brownian motion in an external potential, $\alpha_{D,B\text{-}P}(\Delta t)$ (orange circles), and Brownian motion in an external potential with additional drift, $\alpha_{D,B\text{-}P\text{-}D}(\Delta t)$ (green triangles). For pure Brownian motion, $\alpha_D(\Delta t) = 1$. Equation II.22 then becomes Eq. II.17 and $D(\Delta t)$ is constant as can be seen by comparing blue squares in Figs. III.20 and III.21. When $D(\Delta t)$ changes, so does $\alpha_D(\Delta t)$. Orange circles in both figures show that a decrease in $D(\Delta t)$ correlates with a decrease in $\alpha_D(\Delta t)$. The same is true for an increase of $D(\Delta t)$ and $\alpha_D(\Delta t)$ as can be seen by the green triangles in both figures. When a diffusion coefficient changes, the particle dynamics deviates from pure Brownian motion as already mentioned in the previous paragraph. An anomalous diffusion exponent then quantifies its deviation. It shows with which exponent in time $\mathcal{G}_s(\Delta \boldsymbol{r}, \Delta t)$ gets broader. An $\alpha_D(\Delta t) \neq 1$ thus signifies anomalous diffusion of particles, whereby $\alpha_D(\Delta t) < 1$ is denoted by subdiffusion and $\alpha_D(\Delta t) > 1$ by superdiffusion (cf. Sec. II.1.4). This classification should be treated with caution though, as it already implies

[12] The equal sign in Eq. II.22 is only valid when the units of $D(\Delta t)$ are adapted to the proportionality between $\sigma^2_{\Delta \boldsymbol{r}}(\Delta t)$ and Δt.

[13] Any base can be used to apply Eq. III.36.

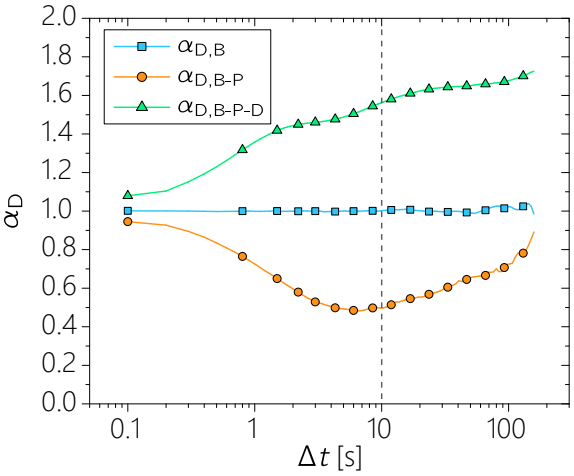

Figure III.21: Time-dependent anomalous diffusion exponents for the same three situations shown in Fig. III.20: pure Brownian motion, $\alpha_{D,B}(\Delta t)$, Brownian motion in an external potential, $\alpha_{D,B\text{-}P}(\Delta t)$, and Brownian motion in an external potential with additional drift, $\alpha_{D,B\text{-}P\text{-}D}(\Delta t)$. $\alpha_{D,B}(\Delta t)$ and $\alpha_{D,B\text{-}P\text{-}D}(\Delta t)$ are obtained from distributions shown in Fig. III.18. There, the self part of the van Hove function was shown for $\Delta t = 10$ s marked as the grey dashed line here.

knowledge about the underlying process, namely that particles diffuse differently from Brownian motion. There might be other processes involved causing $\mathcal{G}_s(\Delta \boldsymbol{r}, \Delta t)$ to become broader or stay narrower than particle diffusion itself. This possibility should be investigated prior to calling any dynamics sub- or superdiffusive when colloids exhibit an anomalous diffusion exponent different from one.

Independent of the diffusive behaviour present—be it subdiffusive or superdiffusive—a characteristic quantity can be defined for almost every system: the Brownian time, t_B. It reads:

$$t_B = \frac{R^2}{2dD_0} \tag{III.37}$$

and is the time a particle takes to diffuse its own radius.[14] In practice, t_B is mostly defined through Brownian motion, where $D(\Delta t)$ is constant and called D_0 [221–225]. It serves as a benchmark to define short-time, where $t \ll t_B$ and $D(\Delta t) = D^s$, and long-time behaviour of a system, where $t \gg t_B$ and $D(\Delta t) = D^l$ [224, 226], and is widely used to quantify deviations of the particle dynamics from standard Brownian motion [221, 222]. In measurements, where particles never diffuse completely freely, D^s can be used to define t_B, yielding

$$t_B = \frac{R^2}{2dD^s}\,. \tag{III.38}$$

When plotting data, normalisation with t_B leads to dimensionless quantities, e.g.

$$\frac{D}{D_0}\left(\frac{\Delta t}{t_B}\right) = \frac{\partial\ \sigma^2_{\Delta \boldsymbol{r}}/R^2}{\partial \Delta t/t_B}\,. \tag{III.39}$$

Using dimensionless quantities facilitates comparison between experiments and helps finding an agreement of experiment and simulation [221, 227].

4.4 Skewness—Bias

In contrast to the first and second moments, the third moment about the mean and related skewness are not often used in colloidal dynamics. To calculate the skewness $\gamma_1(\Delta t)$, the third moment about the mean (cf. Eq. III.26) is normalised by the cubic square root of variance $\sigma^2(\Delta t)$. For one-dimensional displacements, it reads:

$$\widehat{\gamma_1}(\Delta t) = \frac{1}{\widehat{\sigma^3_{\Delta x}}} \int_{-\infty}^{\infty} (\Delta x - \widehat{\langle \Delta x \rangle})^3\, \widehat{\mathcal{P}}(\Delta x, \Delta t)\, \mathrm{d}\Delta x\,. \tag{III.40}$$

[14] This statement is not completely correct, as we compare variance $\sigma^2_{\Delta \boldsymbol{r}}(\Delta t)$ with a squared particle radius. As mentioned in this section, the variance is a statistical quantity and can only be interpreted with Chebyshev's inequality. Thus, t_B represents the time a particle takes to cover more than its radius with a probability of 32 %. For the sake of simplicity and as a rule of thumb this statement is used here.

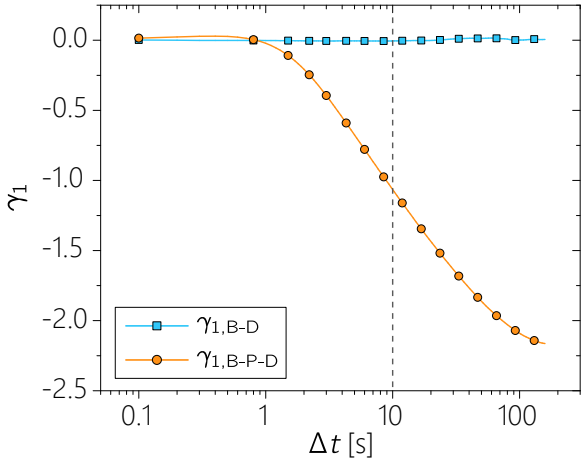

Figure III.22: Time-dependent skewness shown for the two experimental $\mathcal{G}_s(\Delta x)$ which were shown in Fig.III.18. There, the self part of the van Hove function was shown for $\Delta t = 10$ s, marked here as the grey dashed line. The skewness for Brownian motion with drift, $\gamma_{1,\text{B-D}}(\Delta t)$, is depicted by blue squares. For Brownian motion in an external field with additional drift, the skewness, $\gamma_{1,\text{B-P-D}}(\Delta t)$, is shown as orange circles.

This definition is equivalent to the third standardised moment, the third moment of the standardised variable $(\Delta x - \widehat{\langle \Delta x \rangle})/\widehat{\sigma_{\Delta x}}$ [228].[15] The notation of skewness is very diverse. Besides γ_1 used here [228–230], it is also called γ_4 [231], *SK* [205], or $\sqrt{\beta_1}$ [232], all referring to the same quantity.The estimator of $\gamma_1(\Delta t)$ used in this thesis reads:

$$\gamma_1(\Delta t) = \frac{1}{N_S} \frac{\sum_{i=1}^{N_S} (\Delta x_i - \langle \Delta x \rangle)^3}{\sqrt{\sigma_{\Delta x}^2}^3}, \tag{III.41}$$

where $\sigma_{\Delta x}^2(\Delta t)$ is first calculated via Eq. III.29. There are ways to improve Eq. III.41 in terms of biasing [229]. Since there is a great variety leading to different results

[15] The standardised variable is also called z-score [77].

for low N_S, the uncorrected estimator given in Eq. III.41 is used in this thesis.

As the name skewness already reveals, $\gamma_1(\Delta t)$ is a measure for the asymmetry of a distribution. For a perfectly symmetric distribution, like a Gaussian, there are as many values smaller than the mean as there are bigger. As a result the third central moment cancels out and so does $\gamma_1(\Delta t)$. The denominator of Eq. III.41 always stays positive since $\sigma^2(\Delta t) > 0$ for any given distribution. It serves as a normalising factor, so that $\gamma_1(\Delta t)$ indicates the shape of a distribution but not its size or position [77]. When there are more values in a distribution larger than the mean than there are smaller values, then the numerator of Eq. III.41 and therefore $\gamma_1(\Delta t)$ becomes positive. The opposite is true when there is a majority of values smaller than $\langle \Delta x \rangle(\Delta t)$. As deviations from $\langle \Delta x \rangle(\Delta t)$ are weighted to the power of 3, extreme values contribute abundantly to the final result. Thus long tails tend to be overrepresented when $\gamma_1(\Delta t)$ is calculated and mostly determine its sign [77]. Figure III.22 shows $\gamma_1(\Delta t)$ for the two examples given in Fig. III.18. Both $\mathcal{G}_s(\Delta x)$ shown there represent only one point in time, namely $\Delta t = 10$ s, represented by the grey dashed line in Fig. III.22. For Brownian motion with drift, the skewness $\gamma_{1,\,\text{B-D}}(\Delta t)$ (blue squares) vanishes for all Δt as $\mathcal{G}_s(\Delta x)$ is always symmetric about the mean, independent of how strong the drift, i.e. how big the mean is. The orange circles represent the skewness for Brownian particles in an external field with additional drift, $\gamma_{1,\text{B-P-D}}(\Delta t)$—the same example used in Figs. III.20 and III.21 and shown in the lower part of Fig. III.18. It shows a strong tendency to become negative over the course of time, Δt. This is due to $\mathcal{G}_s(\Delta x)$ developing a strong tail left of its mean as time progresses. With the aid of $\gamma_1(\Delta t)$ this development can be quantified.

4.5 Kurtosis—Non-Gaussian Parameter

To complete the list of common moments on PDFs, the fourth moment $\langle \Delta x^4 \rangle(\Delta t)$ and its standardised version $\beta_2(\Delta t)$ are introduced in accordance with Eqs. III.25

and III.40 [205, 230]. For one-dimensional displacements, they read:

$$\widehat{\langle \Delta x^4 \rangle}(\Delta t) = \int_{-\infty}^{\infty} \Delta x^4 \, \widehat{\mathcal{P}}(\Delta x, \Delta t) \, \mathrm{d}\Delta x \tag{III.42}$$

and

$$\widehat{\beta}_2(\Delta t) = \frac{1}{\widehat{\sigma}_{\Delta x}^4} \int_{-\infty}^{\infty} (\Delta x - \widehat{\langle \Delta x \rangle})^4 \, \widehat{\mathcal{P}}(\Delta x, \Delta t) \, \mathrm{d}\Delta x \, . \tag{III.43}$$

The second quantity represents the fourth moment about the mean divided by the squared variance. It is referred to as the kurtosis, where kurtos is the Greek word for curved. For a Gaussian function, one obtains $\beta_2(\Delta t) = 3$. For that reason a second, closely related quantity can be defined:

$$\widehat{\gamma}_2(\Delta t) = \widehat{\beta}_2(\Delta t) - 3 \, , \tag{III.44}$$

where $\widehat{\gamma}_2(\Delta t)$ is called excess kurtosis or simply excess [205, 230]. The excess then quantifies how strongly a distribution deviates from a Gaussian function. The estimator of $\widehat{\gamma}_2(\Delta t)$ in one dimension reads

$$\gamma_2(\Delta t) = \frac{1}{N_\mathrm{S}} \frac{\sum_{i=1}^{N_\mathrm{S}} (\Delta x_i - \langle \Delta x \rangle)^4}{\sqrt{\sigma_{\Delta x}^2}^{-4}} - 3 \, , \tag{III.45}$$

where $\sigma_{\Delta x}^2(\Delta t)$ is calculated via Eq. III.29. Here again, just like with $\gamma_1(\Delta t)$, the plug-in estimator is used instead of a corrected version [229].

Because deviations from $\langle \Delta x \rangle(\Delta t)$ and $\sigma(\Delta t)$ are taken to the power of 4, $\beta_2(\Delta t)$ is always positive. The lower bound of $\gamma_2(\Delta t)$ is defined by the inequality [233, 234]

$$\beta_2(\Delta t) \geq \gamma_1^2(\Delta t) + 1 \, . \tag{III.46}$$

Consequently, the minimal excess kurtosis is found to be -2 and obtained for the Bernoulli distribution with a probability of 0.5. An upper bound for $\gamma_2(\Delta t)$ is not found [77].

Depending on their $\gamma_2(\Delta t)$ value, distributions can be categorised as mesokur-

tic, leptokurtic or platykurtic: they are called mesokurtic for $\gamma_2(\Delta t) = 0$, whilst when $\gamma_2(\Delta t) > 0$, the distribution has a higher $\beta_2(\Delta t)$ than a Gaussian function and can be called leptokurtic–the Greek word for slender—referring to a distribution lesser flat-topped. A distribution with $\gamma_2(\Delta t) < 0$ can be called platykurtic, meaning it is more flat-topped than a Gaussian curve [235]. There are however several possible misconceptions when it comes to interpreting $\gamma_2(\Delta t)$.
Firstly, the terms meso-, lepto-, and platykurtic can be misleading, since they suggest that the peakedness of a distribution is the only defining feature for $\beta_2(\Delta t)$ and $\gamma_2(\Delta t)$. However, deviations are weighted to the power of 4 in kurtosis and excess kurtosis. Displacements that are far away from the mean, so-called outliers, can thus strongly affect $\beta_2(\Delta t)$ and $\gamma_2(\Delta t)$.[16] On the other hand, $\gamma_2(\Delta t)$ is also defined by the variance in its denominator, which is not affected by outliers as much as the fourth moment about the mean in the enumerator of $\gamma_2(\Delta t)$. There is great debate on how to interpret $\gamma_2(\Delta t)$ [236–238]. Whereas Westfall [236] claims that $\gamma_2(\Delta t)$ is mostly determined by the tails of a distribution, Crack [238] disagrees. However, both agree on $\gamma_2(\Delta t)$ not being a measure for the shape of the peak of a distribution. Balanda et al. [237] argue diplomatically, claiming that it is a movement of probability from the shoulders into its centre and tails. This argumentation is also followed here. A large positive $\gamma_2(\Delta t)$ then represents a distribution that is more outlier-prone and more strongly peaked than a Gaussian function.
Secondly, the scale of $\gamma_2(\Delta t)$ about zero is not balanced. As noted above, the lower bound is well-defined and lies at -2, whereas there is no upper bound. Consequently, great care should be taken when comparing negative and positive $\gamma_2(\Delta t)$ values according to their magnitudes as the negative scale is much shorter than the positive one.

In colloidal physics it is common practice [5, 80, 88, 181, 239] to neither use $\beta_2(\Delta t)$ nor $\gamma_2(\Delta t)$ but a similar quantity, called the non-Gaussian parameter

[16] A similar effect was found for $\gamma_1(\Delta t)$ in Sec. III.4.4.

$\alpha_2(\Delta t)$ [240], which is based on moments about zero and can be defined as

$$\alpha_2(\Delta t) = \frac{d}{d+2}\frac{\langle \Delta \boldsymbol{r}^4\rangle(\Delta t)}{\langle \Delta \boldsymbol{r}^2\rangle^2(\Delta t)} - 1\,, \tag{III.47}$$

where d represents the dimension. It can be deduced from a series expansion of the self intermediate scattering function, $f_s(k, \Delta t)$, being the characteristic function of the displacement $\Delta \boldsymbol{r}$ for an isotropic system (cf. Eq. III.14) [5, 181, 241]:

$$\begin{aligned}\ln(f_s(k,\Delta t)) = -\frac{k^2}{2d}\langle \Delta \boldsymbol{r}^2\rangle(\Delta t) + \frac{k^4\langle \Delta \boldsymbol{r}^2\rangle^2(\Delta t)}{8d^2} \\ \times\left(\frac{d}{d+2}\frac{\langle \Delta \boldsymbol{r}^4\rangle(\Delta t)}{\langle \Delta \boldsymbol{r}^2\rangle^2(\Delta t)} - 1\right) + \mathcal{O}(k^6) \quad \text{for} \quad k \to 0\,,\end{aligned} \tag{III.48}$$

where $\ln(\cdot)$ denotes the natural logarithm. For isotropic Brownian motion without drift, the fourth moment about zero is calculated to obey $\langle \Delta \boldsymbol{r}^4\rangle(\Delta t) = (d+2)\langle \Delta \boldsymbol{r}^2\rangle^2(\Delta t)/d$ and thus the non-Gaussian parameter (NGP) vanishes with $f_s = \exp\{-k^2\langle \Delta \boldsymbol{r}^2\rangle(\Delta t)/2d\}$ in that case [5]. Whenever $\mathcal{G}_s(\Delta \boldsymbol{r}, \Delta t)$ does not follow a Gaussian function about zero as it would for Brownian motion, or if $\mathcal{G}_s(\Delta \boldsymbol{r}, \Delta t)$ follows a Gaussian function about zero, but not all spatial directions exhibit the same variance, a finite $\alpha_2(\Delta t)$ is found. Thereby it behaves similarly to the excess kurtosis $\gamma_2(\Delta t)$: it has no upper but a lower bound, $\alpha_2(\Delta t) \geq -2/(d+2)$ [5], and is larger than 0 for distributions heavier tailed than a Gaussian and smaller than 0 for the opposite. The estimator of the NGP reads

$$\alpha_2(\Delta t) = \frac{N_S \sum_{i=1}^{N_S} \Delta x_i^4}{3\left(\sum_{i=1}^{N_S} \Delta x_i^2\right)^2} - 1 \tag{III.49}$$

in one dimension and

$$\alpha_2(\Delta t) = \frac{N_S \sum_{i=1}^{N_S} (\Delta x_i^2 + \Delta y_i^2)^2}{2\left(\sum_{i=1}^{N_S} \Delta x_i^2\right)^2} - 1 \tag{III.50}$$

in two dimensions. Considering all the restrictions that have to be fulfilled in order for $\alpha_2(\Delta t)$ to be equal to zero stated above and the fact that deviations are weighted to the power of 4, it is apparent that NGPs are very sensitive to even small deviations from Brownian motion. Thus great care should be taken when utilising this quantity.

As all the moments in $\alpha_2(\Delta t)$ are taken about zero, unexpected drifts in a measurement can lead to $\alpha_2(\Delta t) \neq 0$ and can be falsely interpreted as non-Brownian behaviour. The same problem is encountered when anisotropic motion is examined in two or three dimensions. Variances depending on spatial directions lead to a nonzero $\alpha_2(\Delta t)$, again possibly falsely interpreted as being non-Brownian motion. There are quantities, such as the multivariate kurtosis [242], that account for all those pitfalls and deviations from ideal isotropic Brownian motion. They signal Gaussian behaviour for any number of spatial coordinates no matter where the mean of each coordinate is situated or how broad the distribution is, as long as it is Gaussian. Depending on the experiment and its demands either $\gamma_2(\Delta t)$ or $\alpha_2(\Delta t)$ can be preferable. When there is no drift in the experiment then $\alpha_2(\Delta t) = \gamma_2(\Delta t)/3$ in one dimension. For all other cases one quantity might be superior to the other. When Brownian motion and isotropy should be tested at the same time and no drift is apparent or expected, $\alpha_2(\Delta t)$ should be chosen. When there is anisotropy and/or drift in particle motion and the main focus question is whether all spatial directions follow a Gaussian function or not, then $\gamma_2(\Delta t)$ might be the better choice. In the work described in this thesis, most of the experiments were analysed in one dimension, but some contained drift. Therefore, $\gamma_2(\Delta t)$ was chosen. To be able to better compare it with one-dimensional NGPs in the literature it is divided by 3 in order to be of the same magnitude and called normalised excess kurtosis:

$$\gamma_\alpha(\Delta t) = \frac{\gamma_2(\Delta t)}{3}, \tag{III.51}$$

where $\gamma_\alpha(\Delta t) = \alpha_2(\Delta t)$ for pure Brownian motion in one dimension. Figure III.23 shows $\alpha_2(\Delta t)$ and $\gamma_\alpha(\Delta t)$ for comparison. For Brownian motion, both curves fall on top of each other and lie around zero, depicted as the black solid

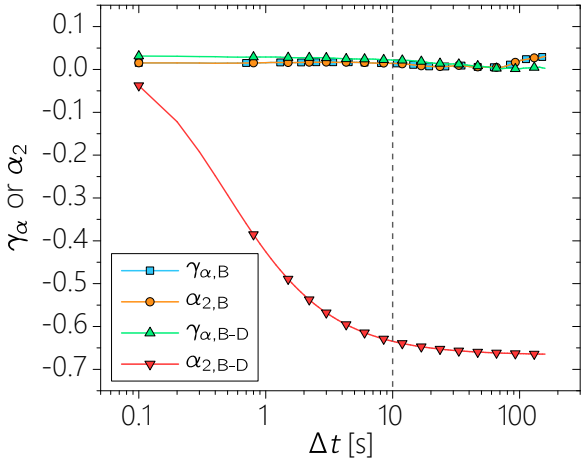

Figure III.23: Time-dependent normalised excess kurtosis, $\gamma_\alpha(\Delta t)$, and non-Gaussian parameter, $\alpha_2(\Delta t)$, shown for Brownian motion and Brownian motion with additional drift. The self part of the van Hove function was shown for the latter in the top of Fig. III.18. There, $\mathcal{G}_s(\Delta x)$ was shown for $\Delta t = 10$ s, marked as the grey dashed line here. For Brownian motion, $\gamma_{\alpha,B}(\Delta t)$ is depicted as blue squares and $\alpha_{2,B}(\Delta t)$ as orange circles. For Brownian motion with additional drift, $\gamma_{\alpha,B\text{-}D}(\Delta t)$ is shown as green triangles and $\alpha_{2,\,B\text{-}D}(\Delta t)$ as red inverted triangles.

and red dashed line. The green dot-dashed and blue double dot-dashed lines show both quantities for Brownian motion with additional drift also shown in the top part of Fig. III.18 for $\Delta t = 10$ s, which is marked by the grey dotted line again. In that case, $\alpha_2(\Delta t)$ decreases steadily in time, whereas $\gamma_\alpha(\Delta t)$ stays at zero. Thus, when an additional drift is foreseen, using $\gamma_\alpha(\Delta t)$ makes more sense as it accounts for the drift and only indicates deviations from expected behaviour.

4.6 Averaging in Various Ways

All the quantities introduced in this chapter are based on the sampled population with $N_S(\Delta t)$ samples given by Eq. III.22. It is this population that defines

what each estimator is calculated to be and what inferences are drawn. Thus the way sampling is done is crucial and can bias a result. In Sec. III.4.1, $N_S(\Delta t)$ was said to be made up of N_M ensembles of different initial conditions, $N_{P,j}$ particles in each ensemble j, and $N_{\Delta t,i}$ samples in time for each particle i:

$$N_S(\Delta t) = \sum_{j=1}^{N_M} \sum_{i=1}^{N_{P,j}} N_{\Delta t,i}(\Delta t_{L,i}, \Delta t, \Delta t_{min}) \,. \tag{III.22}$$

The corresponding $\mathcal{G}_s(\Delta \boldsymbol{r}, \Delta t)$ was also defined in Sec. III.4.1 and reads

$$\mathcal{G}_s(\Delta \boldsymbol{r}, \Delta t) = \frac{1}{N_S} \left(\sum_{j=1}^{N_M} \sum_{i=1}^{N_{P,j}} \sum_{t_0}^{N_{\Delta t,i}} \delta[\Delta \boldsymbol{r} - (\boldsymbol{r}_{ji}(t_0 + \Delta t) - \boldsymbol{r}_{ji}(t_0))] \right) . \tag{III.21}$$

In practice, all three portions—N_M, $N_{P,j}$, and $N_{\Delta t,i}$—are optional as each defines a specific way of conducting the average when calculating quantities introduced in this chapter.

The most obvious average is the one taken over several ensembles made up of $N_P(t)$ particles. In this regard, only particles that are present at a defined starting point t_0, where t is set to be 0, are taken into account. The amount of samples then reduces to

$$N_{S,E}(t) = \sum_{j=1}^{N_M} \sum_{i=1}^{N_P(t \mid 0)} 1 \,, \tag{III.52}$$

where $N_P(t \mid 0)$ denotes the amount of particles present at time t given they were present at $t = 0$. The resulting $\mathcal{G}_{s,E}(\Delta \boldsymbol{r}, t)$ is defined as

$$\mathcal{G}_{s,E}(\Delta \boldsymbol{r}, t) = \frac{1}{N_{S,E}} \left(\sum_{j=1}^{N_M} \sum_{i=1}^{N_{P(t|0)}} \delta[\Delta \boldsymbol{r} - (\boldsymbol{r}_{ji}(t) - \boldsymbol{r}_{ji}(0))] \right) . \tag{III.53}$$

In Eqs. III.52 and III.53, it is apparent that averaging over starting times t_0 was omitted, but only one point in time is defined as being $t = 0$ with the absolute time t starting from there. The ensemble average (EA) is visualised for an averaged quantity at time t_1 in Fig. III.24. It shows a schematic for five particle

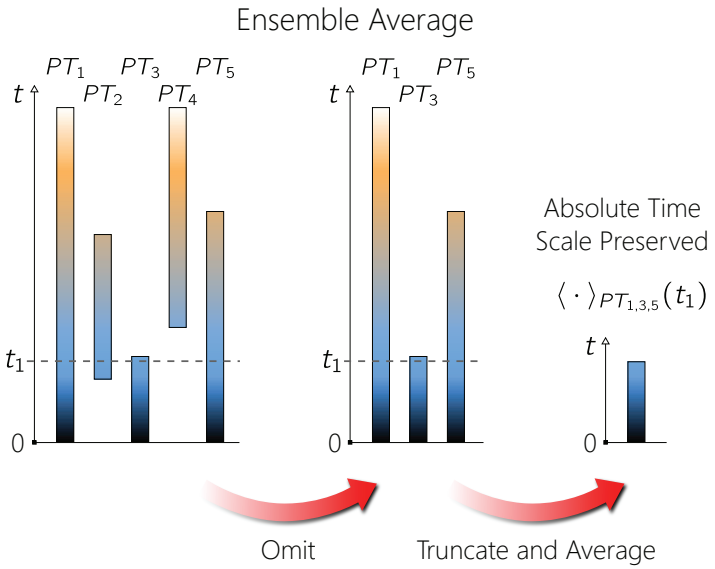

Figure III.24: Schematic for ensemble averaging of particle trajectories marked as PT. First, trajectories that are not present at a defined $t = 0$ are omitted. Then the rest are truncated after a time t_1 and averaged to obtain an averaged quantity for that time. Thereby t_1 represents an absolute time.

trajectories obtained from particle tracking as described in Sec. III.3.1. They are marked with PT and have different starting times and lengths. Evolution in t is indicated with a colour gradient. The process formulated in Eq. III.53 can be thought of as taking only trajectories present at a predefined starting point t_0, where the absolute time t is set to 0. All other trajectories are omitted and kept trajectories are truncated after a specific absolute time t_1. By averaging displacements obtained from the starting and end point of each truncated trajectory, all quantities introduced in this chapter can be obtained for that time. All averaged displacements represent the same time in absolute measures. Thus they are averaged while preserving the absolute time scale, as indicated by the colour gradi-

ent on the right-hand side of Fig.III.24. As a result, $\mathcal{G}_{\mathrm{s,E}}(\Delta\boldsymbol{r}, \Delta t)$ and all related so called ensemble-averaged quantities—marked with an index E—depend on t instead of relative time (also called lag time), Δt. This difference can be crucial depending on the system analysed [88, 190] and will be discussed in more detail later in this section. However, the amount of samples is drastically reduced in Eq. III.52, giving rise to more noisy results when calculating the estimators. In Fig. III.26 a) an ensemble-averaged variance $\sigma^2_{\Delta\boldsymbol{r},\mathrm{E}}(t)$ is plotted and noise is clearly visible. In order to reduce noise, $N_{\mathrm{S,E}}(t)$ is often increased by conducting as many measurements N_{M} as possible.

The counterpart to ensemble averaging is the average over time or starting times t_0. Instead of defining one specific t_0, all points in time during a measurement, except for the last one, can serve as it. The amount of samples then reads:

$$N_{\mathrm{S,T}}(t) = N_{\Delta t}(\Delta t_{\mathrm{L}}, \Delta t, \Delta t_{\mathrm{min}})\,. \tag{III.54}$$

And the self part of the van Hove function becomes:

$$\mathcal{G}_{\mathrm{s,T}}(\Delta\boldsymbol{r}, \Delta t) = \frac{1}{N_{\Delta t}} \left(\sum_{t_0}^{N_{\Delta t}} \delta[\Delta\boldsymbol{r} - (\boldsymbol{r}(t_0 + \Delta t) - \boldsymbol{r}(t_0))] \right). \tag{III.55}$$

Compared to Eq. III.21, only the average over different starting times t_0 is left. That also means Eq. III.55 is used with one particle trajectory only. To better illustrate the time average (TA)—marked with an index T—it is depicted for an averaged quantity at lag time Δt_1 in Fig. III.25. Similar to Fig. III.24 time evolution is visualised with a colour gradient and the particle trajectory is called PT_1. When averaging in time each trajectory is chopped into many equally spaced intervals of a specific size Δt_1. Each of them has an individual starting point t_0 but might overlap, resulting in intervals that are not statistically independent. Subsequently, all displacements obtained from the starting and end point of each interval are averaged. The resulting averaged quantities for Δt_1 represent a mix of displacements measured at different absolute times t, indicated by a brown colour in Fig. III.25. Thus the absolute time scale is lost and Δt_1 represents a

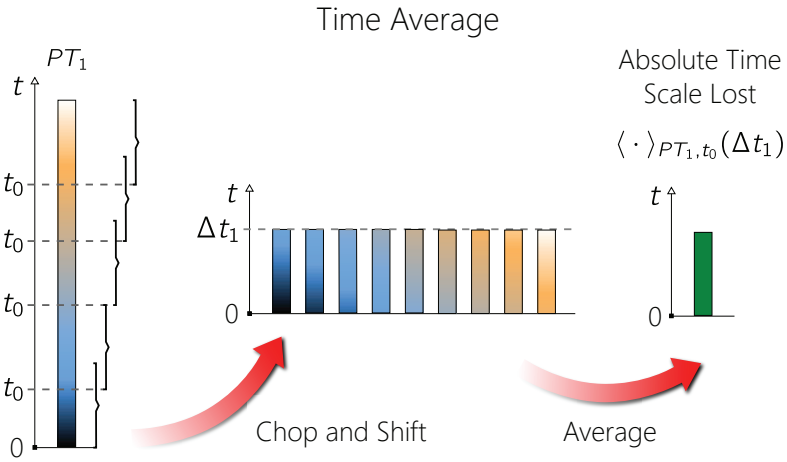

Figure III.25: Schematic for time averaging of a single particle trajectory marked as PT_1. First, the trajectory is chopped into $N_{\Delta t}$ pieces according to a specific time interval Δt_1, with each having an individual t_0. Then these pieces are shifted to $t = 0$ and averaged. The result is a mix of same-sized intervals measured at different absolute times. Thus lag time Δt_1 represents a relative time.

relative time instead of the absolute time t_1. As can be seen by comparison of Figs. III.24 and III.25, time averaging mostly leads to larger sample populations than ensemble averaging. However, unlike the samples in ensemble averages, a majority of the time averaged samples is not independent due to the time overlaps occurring when time averaging. To overcome this issue and maximise the used sample population, both averaging processes can be combined by taking an average over several ensembles as well as starting times t_0—a time and ensemble average (TEA). It is probably the most common average [131, 132, 135, 136, 181, 192] and does not preserve the absolute time scale, but it maximises the amount of samples while minimising the percentage of dependent samples. When taking it, the sample population is defined by Eq. III.22: $N_{\mathrm{S,TE}} = N_{\mathrm{S}}$ as all possible samples are taken into account. Similarly, the self part of the van Hove function is defined by Eq. III.21, i.e. $\mathcal{G}_{\mathrm{s,TE}}(\Delta \boldsymbol{r}, \Delta t) = \mathcal{G}_{\mathrm{s}}(\Delta \boldsymbol{r}, \Delta t)$. As indicated by place-

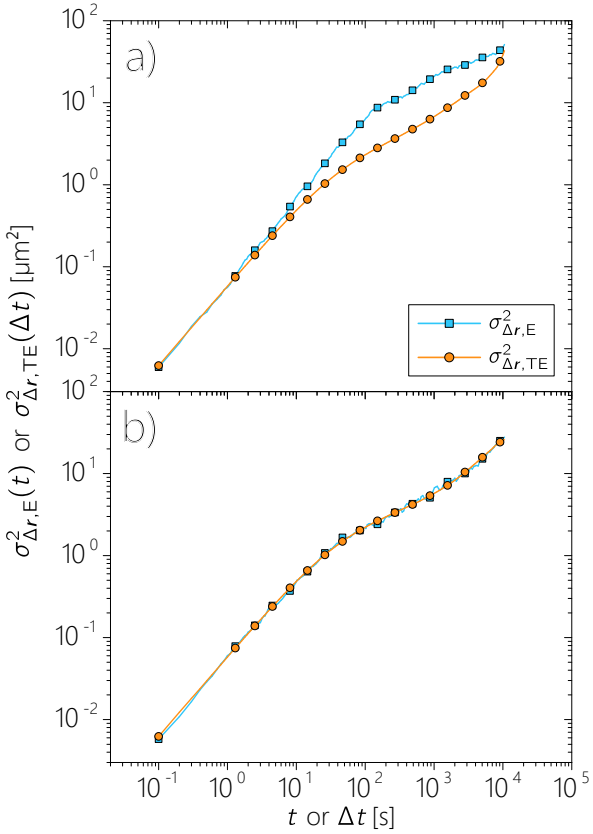

Figure III.26: Examples for ensemble-averaged and time- and ensemble-averaged variances of particle displacements. In a) variances are shown for a system evolving in time. As a consequence, $\sigma^2_{\Delta \boldsymbol{r},\mathrm{E}}(t)$ differs from $\sigma^2_{\Delta \boldsymbol{r},\mathrm{TE}}(\Delta t)$. In b) the same system studied at a later time is shown. Then $\sigma^2_{\Delta \boldsymbol{r},\mathrm{E}}(t)$ and $\sigma^2_{\Delta \boldsymbol{r},\mathrm{TE}}(\Delta t)$ fall on top of each other.

ment of the parentheses in Eq. III.21, all displacements—for trajectory, particle, and measurement—are in practice averaged simultaneously.

Each measurement situation requires a specific way of averaging displacements.

In the work described in this thesis, all of the above mentioned average processes were used, where EA and TEA data were used most. A comparison of the two can be found in Fig. III.26. It shows $\sigma^2_{\Delta \boldsymbol{r},\mathrm{E}}(t)$ and $\sigma^2_{\Delta \boldsymbol{r},\mathrm{TE}}(\Delta t)$ for the same system at two different points in time.The biggest differences between TE and TEA are the size of sample populations and the time scale. The former can be easily seen in both graphs of Fig. III.26: while $\sigma^2_{\Delta \boldsymbol{r},\mathrm{E}}(t)$ (black solid line) happens to be noisy, $\sigma^2_{\Delta \boldsymbol{r},\mathrm{TE}}(\Delta t)$ (red dashed line) is found to be very smooth in both situations. The difference in time scale can be recognised when comparing trends of both curves in both graphs. In Fig. III.26 a), EA and TEA do not show the same result. While $\sigma^2_{\Delta \boldsymbol{r},\mathrm{E}}(t)$ shows the actual time evolution of the system as it depends on absolute times t, $\sigma^2_{\Delta \boldsymbol{r},\mathrm{TE}}(\Delta t)$ shows a mix of the system in earlier and later times t. The difference in both curves shows the time average is not equal to the ensemble average which could be reasoned to show non-ergodicity of the system. As mentioned in Sec. III.4.1, ergodic systems behave according to

$$\lim_{\Delta t_\mathrm{L} \to \infty} \langle \Delta \boldsymbol{r}^2 \rangle_\mathrm{T}(\Delta t) = \langle \Delta \boldsymbol{r}^2 \rangle_\mathrm{E}(t)\,. \tag{III.56}$$

In actual experiments however, observation times, $t_\mathcal{O}$, or often synonymously trajectory lengths, Δt_L, cannot be infinitely long. Similarly, in practice, there is no infinitely large ensemble over which trajectories can be averaged. The ergodicity of a system could only be determined for a limited time span and ensemble size, which is, strictly speaking, not in accordance with the definition of ergodicity. Therefore, in this thesis, a system showing deviating results for EA and TEA at one point in time and coinciding results at a later point (or the other way around) is called evolving. The time in which it evolves is then about the order of the trajectory lengths, Δt_L. Figure III.26 b) shows the same system shown in Fig. III.26 a) for a later point in time. At that moment both curves fall on top of each other, showing exactly the same trend. That means it does not matter, whether absolute or relative times are studied. When both averaging procedures lead to the same behaviour before deviating in a), it can be inferred that the observed system evolved in time. For a system of particles diffusing in a static potential landscape similar to the ones studied here, this evolution can be thought

of as relaxation. There are sources where ergodicity parameters are introduced as a means of quantifying how far a system is from being ergodic at a specific point in time using $\sigma^2_{\Delta \boldsymbol{r},\mathrm{E}}(t)$, $\sigma^2_{\Delta \boldsymbol{r},\mathrm{T}}(\Delta t)$, and $\sigma^2_{\Delta \boldsymbol{r},\mathrm{TE}}(\Delta t)$ [88, 190, 201].

From these observations, it is clear that TEA should be used cautiously. When TEA gives results similar to EA, then TEA is always preferred as its results suffer from a lot less noise. However, when evolving systems are studied, EA should be given preference over TEA, since time averaging blurs the time scale. Sometimes, constraints of the measured system prevent ensemble averaging from being used. That usually happens when only very few or even single particles can or are to be studied [88, 131, 135, 190, 201, 243]. In these situations, TA or TEA are the only possibilities left. When TA or TEA have to be used in evolving systems, comparable results can only be obtained when measurement conditions are kept constant. Systems should be measured in the same time window in their evolution. Changing the size of Δt_L or the stage of evolution at which they are measured can change the results to a large degree when TA or TEA is used [190]. An additional problem occurring when single trajectories are analysed arises due to the dependence of samples when using TA. Especially when Δt gets close to Δt_L, averaged samples are highly statistically correlated as the calculated displacements come from trajectory intervals that overlap to a large extent. As a consequence, estimators introduced in this chapter highly underestimate actual results, yielding unusable data for large Δt. Thus when analysing single particle trajectories, Δt_L often has to be one or more orders of magnitude higher than the largest Δt for which trajectories are analysed.

4.7 Validation of Distribution Describing Quantities

Now that all the quantities used to analyse the particle dynamics have been introduced, their validity is tested on the basis of two examples. Both originate from a situation recurring in this thesis: Brownian particles subject to a drag velocity and an external potential at the same time. As a result, $\mathcal{G}_\mathrm{s}(\Delta x, \Delta t)$ deviates from the case of pure Brownian motion, where it resembles a Gaussian function. In Fig. III.27 a), the values of $\langle \Delta x \rangle$, $\sigma^2_{\Delta x}$, γ_1, and γ_α are telling. The mean gives a

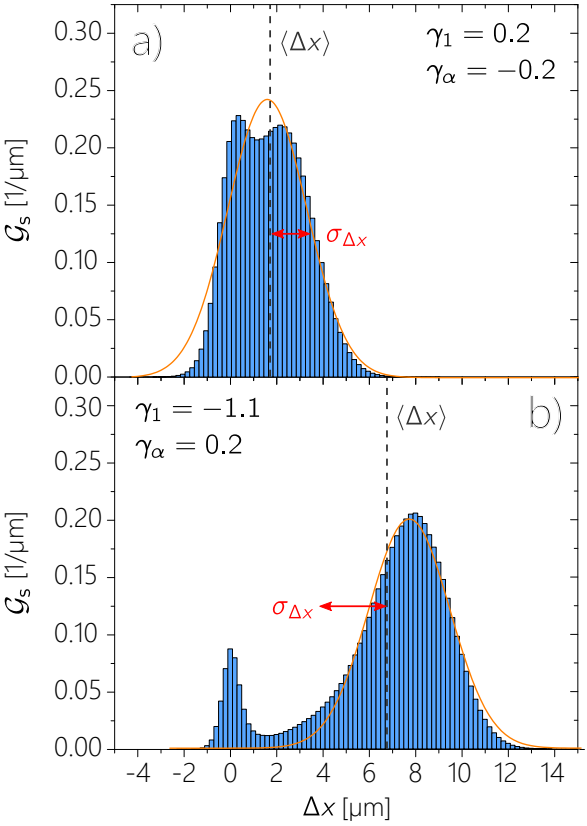

Figure III.27: Two examples of $\mathcal{G}_s(\Delta x)$ for Brownian particles being exposed to two different external potentials and drifts for $\Delta t = 10$ s.[17] Mean, variance, skewness, and normalised excess kurtosis are either marked in the graph or given numerically. In a), $\mathcal{G}_s(\Delta x)$ is well described by given quantities. In b), quantities like $\langle \Delta x \rangle$ and $\sigma^2_{\Delta x}$ can lead to false conclusions.

good indication of where $\mathcal{G}_s(\Delta x)$ is situated and σ_{Δ_x} of how broad it is. The skew-

[17] Both measurements can be found in Sec. VI.

ness γ_1 is calculated to be 0.2. The small positive value indicates a slightly more pronounced tail on the right-hand side of $\mathcal{G}_s(\Delta x)$ which can be found exactly in that manner. The normalised excess kurtosis γ_α is slightly negative and thus indicates small tails or flat-toppedness of a distribution. While the tails of $\mathcal{G}_s(\Delta x)$ are pretty similar to a Gaussian distribution, depicted as orange lines in Fig. III.27, it is definitely more flat-topped than a Gaussian. The value calculated for γ_α resembles just that. Consequently, for the situation resulting in Fig. III.27 a), particle dynamics can be mirrored very well by using given quantities. However, this is not always the case. For the particle dynamics resulting in Fig. III.27 b), these quantities can lead to wrong conclusions. It is the same example that was used throughout this chapter and given in Fig. III.18. Its mean is not where it would be expected from looking at $\mathcal{G}_s(\Delta x)$. Due to its bimodality and long tail, the median would be preferable to $\langle \Delta x \rangle$. Additionally, variance $\sigma^2_{\Delta x}$ indicates a much higher spread in $\mathcal{G}_s(\Delta x)$ than actually observed in the data, which can be an indication for bimodality, but only if it is expected. Compared to these quantities, γ_1 is relatively telling. It is calculated to be negative and therefore suggests a strong tail left of $\langle \Delta x \rangle$, resembling the shape of $\mathcal{G}_s(\Delta x)$ in Fig. III.27 b). The slightly positive γ_α on the other hand is rather small considering the aforementioned tail. This is due to bimodality leading to a large $\sigma^2_{\Delta x}$ in the denominator of γ_α.

To summarise, the quantities introduced in this chapter—mean $\langle \Delta x \rangle(\Delta t)$, variance $\sigma^2_{\Delta x}(\Delta t)$, skewness $\gamma_1(\Delta t)$, and normalised excess kurtosis $\gamma_\alpha(\Delta t)$—are mostly reliable when it comes to illustrating the time-dependency of $\mathcal{G}_s(\boldsymbol{r}, \Delta t)$ of colloidal particles and thus their dynamics. However, each of these quantities on their own are poor indicators of the distributional shape of $\mathcal{G}_s(\boldsymbol{r}, \Delta t)$ [237]. Consequently, when strong deviations from Brownian behaviour—such as multimodal distributions, frequent outliers, or long tails—cannot be generally ruled out, $\mathcal{G}_s(\boldsymbol{r}, \Delta t)$ itself should also be considered before interpreting results.

4.8 The First-Passage Time Distribution

The counterpart to the self-part of the van Hove function, $\mathcal{G}_s(\Delta \boldsymbol{r}, \Delta t)$, in time is the first-passage time distribution, $\mathcal{F}(\Delta t, \Delta \boldsymbol{r})$. While $\mathcal{G}_s(\Delta \boldsymbol{r}, \Delta t)$ describes the

probability of a particle moving a distance $\Delta\boldsymbol{r}$ in a specific time Δt, $\mathcal{F}(\Delta t, \Delta\boldsymbol{r})$ estimates a probability distribution function for the time a particle needs to overcome a specific distance, $\widehat{\mathcal{F}}(\Delta t, \Delta\boldsymbol{r})$. As only one-dimensional first-passage time distributions are discussed in this thesis, considerations are only made for one dimension, x, in the following. Generally, $\widehat{\mathcal{F}}(\Delta t, \Delta x)$ can be defined as the particle flux, $J_x(\Delta x', \Delta t)$, at a certain position, Δx, (cf. Eq II.6):

$$\widehat{\mathcal{F}}(\Delta t, \Delta x) = J_x(\Delta x', \Delta t) = -D \left.\frac{\partial \widehat{\mathcal{P}}(\Delta x', \Delta t)}{\partial x}\right|_{\Delta x' = \Delta x}, \tag{III.57}$$

where $\widehat{\mathcal{P}}(\Delta x', \Delta t)$ is a particle displacement probability density function. There are several ways of defining boundary conditions for the first-passage time calculation, such as semi-infinite or finite systems and different absorbing or reflecting boundaries [87]. Here, we assume a semi-infinite system with an absorbing boundary at $\Delta x' = \Delta x > 0$, so that $-\infty < \Delta x' \leq \Delta x$. When a Brownian particle is placed at $\Delta x' = 0$ inside this system at $\Delta t = 0$, the corresponding $\widehat{\mathcal{P}}(\Delta x', \Delta t)$ can be determined with the aid of the image method [87]:

$$\widehat{\mathcal{P}}(\Delta x', \Delta t) = \frac{1}{\sqrt{4\pi D \Delta t}} \left[-\exp\left\{ -\frac{(\Delta x' - 2\Delta x)^2}{4D\Delta t} \right\} + \exp\left\{ -\frac{\Delta x'^2}{4D\Delta t} \right\} \right]. \tag{III.58}$$

Together with Eq. III.57 this leads to the first-passage time distribution for Brownian particles in one dimension,

$$\widehat{\mathcal{F}}_{\mathrm{B}}(\Delta t, \Delta x) = \frac{\Delta x}{\sqrt{4\pi D \Delta t^3}} \exp\left\{ -\frac{\Delta x^2}{4D\Delta t} \right\}. \tag{III.59}$$

This type of function can also be called a Lévy distribution [244] and is shown as the blue line in Fig. III.28. For large times, $\widehat{\mathcal{F}}_{\mathrm{B}}(\Delta t, \Delta x) \propto \Delta t^{-3/2}$. This type of long-time behaviour means that the mean first-passage time for a Brownian par-

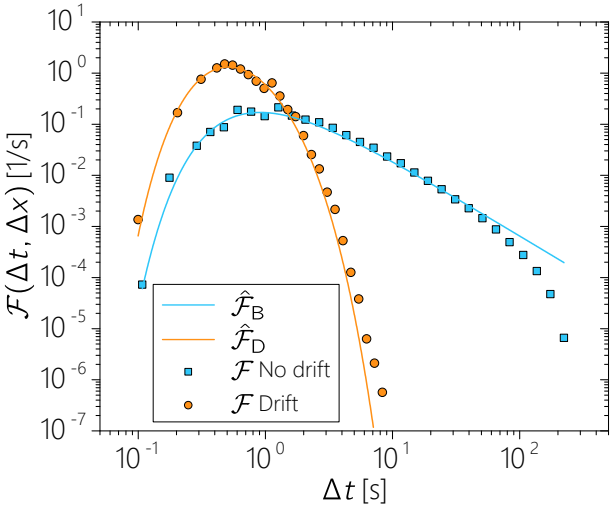

Figure III.28: First-passage time distributions for Brownian motion and Brownian motion with drift. Blue and orange lines represent Eqs. III.59 and III.60, respectively. Corresponding symbols mark experimental results obtained according to Eq. III.61 for the two cases.

ticle in a semi-infinite system is infinite [87]. The probability of a particle reaching the absorbing boundary is however equal to one [87].

In a similar fashion, $\hat{\mathcal{F}}(\Delta t, \Delta x)$ for a particle undergoing Brownian motion drifting with velocity, v_D, can be determined as [87]:

$$\hat{\mathcal{F}}_D(\Delta t, \Delta x) = \frac{\Delta x}{\sqrt{4\pi D \Delta t^3}} \exp\left\{-\frac{(\Delta x - v_D \Delta t)^2}{4D\Delta t}\right\}. \tag{III.60}$$

It is also referred to as the inverse Gaussian (or Wald) distribution function [245] and can be seen in Fig. III.28 as an orange line. It decays exponentially for large times and has a finite mean, namely $\langle \Delta t \rangle(\Delta x) = \Delta x / v_D$.

In order to calculate $\mathcal{F}(\Delta t, \Delta x)$ in a video microscopy experiment, the follow-

ing equations can be used:

$$\mathcal{F}(\Delta t, \Delta x) = \frac{1}{N_\mathrm{t}} \left(\sum_{j=1}^{N_\mathrm{M}} \sum_{i=1}^{N_{\mathrm{P},j}} \sum_{x_0}^{N_{\Delta x,i}} \delta[\Delta t - (t_{ji}(x_0 + \Delta x) - t_{ji}(x_0))] \right) , \quad \text{(III.61)}$$

where

$$N_\mathrm{t}(\Delta x) = \sum_{j=1}^{N_\mathrm{M}} \sum_{i=1}^{N_{\mathrm{P},j}(\Delta x)} N_{\Delta x,i}(\Delta x_{\mathrm{L},i}, \Delta x, \Delta x_\mathrm{min}) \, . \quad \text{(III.62)}$$

These equations are analogous to Eqs. III.21 and III.22, except for being in the time instead of the spatial domain. Consequently, $N_{\Delta x,i}(\Delta x_{\mathrm{L},i}, \Delta x, \Delta x_\mathrm{min})$ represents an integer amount of spatial steps, Δx, that fits into the spatial length of a trajectory, $\Delta x_{\mathrm{L},i}$, while keeping into account a minimum step length, Δx_min, which is defined by the resolution of the used setup. However, in practice, measured quantities are only quantised in time—through the periodic capture of an image—not in space. Thus Eq. III.61 is adapted for practical usage, so that each time a particle covers a distance Δx or more, time Δt is counted. This is done for all particle positions inside a trajectory, x_0, all particles in a measurement, N_P and all measurements, N_M. Blue and orange symbols in Fig. III.28 show $\mathcal{F}(\Delta t, \Delta x)$ obtained experimentally by using Eq. III.61 for particles undergoing Brownian motion and Brownian motion with an additional drift, respectively. Both agree well with their corresponding $\widehat{\mathcal{F}}(\Delta t, \Delta x)$, which are defined by Eqs. III.59 and III.60, except for large Δt. For long times, finite size effects lead to an exponential decay of $\mathcal{F}(\Delta t, \Delta x)$ [87, 246].

IV Colloids Quenched by a One-Dimensional Random Potential

Diffusion in one-dimensional random potentials has been central to several theoretical [247, 248] as well as experimental and simulation studies [131, 227, 249]. Most of them concern the intermediate and long-time reaction of colloidal particles to such potentials. In contrast, the following chapter focusses on the short-time behaviour in a non-equilibrium situation. Particles are randomly distributed before they are quenched by a random potential. The process of quenching, i.e. the immediate impact of the potential on the particles, is examined. Using the SLM setup, a light field consisting of rings with an inherent random pattern (cf. Sec. III.2.1.2) is exerted on dilute samples as described in Sec. III.1.

One-dimensional random potentials similar to that used here are encountered in models of protein diffusion on DNA strands [35, 250] or conducting solids [251, 252]. The underlying processes are not always fully understood, especially in biological environments. Thus, a closer look at the short-time dynamics should give further insight.

1 Colloidal Dynamics in a Static One-Dimensional Random Potential

Before analysing the short-time non-equilibrium dynamics of colloidal particles in a one-dimensional random potential, the general response of colloids to such a potential is of interest. Here, previous results [131, 221] are discussed. These were obtained using the SLM setup (Sec. III.2.1). Colloidal dynamics along the azimuthal direction of the ring was obtained for particles with $R = 1.4$ µm dispersed in D_2O similar to the system described in Sec. III.1. Heavy water was chosen as the dispersion medium since the SLM setup was used (cf. Sec. III.2.1.1), while dispersions were highly dilute to obtain single particle dynamics. Figure IV.1 shows time-dependent variances, $\sigma^2_{\Delta s,\mathrm{TE}}(\Delta t)$, and corresponding anomalous diffusion exponents, $\alpha_\mathrm{D}(\Delta t)$, diffusion coefficients, $D(\Delta t)$, and non-Gaussian parameters, $\alpha_2(\Delta t)$ for varying potential standard deviations, σ_U. In this context, s is the one-dimensional azimuthal coordinate, i.e. the perimeter. Results are replotted from [221], where symbols correspond to experiments [131] and lines to simulations [249]. Variances are normalised by the particle radius $R = 1.4$ µm, diffusion coefficients by the bulk diffusion coefficient, D_b, and times by a hydrodynamic drag-corrected Brownian time, t^*_B [131]. By using Boltzmann statistics together with particle residence times, the standard deviation of the potential could be determined (cf. Sec. III.2.1.3), where larger σ_U correspond to larger local forces imposed on the colloidal particles.

Particle motion inside a one-dimensional random potential is affected on different time scales. This is schematically depicted in Fig. IV.2. Independent of σ_U, the dynamics in Fig. IV.1 shows behaviour close to normal diffusion for small times, $\Delta t \ll t^*_\mathrm{B}$, with $D(\Delta t) \approx D_\mathrm{b}$ and $\alpha_2(\Delta t) \approx 0$ indicating a Gaussian shape of $\mathcal{G}_{\mathrm{s,TE}}(\Delta s, \Delta t)$. Anomalous diffusion exponents at small times show $\alpha_\mathrm{D}(\Delta t) \approx 1$. Brownian behaviour for short times stems from particles diffusing inside local minima of the potential landscape, also called traps here. This is schematically indicated by dark grey arrows in Fig. IV.2. Inside these traps, colloids can diffuse freely at short times. As these minima are of finite size, this behaviour

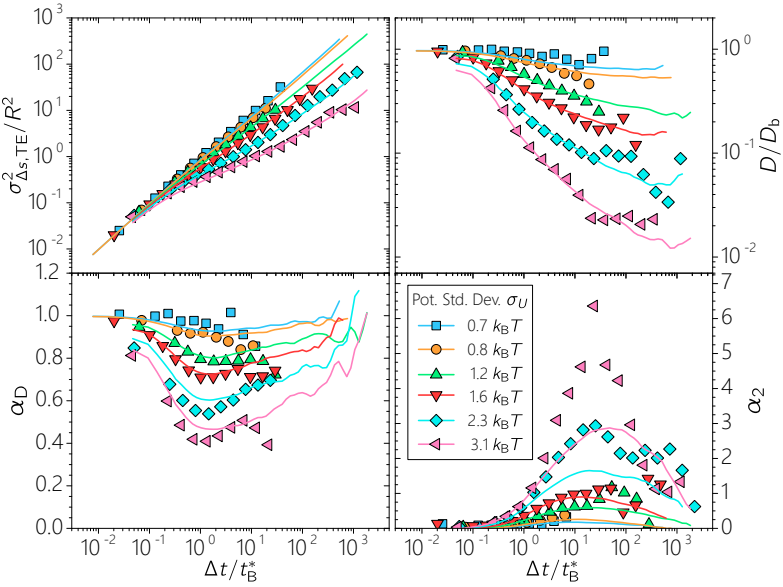

Figure IV.1: Variances of the one-dimensional azimuthal displacements, Δs, normalised by the particle radius, R, diffusion coefficients normalised by the bulk diffusion coefficient, D_b, anomalous diffusion coefficients and non-Gaussian parameters dependent on lag time, Δt, normalised by a hydrodynamic drag-corrected Brownian time, t^*_B, for varying potential standard deviations, σ_U. Symbols correspond to experiments [131] while lines are for simulations [249]. Replotted results published in Ref. [221].

changes when a particle reaches the flanks of a minimum, restricting their diffusion (brown arrow in Fig. IV.2). As a result, motion starts to become transiently subdiffusive for $\Delta t \approx t^*_\mathrm{B}$. In Fig. IV.1, large σ_U-dependent deviations from Brownian motion in $\alpha_\mathrm{D}(\Delta t)$ and $D(\Delta t)$ become apparent. The former drops down to $\alpha_\mathrm{D}(\Delta t) \approx 0.4$ while the latter is reduced by almost two orders of magnitude for the largest σ_U. The larger σ_U is, the stronger the dynamics deviates from Brownian motion, since, on average, flanks (or barriers) between minima become larger for increasing σ_U. Flanks correspond to local forces, where F_lm is the local maximum force a particle has to overcome to reach another local minimum. These

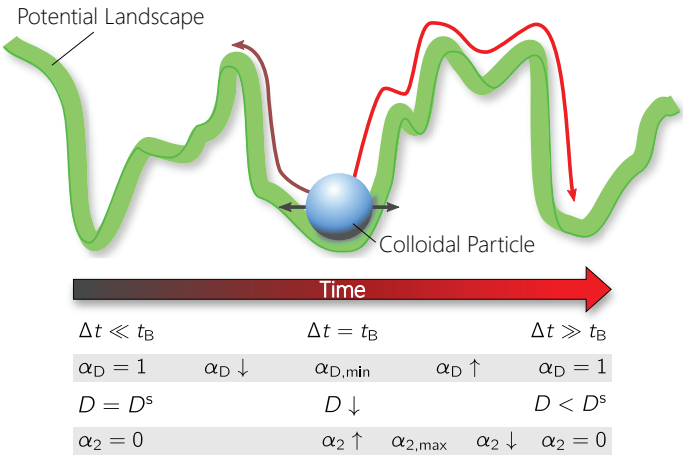

Figure IV.2: Schematic of a particle diffusing in a one-dimensional random potential landscape. Particles show different behaviour depending on the time scale. Differently coloured arrows mark characteristic displacements for each time regime. Qualitative behaviour of relevant quantities (cf. Fig. IV.1) together with the corresponding time scales are given at the bottom.

barriers are the reason why changes in $\alpha_2(\Delta t)$ are delayed compared to changes in $D(\Delta t)$ and $\alpha_D(\Delta t)$. The non-Gaussian parameter reaches its maximum at $\Delta t \approx 20\, t_B$ when some particles have overcome a barrier showing Brownian behaviour, while most are still trapped. This causes $\mathcal{G}_{s,TE}(\Delta s, \Delta t)$ to gain large tails, while its variance, $\sigma^2_{\Delta s,TE}(\Delta t)$, is still governed by trapped particles, resulting in a large α_2. For long times, $\Delta t \gg t_B$, most particles are able to overcome local maxima resulting in $\alpha_D(\Delta t)$ tending towards 1 and $D(\Delta t)$ becoming constant, indicating diffusive behaviour. Diffusion is much slower with the long-time diffusion coefficient, $D^l \lesssim 0.1\, D^s$ for the largest σ_U because particles do not diffuse inside a trap but from minimum to minimum. This dependence was theoreti-

cally determined by Zwanzig [247]:

$$D(t \to \infty) = D_\mathrm{b} \exp\left\{-\frac{\sigma_U^2}{k_\mathrm{B}^2 T^2}\right\} . \tag{IV.1}$$

As particles become diffusive, $\sigma^2_{\Delta s,\mathrm{TE}}(\Delta t)$ is increased relative to the tails in $\mathcal{G}_{\mathrm{s,TE}}(\Delta s, \Delta t)$ and thus diminishes $\alpha_2(\Delta t)$, which tends to zero for long times. The mechanism is depicted by the red arrows in Fig. IV.2. The time particles take to reach the long-time diffusion was found to increase exponentially with σ_U^2 [227], since particles have to surmount barriers instead of circumventing them in order to become diffusive. This circumstance changes when it comes to diffusion in two dimensional random potential landscapes, where particle have more degrees of freedom and reach long-time diffusion earlier (cf. Sec. VI.1).

Particles diffusing in a one-dimensional random potential cannot be described by models like the continuous time random walk or fractional Brownian motion, even though dynamics quantities such as the variance of the particle displacements qualitatively look the same as the ones presented in Fig. IV.1. Neither waiting times in CTRW nor correlations in FBM are space dependent. The one-dimensional random potential described here, on the other hand, is spatially heterogeneous. It does not feature any obstacles and thus cannot be explained by obstructed motion either. It is conceivable however, that the dynamics in a one-dimensional random potential could be explained by heterogeneous diffusion processes, where $D = D(s)$. Minima and maxima of the random potential would then correspond to low and high diffusivity regions respectively, with particles accumulating in low diffusivity regions [88], i.e. potential minima.

2 Theory and Simulations

This chapter contains experimental results which are compared to theory and simulations performed by Michael Schmiedeberg and Hartmut Löwen [253], hence this section summarises the theoretical results and states the simulation parameters.

When a one-dimensional colloidal system is quenched by a random potential, $U(s)$, particles are exposed to an external force, $F_{\mathrm{E}}(s(t))$, where $s(t)$, is the time-dependent particle position. Additionally, they are subject to the randomly fluctuating force due to Brownian motion, $F_{\mathrm{B}}(t)$, with the moments:

$$\langle F_{\mathrm{B}}(t)\rangle_T = 0 \text{ and} \tag{IV.2}$$

$$\langle F_{\mathrm{B}}(t_1)F_{\mathrm{B}}(t_2)\rangle_T = 2k_{\mathrm{B}}T\xi_0\,\delta[t_1 - t_2] = 2D_0\xi_0^2\,\delta[t_1 - t_2]\,, \tag{IV.3}$$

where $\langle\,\cdot\,\rangle_T$ denotes an average over thermal noise. Equations IV.2 and IV.3 illustrate that there is no net force acting on particles due to Brownian motion and there are no correlations between forces at two different times. The equation of motion in one dimension then reads:

$$\xi_0\frac{\partial s}{\partial t} = F_{\mathrm{E}}(s(t)) + F_{\mathrm{B}}(t)\,. \tag{IV.4}$$

The acceleration term was omitted as particles are considered to be overdamped, i.e. viscous forces outweigh inertia [254]. For small displacements, $F_{\mathrm{E}}(s(t))$ can be Taylor-expanded about $s(t) = s(0)$ in Eq. IV.4. This yields:

$$\begin{aligned}\xi_0\frac{\partial s}{\partial t} = {} & F_{\mathrm{B}}(t) + F_{\mathrm{E}}(s(0)) + F'_{\mathrm{E}}(s(0))(s(t) - s(0)) \\ & + \frac{1}{2}F''_{\mathrm{E}}(s(0))(s(t) - s(0))^2 \\ & + \frac{1}{6}F'''_{\mathrm{E}}(s(0))(s(t) - s(0))^3 \\ & + \frac{1}{24}F''''_{\mathrm{E}}(s(0))(s(t) - s(0))^4 + \dots\,,\end{aligned} \tag{IV.5}$$

where an apostrophe stands for a spatial derivative. When Eq. IV.5 is truncated after the second force term, i.e. all terms with $F''(s(0))$ and higher are neglected, the equation of motion for the analytically solvable Brownian oscillator is found. The additional force terms can be treated by using linear pertubation theory with

respect to the Brownian oscillator. A small pertubation displacement is added to the particle position found for the Brownian oscillator. This approach yields a short-time expansion of the disorder-averaged mean square displacement [253]:

$$\begin{aligned}\langle s(t) - s(0)\rangle_{T,U} &= \langle \Delta s^2\rangle_{T,U} \\ &= 2D_0 t + \frac{1}{\xi_0^2}\langle F_{\mathrm{E}}^2(s(0))\rangle_U\, t^2 \\ &\quad + \left(\frac{4D_0}{3\xi_0}\langle F_{\mathrm{E}}^2(s(0))\rangle_U \right. \\ &\quad \left. + \frac{7D_0}{3\xi_0}\langle F_{\mathrm{E}}(s(0))F_{\mathrm{E}}''(s(0))\rangle_U\right)\, t^3 + \mathcal{O}(t^4)\,,\end{aligned} \tag{IV.6}$$

where $\langle\,\cdot\,\rangle_U$ denotes the average over the disorder of the potential $U(s)$. The random potential can be said to have a typical energy, E_U, and the forces caused by it a correlation length, l_F, which yields[1]

$$\langle F_{\mathrm{E}}^2\rangle_U = \frac{E_U^2}{l_F^2}\,, \quad \langle F_{\mathrm{E}}'^2\rangle_U = \frac{E_U^2}{l_F^4} \quad \text{and} \quad \langle F_{\mathrm{E}}F_{\mathrm{E}}''\rangle_U = -\langle F_{\mathrm{E}}'^2\rangle_U\,, \tag{IV.7}$$

with the correlation length of the forces caused by the potential:

$$l_F^2 = \frac{\langle F_{\mathrm{E}}^2\rangle_U}{\langle F_{\mathrm{E}}'^2\rangle_U}\,. \tag{IV.8}$$

A characteristic time can then be defined by means of l_F and reads

$$t_F = l_F^2/2D_0\,. \tag{IV.9}$$

The typical energy, E_U, is defined by the second moment of F_{E} and l_F, but is closely related to the standard deviation of the external potential, σ_U, introduced in Sec. III.2.1.3. Hence, a normalised diffusion coefficient similar to Eq. III.35,

[1] The last part of Eq. IV.7 is valid for physically sensible potentials and follows from integration by parts [253].

$\overline{D}(t) = \langle \Delta s^2 \rangle_{T,U}/t$, can be derived:

$$\frac{\overline{D}(t)}{D_0} = 1 + \frac{E_U}{4k_\mathrm{B}T}\frac{t}{t_F} - \frac{E_U}{8k_\mathrm{B}T}\frac{t^2}{t_F^2} + \mathcal{O}(t^3)\,. \tag{IV.10}$$

As Eq. IV.10 approximates the diffusion coefficient of a single particle quenched by a random potential energy landscape in one dimension up to the second order in time only, it is solely applicable for short times, $t \ll t_F$. In addition, Brownian dynamics simulations [255] were conducted by Michael Schmiedeberg [253] and are compared to the measurements in Sec. IV.4. All simulation results were obtained by averaging over 100,000 non-interacting particles, which were placed randomly before each run. The random potentials used for the simulations are Gaussian-distributed and based on those used in Monte Carlo simulations performed by Hanes et al. [249] (lines in Fig. IV.1). To be able to compare present simulations with previous studies [249] a factor between σ_U, the standard deviation of an external potential, and E_U, the typical energy of a potential, arises: $\sigma_U = 4.405\,E_U$.

3 One-Dimensional Random Potentials for Quenching

To realise an external one-dimensional random potential energy landscape, a light field with a four-ring pattern—as described in Secs. III.2.1.2 and III.2.1.3—was created by means of the Gerchberg-Saxton algorithm and the SLM setup. Rings were chosen to obtain periodic boundary conditions in the azimuthal direction while constraining particle motion in radial direction (cf. Sec. III.2.1.3). As can be seen in Fig. IV.3 a), the desired pattern, $\mathcal{A}_\mathrm{T}^\mathrm{ds}$, consisted of four rings, R0, R1, R2 and R3, centred about the zeroth order with radii, $R_{\mathrm{T},0} = 256$ px, $R_{\mathrm{T},1} = 192$ px, $R_{\mathrm{T},2} = 128$ px and $R_{\mathrm{T},3} = 64$ px, with a width of 3 px and an 8-bit grey level of 255 on a background with grey level 0. This translated to $R_{\mathrm{r},0} \approx 51$ µm, $R_{\mathrm{r},1} \approx 38$ µm, $R_{\mathrm{r},2} \approx 26$ µm and $R_{\mathrm{r},3} \approx 13$ µm in the sample plane (Fig. IV.3 b)). As the diffrac-

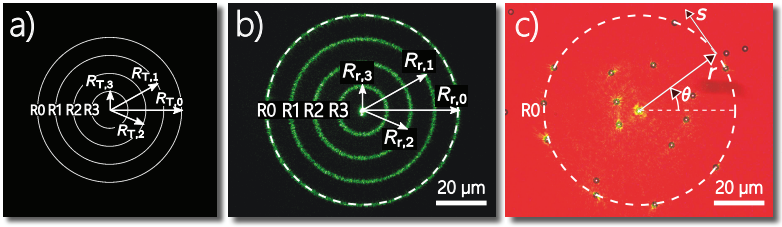

Figure IV.3: a) Desired pattern, $\mathcal{A}_T^{ds}$, used to create the light field shown in b). Radii of the four rings, R_T, are given in the text. b) Micrograph of a four-ring pattern light field used in this chapter. Radii of the four rings, R_r, are given in the text. c) Micrograph of a typical sample, where the outermost ring, R0, with radius, $R_{r,0} \approx 51$ µm, is drawn as a dashed white line. Additionally, axes relevant for the analysis of particle motion are marked as white arrows.

tion efficiency of the SLM decreases with distance from the zeroth order, intensities of the inner ring, R3, were on average the highest while the outer ring, R0, exhibited the lowest intensities. Here, the dynamics in the outermost ring—the white dashed circle in a typical sample in Figs. IV.3 b) and c)—is considered only. To allow for statistically independent experiments, each measurement was conducted using a light field with different speckles, i.e. realisation of randomness, while the overall pattern and speckle distribution was kept constant. Light fields with a consistent pattern and distribution, yet spatially varying speckles, can be generated by cyclically shifting the corresponding kinoform, $\mathcal{A}_K$ [256]. For the measurements discussed here, 49 different realisations of the four-ring pattern were generated.

As the focus lies on a quench of randomly distributed particles by a one-dimensional random potential, the short-time dynamics is most important. At the same time, it is desirable to conduct as many measurements as possible for better statistics. To cover both aspects, namely short and numerous measurements, a cyclic sequence of light fields was created in the sample plane by means of an IDL routine feeding kinoforms to the SLM accordingly (Fig. IV.4). It started with the previously described four-ring pattern that was cycled at 30 different realisations per

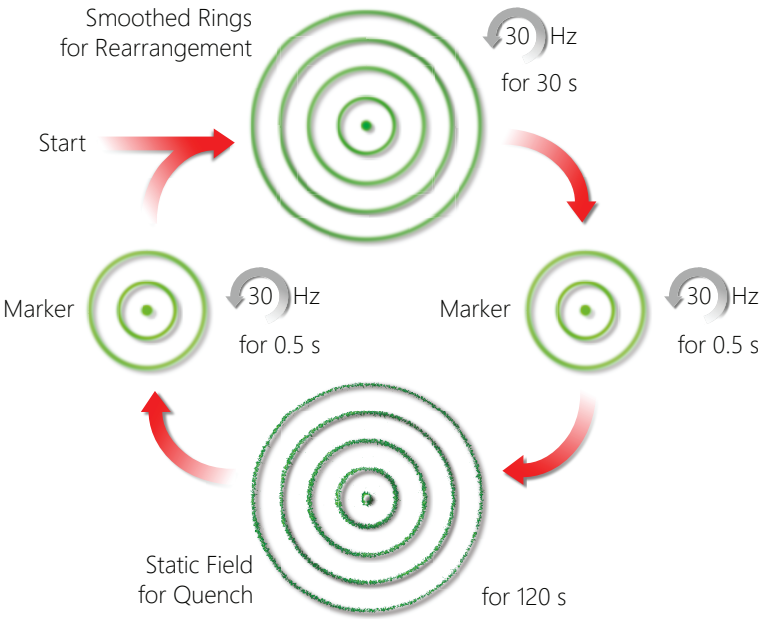

Figure IV.4: Sequence of light fields imposed on the colloidal system. It starts with the four-ring pattern cycled at 30 different realisations per second for 30 seconds. Then, a marker light field with a two-ring pattern is cycled at 30 Hz for 0.5 s. It indicates the start of a static four-ring pattern period, which is used for quenching the colloidal system. After 120 s, the end of the quench is indicated by the marker again. To conclude, the cycled four-ring pattern allows particles to rearrange before they are quenched again.

second for 30 s. Cycling the pattern at this high frequency with different realisations lead to the random landscape being washed out: as the positions of minima and maxima of the potential changed more than two orders of magnitude faster than their Brownian time of $t_B = R^2/2D_0 = 16.3$ s (cf. Sec. III.1), particles did not react. Thus, colloids were effectively exposed to a flat ring potential with no randomness for 30 s. Following this, a marker light field consisting of the two inner rings of the four-ring pattern was cycled at 30 Hz for 0.5 s. It signalled the beginning of a following quenching period, where the actual measurement took

place. As the marker consisted of only two rings, the used laser power was distributed into a smaller area, resulting in a higher intensity in the FOV. This fact was useful for experiment analysis later on. To quench the colloidal system, one of the 49 realisations of a four-ring pattern was used. Each sequence iteration used a different realisation. It was imposed on the particles for 120 s before a second marker signalled the end of quenching. A cycled four-ring pattern concluded the sequence. It was used to let particles rearrange inside the ring before they were quenched again.

4 Measuring the Dynamics

As the SLM setup was used, samples were prepared according to Sec. III.1 with D_2O as the dispersion medium. Particles with $R = 1.4$ µm were used, which formed a quasi-two-dimensional layer at the upper wall of the sample cell. Although highly dilute, the particles tended to accumulate inside the light field during a measurement. Therefore, an IDL routine was used to exclude particles from analysis whose surfaces approached any distance less than R at any point during a measurement. A line fraction, $\varphi_l \approx 0.1$, was obtained and colloids were treated as single particles.

Colloidal samples were quenched at different laser powers, 620 mW $\leq P_\mathrm{L} \leq$ 1.46 W with the sequence shown in Sec. IV.3. Each measurement was about one hour long, resulting in about 24 quenches at 120 s. During that time, the field of view was not changed and particle motion was recorded with 10 FPS, equivalent to $\Delta t_\mathrm{min} = 0.1$ s. For each P_L, five to seven measurements were conducted, summing up to more than 1000 particle trajectories for each laser power.

From Sec. III.2.1.1, it is known that in addition to particle motion, stray light is visible as green halos around particles when the SLM setup is used (cf. Fig. IV.3 c)). Thus, captured colour images could be analysed separately via their red and green channels. While the red channel contained all information about colloidal particles and their movement, the green channel only contained stray light. Since marker light fields had a higher intensity about the centre of the field, the bright-

ness of the green channel of each image could be analysed with IDL programs to find the points in time where a quenching period started and ended. Subsequently, only red channels of images captured during the quenching period were analysed further. The time was reset for each quenching period, resulting in trajectory lengths $\Delta t_\mathrm{L} \leq 120$ s. In order to analyse the dynamics in the azimuthal direction along R0, particle positions were transformed from Cartesian to polar coordinates with the radial component, r, only being allowed to vary ± 1.1 µm about $R_{\mathrm{r},0}$. Together with r, the azimuthal coordinate, θ, was transformed to the perimeter, $s = r\,\theta$, as can be seen in Fig. IV.3 c). Trajectories of all quenching periods and measurements for each P_L were combined and analysed regarding their dynamics in s with only ensemble averages being used. The use of ensemble averages is necessary as the observed system is evolving in time during the quench. In that case, time averages would wash out the dynamics (cf. Sec. III.4).

5 Dynamics of Colloids Quenched by a One-Dimensional Random Potential

The diffusion coefficient, $\overline{D}(t)$, is the main quantity used to visualise the reaction of colloidal particles to a quench by a random potential in one dimension. Figure IV.6 shows $\overline{D}(t)$ and the variance, $\sigma^2_{\Delta s,\mathrm{E}}(t)$, for various values of P_L as symbols as well as corresponding simulation results as lines. To compare measurements and simulations, measured time scales and diffusion coefficients are normalised by the characteristic time, $t_F = l_F^2/2D_0$, and D_0, respectively, where D_0 is the diffusion coefficient for free particles close to the wall of the sample cell (cf. Sec. III.1). In the course of this process, t_F, the correlation length of forces due to the potential, l_F, and σ_U are used as fitting parameters. The former two are found to be $t_F = 0.42$ s and $l_F = 0.23$ µm, where l_F is used to normalise $\sigma^2_{\Delta s,\mathrm{E}}(t)$ in Fig. IV.6 b). From t_F and l_F, $D_0 = 0.06$ µm^2/s is calculated, which agrees with the values obtained for short-time diffusion inside a smoothed ring pattern (cf. Fig. IV.4). With these values, good agreement between measurements and simulations is observed. In order to verify this agreement, Fig. IV.5 shows P_L

of all measurements and the corresponding fitted σ_U of the simulations. Symbol shapes and colours are consistent with those used in Fig. IV.6. They resemble a linear dependence, as can be drawn from the linear fit through the origin indicated by the grey line. This is expected for the used laser power and the resulting potential roughness (cf. Sec. III.2.1.3) and thus validates the fit. To ascertain whether the value of l_F is also reasonable, it is determined by analysing micrographs of the used light field of the outer ring, $I(s)$. It is convolved with the particle weight function, W_P, to obtain $I_\mathrm{P}(s)$ similar to Fig. III.6 b). As $I_\mathrm{P}(s)$ should resemble the potential, $U(s)$, the first and second symmetric spatial derivatives are calculated with MATLAB (The MathWorks, Inc.) to obtain, $I_\mathrm{F}(s)$ and $I'_\mathrm{F}(s)$ in units of grey levels, respectively, which correspond to force F_E and their derivatives, F'_E. Values obtained for $I_\mathrm{F}(s)$ and $I'_\mathrm{F}(s)$ are binned in histograms, which are then fitted by a Gaussian to obtain their variances. The ratio of these variances then yields l_F (cf. Eq. IV.8)[2]. In Fig. IV.5 b) the result for this procedure using different bin sizes for histograms is shown. In total, an average over ten micrographs of different realisations of the four-ring pattern is used. The bin size utilised to create the histograms does not play an important role. In general, Fig. IV.5 b) shows that even this very crude method—using pictures of light fields and treating them as if they were actual potentials—results in values for l_F similar to those found by fitting the results. Therefore, both graphs presented in Fig. IV.5 corroborate the validity of the fit used in Fig. IV.6.

A closer look at Fig. IV.6 a) reveals the overall dynamics of the quenched particles is similar for all used potential roughnesses: the diffusion coefficient first rises quickly indicating superdiffusive behaviour and reaches a maximum, $\overline{D}_\mathrm{max}$, at $t = t_{\overline{D}_\mathrm{max}} \approx 10\, t_F$. It then decreases slowly showing subdiffusivity and does not reach D_0 within times $t \leq 50\, t_F$ shown here. Eventually, $\overline{D}(t)$ drops below D_0 for very long times similar to Fig. IV.1, which is not shown in Fig. IV.6 a) but can be inferred from the levelling of $\sigma^2_{\Delta s,\mathrm{E}}(t)$ for long times in Fig. IV.6 b). The characteristic dynamic behaviour stems from randomly placed particles being

[2] In Eq. IV.8, second moments are used instead of variances. As the mean grey value of $I_\mathrm{P}(s)$ can be defined as the zero point of the corresponding virtual potential, variances and second moments can be used interchangeably.

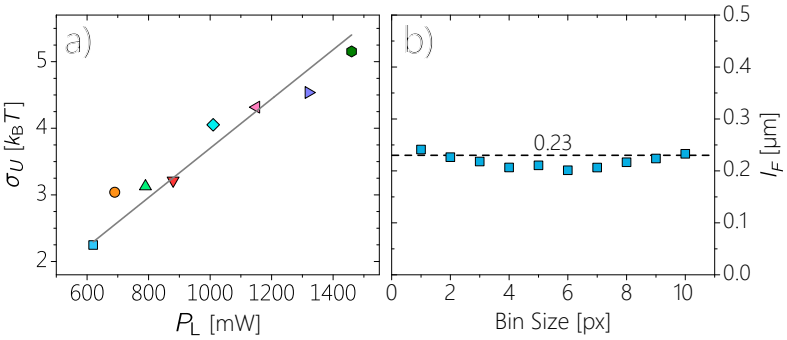

Figure IV.5: Verification of the fit shown in Fig. IV.6. a) Symbols show laser Powers, P_L, of measured diffusion coefficients and standard deviation of potentials, σ_U, belonging to their simulated counterparts for each fit. Symbol colours and shapes are the same as in Fig. IV.6. The grey line corresponds to a linear fit through the origin. b) Correlation lengths of the potential's forces, l_F, depending on the bin size used to determine them. Results are obtained through analysis of micrographs taken of the light field creating the potential. The dashed line corresponds to $l_F = 0.23$ µm as determined by the fit in Fig. IV.6.

suddenly exposed to an external random potential. As initial particle positions and features of the potential are not correlated, some particles are situated at potential maxima. Hence, they are forced to move towards minima by the quench. This potential-driven motion is faster than diffusion and thus manifests itself in an increased $\overline{D}(t)$ and $\sigma^2_{\Delta s,\mathrm{E}}(t)$ rising faster than t (dashed line in Fig. IV.6 b)). Diffusivity reaches its maximum, $\overline{D}_{\max}$, when most particles in the quenched colloidal system are put in motion and have not yet reached a local minimum. As time proceeds, the amount of particles that have reached a minimum constantly rises. As a result, $\overline{D}(t)$ begins to decline and, equivalently, $\sigma^2_{\Delta s,\mathrm{E}}(t)$ starts to level off. The more time elapses, the more particles reach a (local) minimum and get trapped in it. A crossover from a quenched system showing enhanced diffusion to the system described in Sec. IV.1, where motion is hindered by the external potential, takes place. The reason for different short-time behaviours in the results shown here and those described in Sec. IV.1 lies in the different ways of averaging

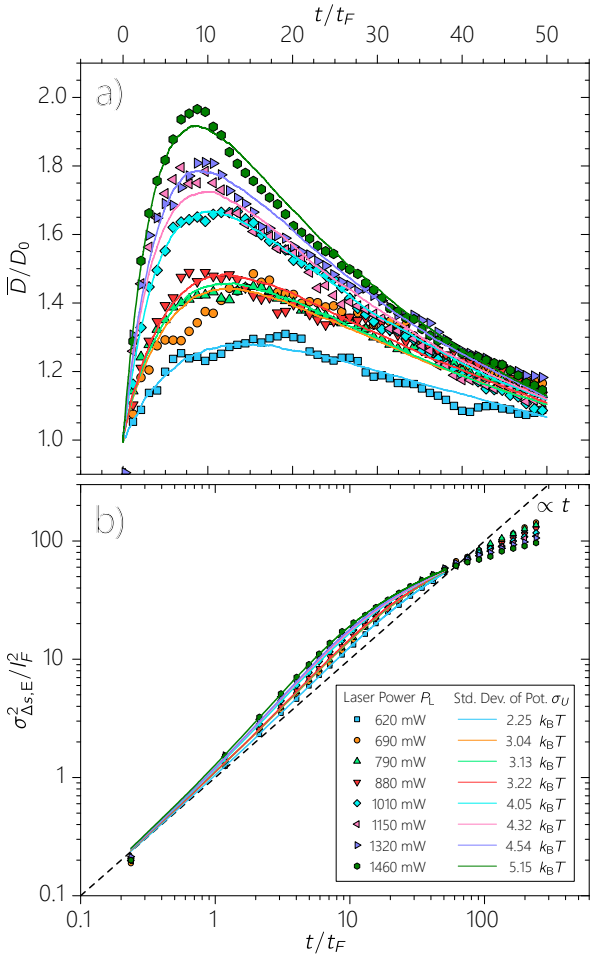

Figure IV.6: Diffusion coefficients, $\overline{D}(t)$, and variances, $\sigma^2_{\Delta s,E}(t)$, of measured (symbols) and simulated (lines) colloidal particles quenched by one-dimensional random potentials with different roughnesses, σ_U. Measured quantities were normalised in order to allow for a comparison with the simulations.

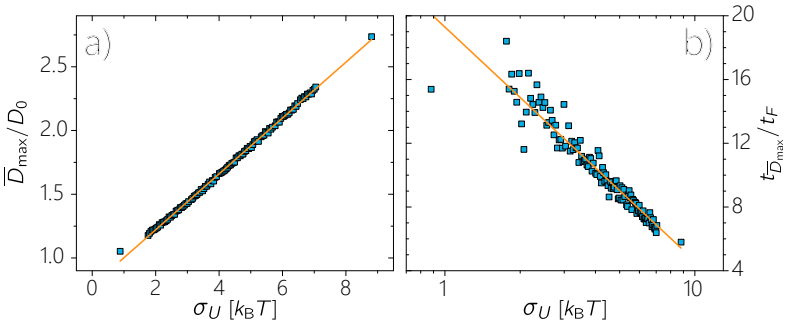

Figure IV.7: Simulation results (symbols) for the maximum diffusion coefficient, $\overline{D}_{\max}$, in a) and the time at which it occurs, $t_{\overline{D}_{\max}}$, in b) depending on the roughness of the potential, σ_U, with which particles are quenched. Orange lines correspond to linear fits. Note that in b) a logarithmic time axis is used.

(cf. Sec. III.4.6).

The maximum value of the diffusion coefficient, $\overline{D}_{\max}$, and the time at which $\overline{D}_{\max}$ is reached, $t_{\overline{D}_{\max}}$, strongly depend on the σ_U imposed on the colloidal system. In Fig. IV.7, simulated $\overline{D}_{\max}(\sigma_U)$ and $t_{\overline{D}_{\max}}(\sigma_U)$ are given. A linear behaviour between $\overline{D}_{\max}(\sigma_U)$ and σ_U is found (symbols in Fig. IV.7 a)) and verified by a linear fit (orange line). However, a non-linear relation is expected for low σ_U, where the linear fit does not agree with the data, since $\overline{D}_{\max} = D_0$ for $\sigma_U = 0\, k_B T$. A larger σ_U necessarily results in larger forces acting on particles. These increased forces cause colloids to move faster, resulting in a higher $\overline{D}_{\max}$. In a similar fashion as $\overline{D}_{\max}(\sigma_U)$ increases, $t_{\overline{D}_{\max}}(\sigma_U)$ decreases for growing σ_U. However, there is a logarithmic relationship between the two as a linear fit of the logarithmically plotted $t_{\overline{D}_{\max}}(\sigma_U)$ (symbols) shows in Fig. IV.7 b). Larger σ_U thus do not only lead to larger $\overline{D}_{\max}$ but also result in an earlier occurrence thereof, while the correlation length of the potential is by design not affected by a change in σ_U.

To gain insight into the kind of super- and subdiffusivity indicated by $\overline{D}(t)$ in Fig. IV.6, the anomalous diffusion exponent, $\alpha_D(t)$, and normalised excess

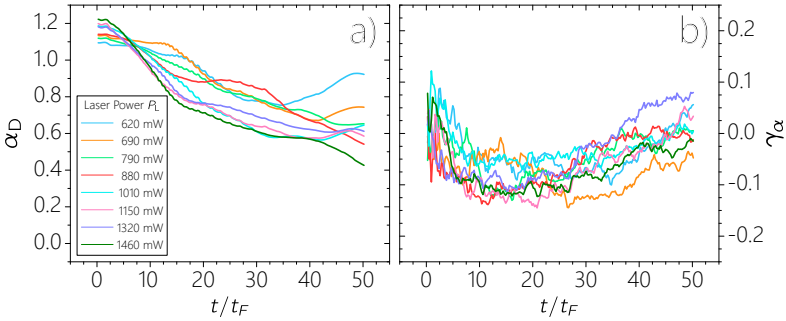

Figure IV.8: Measured time-dependent anomalous diffusion exponents, α_D, in a) and normalised excess kurtoses, γ_α, in b) for varying laser powers, P_L.

kurtosis, $\gamma_\alpha(t)$, are shown in Figs. IV.8 a) and b) for measurements with varying P_L.[3] Two trends can be recognised in Fig. IV.8 a): a larger potential roughness results in more pronounced superdiffusive behaviour for short times and more pronounced subdiffusivity for longer times. The latter was already discussed in Sec. IV.1. The former is a result of the increased forces acting on the particles—similar to the explanation given for $\overline{D}(t)$. However, superdiffusive values of $\alpha_D(t)$ range from 1.05 to 1.25 and show thus a rather small deviation from Brownian behaviour compared to those found in Secs. IV.1 and VI.4. The normalised excess kurtosis on the other hand displays remarkable behaviour. It drops below zero at times $10\,t_F \lesssim t \lesssim 30\,t_F$ before obtaining positive values and showing the same increasing trend at longer times (not shown here) that can be found in Fig. IV.1.[4] This drop in $\gamma_\alpha(t)$ shows that shoulders in the corresponding van-Hove function, $\mathcal{G}_{s,E}(\Delta s, t)$, are pronounced compared to a Gaussian function. Together with the increase in $\overline{D}(t)$ and the superdiffusive $\alpha_D(t)$, this indicates particle displacements, Δs, are enhanced by the initial potential quench, especially for intermediate ranges where the shoulders of $\mathcal{G}_{s,E}(\Delta s, t)$ lie. For longer times, the quench

[3] The corresponding σ_U can be found in the legend of Fig. IV.6.

[4] As $\gamma_\alpha(t)$ is normalised, it can be compared to $\alpha_2(t)$. Time scales are however different as $t_F \neq t_B^*$ and time- and ensemble-averaged data are utilised in Fig. IV.1.

results in trapped particles and $\alpha_{\mathrm{D}}(t)$ drops while $\gamma_{\alpha}(t)$ rises since long tails in $\mathcal{G}_{\mathrm{s,E}}(\Delta s, t)$ develop as explained in Sec. IV.1. The crossover from a superdiffusive system caused by the external random potential quench to a subdiffusive system due to the same potential for later times thus also manifests itself in $\alpha_{\mathrm{D}}(t)$ and $\gamma_{\alpha}(t)$. The higher σ_U, the more pronounced it it is.

6 Discussion

Upon closer inspection, it can be recognised that the distinct short-time behaviour of particles quenched by a random potential landscape, is not seen for the data presented in Fig. IV.1. The measurement conditions are generally the same for the study in Sec. IV.1 and the one presented here and thus should lead to similar results. However, observation times, $t_{\mathcal{O}}$, and data analysis are fundamentally different. While Hanes et al. [131] focussed on long measurements and accordingly the long-time dynamics, $t_{\mathcal{O}}$ was here chosen to be much shorter. This allows for more repetitions of the experiment and thus using ensemble-averaged quantities instead of the time- and ensemble-averaged ones that were used in Ref. [131]. The difference in data analysis is the main reason for the behaviour shown in Fig. IV.6 not being present in Fig. IV.1: the time average in Ref. [131] covers up any reaction of the particles to the initial quench by the random potential (cf. Sec. III.4.6). An additional conclusion that can be drawn from the comparison of Fig. IV.6 and [131] is that the particle reaction to the quench is a onetime event. As ensemble-averaged and time- and ensemble-averaged quantities do not agree, the system evolves. After the initial quench, resulting in superdiffusion for short times, the system evolves so that the short time behaviour becomes diffusive as can be drawn from the time averaged quantities in Fig. IV.1.

Superdiffusive short-time motion together with intermediate subdiffusion and long-time diffusion are seen in the same form for simulated random, periodic and quasicrystalline potentials [227, 257]. Both studies show similar behaviour in $\sigma^2_{\Delta s,\mathrm{E}}(t)$ and $\alpha_{\mathrm{D}}(t)$ to that found here. Furthermore, negative values for $\gamma_{\alpha}(t)$ at short times are also found in a simulation study related to the results discussed

in Sec. IV.1 [249] confirming that a broadening of the shoulders of $\mathcal{G}_{s,E}(\Delta s, t)$ takes place when particles are quenched by a random potential.

Superdiffusive motion with a subsequent decrease of the diffusion coefficient is not only seen for a quench of colloidal particles by a random potential but also for a wide range of other applications: Bodrova et al. [258] investigated Brownian motion in a granular gas in a homogeneous cooling state, which was not only superdiffusive but superballistic before it became subdiffusive. Start-up shear of concentrated colloidal hard spheres also results in superdiffusive behaviour as Koumakis et al. reported [259]. After a subdiffusive regime, particles show superdiffusion and eventually normal diffusion. A very similar time dependence of the dynamics to the one found here is presented by Spiechowicz et al.[260] for Brownian particles moving in a periodic potential: first the dynamics is superdiffusive, then subdiffusive and in the end diffusive. These regimes are exhibited even though particles are driven. A similar observation is made in Sec. VI for particles dragged through a random two-dimensional potential. Furthermore, Najafi et al. [261] showed that quenching carriers in semiconductors with a laser pulse leads to superdiffusion before the diffusion coefficient decreases and reaches its room temperature value.

Besides the superdiffusive short-time behaviour followed by subdiffusion, there is an additional interesting feature seen in Fig. IV.6 b), namely that all curves seem to have a common point of intersection found when the diffusion coefficient of the system, $\overline{D}(t)$ is on the verge of dropping below D_0 at $t \approx 55\, t_F$, where $\sigma^2_{\Delta s,E}(55\, t_F) \approx 60\, l_F^2$. Similar behaviour is found for simulations on particles in a comparable one-dimensional random potential focussing on longer times [227] as well as in periodic and quasicrystalline potential landscapes [257]. However, none of the cited sources come up with an explanation for this distinct feature. As it is not only seen in simulations but also in the measurements presented here, it is unlikely to be a computational artefact. The point of intersection coincides with particle diffusion dropping below D_0. It seems to be a characteristic time and length, at which particles settle inside potential minima after they have undergone the initial quench. Just like the point of intersection, the cor-

relation length of the potential, $l_U \approx R$ (cf. Sec. III.2.1.3), is independent of the roughness, σ_U. Additionally, it corresponds to the average distance of two minima inside $U(s)$. Comparing the point of intersection with l_U and Brownian time, $t_B = R^2/2D_0 \approx l_U^2/2D_0$, which also happens to be about the characteristic time in which a particle covers l_U^2, reveals that the intersection lies at $\approx 1.5\, t_B$ and $\approx 1.6\, l_U^2$. It is thus close to the characteristic time and length scale of the external random potential and might be related to it. Volpe et al. [136] used a similar approach to explain the dynamics in an external potential by introducing a characteristic relaxation time, t_V. However, $t_V \propto 1/\langle F_E \rangle$, where $\langle F_E \rangle$ is the mean of the force exerted on the particles by the external potential. Therefore, t_V is also inversely proportional to the roughness of the external potential, which does not agree with the idea of treating t_B as a relaxation time. However, $t_{\overline{D}_{max}}$ is inversely proportional to σ_U, albeit logarithmically, and might be regarded as a relaxation time inside the random potential.

As stated in the introduction of this chapter, a protein diffusing along a DNA strand can also be modelled by a colloidal particle diffusing in a one-dimensional random energy landscape [35, 250]. It is proposed that a protein changes between a search mode, where the potential caused by the different base pairs are rather narrow and small, and a recognition mode, where the protein is exposed to a larger and broader random potential. A change from search to recognition mode should thus be equivalent to a sudden increase of σ_U. This should result in a temporarily increased diffusion coefficient as found here and may decrease the time the protein needs to find its binding site during the next recognition step.

V Colloids in a Periodically Varying One-Dimensional Random Potential

The motion of colloids in time-dependent potentials has been studied intensively in recent years. Examples include the discovery of mechanisms such as stochastic resonance [262], relevant to climate change, or resonance activation [263], found in biological environments, the theoretical treatment of diffusion inside switching periodic potentials [264] or the experimental realisation of feedback-controlled ratchets [265]. In this chapter, an additional aspect, namely particle diffusion inside a random potential varying between uncorrelated realisations, is discussed. Theory and experiments are based on Sec. IV but instead of quenching colloidal particles only once like in the previous chapter, the one-dimensional random potential was periodically varied. Dilute samples (cf. Sec. III.1) were exerted to different variation periods, which lead to period-dependent behaviour exhibiting enhanced diffusion.

Besides the wide range of colloidal studies, several applications of motion in time-dependent potentials in other scientific fields can be found. Dynamical polymer films can control the motion of nanospheres [266], cancer growth is affected by the frequency of the periodic treatment [267] and random forces of molecular motors in cells enhance intracellular movement [243]. Additionally, Josephson tunnel junctions can be described by a washboard potential, where temperature fluctuations lead to higher escape rates [268]. However, most of the referenced literature focusses on periodic potentials. Here, the effect of varying random potentials on particle diffusion will be analysed.

1 Theory and Simulations

Similar to the approach in Sec. IV, theory and simulations concerning a varying random potential were developed by Hartmut Löwen and Michael Schmiedeberg [253] and are compared to measurements in this chapter. The following is based on Sec. IV.2 and continues the argumentation given there.

Particles are again quenched by a random potential, $U(s)$, like the one described in Sec. III.2.1.3. After a period, τ, particles are abruptly exposed to a different realisation of the random potential while the characteristics of $U(s)$ are kept the same. If different realisations of $U(s)$ are changed in a Markovian way, the ensemble-averaged variance of particle displacements reads:[1]

$$\sigma^2_{\Delta s,\mathrm{E}}(t) = \begin{cases} \sigma^2_{\Delta s,\mathrm{E}}(t) & \text{for } 0 \le t \le \tau \\ \left\lfloor \frac{t}{\tau} \right\rfloor \sigma^2_{\Delta s,\mathrm{E}}(\tau) + \sigma^2_{\Delta s,\mathrm{E}}\left(t - \left\lfloor \frac{t}{\tau} \right\rfloor\right) & \text{for } t > \tau\,. \end{cases} \tag{V.1}$$

For times smaller than τ, particle dynamics are expected to follow the behaviour found for short times as described in Sec. IV. A periodic change of the random potential leads to a recurring quench and thus to a recurrence of the short-time behaviour. This is illustrated by brackets, $\lfloor \cdot \rfloor$, which stand for the floor function rounding a real number to its next smallest integer value. So, for $t = 2.4\,\tau$, a variance of $\sigma^2_{\Delta s,\mathrm{E}}(2.4\,\tau) = 2\,\sigma^2_{\Delta s,\mathrm{E}}(\tau) + \sigma^2_{\Delta s,\mathrm{E}}(0.4\,\tau)$ is expected. Figure V.1 a) schematically depicts this behaviour of a variance curve, showing periodic growth of $\sigma^2_{\Delta s,\mathrm{E}}(t)$.

Accordingly, the diffusion coefficient, $\overline{D}(t) = \sigma^2_{\Delta s,\mathrm{E}}(t)/2t$, can be deduced as:

$$\overline{D}(t) = \begin{cases} \overline{D}(t) & \text{for } 0 \le t \le \tau \\ \frac{1}{2t} \left\lfloor \frac{t}{\tau} \right\rfloor \sigma^2_{\Delta s,\mathrm{E}}(\tau) + \frac{1}{2t}\, \sigma^2_{\Delta s,\mathrm{E}}\left(t - \left\lfloor \frac{t}{\tau} \right\rfloor\right) & \text{for } t > \tau\,. \end{cases} \tag{V.2}$$

In Fig. V.1 b), $\overline{D}(t)$ is schematically shown for two periods. It starts at D_0 and behaves similar to the short-time diffusion for an initial quench (Sec. IV). Its behaviour alters when the external potential is changed for the first time at $t = \tau$.

[1] A Markov chain is a stochastic process, where future states are independent of past states [269].

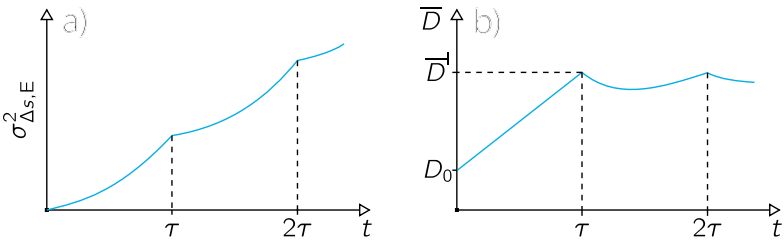

Figure V.1: Schematic illustration of Eqs. V.1 and V.2 in a) and b) drawn as solid lines, respectively. Times at which the external potential is changed, $i\tau$, and long-time diffusion coefficient, $\overline{D}$, are marked as dashed lines.

Instead of periodic growth as seen for $\sigma^2_{\Delta s,E}(t)$, the diffusion coefficient shows oscillatory traits as time proceeds. This behaviour results in a long-time diffusion coefficient $\overline{D} = \sigma^2_{\Delta s,E}(\tau)/2\tau$.

Similar to the simulations presented in Sec. IV, Brownian dynamics simulations were conducted using a Gaussian-distributed potential [253]. The potential roughness was kept constant with $\sigma_U = 4.05\,k_B T$ (cf. Fig. IV.6), while realisations of $U(s)$ were changed in a Markovian way for different periods, τ. Results for each τ were averaged over 100,000 non-interacting particles, which were placed randomly before the start of each simulation run.

2 Measuring the Dynamics

As in Sec. IV, the SLM setup was used to impose a one-dimensional random energy landscape onto colloids. Thus, samples were prepared with D_2O as the dispersion medium and particles with $R = 1.4\,\mu m$ forming quasi-two-dimensional layers at the upper wall of the sample cell (cf. Sec. III.1). The random one-dimensional potential was again created by using the four-ring pattern discussed in Secs. III.2.1.2, III.2.1.3 and IV.3 while only taking into account particles that were situated in the outermost ring, R0. The laser power, P_L, was kept at 1010 mW, corresponding to

$\sigma_U = 4.05\, k_\mathrm{B}T$ (cf. Sec. IV). With the aid of an IDL routine, particles whose surfaces come closer to each other than R were excluded from analysis, leading to an average line fraction $\varphi_l = 0.08$. Hence, colloids are treated as single particles.

To realise a time-varying one-dimensional random potential, a sequence similar to the one presented in Fig. IV.4 was used. It started with the same two-ring pattern as a marker for 30 seconds. Then, the four-ring pattern was varied with a defined period, $0.2\,\mathrm{s} \leq \tau \leq 100\,\mathrm{s}$, for $t_\mathcal{O} = 900\,\mathrm{s}$. During this time, the light field was switched to a different independent realisation after τ by an IDL routine, which sent a signal to the SLM. The Gerchberg-Saxton algorithm was used to calculate 100 independent realisations with each having a different random phase, $\Phi^{(0)}$, as input (cf. Fig. II.18). After the varying potential had been applied for 900 seconds, a second marker indicated the end of a measurement for 30 seconds. During the whole sequence, particle motion was recorded with 10 FPS, equivalent to $\Delta t_\mathrm{min} = 0.1\,\mathrm{s}$. After a sequence, the FOV was moved to a different spot inside the sample cell to start a new measurement. At least 25 measurements were conducted for each τ. This summed up to a minimum of 1500 particles over which quantities were averaged.

With the aid of the markers used in the sequence, only particle motion observed during the time the varying four-ring pattern light field was imposed on the particles, $t_\mathcal{O}$, was analysed. Subsequently, particle trajectories were cut according to the starting point of a period as is schematically depicted in Fig. V.2. If a trajectory started at the beginning of τ it would not be modified at all. If a trajectory started somewhere in the middle of a period, however, it was truncated so that its starting point coincided with the beginning of the next period, i.e. the next realisation of the light field. Then this trajectory was shifted to the very start of the measurement. That way, all trajectories began at the start of a measurement without affecting their time line with respect to the varying external potential. This could be done since all potential realisations were independent and the sample was recurringly quenched (cf. Sec. V.1). Subsequently, all preprocessed trajectories were analysed to obtain ensemble-averaged dynamics quantities using perimeter s introduced in Fig. IV.3.

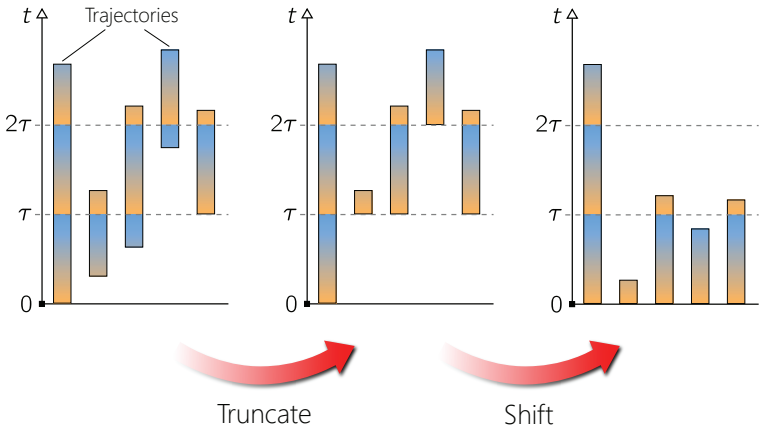

Figure V.2: Schematic illustration of the handling of trajectories. They are truncated so that they start at the beginning of a period, τ. Then they are shifted to make all trajectories start at $t = 0$.

3 Dynamics of Colloids in Periodically Varying One-Dimensional Potentials

Similar to the experiments on the quenched one-dimensional system discussed in Sec. IV, the diffusion coefficient, $\overline{D}(t)$, is the central quantity here. Figure V.3 shows measured (symbols), simulated (coloured lines) and theoretical (black lines and symbols) $\overline{D}(t)$ for varying periods, τ. Measurements are not fitted to results, but are scaled with $t_F = 0.42\,\mathrm{s}$ and $D_0 = 0.06\,\mu\mathrm{m}^2/s$, which are obtained from experiments on the quenched system (Sec. IV). Theory results were calculated according to Eq. V.1: $\sigma^2_{\Delta s,\mathrm{E}}(t \leq \tau)$ for a one-time quenched system at $\sigma_U = 4.05\,k_\mathrm{B}T^2$ was periodically added up for each τ to obtain $\sigma^2_{\Delta s,\mathrm{E}}(t)$. The overall almost perfect agreement between simulations and theory in Fig. V.3 shows the validity of Eq. V.1. Furthermore, measurements agree well with simulations and

[2] Light blue curve in Fig. IV.6 a).

theory. As results were only scaled, not fitted, this corroborates the reliability of the used system and setup as well as the values obtained for t_F and D_0.

In Fig. V.3, diffusion coefficients are plotted in two different ways to show different aspects of particle dynamics in a varying one-dimensional potential. First, Figs. V.3 a) and b) show that diffusion for intermediate and long times can be enhanced for certain values of τ. As a benchmark, the diffusion coefficient $\overline{D}(t) = \overline{D}_{\tau=\infty}(t)$ for a system quenched once, i.e. $\tau \to \infty$, with the same σ_U is plotted with a grey line and symbols. For $\tau \neq \infty$, $\overline{D}(t)$ follows the behaviour of $\overline{D}_{\tau=\infty}(t)$ for short times. When the realisation of the potential is changed at $t = \tau$, $\overline{D}(t)$ starts oscillating. These oscillations result in an increased long-time diffusion coefficient, $\overline{D}^{|}(\tau)$, compared to $\overline{D}_{\tau=\infty}(t \gg t_F)$. When τ is decreased, oscillations of $\overline{D}(t)$ become less pronounced but $\overline{D}(t)$ itself increases. This trend reaches its peak at $\tau = \tau_0 = 12\, t_F$, where τ_0 is referred to as the optimal period. Figure V.3 b) shows that the behaviour is partly reversed for $\tau < \tau_0$: a further decrease of τ results in shallower oscillations. The diffusion coefficient, however, does not rise further but successively decreases and oscillates around $\overline{D}(t) \approx D_0$ for the smallest τ.

In Fig. V.3 c), results shown in Figs. V.3 a) and b) are normalised by τ instead of t_F. It indicates that $\overline{D}(t)$ shows a rather constant behaviour for its values at the points in time where the external potential is changed, i.e. at $t = 1 \ldots 5\, \tau$. Thus, $\overline{D}_5(\tau)$ is introduced as a surrogate for the inaccessible $\overline{D}^{|}(\tau)$ here. It is the averaged diffusion coefficient of the first five periods:

$$\overline{D}_5(\tau) = \frac{1}{5} \sum_{i=1}^{5} \overline{D}(i\tau)\,. \tag{V.3}$$

Figure V.4 shows $\overline{D}_5(\tau)$ for measurements and simulations. The error bars represent the standard deviation for averaging the first five $\overline{D}(i\tau)$ values. Both measurements and simulations agree well and show a resonance curve-like behaviour. This can be explained by the interplay of particle diffusion and periodic change of $U(s)$: for large τ, the diffusion coefficient $\overline{D}_5(\tau)$ is relatively low. At the beginning of each measurement, particles are randomly distributed and dynamics fol-

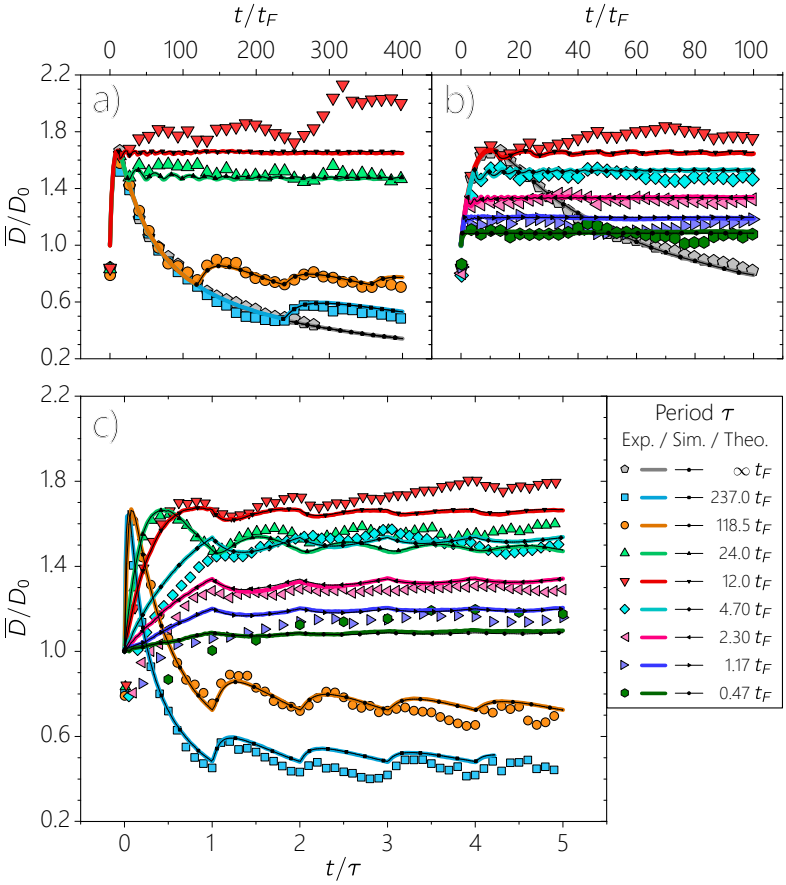

Figure V.3: Time-dependent diffusion coefficients, $\overline{D}(t)$, of measurements (symbols), simulations (lines) and theory (connected black symbols) for colloidal particles in a one-dimensional random potential varied with period τ, normalised by D_0. In a) and b), time is normalised by t_F. Results are spread over two graphs for clarity. The same results are shown in c) with time normalised by τ.

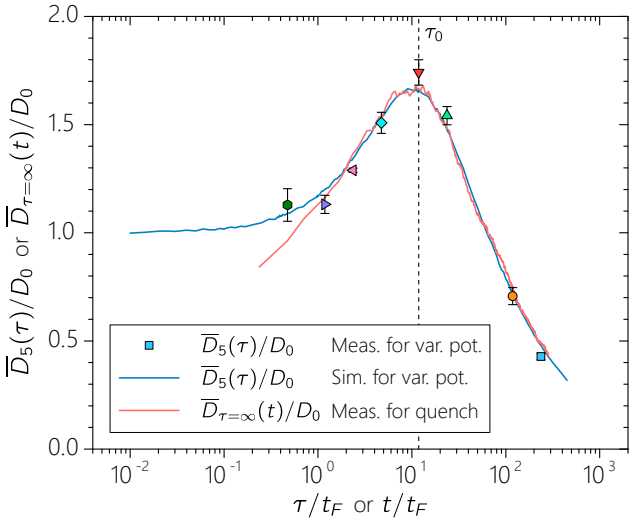

Figure V.4: Period-dependent diffusion coefficients at the first five changes of the external potential, $\overline{D}_5(\tau)$, and time-dependent diffusion coefficient of a once-quenched system, $\overline{D}_{\tau=\infty}(t)$. Results of $\overline{D}_5(\tau)$ are shown for measurements and simulations, whereas only the measured $\overline{D}_{\tau=\infty}(t)$ is shown. Symbol shapes and colours correspond to those used in Fig. V.3.

low $\overline{D}_{\tau=\infty}(t)$ as colloids relax into potential minima after the quench. At $t = \tau$, a new realisation of $U(s)$ is introduced. In relation to this new realisation, particles are again randomly distributed and quenched since the minima of the previous realisation are not correlated with those of the new realisation. Therefore, $\overline{D}(t)$ temporarily increases before dropping to the value it had already reached at $t = \tau$. As τ is large, particles relax into minima, i.e. their diffusion becomes hindered after they have been sped up by the quench. When τ is decreases, the time during whicht particles can react to the external potential also decreases. Diffusion inside potential minima is reduced in time, thus, $\overline{D}(t)$ and equivalently $\overline{D}_5(\tau)$ exhibit larger values. This development displays a climax at the optimal period, τ_0. At $\tau = \tau_0$, diffusion is hindered the least at the potential minima: particles

react to the external potential resulting in enhanced diffusion like they do when $\tau > \tau_0$. Once their fastest diffusion is reached, however, a new realisation of $U(s)$ is introduced, quenching the particles again. No relaxation process at the potential minima occurs for the majority of particles as they do not reach it before the next realisation is introduced. This leads to a maximum in $\overline{D}_5(\tau)$ with diffusion more than 1.5 times faster than D_0. The optimal enhancement of diffusion, i.e. when $\tau = \tau_0$, should be related to the time particles need to cover the correlation length of the potential, l_U. A larger l_U should lead to smaller forces exerted on the particles and thus a larger τ_0.[3] For $\tau < \tau_0$, the time particles are allowed to react to U is smaller than the optimal time τ_0. Potential minima can only be partly exploited by particles to speed up their diffusion. Thus, the smaller τ becomes, the less pronounced the effect of the quench on the particles. For the smallest $\tau = 0.47\, t_F$, the potential changes so fast that particles do not react to it at all. As a consequence, normal diffusion with $\overline{D}(t) = D_0$ is found.

Summing up the behaviour of $\overline{D}(t)$, it can be seen in Fig. V.3 that diffusion coefficients first follow $\overline{D}_{\tau=\infty}(t)$ before they develop horizontal branches at $t = \tau$, which then define $\overline{D}^{\downarrow}(\tau)$. This observation is in accordance with Eq. V.2 and leads to the conclusion that $\overline{D}^{\downarrow}(\tau)$ should behave like $\overline{D}_{\tau=\infty}(t)$. Indeed, Fig. V.4 shows that both quantities—$D_5(\tau)$, in place of $\overline{D}^{\downarrow}(\tau)$, plotted as a blue line and $\overline{D}_{\tau=\infty}(t)$ plotted in red—show the same behaviour except for very small τ. Thus, measurements and simulations fully confirm the theory presented in Sec. V.1.

The second aspect, besides the long-time behaviour of $\overline{D}(t)$, is its oscillatory behaviour. A closer look at Fig. V.3 c) indicates differently shaped diffusion coefficient curves for $\tau > \tau_0$ and for $\tau < \tau_0$. While oscillations in $\overline{D}(t)$ are concave for large τ, exhibiting their local minima at multiples of τ, small values of τ result in convex oscillations with their minima within each period. These two cases are schematically illustrated in Fig. V.5 a). To quantise this qualitative observation,

[3] It is assumed that the light intensity is kept constant in that context.

the first derivative of the normalised diffusion coefficient at $t = \tau$, $\partial_{\overline{D},\tau}$, is used:

$$\partial_{\overline{D},\tau} = \left. \frac{\partial \frac{\overline{D}(t)}{D_0}}{\partial \frac{t}{t_F}} \right|_{t=\tau} . \tag{V.4}$$

In practice, $\overline{D}(t)/D_0$ is linearly fitted in the interval $\tau \leq t \leq 1.1\tau$ for each τ. The slope is taken as $\partial_{\overline{D},\tau}$ (Fig. V.5 a)) and the results can be seen in Fig. V.5 b). For $\tau \ll \tau_0$, the derivative is zero. Oscillations are shallow as can be seen in Fig. V.3. When τ approaches τ_0, $\partial_{\overline{D},\tau}$ becomes negative, thus indicating a convex shape of oscillations. Derivatives are still negative at $\tau = \tau_0$ but show a rising trend and eventually become positive at $\tau \approx 2.5\tau_0$. For any period larger than $2.5\tau_0$, $\partial_{\overline{D},\tau} > 0$ and thus concave oscillations are found. The reason for convex and concave shapes of $\overline{D}(t)$ lies in the situation in which particles find themselves just before the external potential is changed. It is schematically shown in Fig. V.3 c): for $\tau < \tau_0$, particle diffusion is in the course of being sped up by the quench when $U(s)$ is changed (short red arrows). After the change, particles are randomly distributed inside the new realisation of the potential. On average, this leads to more particles being slowed down by the change of the potential than sped up: particles are in the course of being driven by the potential before this process is interrupted by the change of the potential realisation. This results in a decrease of the diffusion coefficient and $\overline{D}(t)$ drops at every multiple of τ leading to a convex shape. The opposite is true for $\tau > \tau_0$ as particles have time to react to the change in $U(s)$. The diffusion coefficient is temporarily enhanced (red arrows) until particles relax in a potential minimum and $\overline{D}(t)$ drops (grey arrows). When the realisation of $U(s)$ changes, most particles are trapped inside a minimum. Thus the new realisation leads to an increase of the diffusion coefficient. Based on the shape of $\overline{D}(t)$ it can therefore be inferred whether the applied τ is larger or smaller than τ_0.

To conclude, the energetic input caused by the varying external potential is considered. Figure V.6 a) shows the average energy gained by the particles due to the change of $U(s)$, $\langle \Delta U \rangle_c(\tau)$, and the corresponding power, $\langle \Delta U \rangle_c / \tau(\tau)$.

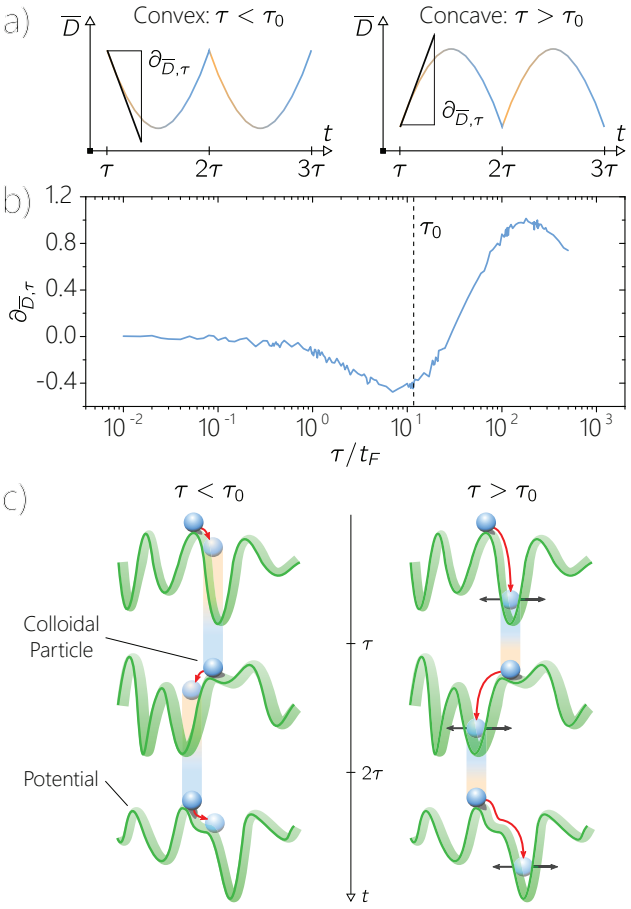

Figure V.5: Illustrations and calculations regarding the shape of $\overline{D}(t)$ for a varying period, τ. a) Schematic illustration of different curve shapes of $\overline{D}(t)$ for $\tau < \tau_0$ and $\tau > \tau_0$. Additionally, the definition of the slope at $t = \tau$, $\partial_{\overline{D},\tau}$, is outlined. b) Period-dependent $\partial_{\overline{D},\tau}$ calculated from simulated diffusion curves. c) Schematic illustration of various diffusive behaviours of particles inside the varying external potential for $\tau < \tau_0$ and $\tau > \tau_0$.

They are calculated from simulations by comparing the energy of all particles before and after the potential change. To normalise, the typical energy of the external potential introduced in Sec. IV.2, $E_U = \sigma_U/4.405 = 0.92\, k_\mathrm{B}T$, is used. The power is then defined by the normalised energy put into the system per normalised period, τ/t_F. Both quantities show monotonic behaviour. The energy input caused by a change of $U(s)$ first rises $\propto \tau$ (blue line) then starts to level off when τ approaches τ_0. For large periods, $\langle \Delta U \rangle_\mathrm{c}(\tau)$ still rises but with a strongly decreased rate. Accordingly, the power is constant for small τ. Since the energy starts to level at around $\tau \approx \tau_0$, the power starts to decrease. At large τ, the almost constant behaviour of energy causes a decrease in $\langle \Delta U \rangle_\mathrm{c}/\tau(\tau)$ that seems to approach an asymptotic slope $\propto \tau^{-1}$. The reason for the behaviour of $\langle \Delta U \rangle_\mathrm{c}(\tau)$ and the ensuing shape of $\langle \Delta U \rangle_\mathrm{c}/\tau(\tau)$ again stems from the interplay of changing realisations of $U(s)$ and particle diffusion therein, as schematically shown in Fig. V.5 c): for $\tau < \tau_0$, the energy linearly rises with τ. Particles diffuse towards the potential minima during τ. The more time they are allowed to diffuse towards minima, the more energy they gain when $U(s)$ is changed. This relation changes at $\tau \approx \tau_0$. Most particles are on the verge of reaching potential minima within τ_0. Thus, a larger τ does not necessarily result in a larger gain in energy. Since $U(s)$ is a random potential, the transition from $\langle \Delta U \rangle_\mathrm{c}(\tau) \propto \tau$ to $\langle \Delta U \rangle_\mathrm{c}(\tau) \approx$ const. does not occur exactly at τ_0 but extends over several orders of magnitude. As the observed power is deduced from $\langle \Delta U \rangle_\mathrm{c}(\tau)$, its behaviour can be explained using the same logic.

From Figs. V.3 and V.6 a), it could be inferred that a change of the realisation of $U(s)$ is most efficient when $\overline{D}_5(\tau)$ is at its maximum and $\langle \Delta U \rangle_\mathrm{c}(\tau)$ starts to level, i.e. when $\tau = \tau_0$. In order to check this, the efficiency parameter $H_\mathrm{c}(\tau)$ is introduced and calculated for the simulations:

$$H_\mathrm{c}(\tau) = \frac{\text{gained diffusion power}}{\text{applied power due to change of } U(s)} = \frac{(\overline{D}_5(\tau) - D_0)\xi_0/t_F}{\langle \Delta U \rangle_\mathrm{c}/\tau(\tau)}\,. \quad \text{(V.5)}$$

In Fig. V.6 b), $H_\mathrm{c}(\tau)$ obtained from simulations is plotted. For very small τ, the efficiency is nearly zero indicating that there is no difference between Brownian

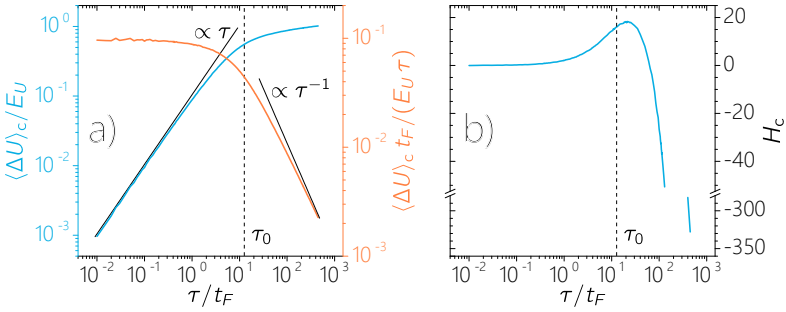

Figure V.6: a) Period-dependent average energy gained by the particles with every change of the external potential, $\langle \Delta U \rangle_c(\tau)$, and the corresponding power, $\langle \Delta U \rangle_c / \tau(\tau)$. b) Period-dependent efficiency parameter, $H_c(\tau)$, defined by Eq. V.5. Quantities are normalised by the typical energy of $U(s)$, E_U and the characteristic time, t_F.

motion and diffusion inside the varying potential. Large values of τ result in a negative H_c due to $\overline{D}_5(\tau)$ lying below D_0. Moreover, it shows that the highest efficiency is obtained for $\tau \approx \tau_0$. However, the maximum of $H_c(\tau)$ lies slightly above τ_0. This might stem from the extended transition region in $\langle \Delta U \rangle_c / \tau(\tau)$ caused by the randomness of $U(s)$. Some particles might be trapped at the end of each period when $\tau \gtrsim \tau_0$, resulting in a diffusion coefficient sightly smaller than $\overline{D}_5(\tau_0)$. However, a value of τ slightly larger than τ_0 amounts to a relatively strong decrease in $\langle \Delta U \rangle_c / \tau(\tau)$ and thus results in the highest efficiency. Thus, the fastest diffusion is found for $\tau = \tau_0$ but it is slightly more efficient when a larger amount of particles have reached a local minimum inside the potential.

4 Discussion

Particle motion with an enhanced diffusion coefficient as found here is also found in biased diffusion in an external potential [212, 270, 271] (see also Sec. VI), where the bias compared to the potential strength typically defines the enhancement of diffusion. Another example is ratchet potentials (Brownian motors) [272–

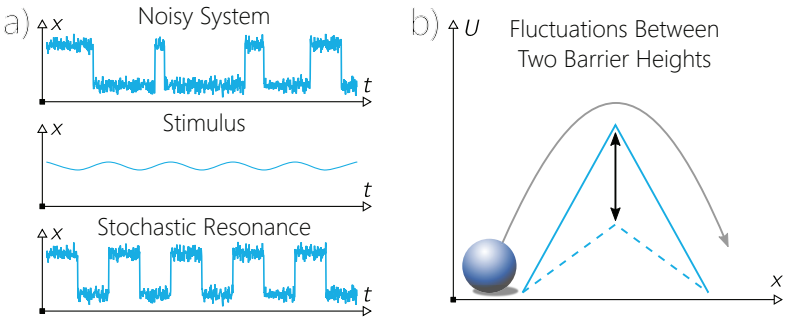

Figure V.7: Schematic illustration of stochastic resonance and resonant activation. a) A noisy system that fluctuates in x over time, t, is exposed to a small sinusoidal stimulus. At stochastic resonance, the system switches states according to the stimulus. b) A triangular barrier, U, fluctuates in time between two heights. a) Redrawn from [280]. b) Based on [263].

274]. Besides enhanced diffusion, directed transport is often seen in these systems [275, 276]. An integral part of ratchet systems is the resonance between the change of the external potential and diffusion. Such resonance curve-like behaviour is also seen in Fig. V.4.

Two prominent mechanisms in this context are stochastic resonance and resonant activation, which are caused by different mechanisms but can be found for similar experimental situations [277]. Stochastic resonance was first described by Benzi, Sutera and Vulpiani in 1981 [262]. It was used to describe climate change [278] and subsequently connected to diffusion in ratchet systems [279, 280]. In stochastic resonance, noise leading to random switching between states is aided by a small external stimulus [281].[4] It is schematically depicted in Fig. V.7 a), where a noisy system fluctuates in time, t, between two spatial states, denoted as x. It is exposed to a small sinusoidal stimulus. Maximum synchronisation of stimulus and reaction of the exposed system is called stochastic resonance [282]. A typical situation would be a Brownian particle situated in one of two adjacent op-

[4] There is an optimal combination of noise and stimulus [281].

tical traps [277]: by additionally exposing the particle to a periodic force with a certain frequency, particle jumps from one trap to the other can be synchronised with the periodic force. The situation presented in this chapter, namely the periodic variation of a random potential, however, is different from stochastic resonance. As a random potential is used, there is no well-defined synchronisation process between τ and the motion of particles. The optimal period, τ_0, is not a reliable indicator in this context, as fastest diffusion is not necessarily correlated with stochastic resonance [277].

Resonant activation, on the other hand, describes a thermally driven particle surmounting a randomly fluctuating barrier [283, 284]. The situation of a triangular barrier changing between two heights is schematically depicted in Fig. V.7 b). Depending on the mean fluctuation frequency of the barrier in comparison to the fluctuations of the thermally driven particle, times to surmount the barrier can reach a minimum leading to a maximum in diffusion, i.e. resonant activation. This was first reported by Doering and Gadoua in 1992 [263]. This type of resonance phenomenon can be found in, e.g., myoglobin, which dynamically opens and closes gates for ligands [285]. When compared to the periodically varying random potentials discussed in this chapter, resonant activation shows similarities. In both situations, barriers change dynamically leading to a maximum in diffusion coefficients. However, the barriers used here switch between random states with a fixed rate, whereas in the generic case of resonant activation, the barriers switch randomly between two fixed states with a mean rate. Additionally, in resonant activation, barriers typically hinder diffusion and are surmounted by thermally driven particles. In the present experiment, barriers cannot only hinder particle diffusion but also enhance their motion, resulting in a maximum diffusion coefficient larger than D_0. If resonant activation is also extended to negative barriers, enhanced diffusion seems possible. Still, the thermal drive with which particles surmount a barrier is integral to resonant activation. In the present experiment on the other hand, Brownian motion would not be integral in reaching a resonance-like curve such as that shown in Fig. V.4. This can be inferred from two observations made in Secs. V.3 and IV.5. First,

from Sec. V.3, it is known that $\overline{D}_5(\tau)$ (or $\overline{D}^{\mathrm{I}}(\tau)$) behaves similarly to $\overline{D}_{\tau=\infty}(t)$. Second, in Sec. IV.5, the σ_U-dependence of $\overline{D}_{\tau=\infty}(t)$ is presented. It gets more peaked and the maximum rises linearly (cf. Figs. IV.6 a) and IV.7 a)) as σ_U is increased. Therefore, the less relevant diffusion becomes compared to σ_U, the less broad and higher peaked is the resonance-like curve found for $\overline{D}_5(\tau)$. Brownian motion does play a role in the experiment, however, it is not integral like it is for resonant activation. In conclusion, neither stochastic resonance, nor resonant activation fully resemble the situation presented here, even though resonance activation seems to be related to it.

Besides the two mentioned resonance phenomena, several studies of diffusion in dynamic potentials have been conducted and show resonance-like behaviour of the diffusion coefficient. Dubkov and Spagnolo [264, 286] theoretically considered one-dimensional periodic potentials alternating with their inverse. They found enhanced diffusion at certain frequencies for all considered potentials that have a finite first derivative—a rectangular potential only lead to a reduced diffusion coefficient. Larger potentials lead to a stronger enhancement of diffusion, even for very large barriers where Brownian motion does not play a role. This finding is in agreement with the behaviour shown in Fig. IV.6 and thus corroborates the reasoning that the presented experiment cannot be fully explained by resonant activation.

In an experimental study of diffusion through a channel of varying width [287], Bleil et al. also saw a resonant behaviour of the measured diffusion. They claimed it to be related to resonant activation albeit not identical and thus laid out an argument similar to the one presented here. Even though diffusion coefficients larger than D_0, like those shown here for τ_0, were not found, they suspected enhanced diffusion under the right conditions.

Instead of periodic potentials, Douglass et al. [139] measured and simulated particle diffusion in a randomly varying three-dimensional speckle field. Unlike here, they found superdiffusion. As the potential is similar to the one described in this thesis, either the additional dimensions or the method of changing the potential, namely a random variation that was caused by particle diffusion itself,

might be the reason for the differences in diffusive behaviour between the studies of Douglass et al. and that presented here.

An experimental study using a varying potential very closely resembling the one described in this thesis was conducted by Bianchi et al. [288]. They also used a one-dimensional random potential created by light through an SLM. When varying it, they found resonance-like behaviour with enhanced diffusion. However, unlike here, the different potential realisations they used were correlated. The time with which the autocorrelation of the potential decayed was used as the variation parameter—corresponding to τ used here. Therefore, this study yielded results similar to the ones found here even though different preconditions were used.

To conclude, the resonance-like behaviour with enhanced diffusion at $\tau = \tau_0$ found for diffusing particles in a varying one-dimensional random potential shows signs of several physical phenomena. It is an interplay of D_0, l_U, τ and the absence of correlation between consecutive potential realisations, which is related to resonant activation. In the literature it was shown that enhanced diffusion is reached for correlated potentials [139]. The results presented here prove, however, that correlation is not necessary to obtain $\overline{D}^{\mathrm{I}} > D_0$. They show that diffusion can also be enhanced by periodically changing uncorrelated random potentials.

VI Colloids Dragged Through a Static Two-Dimensional Random Potential

The dynamics of colloidal particles exposed to two-dimensional random potentials has recently been investigated [135, 136, 190, 289]. It was found that inside such a potential, particle motion is diffusive for times $\Delta t \ll t_B$, followed by a transient subdiffusive behaviour for $\Delta t \approx t_B$ and Brownian motion for $\Delta t \gg t_B$. In [135, 190], the setups introduced in Secs. III.2.1 and III.2.2 were used to create two-dimensional random potential landscapes by means of light. In the experiments described in this chapter, dilute colloidal suspensions were dragged in one dimension while being exposed to the two-dimensional light field created by the diffuser setup. In general, particles dragged through a medium or potential find wide applications in microrheology [290–292], sorting [293, 294] or friction [18, 295]. While many of these studies focus on periodic potentials, particles dragged through random potential energy landscapes are the focus here. The dragging force results in biased Brownian motion through these potentials. A similar system has been studied by simulations [212] and is compared to the experiments described here.

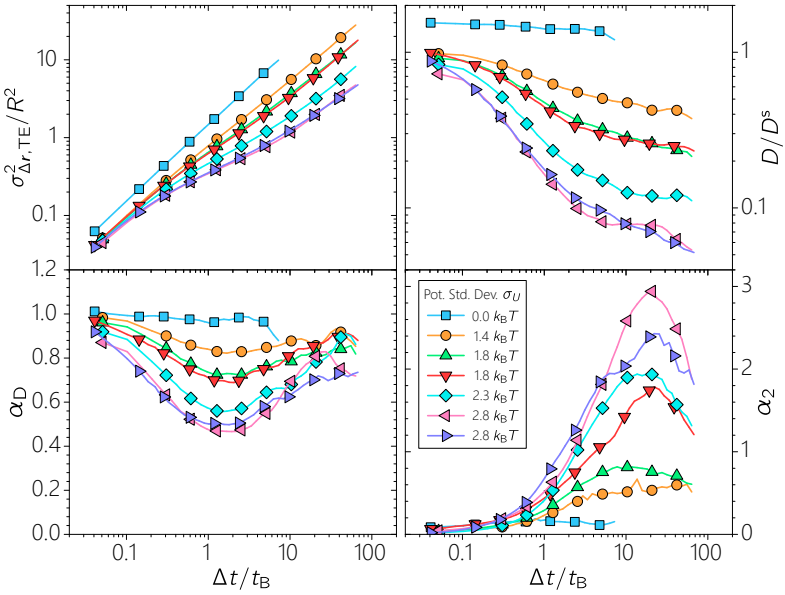

Figure VI.1: Dynamics of colloids in a two-dimensional random potential: variances of the two-dimensional displacements, $\Delta \boldsymbol{r}$, normalised by the particle radius, R, diffusion coefficients normalised by the short-time diffusion coefficient with a light field present, D^s, anomalous diffusion coefficients and non-Gaussian parameters dependent on lag time, Δt, normalised by Brownian time, t_B, for varying potential standard deviations, σ_U. Replotted results published in Ref. [135].

1 Colloidal Dynamics in a Static Two-Dimensional Random Potential

In this chapter, experiments in which particles were dragged through a static random potential are described. It is hence crucial to understand the generic case of Brownian motion without an additional dragging force in such a potential, as discussed in Refs. [135, 190, 221]. The points made in this section are based on these studies. Both the SLM and diffuser setup can be used to generate two-

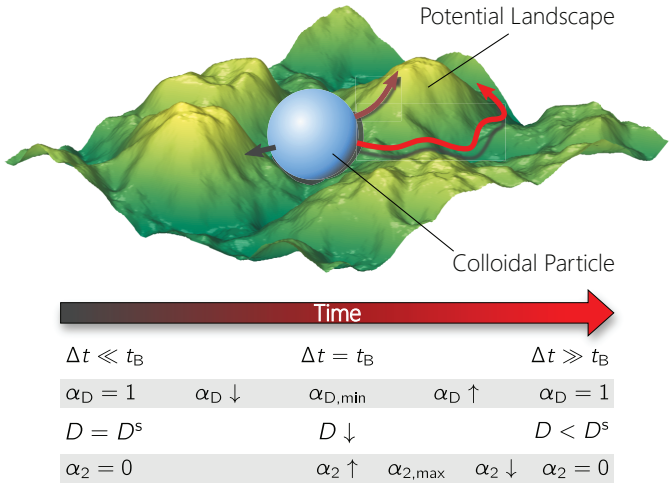

Figure VI.2: Schematic of a particle diffusing on different time scales in a two-dimensional random potential landscape. Each time scale corresponds to characteristic displacements marked by differently coloured arrows. At the bottom, time scales with qualitative behaviour of relevant quantities shown in Fig. VI.1 are given.

dimensional random potential energy landscapes. The resulting dynamics described in this section mostly stems from measurements conducted with the SLM setup [135] but are found to be similar when the diffuser setup is used [190]. The graphs in Fig. VI.1 are replotted from [135]. They show variances, $\sigma^2_{\Delta \boldsymbol{r},\mathrm{TE}}(\Delta t)$, anomalous diffusion exponents, $\alpha_\mathrm{D}(\Delta t)$, diffusion coefficients, $D(\Delta t)$, and non-Gaussian parameters, $\alpha_2(\Delta t)$, for two-dimensional displacements, $\Delta \boldsymbol{r}$, and varying potential roughnesses, σ_U. A larger σ_U corresponds to larger local forces imposed on the particles by the external potential. Roughnesses were determined by comparison of measured $\sigma^2_{\Delta \boldsymbol{r},\mathrm{TE}}(\Delta t)$ to corresponding simulation results. Particles with $R = 1.4\,\mu\mathrm{m}$ were highly diluted in D_2O—the same system described in Secs. III.1, IV and V. Hence, they can be treated as single particles.

Motion inside a two-dimensional realisation of a random potential is affected

very similar to that in one dimension described in Sec. IV.1. It is depicted in Fig. VI.2 in the same fashion as in Fig. IV.2. Diffusion is affected on different time scales and can again be divided into three regimes: $t \ll \Delta t_\mathrm{B}$, $\Delta t \approx t_\mathrm{B}$ and $\Delta t \gg t_\mathrm{B}$. All curves in Fig. VI.1 show behaviour close to normal diffusion for $\Delta t \ll t_\mathrm{B}$. When $\sigma_U > 0$, $\sigma^2_{\Delta \boldsymbol{r},\mathrm{TE}}(\Delta t)$ is shifted to lower values compared to the case where $\sigma_U = 0$. The short-time diffusion coefficient, D^s, is roughly half compared to when no light field is imposed on the particles. This is due to the scattering force that presses particles closer to the bottom of the sample cell, resulting in a smaller short-time diffusion coefficient (cf. Eq.III.3).

Besides this difference, all relevant parameters, $\alpha_\mathrm{D}(\Delta t)$, $D(\Delta t)$ and $\alpha_2(\Delta t)$, behave qualitatively in two dimensions as they do in one as can be seen by comparison of Figs. IV.1 and VI.1 [221]. Mechanisms leading to this behaviour are also similar. Particles first diffuse normally inside traps for short times marked by the dark grey arrow in Fig. VI.2. When they reach the flanks of a two-dimensional potential at $\Delta t \approx t_\mathrm{B}$, $D(\Delta t)$ starts to decrease (brown arrow). For long times, motion again becomes diffusive with $D(\Delta t) < D^\mathrm{s}$, as indicated by the red arrow. However, quantitatively there are some differences. For similar σ_U, motion is less affected by a two-dimensional random potential than it is in one dimension. Parameters show smaller extreme values. Additionally, Brownian motion for long times is reached earlier in two dimensions [221]. This is due to the additional degree of freedom particles have in a two-dimensional random potential. In one dimension, potential barriers necessarily have to be surmounted. In two dimensions, particles can either surmount or circumvent barriers. Therefore, Eq.IV.1, which predicts the long-time diffusion in a one-dimensional random potential, becomes non-applicable. Instead

$$D(t \to \infty) = D_\mathrm{b} \exp\left\{-\frac{\sigma_U^2}{2\,k_\mathrm{B}^2 T^2}\right\}. \tag{VI.1}$$

holds [296]. Compared to Eq. IV.1, its exponent is halved accounting for the faster long-time diffusion in two dimensions.

Since the dynamics in two-dimensional random potentials are similar to those

in one dimension, the models applicable for explaining this dynamics are also the same: Theoretical models implicitly referring to homogeneous media like CTRW and FBM are again not suitable as the two-dimensional random potential is heterogeneous in space (cf. Sec. II.1.4). Explaining the dynamics with heterogeneous diffusion processes, however, where the potential, $U(x, y)$, can be mapped on diffusivities, $D(x, y)$, is conceivable for a static two-dimensional random potential—similar to the situation in one dimension.

The results for particle diffusion in a two-dimensional random potential shown in Fig. VI.1 were obtained using the light field created by the SLM setup. To check whether the diffuser setup used in this chapter yields the same results, similar measurements were conducted for $P_\mathrm{L} = 917\,\mathrm{mW}$ and 2600 mW. The anomalous diffusion exponents were plotted in Fig. VI.3 together with the results shown in Fig. VI.1. Both setups yield very similar results. Curves measured in the diffuser setup follow exactly the same trend as those obtained from the SLM setup, with $P_\mathrm{L} = 917\,\mathrm{mW}$ lying between $\sigma_U = 1.4$ and $1.8\,k_\mathrm{B}T$ and $P_\mathrm{L} = 2600\,\mathrm{mW}$ being in agreement with $\sigma_U = 2.8\,k_\mathrm{B}T$. Differences are only seen for $t > 10\,t_\mathrm{B}$, where both curves measured with the diffuser setup deviate slightly from those measured with the SLM setup. These deviations originate from the use of different observation times, which can lead to deviations when time and ensemble averages are calculated (cf. Sec. III.4.6). Concluding, both setups yield comparable results for particle motion in two-dimensional random potentials. Consequently, the results presented in this chapter represent an expansion of the experiment introduced in Ref. [135].

2 Application of Constant Drag Forces to Colloidal Suspensions

From the previous section, the dynamics of colloidal particles in static two-dimensional random potentials are known. This section explains how this dynamics can be changed by applying a one-dimensional constant drag force to particles diffusing inside the random potential. In order to do so, the piezo stage

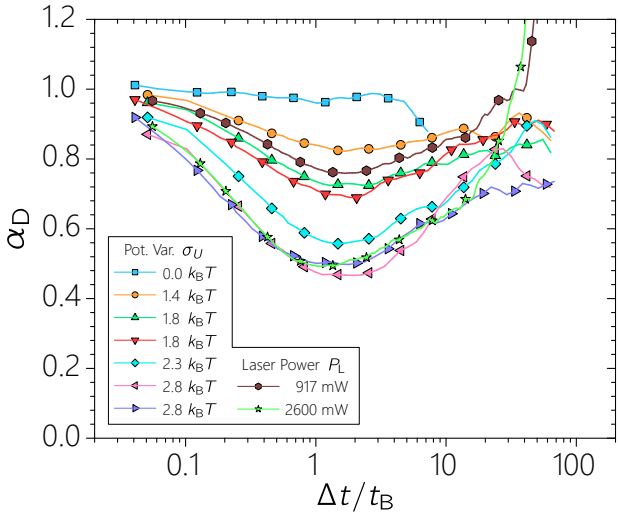

Figure VI.3: Replotted results for the time- and ensemble-averaged α_D published in Ref. [135] in comparison with results obtained from measurements conducted with the diffuser setup. The curves measured in this thesis fit well with those from [135].

of the diffuser setup introduced in Sec. III.2.2 was utilised. It can move independently in both directions perpendicular to the propagation direction of the laser light and thus in both directions of the two-dimensional layer in which particles diffuse. In each dimension, it can cover a distance of 300 µm and has a resolution of 0.6 nm [175]. By moving the sample cell with a drag velocity, v_D, a drag force, F_D, is imposed on the particles due to the friction between sample cell, dispersion medium and colloids:

$$F_D = \xi\, v_D = \frac{k_B T}{D}\, v_D\,. \tag{VI.2}$$

In the bulk, $\xi = \xi_b$, whereas close to the wall of the sample cell, where the two-dimensional particle layer is actually situated, $\xi = \xi_0$, which yields $F_D = k_B T\, v_D / D_0$ (cf. Sec. III.1).

Throughout the work outlined in this thesis, only one-dimensional drag forces

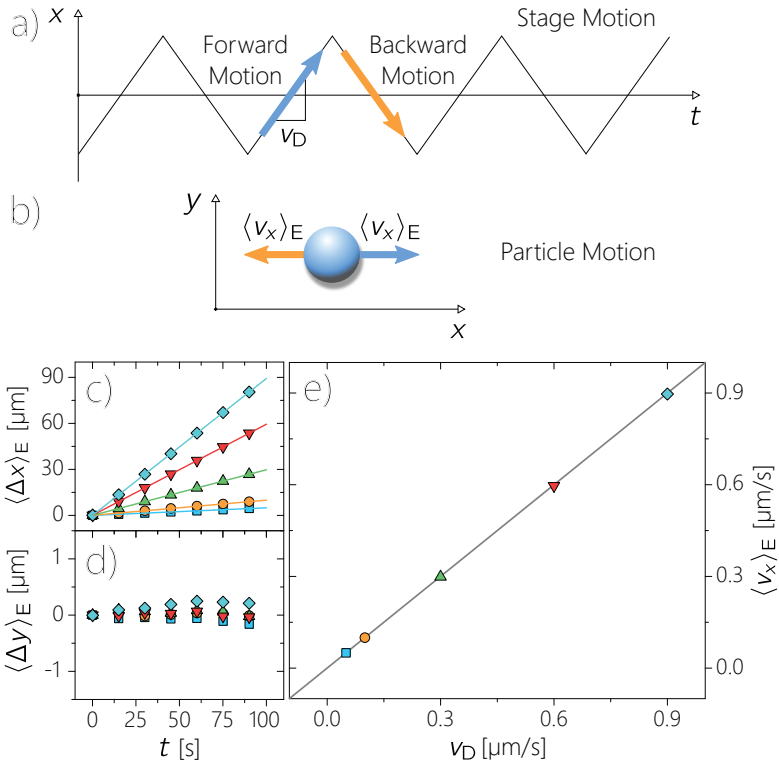

Figure VI.4: Characterisation of the drag force exerted on colloidal suspensions by movement of a piezo stage. a) A schematic of the stage movement in the x-direction dependent on time, t, is shown. b) The movement of the stage introduced in a) results in a one-dimensional time-dependent particle movement. c) Ensemble-averaged mean displacements in the x-direction, $\langle \Delta x \rangle_E(t)$, for different drag speeds, v_D, to determine $\langle v_x \rangle_E(v_D)$ of particles. d) Ensemble-averaged mean displacements in the y-direction, $\langle \Delta y \rangle_E(t)$, for different values of v_D. e) Speeds in the x-direction, $\langle v_x \rangle_E(v_D)$, determined from c). The grey line corresponds to a linear fit through the origin.

were imposed on the colloidal particles. This dimension is referred to as the x-direction. To test the ability of the piezo stage to exert forces on colloidal suspensions, several measurements with different dragging speeds, v_D, in the x-direction

were conducted. A triangular function with varying amplitude but constant frequency of 0.0015 Hz was fed to the stage with the aid of LabView software (Fig. VI.4 a)). This resulted in different constant values of v_D while keeping the periods of the oscillations constant at 666.7 s for all measurements. Each triangular period consisted of two parts: the motion from minimum to maximum called forward as it moves particles in the positive x-direction and the motion from maximum to minimum called backward (Fig. VI.4 a), b)). By cutting all particle trajectories at each extreme value, forward and backward motion could be analysed independently. Backward motion was inverted when trajectories were analysed and combined with the forward motion to improve statistics. This method rendered all dragging forces as being in the positive x-direction.

Due to the density of the dispersion medium, ϱ_M, there might have been inertial contributions to the force acting on particles, whereas viscous forces countered these contributions. The ratio of both is the Reynolds number [254, 297]

$$\mathrm{Re} = \frac{\varrho_M \, v_D^2/R}{\eta \, v_D/R^2} = \frac{\varrho_M \, v_D \, R}{\eta}, \tag{VI.3}$$

where the numerator represents inertia and the denominator viscous forces. For typical values of $\varrho_M \approx 1000\,\mathrm{kg/m^3}$, $v_D \approx 1\,\mu\mathrm{m/s}$, $R = 1.4\,\mu\mathrm{m}$ and $\eta = 1\,\mathrm{mPa\,s}$, the Reynolds number is calculated to be $\mathrm{Re} = 1.4 \times 10^{-6}$. For these conditions, inertial forces are hence much smaller than viscous forces and can be neglected. Particles move with the dispersion medium by which they are surrounded and their motion is thus overdamped [254, 298, 299]. As can be deduced from Fig. VI.4 a), the velocity of the sample cell is theoretically infinite at the turning points. In practice, it can still be relatively high and could lead to inertial contributions as Re increases with v_D. For this reason, 15 seconds before and after each extreme value of the triangular movement were excluded from analysis resulting in $\Delta t_L \leq 303.3$ s. Fig. VI.4 c)–e) show ensemble-averaged results for different values of v_D exerted on colloidal particles with $R = 1.4\,\mu\mathrm{m}$ dispersed in H_2O. Samples were prepared according to Sec. III.1, where $\varphi_A < 0.01$. Each v_D was measured three times while each measurement consisted of three oscillation periods result-

ing in an average of 18 forward and backward motions. From the mean displacements, $\langle \Delta x \rangle_{\mathrm{E}}(t)$, shown in Fig. VI.4 c), $\langle v_x \rangle_{\mathrm{E}}(v_{\mathrm{D}})$ was determined by fitting lines through the origin and extracting the slopes. As $\langle \Delta x \rangle_{\mathrm{E}}(t)$ shows linear behaviour for all v_{D} over the whole time range, inertia effects can be ruled out. Figure VI.4 e) shows the relation between drag velocity applied by the piezo stage and velocity of particles in the x-direction. The grey line has a slope of one and zero intercept, showing $\langle v_x \rangle_{\mathrm{E}}(v_{\mathrm{D}}) = v_{\mathrm{D}}$. Additionally, $\langle \Delta y \rangle_{\mathrm{E}}(t)$ is plotted in Fig. VI.4 d) revealing that there is no biased motion in the y-direction. Concluding, particles inside the sample cell follow the movement of the piezo stage, where $\langle v_x \rangle_{\mathrm{E}}(v_{\mathrm{D}}) = v_{\mathrm{D}}$ and $\langle v_y \rangle_{\mathrm{E}}(v_{\mathrm{D}}) \approx 0$. Their dynamics does not show inertia effects for the velocities applied when the turning points are excluded from analysis and can thus be considered overdamped.

3 Measuring the Dynamics

Samples were prepared according to Sec. III.1. They consisted of colloidal particles with $R = 1.4\,\mu\mathrm{m}$ dispersed in purified water which sedimented and formed a two-dimensional layer of $\varphi_A \leq 0.02$. Samples were thus dilute and colloids can be considered as single particles. As described in Sec. VI.2, constant drag velocities were created by a triangular function input to a piezo stage in the diffuser setup with different amplitudes but a constant frequency of 0.0015 Hz, resulting in $0.05\,\mu\mathrm{m/s} \leq v_{\mathrm{D}} \leq 0.9\,\mu\mathrm{m/s}$. Particle motion was recorded for about 2 h with 10 FPS, i.e. $\Delta t_{\mathrm{min}} = 0.1$ s. As already stated in Sec. VI.2, trajectories were cut after each forward and backward motion to obtain better statistics and a time window of 30 seconds about the turning points was excluded from analysis, yielding $\Delta t_{\mathrm{L}} \leq 303.3$ s. During the 30 seconds about the turning points of the stage movement that were excluded from analysis, the rotation mount that houses the Engineered Diffuser (ED, cf. Fig. III.2) was additionally rotated at a maximum speed of 20°/s. This resulted in the random light field and thus the potential rotating at the same speed. Colloidal particles could not react to the quickly moving potential as viscous forces prevented them from doing so. As a consequence, the

potential got smeared out and particles diffused as if they were free with only the scattering force acting on them (cf. Sec. V). This allowed for the particles to rearrange before each forward and backward motion and left the ED at a different position every time. In this way, each forward and backward motion can be considered statistically independent. Each trajectory then started after the rotation had been stopped and was cut just before the rotation started. Timing of these steps was done frame-wise by LabView software.

Each measurement was performed at least three times, resulting in at least 66 independent forward and backward motions, where each time around 80 particles were present in the FOV, i.e. up to about 5000 particles in total. This allows for the use of ensemble averages instead of time and ensemble averages (cf. Sec. III.4.6). Three measurements series were conducted: two with v_D varying from 0 to 0.9 µm/s and constant laser power $P_L = 917$ mW and 2600 mW, and one with P_L varying from 0 to 2600 mW and constant $v_D = 0.9$ µm/s. Since optical forces were present in almost all the measurements discussed in this chapter, D^s is used to normalise quantities instead of D_0. To determine $t_B = R^2/2dD^s$ for all measurements, $\sigma_E^2(t)$ at the smallest time, $t = 0.1$ s, was analysed in the x- and y-directions for $P_L = 917$ mW and 2600 mW as both powers were found to yield similar results. After averaging $\sigma_E^2(0.1\,\mathrm{s})$ for both directions and laser powers and dividing the result by 0.1 s, the one-dimensional short-time diffusion coefficient and the Brownian time were determined to $D^s = 0.09\,\mu\mathrm{m}^2/\mathrm{s}$ and $t_B = 10.9$ s, respectively. Short-time diffusion with particles subject to an optical field was found to be slower than D_0 as it is reduced by optical forces pressing particles against the bottom of the sample cell and reducing h to 2.0 µm. Consequently, no particles left the FOV through the third dimension during the measurements. Going further, D^s is used to calculate dragging forces via

$$F_D = \frac{k_B T}{D^s} v_D = \frac{R}{D^s} v_D \frac{k_B T}{R} = 15.6 \frac{\mathrm{s}}{\mu\mathrm{m}} v_D \frac{k_B T}{R} \qquad \text{(VI.4)}$$

and lies between 0.8 and 14.0 $k_B T/R$.

4 Dynamics of Colloids Dragged Through a Two-Dimensional Random Potential

In order to compare measurements of particles dragged through a two-dimensional random potential to those shown in Sec. VI.1 [135] and simulation results [212], quantities describing the van-Hove functions of particle displacements, such as variance and kurtosis, are used. We focus on ensemble-averaged quantities here. Results are split into constant-P_L and constant-v_D series and discussed separately for the direction parallel, x, and perpendicular, y, to the drag force. Later, results are analysed in terms of first-passage time distributions in order to shed further light on underlying mechanisms.

4.1 Constant Potential Roughness with Varying Drag Forces

At first, motion parallel to v_D, the x-direction, is considered. In Fig. VI.5, the one-dimensional variance, $\sigma^2_{\Delta x,\mathrm{E}}(t)$, the anomalous diffusion exponent, $\alpha_{\mathrm{D},x}(t)$ and the diffusion coefficient, $D_x(t)$, are shown for varying F_D, where $P_\mathrm{L} = 917\,\mathrm{mW} = P_1$ (left) and $P_\mathrm{L} = 2600\,\mathrm{mW} = P_2$ (right). Both $\alpha_{\mathrm{D},x}(t)$ and $D_x(t)$ are calculated using a smoothing filter (cf. Sec. III.4.3). The ensemble-averaged mean speed—also referred to as transport—$\langle v_x\rangle_\mathrm{E}(t)$, skewness, $\gamma_{1,x}(t)$, and normalised excess kurtosis, $\gamma_{\alpha,x}(t)$ for both powers are given in Fig. VI.6. The former is derived via $\langle v_x\rangle_\mathrm{E}(t) = \partial\langle\Delta x\rangle_\mathrm{E}(t)/\partial t$ by taking a finite difference quotient (cf. Eq. III.34). Additionally, the self part of the van-Hove function, $\mathcal{G}_{\mathrm{s,E}}(\Delta x, t)$, is plotted together with actual displacements in the x- and y-directions, also called displacement clouds, for P_1 in Fig. VI.7 and for P_2 in Fig. VI.8.[1]

When $F_\mathrm{D} = 0.0\,k_\mathrm{B}T/R$, particles qualitatively show the same behaviour discussed in Sec. VI.1 for the dynamics inside a static two-dimensional random potential. Brownian motion is found for $t < t_\mathrm{B}$ indicated by $\alpha_{\mathrm{D},x}(t)$, $D_x(t)$ and $\gamma_{\alpha,x}(t)$ in Figs. VI.5 and VI.6 and can be seen by the Gaussian fits shown with

[1] As Figs. VI.5, VI.6, VI.7 and VI.8 are equally the focus of the following, discussions of dynamic quantities are not always given together with the figure in which they can be found going further.

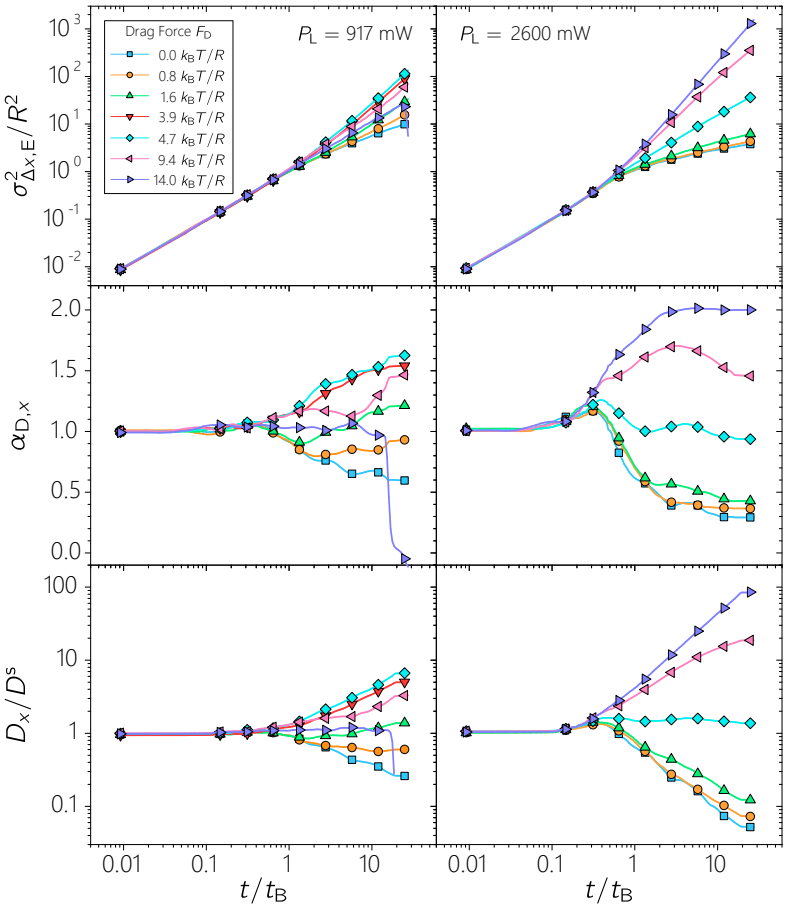

Figure VI.5: First part of ensemble-averaged results for particle dynamics in the direction parallel to v_D (x-direction) for two constant P_L and varying F_D. The left-hand side shows results for $P_L = P_1 = 917$ mW, the right-hand side for $P_L = P_2 = 2600$ mW.

dashed black lines in Figs. VI.7 and VI.8. As expected from Fig. VI.1 and [135], particles show subdiffusive behaviour at times $t > t_B$, as particles reach the flanks

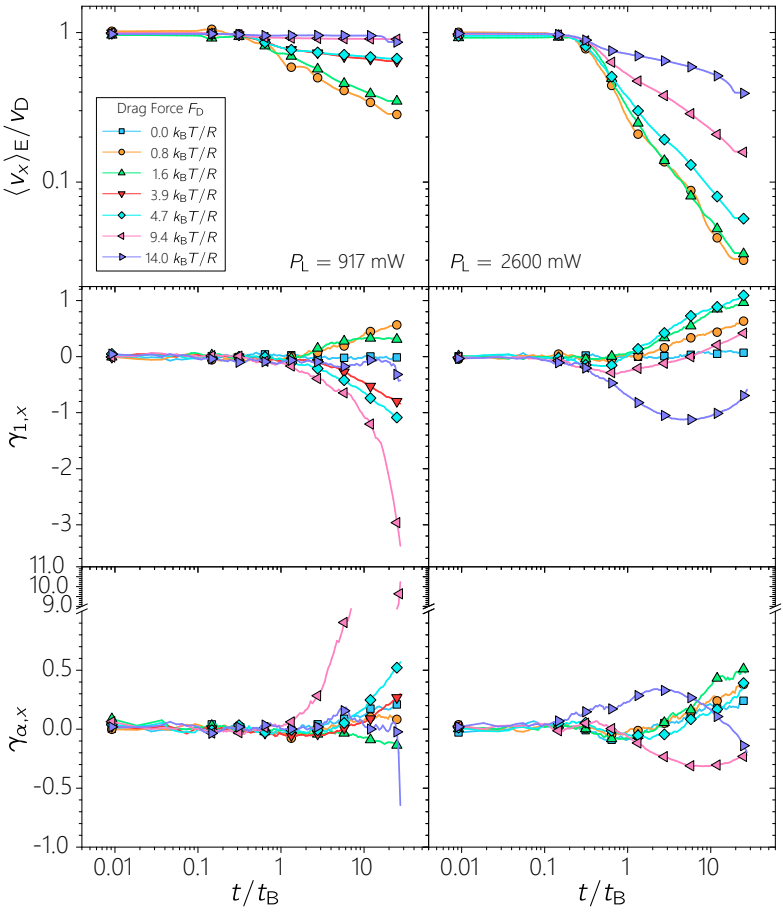

Figure VI.6: Second part of ensemble-averaged results for particle dynamics in the direction parallel to v_D (x-direction) for two constant P_L and varying F_D. The left-hand side shows results for $P_L = P_1 = 917$ mW, the right-hand side for $P_L = P_2 = 2600$ mW.

of the local minimum in which they are trapped. Higher power yields more pro-

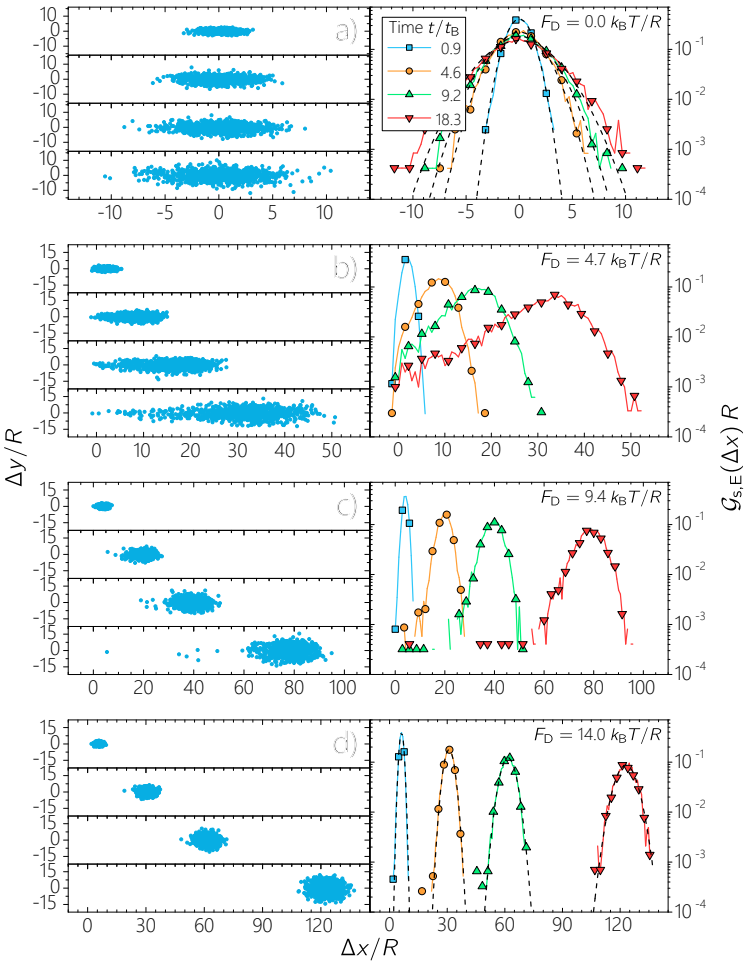

Figure VI.7: Ensemble-averaged displacement clouds (left) and van-Hove functions (right) for $P_L = P_1 = 917$ mW and four different normalised times and dragging forces: a) $F_D = 0.0\,k_BT/R$, b) $F_D = 4.7\,k_BT/R$, c) $F_D = 9.4\,k_BT/R$, d) $F_D = 14.0\,k_BT/R$.

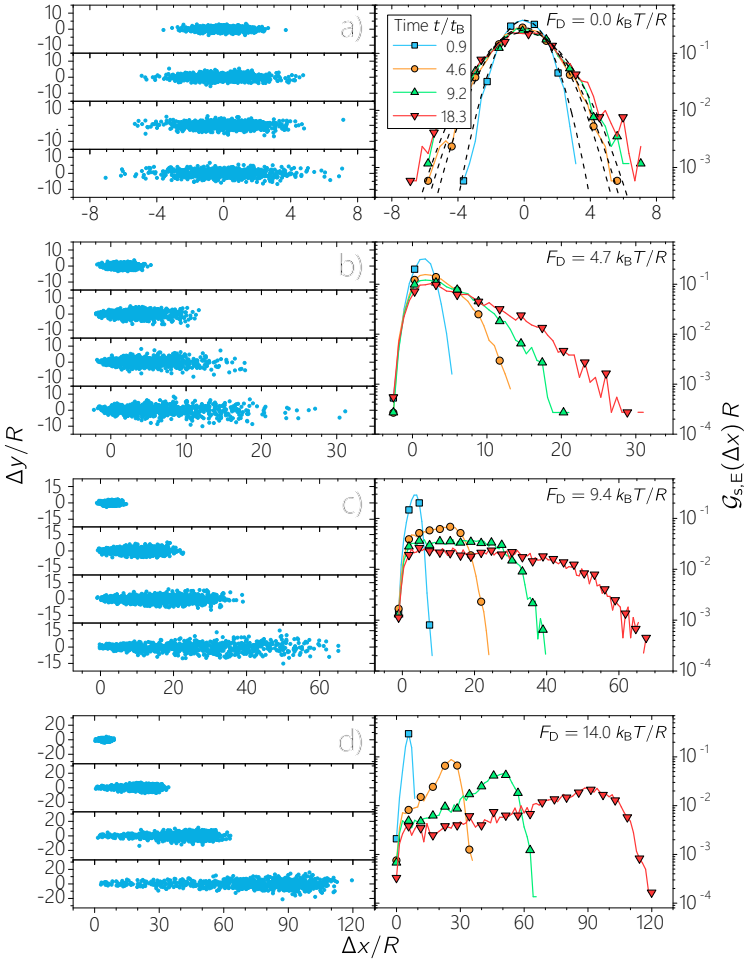

Figure VI.8: Ensemble-averaged displacement clouds (left) and van-Hove functions (right) for $P_L = P_2 = 2600$ mW and four different normalised times and dragging forces: a) $F_D = 0.0\,k_BT/R$, b) $F_D = 4.7\,k_BT/R$, c) $F_D = 9.4\,k_BT/R$, d) $F_D = 14.0\,k_BT/R$.

nounced subdiffusion as particles are less likely to escape their traps.[2] This is not only reflected in a more developed plateau of $\sigma^2_{\Delta x,\mathrm{E}}(t)$, but also in a more strongly reduced $\alpha_{\mathrm{D},x}(t)$ and $D_x(t)$. Additionally, $\gamma_{\alpha,x}(t)$ increases, since $\mathcal{G}_{\mathrm{s,E}}(\Delta x, t)$ is not Gaussian but develops pronounced tails, which can be seen in Figs. VI.7 a) and VI.8 a), where the Gaussian fits fail for $t > t_\mathrm{B}$. These tails develop because most particles are trapped in a local minimum with a few escaping their traps. Displacement clouds are symmetric in the x- and y-directions but show high concentrations around the origin. Besides the apparent subdiffusivity for vanishing drag forces at $t > t_\mathrm{B}$, $\alpha_{\mathrm{D},x}(t)$ and $D_x(t)$ also show a positive bump at $t \approx 0.5\, t_\mathrm{B}$. This bump is present in all curves but most pronounced for P_2. It stems from the particles finding the first local minimum in the external potential. The attraction of the traps is reflected in a temporarily faster diffusion for most of the particles alike, similar to the dynamics more thoroughly discussed in Secs. IV and V.

For very strong drag forces compared to the mean local maximum force exerted by the external potential, $\langle F_\mathrm{lm}\rangle$, namely $F_\mathrm{D} = 14.0\, k_\mathrm{B}T/R$ and P_1, Brownian motion is found throughout the whole measurement. When particles are dragged by v_D, the resulting force F_D is added to the forces acting on the particles due to the potential landscape. If F_D is larger than all the forces originating from the potential landscape, particles will diffuse as if they were free. As a result, $\alpha_{\mathrm{D},x}(t) = 1$, $D_x/D^\mathrm{s}(t) = 1$ and $\gamma_{\alpha,x}(t) = 0$ indicating Brownian behaviour for all times when $F_\mathrm{D} = 14.0\, k_\mathrm{B}T/R$ and P_1 in Figs. VI.5 and VI.6. Transport is not affected by the external potential landscape with $\langle v_x\rangle_\mathrm{E}/v_\mathrm{D}(t) = 1$ for the whole measurement as potential barriers are smoothed due to the dragging force. Thus, $\mathcal{G}_{\mathrm{s,E}}(\Delta x, t)$ can be fitted by a Gaussian with non-zero mean at all times as can be seen by the dashed black lines in Fig. VI.7 d). The mean then follows $\langle \Delta x\rangle_\mathrm{E}(t) = v_\mathrm{D}\, t$ proving that particles conduct Brownian motion with a constant drift and the external potential does not affect them. Hence, the corresponding particle displacement clouds are symmetric in both directions and

[2] The curves for $F_\mathrm{D} = 0.0\, k_\mathrm{B}T/R$ are based on the same data as the curves shown for both powers in Fig. VI.1. They only differ in the averages taken: here, the ensemble average is used, whereas in Fig. VI.1, the time and ensemble average is shown.

spread out due to Brownian motion only.

In between the case of no drag, where particles are clearly affected by the external potential landscape, and very strong drag, where F_D outweighs forces from the external potential, particle motion along v_D passes through three additional regimes, as found for both powers. When F_D is small compared to forces acting on the particles due to the potential landscape, only a few colloids are dragged with v_D, while most of the particles are trapped inside the random potential. This is the case for $F_D \leq 1.6\, k_B T/R$ at P_1 and $F_D \leq 4.7\, k_B T/R$ at P_2—about three times the force compared to P_1. At these values for F_D, subdiffusive behaviour is mitigated with $\alpha_{D,x}(t)$ and $D_x(t)$ not being decreased as strongly as they are for $F_D = 0.0\, k_B T/R$. Restricted motion due to the external potential is somewhat compensated by dragging forces. Yet particle transport decreases to around $1/3\, v_D$ for P_1 and $1/30\, v_D$ for P_2. Compensation of trapping forces by F_D can lead to the specific case where $\alpha_{D,x}(t)$ and $D_x(t)$—the most frequently used indicators for anomalous diffusion—indicate Brownian motion for $t > t_B$, even though particles do not behave accordingly as can be seen for, e.g., $F_D = 4.7\, k_B T/R$ at P_2 in Fig. VI.5. The positive values of $\gamma_{1,x}(t)$ and $\gamma_{\alpha,x}(t)$ in Fig. VI.6 as well as the displacement clouds and $\mathcal{G}_{s,E}(\Delta x, t)$ reveal the misleading nature of $\alpha_{D,x}(t)$ and $D_x(t)$ in these situations. The van-Hove function shows a strong bias towards positive Δx values with most particles being trapped in potential minima. Colloids that are dragged along x are also not trapped in y, leading to a displacement cloud similar to one created by an atomiser.

When F_D is about as strong as the average local maximum force applied by the external potential, $\langle F_{lm} \rangle$, particles are spread along F_D in an even fashion. It is conceivable, that some particles are trapped in the deep minima of the random potential, some diffuse as if they were free and some alternate between being trapped and escaping, which would result in an enhanced spread of the van Hove function. This behaviour might be seen for $F_D = 9.4\, k_B T/R$ and P_2, where $\alpha_{D,x}(t) \approx 1.5$ and $D_x(t) \approx 10\, D^s$ for long times indicating strong superdiffusive motion. On the other hand, transport is still highly restricted to $0.2\, v_D$. In

that context, the most telling quantity is $\gamma_{\alpha,x}(t)$. It shows highly negative values[3] for $t > t_\mathrm{B}$ and reveals the even spread of particles along x that can also be seen in Fig. VI.8 c). This type of particle motion also emphasises the points made in Secs. III.4.3 and III.4.7, namely that $\alpha_\mathrm{D} > 1$ is not necessarily caused by superdiffusive motion and should not be treated as such before having a look at $\mathcal{G}_\mathrm{s,E}$. Here, particles do not diffuse faster than normal but are spread artificially due to the external potential which partially traps them. Consequently, $\alpha_\mathrm{D}(t)$ and $D(t)$ should here be interpreted as an indicator for the spread of particles rather than their diffusion.

For drag forces stronger than $\langle F_\mathrm{lm}\rangle$, most particles follow v_D with a few being trapped. This is the case here for $1.6\,k_\mathrm{B}T/R < F_\mathrm{D} < 14.0\,k_\mathrm{B}T/R$ at P_1 and $F_\mathrm{D} = 14.0\,k_\mathrm{B}T/R$ at P_2. The simplest way to see the transition from small F_D, where most particles are trapped, to large F_D, where most particles diffuse as if they were free, is by looking at $\gamma_{1,x}(t)$. When $\gamma_{1,x}(t) > 0$, forces due to the potential are mostly larger than F_D. When $\gamma_{1,x}(t) < 0$, the opposite is true. Similar to the case where F_D is comparable to $\langle F_\mathrm{lm}\rangle$, $\alpha_{\mathrm{D},x}(t)$ and $D_x(t)$ indicate superdiffusivity at long times. A drag force, $F_\mathrm{D} = 14.0\,k_\mathrm{B}T/R$, at P_2 yields $\alpha_{\mathrm{D},x}(t) = 2$ over an order of magnitude in t showing not only superdiffusive but ballistic motion. From the last paragraph, it is known that this is due to the enhanced spread of $\mathcal{G}_\mathrm{s,E}(\Delta x, t)$ caused by trapped particles, where the seemingly ballistic case of $\alpha_\mathrm{D} = 2$ represents the fastest rate with which $\mathcal{G}_\mathrm{s,E}(\Delta x, t)$ can spread in this system. Larger potential roughnesses can thereby lead to wider spreads, i.e. stronger enhancements of $\alpha_{\mathrm{D},x}(t)$ and $D_x(t)$. Due to the relatively large F_D, transport is only decreased to about $0.6\,v_\mathrm{D}$ for P_1 and to $0.3\,v_\mathrm{D}$ for P_2. The displacement clouds as well as $\mathcal{G}_\mathrm{s,E}(\Delta x, t)$ show a left-sided tail (Fig. VI.7 b) and Fig. VI.8 d)). The overall shape of the clouds thus resembles a comet instead of the atomised-like shape seen with small F_D. As most of the particles move with v_D, a tail in $\mathcal{G}_\mathrm{s,E}(\Delta x, t)$ due to the trapped particles develops. This (temporarily) results in positive values of $\gamma_{\alpha,x}(t)$, for example for $F_\mathrm{D} = 4.7\,k_\mathrm{B}T/R$ at P_1 and $F_\mathrm{D} = 14.0\,k_\mathrm{B}T/R$ at P_2, which are more pronounced than for the case of smaller

[3] From Sec. III.4.5 it is known that γ_α has a short negative scale.

drag forces.

A very distinctive case can be found for $F_D = 9.4\, k_B T/R$ at P_1. At this combination, F_D is so much stronger than $\langle F_{lm} \rangle$ that almost all particles diffuse as if they were free. Only a tiny number of colloids are trapped (cf. Fig. VI.7 c)). This leads to $\alpha_{D,x}(t)$ and $D_x(t)$ behaving inconsistently. Neither shows a clear trend. Additionally, $\gamma_{\alpha,x}(t)$ increases dramatically, showing values 20 times as large as the second largest, while transport is almost not affected at all. This odd behaviour is less a distinct feature of the system than of the quantities used to describe it and will be talked about more when these measurements are compared to simulations.

Summarising, the motion in the x-direction passes through several different regimes depending on how strong F_D is compared to the forces caused by the external random potential. The comparison of two different laser powers shows that the characteristic regimes are in general found for every potential roughness but are more pronounced for larger σ_U. This suggests Brownian motion plays a key role, also at high F_D. It increases the probability of particles overcoming a local potential maximum depending on P_L or equivalently σ_U. Thus, Brownian motion mitigates the combined effect of F_D and $U(x, y)$ all the more when smaller σ_U are used. Additionally, it leads to larger transport for similar conditions when σ_U is smaller, e.g. $F_D = 1.6\, k_B T/R$ at P_1 and $F_D = 4.7\, k_B T/R$ at P_2.

Motion perpendicular to v_D, in the y-direction, does not show regimes as distinct as those in the x-direction, but a rather systematic reaction to drag forces. In Fig. VI.9, $\alpha_{D,y}(t)$, $D_y(t)$ and $\gamma_{\alpha,y}(t)$ are presented. As expected, particles show the exact same behaviour in y as in x for all quantities when $F_D = 0.0\, k_B T/R$. The subdiffusive motion is again more pronounced for P_2. When F_D is increased, subdiffusion is successively mitigated—as seen in the x-direction for small F_D—as indicated by $\alpha_{D,y}(t)$ and $D_y(t)$. However, no indication for superdiffusion is found. A force in the x-direction thus smooths the particle-potential interaction in the y-direction, yet does not lead to superdiffusion as it can in x. When a single particle is dragged out of a local minimum, its motion is less affected

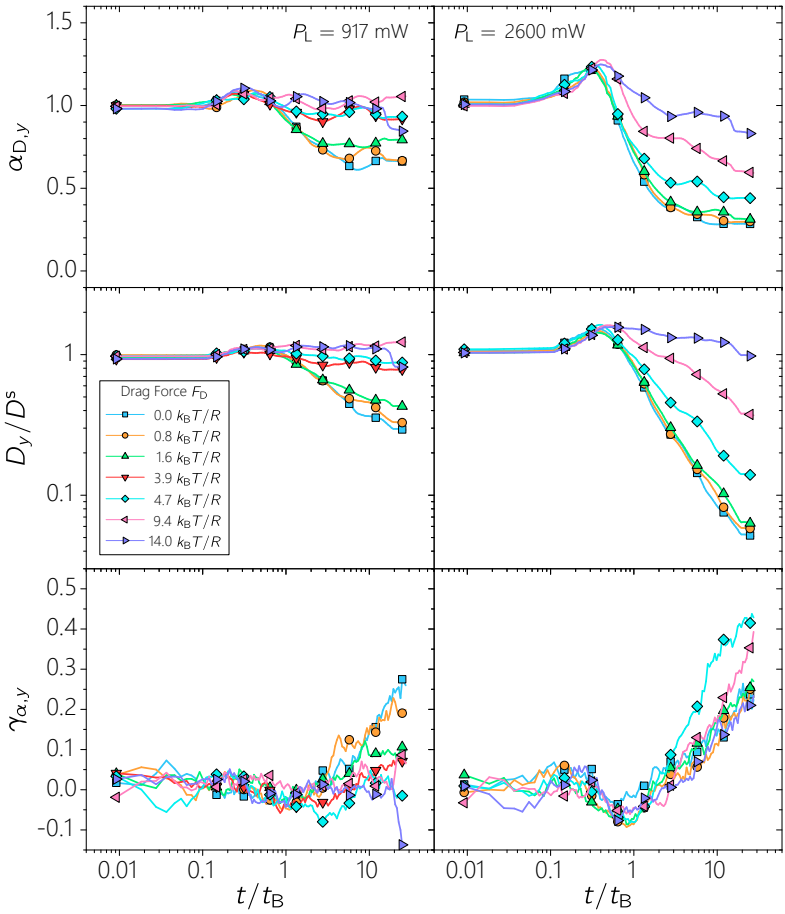

Figure VI.9: Ensemble-averaged results for particle dynamics in the direction perpendicular to v_D, corresponding to the y-direction, for two constant P_L and varying F_D. The left-hand side shows results for $P_L = P_1 = 917$ mW while on the right-hand side results for $P_L = P_2 = 2600$ mW are shown.

in both directions, reflecting a coupling between x and y. This can be seen in Figs. VI.7 and VI.8: the displacement clouds are narrow (in y) for small Δx and wider for larger displacements. A peculiar case in this respect is that for intermediate forces, $F_\mathrm{D} = 4.7\, k_\mathrm{B}T/R$ and $9.4\, k_\mathrm{B}T/R$ at P_2, where the combination of external potential and constant drag force lead to a slightly more pronounced $\gamma_{\alpha,y}(t)$ than for other values of F_D. Only few particles diffuse as if they were free and spread in the y-direction, while the majority are trapped (Fig. VI.8 b)). This leads to relatively large tails for $\mathcal{G}_{\mathrm{s,E}}(\Delta y, t)$ and thus the slight increase in $\gamma_{\alpha,y}(t)$.

For very large F_D compared to the applied external potential, e.g. $F_\mathrm{D} = 14.0\, k_\mathrm{B}T/R$ at P_1, subdiffusion completely vanishes and particles diffuse as if they were free in both directions. Figure VI.10 shows $\mathcal{G}_{\mathrm{s,E}}$ for different times t in x and y for this situation, where points correspond to the x-, and lines to the y-direction. In the x-direction, displacements were shifted by $\langle \Delta x \rangle_\mathrm{E}(t)$ to centre them about the origin. Both $\mathcal{G}_{\mathrm{s,E}}$ fall on top of each other. Particles conduct the same displacements parallel and perpendicular to v_D. They show Brownian motion with the same diffusion coefficient in x and y. Thus, when drag forces are very large, particles move independently of the external random potential landscape that otherwise couples motion in both spatial directions.

The positive bump present in $\alpha_{\mathrm{D},y}(t)$ and $D_y(t)$ for all measurements at $t \approx 0.5\, t_\mathrm{B}$ is also found for the x-direction (cf. Fig. VI.5). It originates from the same phenomenon, which also causes $\gamma_{\alpha,y}(t)$ to shortly extend to negative values[4] and is extensively discussed in Sec. IV. At the start of each measurement, particles are randomly distributed. After roughly $0.5\, t_\mathrm{B}$, most particles are attracted by a local minimum, causing them to move faster for a short period of time. This attraction manifests itself through a temporary increase in $\alpha_\mathrm{D}(t)$ and $D(t)$ and a decrease in $\gamma_\alpha(t)$ for both directions as $\mathcal{G}_{\mathrm{s,E}}(\Delta x, t)$ and $\mathcal{G}_{\mathrm{s,E}}(\Delta y, t)$ are stretched slightly.

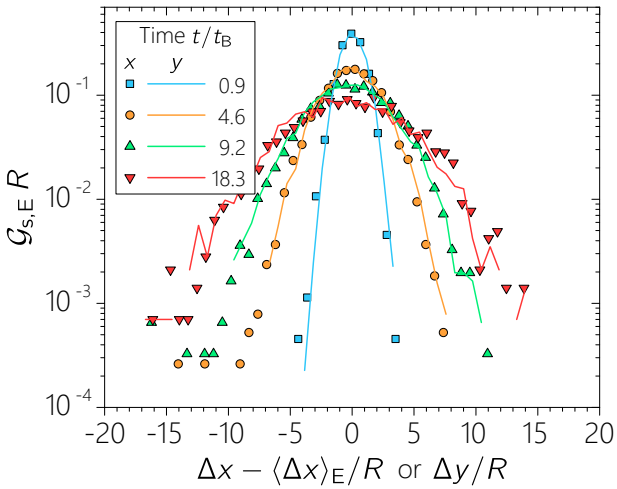

Figure VI.10: Drift-corrected van-Hove functions, $\mathcal{G}_{s,E}$, in x- and y-direction for $P_L = P_1$ and $F_D = 14.0\,k_B T/R$, i.e. the case of F_D being very large compared to forces exerted by the external potential, at different normalised times t/t_B. Symbols and lines indicate the x- and y-direction, respectively.

4.2 Constant Drag Force with Varying Potential Roughnesses

To verify the observations made for constant potential roughness and varying drag forces, the laser power was varied while the drag velocity was kept constant. The results are presented in this section. Results for $\langle v_x \rangle_E(t)$ and $\gamma_{1,x}(t)$ as well as $\alpha_D(t)$, $D(t)$ and $\gamma_\alpha(t)$ for both directions can be seen in Fig. VI.11. Due to the large v_D used here, particles tend to leave the FOV at the end of each forward and backward motion of the piezo stage. Therefore, quantities for $t \gtrsim 10 t_B$ should be interpreted with caution.

For all P_L, $\gamma_{1,x}(t) \leq 0$ indicating a left-sided tail of $\mathcal{G}_{s,E}(\Delta x, t)$. This im-

[4] The negative hump in $\gamma_{\alpha,y}(t)$ can also be seen for the x-direction. Due to the wide range of values covered by $\gamma_{\alpha,x}(t)$, it was not mentioned there.

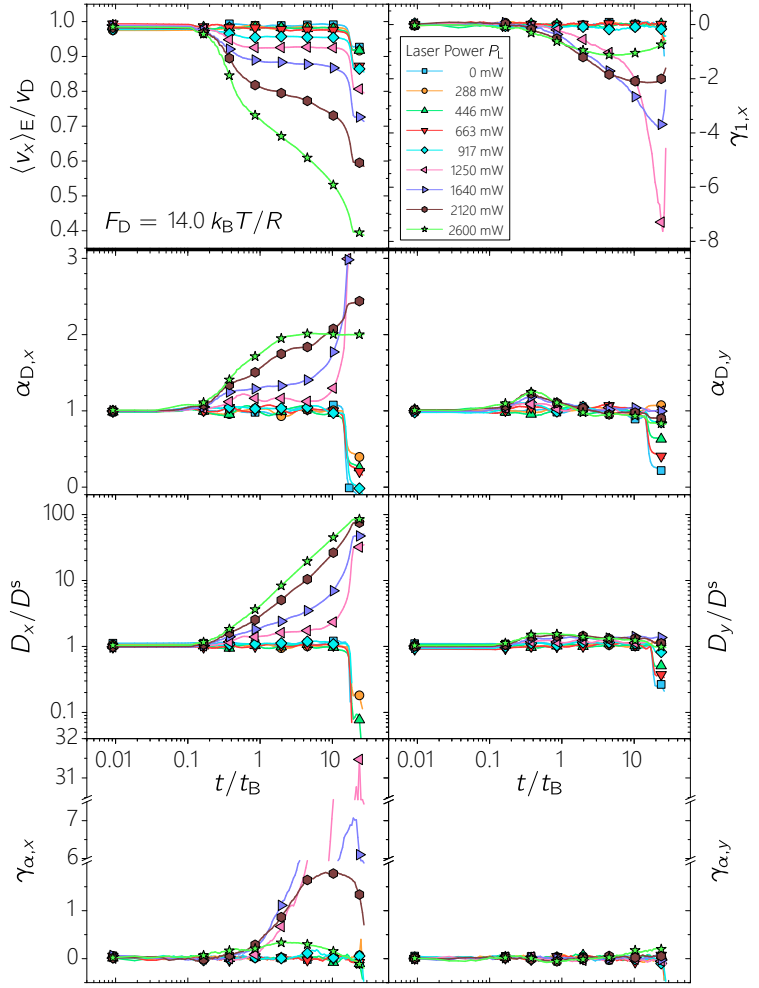

Figure VI.11: Ensemble-averaged results for particle dynamics in the x- and y-directions for $F_D = 14.0\, k_B T/R$ and varying P_L. While the top row shows quantities in the x-direction only, the lower three rows show a comparison for both directions.

plies that all the measurements shown in Fig. VI.11 fall into the regime where F_D is larger than $\langle F_{lm} \rangle$. In the previous section, this regime was found for $F_D \geq 3.9\, k_B T/R$ at P_1 and $F_D = 14.0\, k_B T/R$ at P_2. The same qualitative results found there are thus expected to be recovered in Fig. VI.11.

For $P_L \leq 663$ mW, neither the motion in the x-direction nor in the y-direction show any peculiarities. Transport, $\langle v_x \rangle_E(t)$, as well as $\gamma_{1,x}(t)$ are not affected by the external potential. Additionally, $\alpha_D(t)$, $D(t)$ and $\gamma_\alpha(t)$ indicate normal behaviour for all times in both directions. Thus, for these P_L, F_D is much larger than all the forces exerted on particles by the external potential and consequently, colloids diffuse as if they were free. For $P_L = P_1 = 917$ mW, only $\langle v_x \rangle_E(t)$ shows a slight deviation from its value for normal diffusion, v_D. The other studied parameters are unaffected. This shows that the case where $F_D = 14.0\, k_B T/R$ and $P_L = P_1$ presented in Sec. VI.4.1 is on the edge of F_D being large enough to overcome every barrier in the external potential.

For $P_L > 917$ mW, particle motion is affected in a successively stronger manner. For values of P_L slightly larger than P_1, the same behaviour as in Fig. VI.7 c) is observed: only very few particles are trapped leading to slightly diminished transport together with a highly negative $\gamma_{1,x}(t)$ and highly positive $\gamma_{\alpha,x}(t)$. The larger P_L becomes, the more the transport is reduced as particles tend to be more affected by the external potential. For the largest power $P_L = P_2$, $\alpha_{D,x}(t)$ and $D_x(t)$ show the strongest deviation from Brownian motion as already discussed in Sec. VI.4.1. The displacement cloud then shows the comet-like shape presented in Fig. VI.8 d).

In the y-direction, particles generally do not deviate strongly from Brownian behaviour. Similar to the x-direction, the effect of the external potential becomes visible for $P_L \geq P_1$, even though only light non-Brownian behaviour can be observed: an increase of P_L leads to a more pronounced bump in $\alpha_{D,y}(t)$ at $t \approx t_B$. It reflects the first time particles occupy a local minimum after being distributed randomly at the beginning of each measurement as mentioned before. Larger P_L correspond to larger forces directing particles towards potential minima. Therefore, the bump in $\alpha_{D,y}(t)$ grows when P_L is increased.

Summarising, the system is changed from a Brownian motion regime for very low P_L (Fig. VI.7 d)) via a regime where very few particles are affected by the external potential (similar to Fig. VI.7 c)) to a regime where large amounts of particles are (temporarily) trapped by the potential landscape leading to comet-like displacement clouds for the highest P_L (Fig. VI.8 d)). This reflects the same qualitative behaviour discussed in the previous section. A reason for the lack of quantitative agreement between the case of a varying drag force with constant optical forces (Sec. VI.4.1) and varying optical forces with a constant drag force presented in this section might be the presence of Brownian motion. The interplay of drag force, optical forces and Brownian motion has the effect that not only is the ratio of drag force to optical forces relevant but also their magnitude compared to the forces originating from Brownian motion. The larger F_D and P_L become, the less relevant is Brownian motion for the particle dynamics. Measurements for $F_D = 4.7\, k_B T/R$ at P_1 and for $F_D = 14.0\, k_B T/R$ at P_2 have a similar ratio of drag force to optical forces. Consequently, measured quantities show similar results for both cases. However, particles exerted to the larger potential roughness, $P_L = P_2$, show stronger effects in $\alpha_{D,x}(t)$, $D_x(t)$ and the displacement clouds. This might be due to Brownian motion being less likely to smear out the external potential for larger P_L.

4.3 First-Passage Time Distribution

Normalised first-passage time distributions in the x- and y-directions with $\Delta x = 2\,R$ for nearly all measurements presented in this chapter are shown in Fig. VI.12, where symbols correspond to experimental data. For $\Delta t > 10\, t_B$, most of them show the characteristic exponential decay caused by the finite size of the field of view during the experiment (cf. Sec. III.4.8) and should thus only be interpreted for $\Delta t \lesssim 10\, t_B$. The length, $\Delta x = 2\,R$, was chosen to lie slightly above the correlation length of the external potential, $l_U = 1.3\,R$ (cf. Sec. III.2.2.2). In Fig. VI.12 a) and c), measured first-passage time distributions in the x-direction, $\mathcal{F}_x(\Delta t)$, with P_1 and P_2 for varying F_D are shown, respectively. Coloured lines refer to Eq. III.60 with Δx, D^s and v_D being fixed inputs, which corresponds to

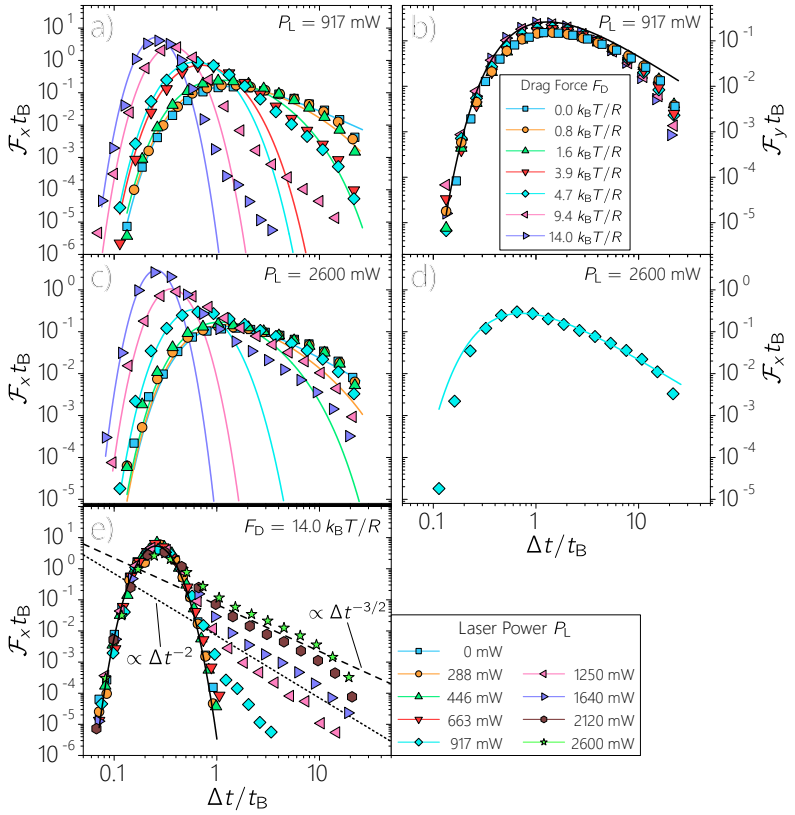

Figure VI.12: Normalised first-passage time distributions in the x- and y-directions with $\Delta x = 2R$ for varying P_L and F_D. Symbols correspond to measured $\mathcal{F}$ while lines show Eq. III.60 with fixed inputs if not stated otherwise. a) First-passage time distributions in the x-direction for $P_L = P_1$ and varying F_D. b) First-passage time distributions in the y-direction for $P_L = P_1$ and varying F_D. The black line corresponds to Eq. III.59. c) First-passage time distributions in the x-direction for $P_L = P_2$ and varying F_D. d) First-passage time distribution in x-direction for $P_L = P_2$ and $F_D = 4.7\, k_BT/R$ with a fit of Eq. III.59. e) First-passage time distribution in x-direction for $F_D = 14.0\, k_BT/R$ and varying P_L with a fit of Eq. III.60 and two different slopes indicated.

the theoretical prediction for particles undergoing Brownian motion with a drag velocity. For short times, $\mathcal{F}_x(\Delta t)$ agrees well with theory. Short Δt correspond to relatively fast diffusion, for which particles that are not strongly trapped are responsible. Thus an agreement between theory and experiment is intuitively expected for small Δt. This changes for larger Δt as $\mathcal{F}_x(\Delta t)$ shows a slower decay than theory predicts. Particles are partly trapped by the external potential leading to an increase in $\mathcal{F}_x(\Delta t)$ for larger Δt. When P_L is kept constant, this slower decay becomes more obvious for higher F_D, where $\mathcal{F}_x(\Delta t)$ partly shows a kink. The increased deviation between experiment and theory for large Δt as well as the kink indicate that there are various particle species—some diffusing as if they were free, some trapped inside the external potential. With larger F_D, the discrepancy in motion of free and trapped particles increases leading to stronger deviations from theory and a more pronounced kink in $\mathcal{F}_x(\Delta t)$.

In Fig. VI.12 b), $\mathcal{F}_y(\Delta t)$ for P_1 is shown. For other P_L, $\mathcal{F}_y(\Delta t)$ looks similar (not shown here). The black line corresponds to Eq. III.59, the theoretical prediction for particles undergoing Brownian motion without a drag velocity, with $\Delta x = 2\,R$ as an input, since there is no drag force expected in y. In general, deviations between experiment and theory are rather small. For $\Delta t < t_\mathrm{B}$, $\mathcal{F}_y(\Delta t)$ agrees well with the theory for the same reasons given for the x-direction. For large Δt, $\mathcal{F}_y(\Delta t)$ shows a slightly more slowly decaying tail for low F_D, reflecting particles being trapped inside the external potential landscape. This implies that tails decay slower than $\propto \Delta t^{-3/2}$. When F_D becomes larger, more particles reach Δx in shorter times and the tails of $\mathcal{F}_y(\Delta t)$ decay successively faster. For large drag forces, e.g. $F_\mathrm{D} = 14.0\,k_\mathrm{B}T/R$ for P_1, the external potential landscape is washed out. Consequently, almost all particles diffuse as if they were free and $\mathcal{F}_y(\Delta t \lesssim 10\,t_\mathrm{B})$ agrees well with the theory for Brownian motion.

In Fig. VI.12 e), $\mathcal{F}_x(\Delta t)$ is shown for constant $F_\mathrm{D} = 14.0\,k_\mathrm{B}T/R$. The black line corresponds to Eq. III.60 with $\Delta x = 2\,R$, D^s and v_D as fixed inputs. The dashed line indicates a decay $\propto \Delta t^{-3/2}$, which is predicted for Brownian motion for large Δt and the dotted line a decay $\propto \Delta t^{-2}$. The latter represents the threshold of finite mean first-passage times, $\langle \Delta t_{\Delta x} \rangle$, for a power-law decay: when

$\mathcal{F}_x(\Delta t)$ decays faster than $\propto \Delta t^{-2}$, $\langle \Delta t_{\Delta x} \rangle$ is finite, otherwise it is not. In a previous paragraph, it was argued that a kink in $\mathcal{F}_x(\Delta t)$ develops for large discrepancies in the motion of trapped and free particles. This can be seen in Fig. VI.12 e), too. For small P_L, the drag force dominates and $\mathcal{F}_x(\Delta t)$ does not deviate from theory. When $P_\mathrm{L} = P_1$, a relatively strong kink with a tail decaying faster than $\propto \Delta t^{-2}$ is formed (see also the blue triangles in Fig. VI.12 a)). For $P_\mathrm{L} > P_1$, and thus larger $\langle F_\mathrm{lm} \rangle$, more particles are trapped on longer time scales. The kink in $\mathcal{F}_x(\Delta t)$ becomes less pronounced but stronger tails form, which decay slower than $\propto \Delta t^{-2}$ resulting in infinite mean first-passage times. For the largest P_L, tails decay $\propto \Delta t^{-3/2}$ similar to theoretical predictions for Brownian motion. Thus, particle dynamics change from having a mean first-passage time which is finite for low P_L to an infinite $\langle \Delta t_{\Delta x} \rangle$ for high laser powers.

For the peculiar case of $P_\mathrm{L} = P_2$ and $F_\mathrm{D} = 4.7\, k_\mathrm{B}T/R$, i.e. where Brownian behaviour is indicated by $\alpha_{\mathrm{D},x}(t)$ and $D_x(t)$ (cf. Fig. VI.5), $\mathcal{F}_x(\Delta t)$ deviates by several orders of magnitude from the theoretical curve for Brownian motion with drift. Since other quantities also indicate Brownian motion for this case, a curve based on the theory of first-passage times without drift, Eq. III.59, is included in Fig. VI.12 d) with which $\mathcal{F}_x(\Delta t)$ largely agrees—especially for large Δt. However, from $\gamma_{1,x}(t)$ and $\gamma_{\alpha,x}(t)$ it is known that $\mathcal{G}_{\mathrm{s,E}}(\Delta x, t)$ is skewed for this case. The first-passage time distribution, as defined here, only focusses on displacements in the positive x-direction. Since $\mathcal{F}_x(\Delta t)$ follows the theoretical curve of Brownian motion, the dynamic behaviour of particles with displacements $\Delta x \geq 2R$ in the direction of F_D is seemingly similar to that of Brownian motion. This is also visible in Fig. VI.8 b), where $\mathcal{G}_{\mathrm{s,E}}(\Delta x \geq 2R, t)$ can be fitted by the positive half of a Gaussian function. Thus for this particular combination of P_L and F_D, particles act as if they were undergoing Brownian motion without drift.

5 Discussion

Simon et al. [212] investigated the system realised here experimentally through simulations. They integrated the underlying Langevin equations and averaged

over 400 overdamped particles and 20 realisations of the external potential. The two-dimensional external random potential was assumed to be normally distributed. Hence, it is different from the gamma-distributed potential created by the diffuser setup used here. Simon et al. claim however that the correlation length, l_U, is one of the most important features when it comes to comparing potentials. Their Gaussian potential has a correlation length of about 1 in their normalised length scale, similar to l_U for the normalised radial dimension r/R of the potential used here, which is determined to be 1.3 (cf. Sec. III.2.2.2). Furthermore, they found that qualitatively the same transport and diffusion regimes are exhibited for all the differently distributed potentials they analysed—Gaussian, exponential and power law. Thus, their findings should be comparable with the results obtained in this chapter.

Indeed, the same regimes found here are found in Ref. [212]. For very low forces compared to $\langle F_{\mathrm{lm}} \rangle$, almost all particles are trapped leading to a displacement cloud looking like aerosol coming out of an atomiser as well as subtransport and subdiffusion in both spatial directions. For very large forces, transport and diffusion are not anomalous. However, Simon et al. see a different diffusion coefficient for the x- and y-directions, which they attribute to the symmetry-breaking nature of F_{D}, which is said to smooth potential barriers along its direction. The results presented here do not show this difference in diffusion, as can be seen in Fig. VI.10. When F_{D} is larger than the forces exerted on the particles by the external potential, only forces due to Brownian motion should be acting on particles. From [212] it is not clear how the complete smoothing of the external potential barriers by a drag force in one direction leads to Brownian motion parallel to F_{D} and Brownian motion with a different diffusion coefficient in the perpendicular direction. Having the same D in both directions for very large F_{D}, like the results shown here, seems more intuitive. The external potential landscape is completely flattened by F_{D} in both directions, yielding the same situation found for dragged particles without an external random potential. Further investigation on very large F_{D} compared to $\langle F_{\mathrm{lm}} \rangle$, especially for P_2, might give more insight into this discrepancy between simulations and experiment.

Besides the two extreme regimes, two additional cases are shown in Ref. [212] that are also found here. For drag forces stronger than most of the forces exerted by the external potential, i.e. $1.6\,k_\mathrm{B}T/R < F_\mathrm{D} < 9.4\,k_\mathrm{B}T/R$ at P_1 and $F_\mathrm{D} = 14.0\,k_\mathrm{B}T/R$ at P_2, a large amount of particles are dragged from local potential minima to minima while a minority stay trapped. Simon et al. describe this situation as subtransport with superdiffusion and present qualitatively the same comet-like displacement cloud as shown in Figs. VI.7 b) and VI.8 d). As stated before, these measurements show superdiffusive features in $\alpha_{\mathrm{D},x}(t)$ and $D_x(t)$. However, this is rather due to the enhanced spread of trapped and free particles caused by F_D than the colloids themselves diffusing faster. Thus, calling this regime superdiffusive should be done cautiously.

Simon et al. also found a regime that is hard to describe by common quantities, such as D. This is also found here for P_1 and $F_\mathrm{D} = 9.4\,k_\mathrm{B}T/R$, where $D_x(t)$ fluctuates and extreme values of $\gamma_{1,x}(t)$ and $\gamma_{\alpha,x}(t)$ are found. This is caused by only a few particles being trapped while the vast majority are dragged with v_D and can be seen in the displacement clouds in Fig. VI.7 c). Even though the peculiar case where $F_\mathrm{D} \approx \langle F_\mathrm{lm} \rangle$, yielding $D_x(t)/D^\mathrm{s} \approx 1$ and $\alpha_{\mathrm{D},x}(t) \approx 1$, is not considered by Simon et al., it is likely that it can be obtained through their simulations as all other regimes found in the experiments are also found in Ref. [212]. In general, there is a very good qualitative agreement between the simulations done in Ref. [212] and the results shown here. Further investigation might lead to quantitative agreement as well and might help ruling out the contradictions in both studies.

Additionally to the simulations conducted by Simon et al., the results can be compared to a phenomenon called giant diffusion. It was first described analytically by Reimann et al. [270] and describes the anomalous behaviour of Brownian particles being subject to a tilted periodic potential. When the force due to the tilt—corresponding to F_D used here—together with the thermal energy of a particle are much smaller than the maximum force of the periodic potential, particles are trapped in the minima on virtually all time scales [169]. For very strong tilts, colloids are not affected by the external periodic potential. When the tilt ex-

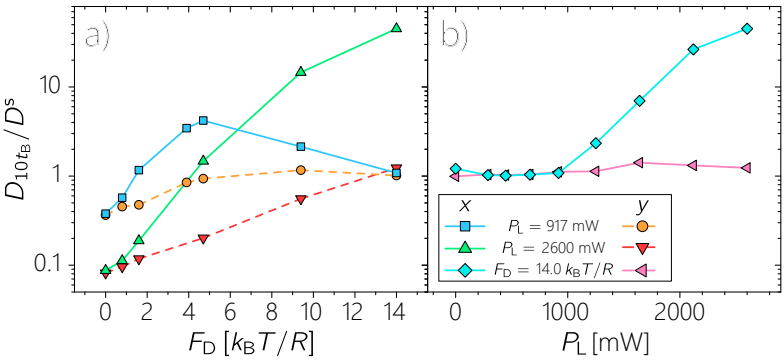

Figure VI.13: Normalised diffusion coefficients at $t = 10\,t_B$, D_{10t_B}/D^S, in x- and y-direction for all measurements presented in this chapter. The x-direction is represented by solid lines while the y-direction is shown as dashed lines.

erts a so-called critical force on the particles, however, some are able to overcome the barriers due to Brownian motion and some are not. The result is an enhanced spread in the particle displacement distribution—also referred to as $\mathcal{G}_s$—and thus an increased diffusion coefficient. This increase in D is called giant diffusion and was studied extensively theoretically [279, 300, 301] and experimentally [33, 169, 302, 303]. The larger the thermal energy, k_BT, the more blurred is the transition and the less extreme is the enhancement of the normalised D [270]. In order to visualise this behaviour, long-time diffusion coefficients, D^l, are plotted against the tilt subject to the periodic potential in the literature. This leads to curves resembling a resonance peak, where D^l/D_0 tends to 0 for small tilts and to 1 for large tilts. To compare the behaviour of colloids driven across a periodic potential to that for particles driven across the two-dimensional random potential, diffusion coefficients at $t = 10\,t_B$, D_{10t_B}, are plotted for varying F_D and P_L in Figs. VI.13 a) and b), respectively. In general, it cannot be assumed that D_{10t_B} has reached the long-time limit. Still, Fig. VI.13 gives a good overview on the qualitative dependence of the diffusion coefficient on F_D and P_L.

In the y-direction, shown as dashed lines, $D_{10t_B}(F_D)$ rises for larger F_D until it approaches D^s for the largest drag forces as expected (Fig. VI.13 a)). A larger P_L leads to a steeper slope for $D_{10t_B}(F_D)$ in this respect: particles show slower diffusion at low drag forces when P_L is high. For large drag forces, however, particle diffusion will eventually show $D_{10t_B} = D^s$. This results in a steeper increase of D_{10t_B} for larger P_L.

Diffusion in the x-direction, marked with solid lines, strongly resembles the resonance curves found for giant diffusion. For $P_L = 917$ mW, $D_{10t_B}(F_D)$ starts below D^s, rises to a maximum and then drops to D^s. The same trend with a higher maximum can be attributed to the curve for $P_L = 2600$ mW. Even though not enough data is available to fully prove that assumption, a shift of the resonance curve to higher F_D is expected when P_L increases, since larger drag forces are needed to get particles out of the traps. This trend is also found in Fig. VI.13 b). For increasing P_L and constant F_D, a larger value of $D_{10t_B}(P_L)$ is found. In giant diffusion with a periodic potential, Brownian motion acts as a random ingredient that enables particles to overcome the barriers for drag forces smaller than the force due to the potential. Without Brownian motion, there would only be a running or trapped state. When a random potential is present like it is here, there are two random ingredients—Brownian motion and the random forces by the external potential. Thus the random potential landscape should give rise to a less well-defined critical force compared to the periodic potential. As there is not just one but several randomly distributed barrier heights, a broader transition around the resonance of $D_{10t_B}(F_D)$ can be expected as well. A quantitative comparison between both potential types cannot be done at this point, but is certainly of high interest to understand the difference between colloids dragged through periodic and random potentials at comparable barrier heights.

Besides the two examples thoroughly discussed here, there are several other studies on colloids driven through potentials, such as in Ref. [304], where giant diffusion was found for a triangular potential, in Ref. [305], where the two-dimensional potential is composed of arrays of symmetric obstacles, in Ref. [273], where an enhancement of diffusion perpendicular to the driving force was found

or in Refs. [134, 171], where one-dimensional periodic potentials with maxima much larger than the thermal energy are used. Furthermore, there are theoretical studies with particles changing states from mobile to immobile, which resembles the situation presented here in rather abstract and slightly different fashion [306]. In addition to the overdamped case considered here, there are studies [214, 301, 307] on underdamped particles dragged through potentials finding stronger enhancement in diffusion in periodic potentials and a more rapid change in regime for random potentials. All of the aforementioned studies show qualitative similarities to the results shown here, e.g. an enhancement of the diffusion coefficient, which is explained here by the interplay of dragged and trapped particles that leads to an artificial spread in $\mathcal{G}_s$. A quantitative comparison is not possible however, as the situations described in the cited references partly differ substantially from the experiments presented here.

VII Binary Colloidal Suspensions in Two-Dimensional Static Light Fields

In the experiments described thus far in this thesis, systems consisting of only particle type were described. In this chapter, the contrast to binary mixtures is made, i.e. two distinctly different particle sizes. The smaller of the two—also called tracers—corresponds to the particles introduced in Sec. III.1 and have been used throughout this work. They are about a third the size of the larger species, which are referred to as obstacles. While the small colloids are always dilute, the concentration of the big ones is varied. The binary mixture of large and small particles was exposed to the light field characterised in Sec. III.10 and its dynamics are studied. The two particle species behave differently under the influence of the light field. While the smaller particles almost diffuse freely, the dynamics of the larger ones can be tuned from highly restricted to only being affected by neighbouring particles. This gives rise to a system with obstructed motion similar to a Lorentz gas. The idea of obstructed motion—small tracer diffusion affected by larger obstacles—is relevant for describing ion conductors [308], protein transport in membranes [4, 5, 309] and motion in crowded environments, such as cells [82, 310], even though biological processes are thought of as being generally more complex [6]. Results presented here were in part obtained in the course of two bachelor's theses, namely "Binäre kolloidale Dispersionen in zweidimensionalen optischen Feldern" by René Hermann and "Binäre Mischungen von Kolloiden in rauen Laser-Potentialen" by Sebastian Horstmann.

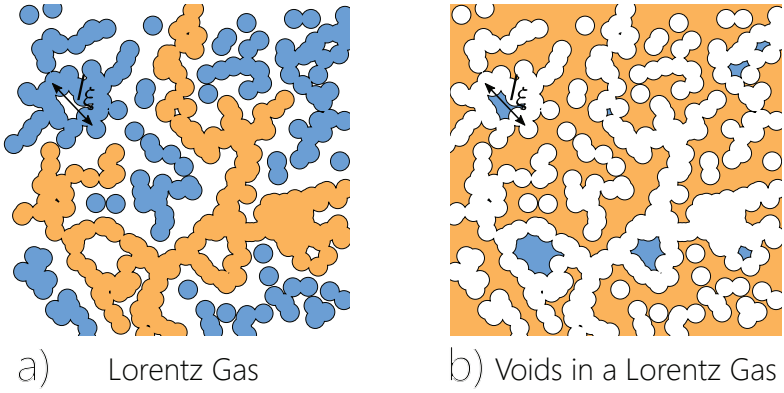

Figure VII.1: Schematic of a two-dimensional Lorentz gas and its voids. a) Finite clusters are marked in blue. The infinite cluster is orange. The characteristic length l_ξ is a measure for the size of finite clusters. b) The infinite void is marked in orange, whereas the finite voids are blue. Length l_ξ this time represents the size of finite voids. Adapted from [99].

1 Obstructed Motion: Diffusion in a Lorentz Gas

In 1905 Lorentz extended the Drude model of electrical conduction. He proposed a model of ballistic electrons, which are elastically scattered off fixed spherical atoms, where interactions between electrons do not play a role, so that electrons can be thought of as single particles [311].[1] This model is the base for what is now considered a Lorentz gas: periodic or aperiodic scatterer arrangements of two, three or more dimensions [312]. In this thesis, a Lorentz gas is defined as an infinite system of hard sphere-like scatterers, whose fixed positions are randomly distributed [5, 222]. In two dimensions, this corresponds to randomly placed discs that might also overlap, as seen in Fig. VII.1 a). Such a Lorentz gas can be described by percolation theory, e.g. as found in Refs. [5, 99, 222]. With an increasing density of obstacles, n_O, there is an increasing probability of discs overlapping. Overlapping scatterers can be summarised and called a cluster with

[1] In addition, Lorentz implicitly assumed the scatterers were of low density [312].

a typical length, l_ξ. It is typical in the sense that the probability of finding a cluster larger than l_ξ is at least exponentially suppressed [5]. Therefore, l_ξ can also be referred to as the size of the largest finite clusters [5, 222]. At a certain critical density, $n_{\mathrm{O,c}}$, a cluster spanning the whole system is formed. This is called the percolation transition as the incipient infinite cluster percolates through the infinite system. In Fig. VII.1 a) finite clusters are marked in blue, whereas the infinite cluster is orange. The latter corresponds to a fractal, which means that it is self-similar and, in two dimensions, occupies an area of

$$A_\infty(r) \propto r^{d_\mathrm{f}} \tag{VII.1}$$

within a circle of radius r, where d_f defines the fractal dimension with $d_\mathrm{f} < d$ [5]. The fractal dimension of a two-dimensional Lorentz gas can be determined to be $d_\mathrm{f} = 91/48$ [313]. The typical length, also called the characteristic length, l_ξ, can only be defined for finite clusters. Around the percolation transition, it diverges with a power law as

$$l_\xi \propto |n - n_{\mathrm{O,c}}|^{-\nu}, \tag{VII.2}$$

where ν is a critical exponent and reads $4/3$ in two dimensions [313]. For densities higher than the percolation transition, l_ξ defines the length-scale, above which the infinite cluster can be treated as homogeneous [5, 99]. Additionally, it serves as a measure for the size of finite clusters in the percolating system [99].

In this thesis, the voids arising from the arrangement of obstacles are of interest, as seen in Fig. VII.1 b). The same formalism used for obstacles in the previous paragraph can also be applied to the voids in a Lorentz gas. The quantities describing the system do not change—only the way of interpreting them. A higher n_O leads to a lower probability of finding an infinite void—exactly the opposite of what was stated in the previous paragraph. The characteristic length, l_ξ, is not interpreted as the size of a finite cluster but as the typical size of finite voids marked blue in Fig. VII.1 b), where the infinite void is shown in orange. The whole system can be thought of as being similar to a Swiss cheese: it consists of void space allowing for free transport interrupted by randomly placed obstacles [5].

Diffusion in such a system is considered as obstructed motion and is of high interest as a model for biological samples [4, 309, 314], ion-conducting glasses [315, 316], or nuclear collisions [317]. When (infinitely) small particles, called tracers, diffuse in a Lorentz gas, their dynamics is altered compared to Brownian motion due to the presence of obstacles [222, 314] as illustrated in Fig. VII.2 and briefly discussed in Sec. II.1.4. Small orange tracers diffuse inside voids created by a matrix of blue obstacles. At a critical density of obstacles, $n_{\mathrm{O,c}}$, only one infinite void cluster remains, giving rise to a localisation transition [222]. For densities larger than $n_{\mathrm{O,c}}$, only finite voids are present and lead to tracer particles being localised. Tracers diffusing in percolating void clusters can generally be explained by diffusion in fractals [5, 99]. The MSD at the percolation (or localisation) transition then follows

$$\langle \Delta \boldsymbol{r}^2 \rangle_{\infty_{\mathrm{V}}} \propto t^{\frac{2}{d_{\mathrm{w}}}} , \tag{VII.3}$$

where $\langle \cdot \rangle_{\infty_{\mathrm{V}}}$ refers to the MSD being obtained by averaging over motion inside the infinite void cluster only. Equation VII.3 is valid for times far beyond the microscopic time scale, where $t \gg R_{\mathrm{O}}^2 / D_{0,\mathrm{T}}$ with the radius of an obstacle R_{O} and the free diffusion coefficient of a tracer $D_{0,\mathrm{T}}$. The exponent d_{w} is called the walk dimension and describes the dimension of a random walk conducted by a particle when diffusing inside a fractal. For Brownian motion, $d_{\mathrm{w}} = 2$, but for diffusion in fractals, like in a percolating void cluster, $d_{\mathrm{w}} \neq 2$, indicating anomalous diffusion, i.e. $\alpha_{\mathrm{D}} \neq 1$. Inside the incipient infinite void cluster, particle movement is limited by the obstacles and subdiffusion with $d_{\mathrm{w}} > 2$ is expected. For the Lorentz gas in two dimensions, $d_{\mathrm{w}} = 2.878$ is found [5, 313].

Diffusion in a Lorentz gas at the localisation transition does not only include diffusion inside an infinite void cluster, but also all finite clusters as schematically depicted by the lower tracer in Fig. VII.2. When an average over diffusing particles in all void clusters—differently sized finite clusters and the infinite cluster—is used, the MSD reads [5]

$$\langle \Delta \boldsymbol{r}^2 \rangle \propto t^{\frac{2}{d_z}} \tag{VII.4}$$

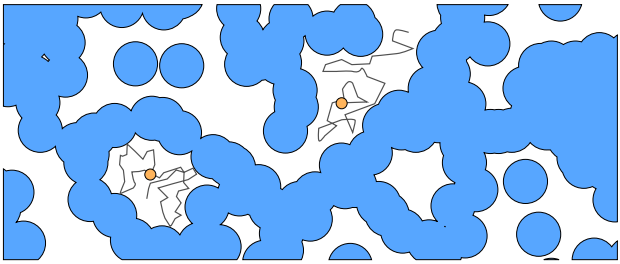

Figure VII.2: Schematic illustration of small tracers (orange) diffusing inside a Lorentz gas formed by overlapping obstacles (blue).[1]

with the dynamic exponent, d_z:

$$d_z = \frac{d_w}{1-(d-d_f)/2} > d_w\,. \tag{VII.5}$$

For a two-dimensional Lorentz gas, $d_z = 3.036$ is found [222, 313]. Equation VII.4 is valid for $R_O^2/D_{0,T} \ll t \ll t_\infty$, where t_∞ refers to the long-time limit.

To summarise, for very low densities, $n_O \ll n_{O,c}$, Brownian motion with $\alpha_D = 1$ is expected as particle motion is hardly affected by obstacles. When $n_O < n_{O,c}$, particles diffuse within infinite void clusters, which can be treated as homogeneous for length scales larger than l_ξ. As a result, the dynamics is transiently subdiffusive inside the percolating cluster and becomes diffusive for MSDs larger than l_ξ^2 at long times, t_∞ [5, 222]. At the critical density $n_O = n_{O,c}$, only one infinite void cluster is present, resulting in $\alpha_D = 2/d_z \approx 0.66$. When $n_O > n_{O,c}$, particles only diffuse in finite void clusters, within which they are caged. Thus, the MSD levels off at a value around the characteristic cluster size, l_ξ, so that $\alpha_D = 0$ for long times, t_∞ [5, 222].

2 Creation of Restricted Obstacles

To create a system exhibiting obstructed motion, the diffusion of small tracer particles has to be affected by the presence of large obstacle particles. In the case of a Lorentz gas, obstacles are fixed and can overlap, while tracers diffuse through the resulting voids. In colloidal physics, a Lorentz gas can be realised by using a suspension of two particle species with different sizes, where the larger particles are fixed [318]. However, overlap of obstacles is usually not possible and diffusing tracers are not infinitely small in an experiment making it differ from the ideal Lorentz model introduced in Sec. VII.1.

To experimentally realise a system similar to a Lorentz gas and additionally be able to tune obstacle particle motion from being highly restricted to diffusive, the diffuser setup described in Sec. III.2.2 is used. From Eqs. II.31 and II.34 and Fig. II.11 it is known that optical forces depend on the particle radius R as does the potential arising from the interaction between colloids and a light field. To quantify this behaviour, dilute samples of differently-sized polystyrene particles (R = 0.8, 1.05, 1.4, 2.05, 2.5, 2.9 µm: Sulfate Latex, Molecular Probes Inc.; R = 1.56 µm: Micro Particles Based on Polystyrene, Fluka Analytical; R = 4.16 µm: Non-Functionalized Polymer Microspheres, Bangs Laboratories Inc.) dispersed in purified water (Purelab Flex, ELGA LabWater, electrical resistivity $18.2{\cdot}10^4\ \Omega$m) with area fractions $\varphi_A < 0.04$ are produced according to Sec. III.1. The laser was used at the maximum output, P_L = 2.6 W. Particles were observed at 7.5 FPS for 59600 frames corresponding to an observation time $t_\mathcal{O} \approx 2.21$ h (Camera: Pike F-032B, Allied Vision Technologies GmbH)[2]. The FOV analysed with the routines mentioned in Sec. III.3 was 460 × 460 px, which is equal to 171 µm × 171 µm.

The time- and ensemble-averaged variance, $\sigma^2_{\Delta\boldsymbol{r},\mathrm{TE}}(\Delta t)$, of the two-dimensional particle displacements, $\Delta\boldsymbol{r}$, for different radii, R, can be seen in Fig. VII.3. For Brownian motion, $\sigma^2_{\Delta\boldsymbol{r},\mathrm{TE}}(\Delta t) \propto \Delta t$, as indicated by the black dashed line. Independent of R, all particles show a diffusive regime for small times $\Delta t < 1$ s followed by a transient subdiffusive regime for 1 s $< \Delta t <$ 100 s, where $\sigma^2_{\Delta\boldsymbol{r},\mathrm{TE}}(\Delta t)$

[2] This is the only time a camera differing from the one introduced in Sec. III.2.2 was used

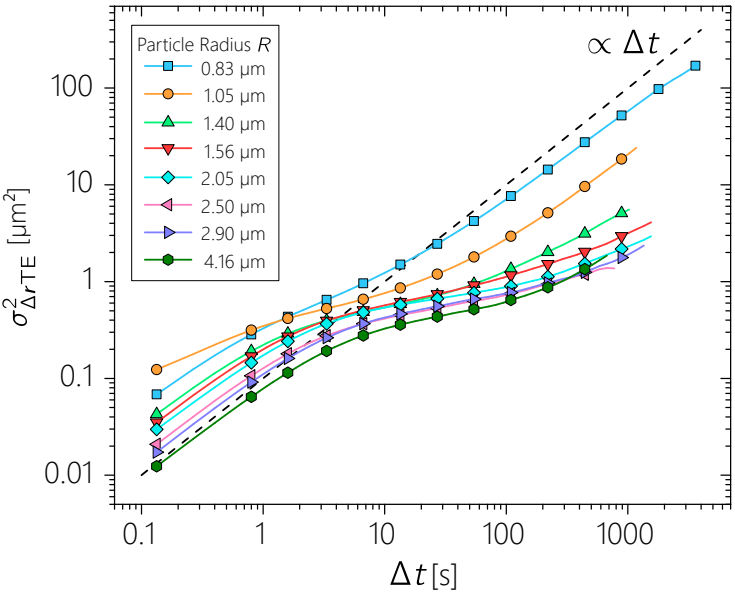

Figure VII.3: Time- and ensemble-averaged variance of two-dimensional displacements, $\Delta\boldsymbol{r}$, for particles of different radii R exposed to the light field created by the diffuser setup at $P_\mathrm{L} = 2.6$ W. The black dashed line corresponds to $\sigma^2_{\Delta\boldsymbol{r},\mathrm{TE}}(\Delta t) \propto \Delta t$ resembling Brownian motion.

increases slower than $\propto\Delta t$. For long times, $\Delta t > 100$ s, the dynamics becomes diffusive again with a diffusion coefficient lower than that for short times. This behaviour is thoroughly explained for a single particle size in Sec. VI.1. It was studied experimentally for the same two-dimensional random potential used here and a similar one in Refs. [190] and [135], respectively. Here, the effect of particle size is the focus. Colloids of all sizes are exposed to the same light intensity and accordingly show the same general behaviour. Yet the effect of the external light field on particle dynamics becomes stronger with increasing R and plateau regions in $\sigma^2_{\Delta\boldsymbol{r},\mathrm{TE}}(\Delta t)$ become more pronounced at intermediate times. For the

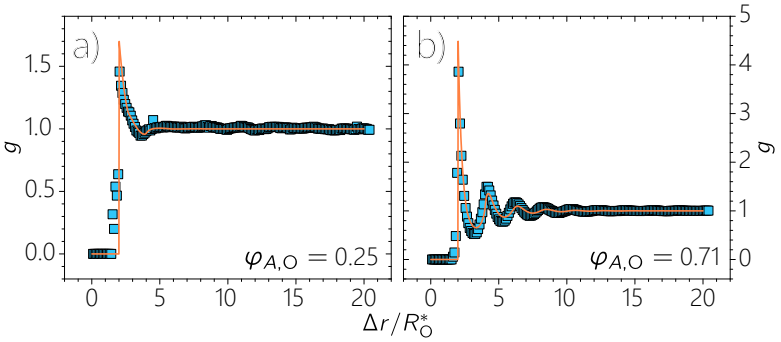

Figure VII.4: Obstacle-obstacle radial distribution functions for two different obstacle area fractions: a) $\varphi_{A,O} = 0.25$ with $\varphi_{A,T} = 0.08$. b) $\varphi_{A,O} = 0.71$ with $\varphi_{A,T} = 0.04$. Measured $g(\Delta r)$ are plotted as blue squares while calculated $g(\Delta r)$ using the Ornstein-Zernicke equation and a hard-sphere potential [319] are plotted as orange lines. The corrected obstacle radius, R_O^*, is used to normalise Δr.

smallest particle size, the deviation from Brownian motion is relatively small with a minimal anomalous diffusion exponent, $\alpha_{D,min} = 0.54$, while for the largest particle size, $R = 4.16$ µm, $\alpha_{D,min} = 0.23$, indicating stronger subdiffusion for larger R. Thus, at equal light field intensities, larger particles are more restricted in their motion than smaller ones.

As a result, there should be a laser power P_L, where particles with a large R are restricted in their motion, while smaller particles can diffuse virtually freely, i.e. large particles act as obstacles and the smaller ones as tracers. It is not experimentally possible to work with infinitely small tracers in a colloidal system. Therefore, finitely-sized tracers with $R_T = 1.4$ µm are used. They are chosen to be big enough so that they can be found and tracked properly in a video microscopy experiment (cf. Sec. III.3.2.1) while having a large enough number in the FOV to obtain good statistics. The size of the obstacles is chosen to be $R_O = 4.16$ µm. They are about three times larger than the tracers, but at the same time, still small enough to create a system composed of several differently sized clusters and voids inside the FOV.

Obstacle-obstacle interactions are investigated in terms of the obstacle-obstacle radial distribution function, $g(\Delta r)$, calculated using a routine made available by Eric Weeks [192]. In Fig. VII.4, it can be seen as blue symbols for $\varphi_{A,\mathrm{O}} = 0.25$ and $\varphi_{A,\mathrm{T}} = 0.08$ as well as $\varphi_{A,\mathrm{O}} = 0.71$ and $\varphi_{A,\mathrm{T}} = 0.04$ without any external potential acting on the system. The first peak of the non-normalised $g(\Delta r)$ for the highly concentrated sample (not shown here), $\varphi_{A,\mathrm{O}} = 0.71$, is situated at 7.9 µm corresponding to a corrected obstacle radius of $R_{\mathrm{O}}^{*} = 3.95$ µm. Neither the calculation, which was performed using more than 50 million coordinates that were determined with subpixel accuracy [191], nor the bin size of $g(\Delta r)$, which was chosen to be 0.2 µm, can account for such a deviation. Additional heterodyne near field scattering [320] and heterodyne near field velocimetry [321] measurements resulted in particle radii of 4.01 µm and 4.05 µm, respectively. They corroborate the notion that the actual size of the obstacle particles is $\lesssim 5$ % lower than that given by the manufacturer. The tracer-tracer radial distribution function (not shown here), on the other hand, indicates the same size given by the manufacturer, i.e. $R_{\mathrm{T}} = 2.8$ µm.

Orange lines in Fig. VII.4 correspond to numerical solutions of the Ornstein-Zernicke equation [198] for a monodisperse binary system made up of hard spheres [319]. The Ornstein-Zernicke equation relates the total correlation function of two particles $h(\Delta r) = g(\Delta r) - 1$ to direct and indirect interactions of the particle ensemble and is solved using the modified Verlet approximation [322]. To fit the measurements, a 10 % smaller area fraction has to be assumed, which also corroborates the assumption of the obstacles being slightly smaller than $R_{\mathrm{O}} = 4.16$ µm. The measured and calculated $g(\Delta r)$ agree well for both area fractions. Hence, it can be concluded that particles inside the binary mixture behave like hard spheres [319] and cannot overlap as they would in the idealised Lorentz gas. Even though tracers are small, although not infinitely small as in the Lorentz gas, and obstacles cannot overlap, the system made up of tracers with $R_{\mathrm{T}} = 1.4$ µm and obstacles with $R_{\mathrm{O}} = 4.16$ µm is close to the conditions of the ideal model.

2.1 Finding an Appropriate Laser Power

To find the value of P_L which results in freely diffusing tracers and highly restricted obstacles, a mixture of polystyrene particles with sizes $R_\mathrm{T} = 1.4\,\mu\mathrm{m}$ (Sulfate Latex 8 % w/v, $2R = 2.8\,\mu\mathrm{m}$, polydispersity 3.2 %, Molecular Probes Inc.) and $R_\mathrm{O} = 4.16\,\mu\mathrm{m}$ (Non-Functionalized Polymer Microspheres, P(S/2% DVB), 10 % solids, $2R = 8.311\,\mu\mathrm{m}$, polydispersity 5-10 %, Bangs Laboratories Inc.) dispersed in purified water was prepared according to Sec. III.1. Area fractions of the tracers were $\varphi_{A,\mathrm{T}} < 0.08$ so that the system was always in a dilute regime. Obstacles had an intermediate concentration with $\varphi_{A,\mathrm{O}} = 0.27 \pm 0.01$[3], since $\varphi_{A,\mathrm{O}}$ is varied in an experiment discussed later and should represent a generic value. The laser power was varied from 0 to 2.6 W. The FOV was 1024×1024 px, corresponding to $247\mu\mathrm{m} \times 247\,\mu\mathrm{m}$. The measurements were analysed for $t_\mathcal{O} = 3\,\mathrm{h}$, corresponding to 108000 images. All tracks shorter than one minute were not taken into account to eliminate very short tracks and thus possibly falsely found particles (cf. Sec. III.3.3).

The time- and ensemble-averaged variance, $\sigma^2_{\Delta\boldsymbol{r},\mathrm{TE}}(\Delta t)$ and the corresponding anomalous diffusion exponent, $\alpha_\mathrm{D}(\Delta t)$ for tracers and obstacles for different P_L are shown in Fig. VII.5. When P_L is increased, particle motion tends to be more subdiffusive at times $1\,\mathrm{s} < \Delta t < 1000\,\mathrm{s}$ for both tracers and obstacles. This behaviour is known from Sec. VI.1 and [135, 190] and stems from P_L corresponding to the potential roughness, σ_U, where a larger roughness corresponds to deeper potential minima in which particles can be trapped. These deeper minima lead to stronger subdiffusion. From Sec. VII.2, it is also known that differently sized particles feel differently strong potentials at equal P_L. For no field and $P_\mathrm{L} = 34.4\,\mathrm{mW}$, this feature is not seen as the potential does not exist or is too weak. Both particle species show slight subdiffusion for $\sigma_{\Delta r} \gtrsim 10\,\mu\mathrm{m}^2$ due to the non-dilute particle concentration [323]. For $P_\mathrm{L} \geq 446\,\mathrm{mW}$, the different response to the applied light field becomes apparent. The minimum of $\alpha_\mathrm{D}(\Delta t)$ is smaller for the obstacles than for the tracers. To obtain a system with diffusive tracers and restricted obstacles giving rise to obstructed motion, a value of P_L

[3] The interval given for $\varphi_{A,\mathrm{O}}$ represents the standard deviation.

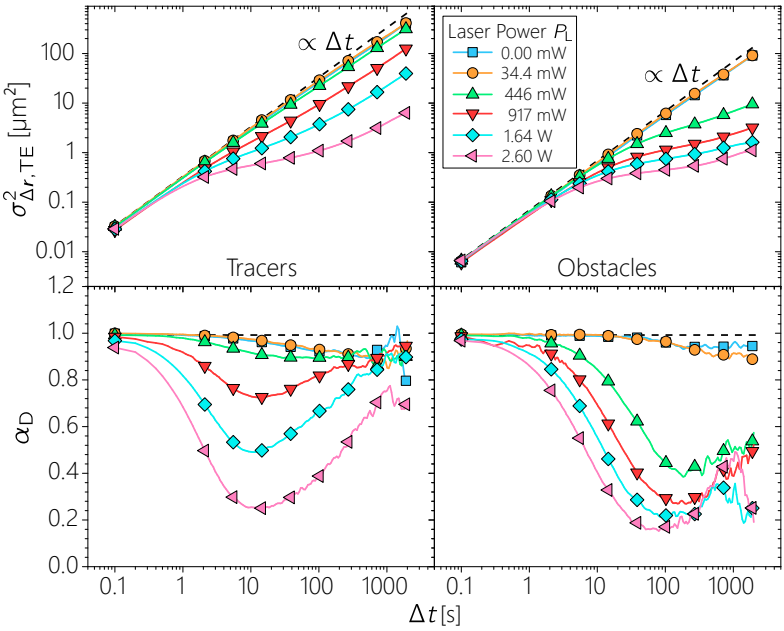

Figure VII.5: Time- and ensemble-averaged variance of two-dimensional displacements, $\Delta \boldsymbol{r}$, and corresponding anomalous diffusion exponents for particles of radii $R_T = 1.4$ µm, called tracers, and $R_O = 4.16$ µm, called obstacles, with the area fractions $\varphi_{A,T} < 0.08$ and $\varphi_{A,O} = 0.27 \pm 0.01$. They are exposed to the light field created by the diffuser setup at varying laser powers P_L. The black dashed lines correspond to the theoretical result for Brownian motion.

has to be picked, where $\alpha_D(\Delta t) \approx 1$ for the tracers throughout the measurement, while $\alpha_D(\Delta t)$ for the obstacles is as small as possible. The measurement that most closely meets these requirements is the green line with upward pointing triangular symbols in Fig. VII.5. For $P_L = 446$ mW, tracers are hardly affected by the imposed light field, while the motion of obstacles is highly restricted. This restriction can be weakened without altering tracer motion by lowering P_L. When the laser power is decreased, obstacles are less affected by the external potential created

by the light field (cf. VI.1). This results in a two-dimensional system with tracers and obstacles, whose obstacle motion can be tuned from highly restricted for $P_\mathrm{L} = 446$ mW—similar to a Lorentz gas—to free diffusion for $P_\mathrm{L} = 0$ mW—like in binary mixtures [224, 323].

3 Measuring the Dynamics

A system exhibiting obstructed motion can be realised by using tracers with $R_\mathrm{T} = 1.4$ µm and obstacles with $R_\mathrm{O} = 4.16$ µm exposed to the two-dimensional light field coming from the diffuser setup (cf. Fig. VII.5). The dynamics of this system was studied for varying obstacle area fractions $0.00 \leq \varphi_{A,\mathrm{O}} \leq 0.88$ and laser powers $0\ \mathrm{mW} \leq P_\mathrm{L} \leq 446\ \mathrm{mW}$. Samples were prepared as described in Sec. VII.2.1. Particles were observed for $t_\mathcal{O} = 3$ h with 10 FPS adding up to 108000 images. The area fraction of tracers was $\varphi_{A,\mathrm{T}} \leq 0.05$, so that tracer-tracer interactions were negligible and colloids effectively act as single particles. Using a FOV of 247 µm × 247 µm, $\varphi_{A,\mathrm{T}}$ translates to tracer particle numbers of less than 695. All trajectories shorter than 60 seconds were omitted, which is necessary to rule out trajectories made up of falsely found particles due to particle concentration (cf. Sec. III.3.2.1). The rather small number of tracers reduces further as particles enter and leave the FOV resulting in many particle trajectories, Δt_L, being less than 108000 steps. This leads to noise in the calculated dynamical quantities, especially for large times, when ensemble averages are used. To reduce noise, the time and ensemble average can be used instead, which is advised to be used in non-evolving systems only (cf. Sec. III.4.6).

To make sure the measured systems were not evolving in time, a generic sample with an intermediate concentration, $\varphi_{A,\mathrm{O}} = 0.26$, and $\varphi_{A,\mathrm{T}} = 0.08$ was observed for a total of five hours. These five hours were split up into three measurement intervals of $t_\mathcal{O} = 3$ h, where the first interval starts with the particles being exposed to the laser field, the second measurement starts one hour later and the third one two hours later. A comparison between the ensemble-averaged variance of two-dimensional displacements, $\sigma^2_{\Delta\boldsymbol{r},\mathrm{E}}(t)$, and the time and ensem-

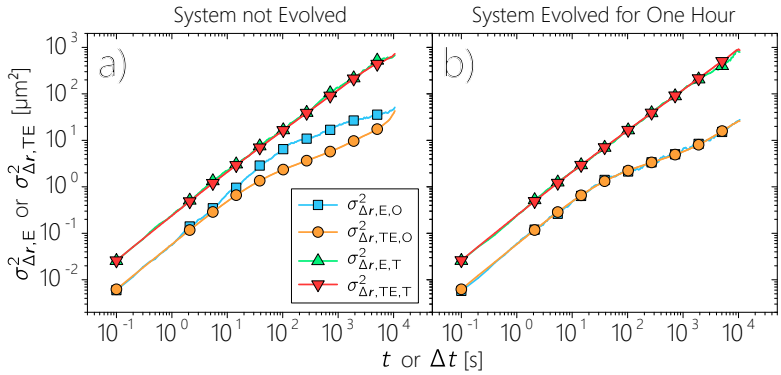

Figure VII.6: Ensemble- as well as time- and ensemble-averaged variances for a generic sample with $\varphi_{A,\mathrm{O}} = 0.26$ and $\varphi_{A,\mathrm{T}} = 0.08$. a) The measurement starts with particles being exposed to the external potential and lasts three hours. Differently averaged quantities do not show the same result. b) The system is exposed to the external potential and could evolve for one hour prior to being observed for three hours. As a result, $\sigma^2_{\Delta r,\mathrm{E}}$ and $\sigma^2_{\Delta r,\mathrm{TE}}$ fall on top of each other.

ble average, $\sigma^2_{\Delta r,\mathrm{TE}}(\Delta t)$, for the first and second measurement interval is shown in Figs. VII.6 a) and b), respectively. For tracers, $\sigma^2_{\Delta r,\mathrm{E,T}}(t)$ shows a small difference to $\sigma^2_{\Delta r,\mathrm{E,TE}}(\Delta t)$, in the first measurement interval (Fig. VII.6 a)). Thus, their dynamics slightly evolves in the first three hours after being exposed to the light field. In Fig. VII.6 b), no such difference is observed. The same, but more apparent, is true for obstacles. In Fig. VII.6 a), $\sigma^2_{\Delta r,\mathrm{E,O}}(t)$ differs from $\sigma^2_{\Delta r,\mathrm{TE,O}}(\Delta t)$ indicating an evolution of the obstacle dynamics. When the system has been exposed to the external potential for one hour and then measured for three hours, this difference is gone. The same measurement was also conducted for concentrations reaching up to $\varphi_{A,\mathrm{O}} = 0.88$, leading to the same result (not shown here): the system evolves during the first hour after the first exposure to the light field. After that, ensemble and time and ensemble average give the same result showing the system has reached a steady state. Therefore, in the following, particles are recorded for four hours with 10 FPS. Only the last three hours are analysed

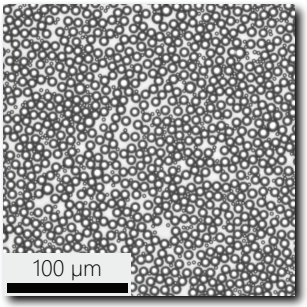

Figure VII.7: Typical micrograph of the measurements discussed in this chapter, where $\varphi_{A,O} = 0.68$.

with video microscopy routines, where time and ensemble averages are taken. Dynamical quantities are normalised by the short-time diffusion coefficient of tracers for $\Delta t = t \lesssim 1$ s without any obstacles present, $D^{s}_{T,0} = 0.8\ \mu m^2/s$,[4] and the corresponding two-dimensional Brownian time, $t_{B,T} = R_T^2/4D^{s}_{T,0} = 6.125$ s.

4 Dynamics Depending on Obstacle Concentration: The Lorentz Gas

A light field with a constant $P_L = 446$ mW was used to create highly restricted obstacle particles and tracers were added, which should not be affected by the external potential. Figure VII.7 shows a typical micrograph of such a measurement, where small tracer particles diffuse inside voids created by the bigger obstacle particles for an obstacle concentration $\varphi_{A,O} = 0.68$. In the following, the effect of $\varphi_{A,O}$, on tracer diffusion is discussed and compared to the extreme case of obstructed motion, where all obstacles are static, i.e. the Lorentz gas.

[4] Ideally, $D^{s}_{T,0}$ corresponds to $D_{0,T}$, the unaffected diffusion coefficient of the tracers introduced in Sec VII.1.

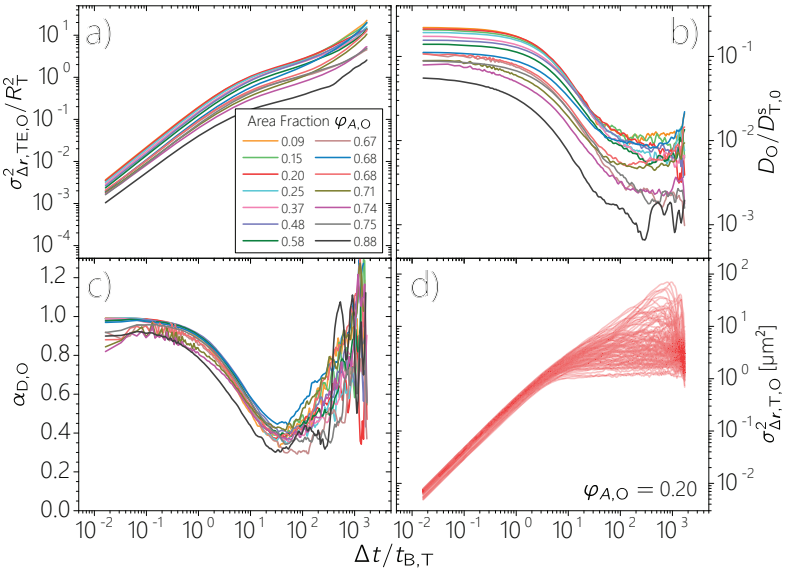

Figure VII.8: Measured obstacle dynamics for different obstacle area fractions, $\varphi_{A,O}$. a) Time- and ensemble-averaged variance normalised by the radius of a tracer R_T. b) Diffusion coefficient normalised by the short-time tracer diffusion coefficient at $\varphi_{A,O} = 0$, $D^s_{T,0}$. c) Anomalous diffusion exponent. d) Time-averaged variance for single obstacle trajectories with $\varphi_{A,O} = 0.20$.

4.1 Obstacle Motion Inside the Potential Landscape

Before focussing on the motion of tracers inside the voids created by obstacles, the dynamics of obstacle particles is discussed as a function of their concentration, $\varphi_{A,O}$. For obstacle motion inside the random potential landscape, $\sigma^2_{\Delta \boldsymbol{r},TE,O}(\Delta t)$ along with the corresponding $\alpha_{D,O}(\Delta t)$ and $D_O(\Delta t)$ can be seen in Figs. VII.8 a)–c). Each curve corresponds to one measurement of $t_{\mathcal{O}} = 1 + 3$ h with $\varphi_{A,O}$ as indicated. Four additional measurements were conducted but are not shown as their curves indicated superdiffusive behaviour, which is not expected and can only be explained by flawed execution of the experiment. For

all $\varphi_{A,\mathrm{O}}$, a distinctive yet similar trend is seen in $\sigma^2_{\Delta\boldsymbol{r},\mathrm{TE,O}}(\Delta t)$. It is the same behaviour as discussed in Secs. VI.1 and VII.2. Below $\Delta t \approx 0.1\, t_{\mathrm{B,T}}$ and $\sigma_{\Delta\boldsymbol{r},\mathrm{TE,O}}(\Delta t) \approx 0.01\, R_{\mathrm{T}}$, obstacle motion corresponds to Brownian motion showing $\alpha_{\mathrm{D,O}} \approx 1$ and diffusion coefficients $D_{\mathrm{O}} \approx 0.1\, D^{\mathrm{s}}_{\mathrm{T},0}$, where, of course, $D^{\mathrm{s}}_{\mathrm{T},0}$ is larger than that of the obstacles. Around the correlation length of the external potential, $l_U \approx R_{\mathrm{T}}$, the variance $\sigma^2_{\Delta\boldsymbol{r},\mathrm{TE,O}}(\Delta t)$ begins to indicate a deviation from Brownian motion. Above this threshold, obstacles reach the flanks of the minima in which they are trapped and are thus strongly influenced by the external potential. Their motion becomes strongly subdiffusive, showing anomalous diffusion exponents around 0.4 and diffusion coefficients that drop below $0.01\, D^{\mathrm{s}}_{\mathrm{T},0}$. For $\Delta t > 50\, t_{\mathrm{B,T}}$, $\sigma^2_{\Delta\boldsymbol{r},\mathrm{TE,O}}(\Delta t)$ show more diffusive behaviour with a rising value of $\alpha_{\mathrm{D,O}}(\Delta t)$ and almost constant $D_{\mathrm{O}}(\Delta t)$. This stems from obstacles diffusing from one potential minimum to the next with a constant long-time diffusion coefficient, $D^{\mathrm{l}}_{\mathrm{O}}$, two orders of magnitude below $D^{\mathrm{s}}_{\mathrm{T},0}$ (cf. Sec. VI.1). Thus, obstacles are highly restricted in their diffusive motion, which is consistent with the results shown in Fig. VII.5.

Figure VII.8 d) additionally shows $\sigma^2_{\Delta\boldsymbol{r},\mathrm{T,O}}(\Delta t)$ with $\varphi_{A,\mathrm{O}} = 0.20$ for 100 randomly chosen particles that were in the FOV for the whole measurement. At this area fraction, obstacles are so numerous that single particle variances give insightful results, while being so dilute that inter-particle interactions do not play a prominent role. The distinctive drop of all variances for $\Delta t \gtrsim 1000\, t_{\mathrm{B,T}}$ stems from the statistical correlation of samples for Δt approaching Δt_{L} (cf. Sec. III.4.6). Most of the time-averaged single trajectory variances of the obstacles level off at $\sigma^2_{\Delta\boldsymbol{r},\mathrm{T,O}}(\Delta t) \leq 10\ \mu\mathrm{m}^2 \approxeq 5\, R^2_{\mathrm{T}}$ indicating that obstacles are trapped inside a local minimum of the external potential for the whole observation time. Only a minority of particles show $\sigma^2_{\Delta\boldsymbol{r},\mathrm{T,O}}(\Delta t)$ not levelling off corresponding to an only partly restricted motion.

Besides the influence of the external potential, inter-particle interactions can play an important role. The higher the concentration of the obstacles, the more restricted their motion since the area they can cover becomes smaller. This intuitive correlation has already been described for two-dimensional diffusion with-

out any external potential landscape [180, 323]. It is also valid for the present case, where $P_\mathrm{L} \neq 0$ mW, as can be seen from $\sigma^2_{\Delta\boldsymbol{r},\mathrm{TE,O}}(\Delta t)$ and $D_\mathrm{O}(\Delta t)$. Both quantities are successively shifted to lower values when $\varphi_{A,\mathrm{O}}$ is increased. The highest concentrated sample exhibits a long-time diffusion coefficient which is one order of magnitude lower than that for the lowest area fraction.

4.2 Tracer Motion Depending on Obstacle Concentration

From Secs. VII.2.1 and VII.4.1, it is known that obstacles are highly affected by the external random potential landscape imposed on the sample. This leads to diffusion coefficients two orders of magnitude lower than $D^\mathrm{s}_{\mathrm{T},0}$, while tracers are barely affected. Depending on the obstacle concentration, as described by the area fraction, $\varphi_{A,\mathrm{O}}$, obstacle particles can form clusters with a characteristic length, l_ξ, similar to the situations described in Sec. VII.1. Tracers ($\varphi_{A,\mathrm{T}} \leq 0.05$) diffuse through the voids created by the highly restricted, almost static obstacles. In Figs. VII.9 a)–d), the variance, $\sigma^2_{\Delta\boldsymbol{r},\mathrm{TE,T}}(\Delta t)$, diffusion coefficient, $D_\mathrm{T}(\Delta t)$, anomalous diffusion exponent, $\alpha_{\mathrm{D,T}}(\Delta t)$ and averaged normalised excess kurtosis, $\overline{\gamma_{\alpha,xy}}(\Delta t) = (\gamma_{\alpha,x}(\Delta t) + \gamma_{\alpha,y}(\Delta t))/2$, of tracer motion are shown for different obstacle area fractions. Results for times $\Delta t > 300\ t_{\mathrm{B,T}}$ should be interpreted with caution as they are very noisy. Therefore, only results for $\Delta t \lesssim 300\ t_{\mathrm{B,T}}$ are taken into consideration.

By comparing Figs. VII.8 a) and b) to Figs. VII.9 a) and b), it can be seen that the tracers are in general more mobile than the obstacles. Their diffusion coefficients only obtain similar values for high $\varphi_{A,\mathrm{O}}$. This corroborates the picture of voids formed by almost static obstacles through which free tracers diffuse. For $\varphi_{A,\mathrm{O}} = 0.0$, no indication of anomalous behaviour is found in $\sigma^2_{\Delta\boldsymbol{r},\mathrm{TE,T}}(\Delta t)$, whereas $D_\mathrm{T}(\Delta t)$, $\alpha_{\mathrm{D,T}}(\Delta t)$ and $\overline{\gamma_{\alpha,xy}}(\Delta t)$ show slight deviations from Brownian motion at $\Delta t \approx t_{\mathrm{B,T}}$, reminiscent of colloidal particles in an external potential landscape (Sec. VI.1). It exhibits a very mild form however, where $\alpha_{\mathrm{D,T}} > 0.95$ and $\overline{\gamma_{\alpha,xy}} < 0.2$, and should thus not be critical in the following discussion. In general, tracer motion is slowed down for all observed obstacle area fractions $0.09 \leq \varphi_{A,\mathrm{O}} \leq 0.88$. From Sec. VII.1, three different regimes are expected

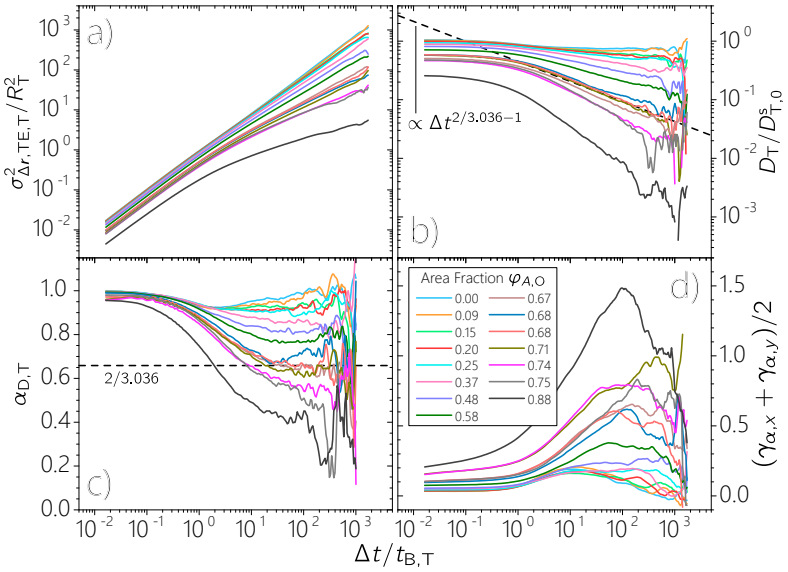

Figure VII.9: Tracer dynamics for different obstacle area fractions $\varphi_{A,O}$. a) Time- and ensemble-averaged variance normalised by the radius of a tracer, R_T. b) Diffusion coefficient normalised by the short-time tracer diffusion coefficient at $\varphi_{A,O} = 0$, $D^s_{T,0}$. c) Anomalous diffusion exponent. d) Normalised excess kurtosis averaged over x- and y-direction.

for a Lorentz gas, where, for low obstacle concentrations, tracers should exhibit diffusive motion at long times, and high $\varphi_{A,O}$ should result in an upper threshold for the variance, $\sigma^2_{\Delta \boldsymbol{r},TE,T}(\Delta t)$. Between these extreme cases, a transition regime following Eq. VII.4 should be found.

For low to intermediate obstacle area fractions, $0.09 \leq \varphi_{A,O} \leq 0.58$, the results in Fig. VII.9 show diffusive short-time motion, where $D^s_T = D_T(\Delta t \ll t_{B,T})$ successively decreases with increasing obstacle concentration. For $\varphi_{A,O} < 0.37$, transient subdiffusive behaviour can be seen for $0.1\ t_{B,T} < \Delta t < 300\ t_{B,T}$. During this time span, $D_T(\Delta t)$ continuously drops from a constant short-time diffusion coefficient slightly below $D^s_{T,0}$ to a constant value $< D^s_T$ for long times.

The anomalous diffusion exponent exhibits $\alpha_{\mathrm{D,T}}(\Delta t) \gtrsim 0.90$, then rises back to 1.0 and $\overline{\gamma_{\alpha,xy}}(\Delta t) \approx 0.2$ before it drops to 0.0, indicating Gaussian behaviour for long times. These trends can be explained by limited obstruction due to the larger particles, which form clusters with a characteristic length, l_ξ (cf. Sec. VII.1): at intermediate times, tracers feel the presence of (clustered) obstacles and thus exhibit subdiffusive motion as they cannot diffuse freely. At longer times and therefore larger length scales, the finiteness of clusters, or the infiniteness of voids through which tracers diffuse, takes effect. Tracer motion is not affected by obstacles on length scales larger than l_ξ—most obstacle clusters are smaller—and becomes Brownian again.

When $0.37 \leq \varphi_{A,\mathrm{O}} \leq 0.58$, a return to Gaussian behaviour for long times is no longer visible. In Fig. VII.9 a), deviations from Brownian motion in $\sigma^2_{\Delta \boldsymbol{r},\mathrm{TE,T}}(\Delta t)$ become apparent. At long times, $D_{\mathrm{T}}(\Delta t)$ does not become completely constant. It decreases slightly, but continuously with time. The anomalous diffusion exponent increases for long times but does not return to 1.0. The minimum of $\alpha_{\mathrm{D,T}}(\Delta t)$ shifts to larger Δt and decreases for an increasing obstacle concentration. Additionally, $\overline{\gamma_{\alpha,xy}}(\Delta t)$ displays maxima of values $\lesssim 0.4$ and does not drop to 0.0 for long times. Tracers at $0.37 \leq \varphi_{A,\mathrm{O}} \leq 0.58$ generally show the same behaviour as observed for $\varphi_{A,\mathrm{O}} < 0.37$: diffusive motion at short times, $\Delta t \ll t_{\mathrm{B,T}}$, is followed by a $\varphi_{A,\mathrm{O}}$-dependent, pronounced subdiffusive motion at intermediate times, $0.1\, t_{\mathrm{B,T}} < \Delta t < 300\, t_{\mathrm{B,T}}$. For long times, $\Delta t \ggg t_{\mathrm{B,T}}$, tracer motion tends to become Brownian again. The absence of Brownian behaviour for long times when $0.37 \leq \varphi_{A,\mathrm{O}} \leq 0.58$ compared to when $\varphi_{A,\mathrm{O}} < 0.37$ can be explained by the increased size of obstacle clusters for $\varphi_{A,\mathrm{O}} \geq 0.37$. When l_ξ is so large that tracers do not cover this distance during Δt_{L}, Brownian behaviour cannot be seen for long times. Yet for $0.37 \leq \varphi_{A,\mathrm{O}} \leq 0.58$, a tendency towards diffusive tracer motion is found. These observations then allow for l_ξ to be estimated from $\sigma^2_{\Delta \boldsymbol{r},\mathrm{TE,T}}(\Delta t)$. For example, when $\varphi_{A,\mathrm{O}} = 0.25$, it lies around $\sqrt{70}\, R_{\mathrm{T}}$.

For very high obstacle area fractions, $\varphi_{A,\mathrm{O}} > 0.71$, $\sigma^2_{\Delta \boldsymbol{r},\mathrm{TE,T}}(\Delta t)$ does not only deviate from normal diffusion but tends to level off. Accordingly, $D_{\mathrm{T}}(\Delta t)$ decreases with time and $\alpha_{\mathrm{D,T}}(\Delta t)$ does not exhibit a minimum but also decreases.

Throughout the whole measurement, tracer motion is non-Gaussian with $\overline{\gamma_{\alpha,xy}}(\Delta t)$ exceeding values of 0.5 and not going back to 0.0. This behaviour stems from the high concentration of obstacles leading to voids caging the tracers to a finite area. This finiteness leads to an upper threshold of $\sim l_\xi^2$ for the area that tracers can cover (cf. Sec. VII.1). Consequently, $\sigma^2_{\Delta \boldsymbol{r},\mathrm{TE,T}}(\Delta t)$ should level off at about l_ξ^2 and $D_\mathrm{T}(\Delta t)$ as well as $\alpha_{\mathrm{D,T}}(\Delta t)$ should decrease until both reach zero. For $\varphi_{A,\mathrm{O}} = 0.88$, $\sigma^2_{\Delta \boldsymbol{r},\mathrm{TE,T}}(\Delta t)$ tends to level off and only reaches a quarter of an obstacle diameter during the available Δt_L but does not become constant. This indicates that a longer observation time would be needed to experimentally prove the theoretical predictions stated in Sec. VII.1.[5]

Between low and high obstacle area fractions, a transition regime is observed in Fig. VII.9. It is most pronounced in $\alpha_{\mathrm{D,T}}(\Delta t)$, which tends to return to 1.0 for $\varphi_{A,\mathrm{O}} \leq 0.58$ and steadily decreases for $\varphi_{A,\mathrm{O}} > 0.71$. For $0.67 \lesssim \varphi_{A,\mathrm{O}} \lesssim 0.71$ however, $\alpha_{\mathrm{D,T}}(\Delta t)$ levels off at around 2/3.036—the value expected for diffusion at the critical density in a two-dimensional Lorentz gas (cf. Sec.VII.1) [222, 313]. A similar trend can be seen in $D_\mathrm{T}(\Delta t)$, which scales as $\Delta t^{2/3.036-1}$, while it levels for low $\varphi_{A,\mathrm{O}}$ and increasingly drops faster as time proceeds for high obstacle area fractions. In $\overline{\gamma_{\alpha,xy}}(\Delta t)$, no particular trend can be seen for concentrations in the transition regime. Maximum values lie around 0.6–0.8 and do not drop to 0.0 for long times, thus blending in well with data seen for lower and higher $\varphi_{A,\mathrm{O}}$. The peculiar behaviour of tracer motion in the transition regime can be explained by means of the Lorentz gas and percolation. When $\varphi_{A,\mathrm{O}}$ is increased, the system changes from featuring several infinite voids to only having finite voids. At a specific concentration during that transition, only one infinite, percolating void is present. This void, together with all other finite voids, results in $\sigma^2_{\Delta \boldsymbol{r},\mathrm{TE,T}}(\Delta t) \propto \Delta t^{2/3.036}$. According to Fig. VII.9, this specific area fraction is reached when $0.67 \leq \varphi_{A,\mathrm{O}} \leq 0.71$ and can thus be identified as the critical density of the system causing the localisation transition, $\varphi_{A,\mathrm{O,c}}$ (cf. Sec. VII.1).

[5] As the largest Δt_L lasted three hours, an increase of two orders of magnitude would result in one measurement lasting several weeks and is thus not feasible.

4.3 Discussion

The previous section revealed the system used here, made up of highly restricted obstacles with smaller tracers diffusing inside the resulting voids, closely resembles the case of diffusion inside an idealised Lorentz gas described in Refs. [5, 222]. Tracer motion for long times changes from being diffusive for a low obstacle concentration to constant subdiffusion for the localisation transition before it tends to be localised for very high $\varphi_{A,O}$. The present results show the same exponent, $2/d_z = 2/3.036$, for diffusion at the critical obstacle area fraction, $\varphi_{A,O,c}$, as proposed in Refs. [5, 222]. From Fig. VII.9, $\varphi_{A,O,c} \approx 0.68$ can be inferred.[6] Bauer et al. [222] observe a critical density of $n^*_{O,c} = 0.359$, which translates to $\varphi^*_{A,O,c} = n^*_{O,c}\,\pi = 1.129$. This value stems from the idealised Lorentz model, where obstacles can overlap. This is different from the present case where φ_A values larger than 1.0 are not feasible. The value of φ_A can be adjusted by models that mimic the present situation more closely (see below). Simulations on non-Gaussian parameters of tracer motion in a three-dimensional Lorentz gas showed increasingly non-Gaussian behaviour for higher obstacle concentrations similar to that found here [324]. A further investigation of the dynamic characteristics of the studied system by relating the long-time diffusion coefficient to a so-called separation parameter, like in Refs. [222, 325], did not yield reliable results. A reason for this might be problems in determining the long-time D_T as it was not feasible to conduct measurements long enough for the system to adopt a certain constant diffusion coefficient at the end of each measurement.[7]

The system investigated here differs from the idealised Lorentz gas as obstacles are highly restricted in their motion but not fixed, obstacles cannot overlap, tracers are not infinitely small and the observed area is finite. The latter is found to change the critical obstacle area fraction to slightly higher values following

[6] There are several curves in Fig. VII.9 c) whose plateau values are close to $2/3.036$. The red curve reflecting $\varphi_{A,O,c} = 0.68$ fits best.

[7] To reliably cover the eight to ten orders of magnitude in time Schnyder et al. [325] and Bauer et al. [222] used to determine long-time diffusion coefficients, one measurement would have to last three to five orders of magnitude longer than those presented here. That would amount to about 10^3 h $\widehat{=}$ weeks.

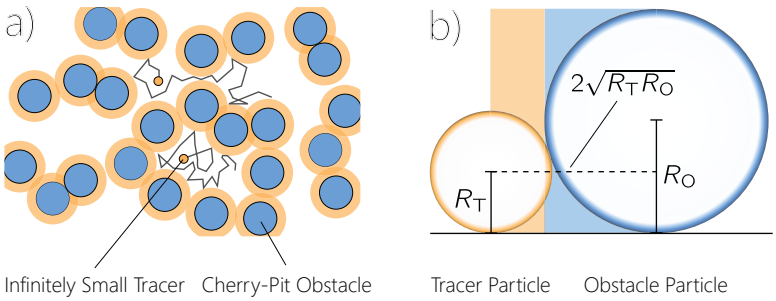

Figure VII.10: The cherry-pit model and its application to the present situation. a) Schematic of the cherry-pit model with obstacles made up of a non-overlapping core (blue) and a shell (orange) that cannot be penetrated by the small tracers (orange) which diffuse inside the voids. b) Due to gravity, the interaction distance is not equal to $R_T + R_O$ but $2\sqrt{R_T R_O}$. Coloured backgrounds indicate core and shell of an equivalent cherry-pit obstacle. a) adapted from [325, 326].

$\varphi_{A,O,c}(\sqrt{A_{FOV}}) - \varphi_{A,O,c} \sim 1/\sqrt{A_{FOV}}^{1/\nu}$ [327], where ν is a critical exponent and reads $4/3$ in two dimensions [313].

To tackle the finiteness of tracers, Berry et al. [328] suggest adjusting the obstacle-occupied area by including the tracer radius. Not only are the tracers finite but there are also no overlaps between obstacles, hence the so-called cherry-pit model introduced by Salvatore Torquato in 1984 [329, 330] is favoured over the approach of Berry et al. here [325, 326] (Fig. VII.10). It takes the finite size of a tracer particle into account by introducing a partially interpenetrable shell around each obstacle, depicted in orange in Fig. VII.10 a). An obstacle is made up of an impenetrable core—similar to a cherry pit, depicted in blue—and the shell which can only be penetrated by the shell of another obstacle. When clusters are formed, obstacle cores cannot overlap, in contrast to the shells, which can. The tracers (depicted in orange) diffusing inside the voids created by cherry-pit obstacles are not allowed to penetrate the shells. Finite tracer particles can then be treated as if they were infinitely small. The size of the obstacle cores corresponds to the size of obstacle particles. The shells' size on the other hand depends on both tracer and

obstacle sizes. It is also called the interaction distance and is equal to $R_T + R_O$ for a purely two-dimensional system [325]. The sample used in this work is not purely two-dimensional but rather quasi-two-dimensional. Due to gravity, tracer and obstacle particles sediment and are situated close to the bottom of the sample cell. As they have a different size, their distance projected on two dimensions is smaller than $R_T + R_O$, as indicated by a dashed line in Fig. VII.10 b), and can be determined to be $2\sqrt{R_T R_O}$. The orange and blue backgrounds are the resulting shell and core, respectively. For the cherry-pit model, the critical area fraction, $\varphi_{A,C,c}$, depends on the obstacle area fraction as well as the tracer and obstacle size. Schnyder et al. [325] determined critical densities depending on the obstacle area fraction. For the value determined from Fig. VII.9, $\varphi_{A,O,c} = 0.68$, they find a critical cherry-pit area fraction, $\varphi^*_{A,C,c} \approx 0.25\,\pi = 0.79$. To compare this value to $\varphi_{A,O,c}$,

$$\varphi_{A,C,c} = \frac{N_{FOV,O}\,\pi\,4\,R_T R_O}{A_{FOV}} \tag{VII.6}$$

has to be determined, where $N_{FOV,O}$ is the number of obstacles in the field of view. From $\varphi_{A,O,c}$, the number of obstacle is found to be $\approx$ 760, which then yields $\varphi_{A,C,c} \approx 0.91$, close to the $\varphi^*_{A,C,c} \approx 0.79$ found in Ref. [325]. When the corrected obstacle radius R^*_O is used (cf. Sec. VII.2), $\varphi_{A,C,c}$ is calculated to be 0.87. Considering the observed area used in the work described in this thesis is much smaller than the box used in Ref. [325], which slightly increases critical area fractions, the value for $\varphi_{A,O,c}$ obtained here agrees well with the literature. Similar to the ideal Lorentz gas, the cherry-pit model causes subdiffusion over several orders of magnitude in time at the critical concentration. Schnyder et al. [325] found an anomalous diffusion coefficient slightly below $2/d_z$. As d_z is believed to be a universal exponent for transport in two-dimensional percolating clusters [331], they argue that they overestimated the critical area fraction causing them to get lower values. This underestimation of d_z is not found here, corroborating that it is a universal exponent.

Another difference between an ideal Lorentz gas and the present system is the obstacle motion. In a Lorentz, gas obstacles are fixed, whereas here obstacle mo-

tion is highly restricted but still takes place. Berry et al. [328] investigated obstructed motion for this very case, where so-called Ornstein-Uhlenbeck obstacles were simulated. These obstacles are not fixed but conduct Browninan motion with a feedback relaxation restricting the area they cover to a small region. Thus, this model is very close to the obstacles used in the work described in this thesis, which are also confined to certain regions due to the interaction with the external potential landscape, as can be seen by the levelling variances in Fig. VII.8 d). Berry et al. found that subdiffusion similar to a Lorentz gas does not extend over the whole simulation time, which lasted five orders of magnitude, for Ornstein-Uhlenbeck obstacles diffusing less than an order of magnitude slower than the tracers, i.e. $D^{\mathrm{s}}_{\mathrm{O},0}/D^{\mathrm{s}}_{\mathrm{T},0} > 0.1$. For slower obstacles, subdiffusion with $D_{\mathrm{T}} \propto \Delta t^{2/3.036-1}$ is found. As the obstacles used here have a diffusion coefficient two orders of magnitude lower than that of the tracers, the present results agree well with these observations. Whether the obstacles used in this work create an ideal Lorentz gas or are rather of the Ornstein-Uhlenbeck type that eventually result in diffusive tracer motion as suggested by [328], cannot be resolved completely. Considering the big difference in diffusion coefficients between obstacles and tracers together with the findings in Ref. [328], observation times would have to be much larger than five orders of magnitude to clarify this question.

Besides Ornstein-Uhlenbeck obstacles, the cherry-pit model and finite measurement areas, several other extensions of obstructed motion in a Lorentz gas, such as soft obstacle-tracer interactions, which lead to a rounding of the localisation transition [325], have been studied. Zeitz et al. simulated active tracers in a two-dimensional Lorentz gas that reached similar subdiffusive regimes faster than passive ones [332]. Furthermore, tracers driven through a Lorentz gas are found to have diffusion coefficients enhanced by several orders of magnitude, similar to the case of giant diffusion [270] and particles driven through a random potential energy landscape (cf. Sec. VI). Instead of changing interactions or tracer movement, the Lorentz gas itself can be modified by increasing the mobility of the otherwise fixed obstacles [20, 328, 333]. How this changes the diffusion of tracers is discussed in the following section.

5 Dynamics Depending on Obstacle Mobility

In the previous section, a Lorentz gas-like system was introduced by restricting the motion of obstacle particles via an external random potential energy landscape created by light while smaller tracer particles diffused through the resulting voids. In this section, the restriction of obstacle motion caused by the external potential is (partly) removed by changing the potential roughness. From Sec. VI.1, the laser power is known to change σ_U, where larger P_L lead to a higher roughness and a stronger effect on particle motion. Lowering the laser power thus results in less restricted obstacle motion. How this alteration affects tracer diffusion forms the focus of this section.

Figures VII.11 a) and b) show the variance $\sigma^2_{\Delta \boldsymbol{r},\mathrm{TE,O}}(\Delta t)$ and diffusion coefficient $D_\mathrm{O}(\Delta t)$ (inset) of obstacle motion for three different P_L and two obstacle area fractions, $\varphi_{A,\mathrm{O}} = 0.68$ and 0.74, respectively. They can be regarded as the equivalent to Figs. VII.8 a) and b), with P_L being the varying parameter instead of $\varphi_{A,\mathrm{O}}$. Obstacle area fractions are chosen so that they represent $\varphi_{A,\mathrm{O,c}} = 0.68$ and a value slightly above it. Curves in red and pink are also shown in Fig. VII.8 using the same colours. In accordance with Secs. VI.1 and VII.4.1, $\sigma^2_{\Delta \boldsymbol{r},\mathrm{TE,O}}(\Delta t)$ and $D_\mathrm{O}(\Delta t)$ follow the same trend for all three laser powers. After a diffusive regime for $\Delta t < t_{\mathrm{B,T}}$, obstacle dynamics are subdiffusive until $\Delta t > 100\, t_{\mathrm{B,T}}$. For larger times, obstacles are diffusive again with a reduced diffusion coefficient. The reduction in $D_\mathrm{O}(\Delta t)$ strongly depends on the applied P_L: for the laser power, $P_\mathrm{L} = 446$ mW, used in the previous Section VII.4, diffusion is slower by about an order of magnitude than with no external potential applied. A third measurement with a slightly reduced P_L for both $\varphi_{A,\mathrm{O}}$ results in a D_O for long times that lies between the values for $P_\mathrm{L} = 446$ mW and $P_\mathrm{L} = 0$ mW. The reason for this P_L-dependent diffusive behaviour of the obstacle particles was given in Sec. VI.1.

An additional aspect to consider beyond the previously discussed measurements is the effect concentration has on dynamics, even when $P_\mathrm{L} = 0$ (cf. Sec. VII.4.1). From Fig. VII.8 d), it can be seen that not all particles are affected in the same manner by the external potential at $P_\mathrm{L} = 446$ mW: most of them are trapped while some diffuse more freely. To visualise how this changes when P_L

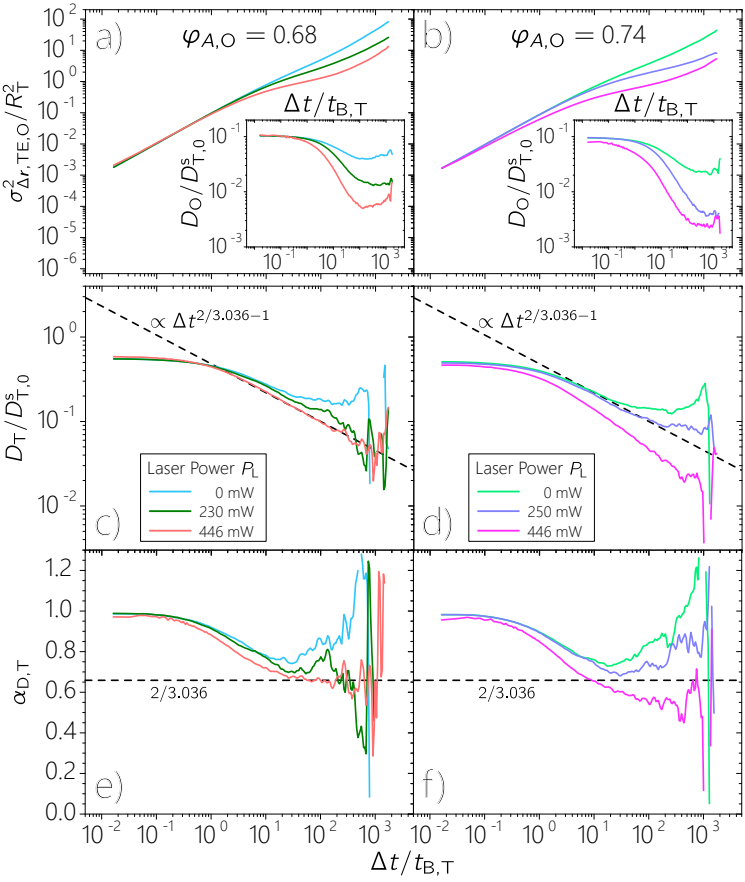

Figure VII.11: Obstacle and tracer dynamics for different P_L and two $\varphi_{A,O}$. a) and b) Normalised time- and ensemble-averaged variances of obstacle motion for $\varphi_{A,O} = 0.68$ and $\varphi_{A,O} = 0.74$ with the corresponding normalised diffusion coefficients as insets. c) and d) Normalised diffusion coefficients of tracer motion for $\varphi_{A,O} = 0.68$ and $\varphi_{A,O} = 0.74$ with the slope for the localisation transition drawn as dashed lines. e) and f) Anomalous diffusion exponents of tracer motion for $\varphi_{A,O} = 0.68$ and $\varphi_{A,O} = 0.74$ with the value for the localisation transition drawn as dashed lines.

is decreased, the time-averaged variances, $\sigma^2_{\Delta \boldsymbol{r},\mathrm{T,O}}(\Delta t)$, of 100 randomly chosen single obstacle particle trajectories from all obstacle particles present throughout a whole measurement are plotted in Fig. VII.12. It represents the same measurements shown in Fig. VII.11 b), where $\varphi_{A,\mathrm{O}} = 0.74$. Additionally, the probability density function of the logarithmically normalised time-averaged variance, $\mathcal{P}(\log(\sigma^2_{\Delta \boldsymbol{r},\mathrm{T,O}}))$, is shown for four times, $\Delta t \approx 0.1$, 1, 10 and 100 $t_{\mathrm{B,T}}$. These times are marked by the dashed lines on the left-hand side. Figure VII.12 indicates a strong reduction in the number of trapped obstacles as P_{L} is successively decreased. At $P_{\mathrm{L}} = 446$ mW, a large number of particles are trapped, showing $\sigma^2_{\Delta \boldsymbol{r},\mathrm{TO}} < R^2_{\mathrm{T}}$ for $\Delta t \approx 100\ t_{\mathrm{B,T}}$. This changes at $P_{\mathrm{L}} = 250$ mW and 0 mW, where the restriction of obstacle diffusion is largely weakened. Constantly trapped particles with levelling variances below R^2_{T} are no longer seen. In contrast to $P_{\mathrm{L}} = 446$ mW, the applied external potential energy landscape at lower powers does not feature strong enough traps to keep obstacle motion to a fraction of the tracer radius. At $P_{\mathrm{L}} = 0$ mW, obstacle particles are not trapped. They are only affected by neighbouring obstacles since $\varphi_{A,\mathrm{O}} \neq 0$. Thus there is a striking difference in obstacle dynamics for the three different laser powers as they go from being highly restricted for $P_{\mathrm{L}} = 446$ mW to a behaviour which only mildly deviates from Brownian motion.

How this difference manifests itself in the tracer motion can be seen in Figs. VII.11 c)–f). They show the normalised tracer diffusion coefficient, $D_{\mathrm{T}}(\Delta t)$, and anomalous diffusion exponent, $\alpha_{\mathrm{D,T}}(\Delta t)$, for the same $\varphi_{A,\mathrm{O}}$ and P_{L} for which the obstacle dynamics is shown in Figs. VII.11 a) and b). The curves in red and pink for $P_{\mathrm{L}} = 446$ mW are plotted in the same colours in Fig. VII.9 b) and c). The red curves in Fig. VII.11 c) and e) represent $\varphi_{A,\mathrm{O}} = \varphi_{A,\mathrm{O,c}} = 0.68$ at $P_{\mathrm{L}} = 446$ mW and thus exhibit the localisation transition-characteristic slope in $D_{\mathrm{T}}(\Delta t)$ and plateau in $\alpha_{\mathrm{D,T}}(\Delta t)$ (shown as dashed lines). When the laser power is lowered for $\varphi_{A,\mathrm{O}} = 0.68$, $D_{\mathrm{T}}(\Delta t)$ successively decays in a slower fashion. It even forms a plateau for $\Delta t > 100\ t_{\mathrm{B,T}}$ when no external potential is present. The same behaviour is reflected in $\alpha_{\mathrm{D,T}}(\Delta t)$, where a rising trend can be seen for $\Delta t \gtrsim 50\ t_{\mathrm{B,T}}$ when $P_{\mathrm{L}} = 230$ mW and a return to 1 when no potential is imposed on the ob-

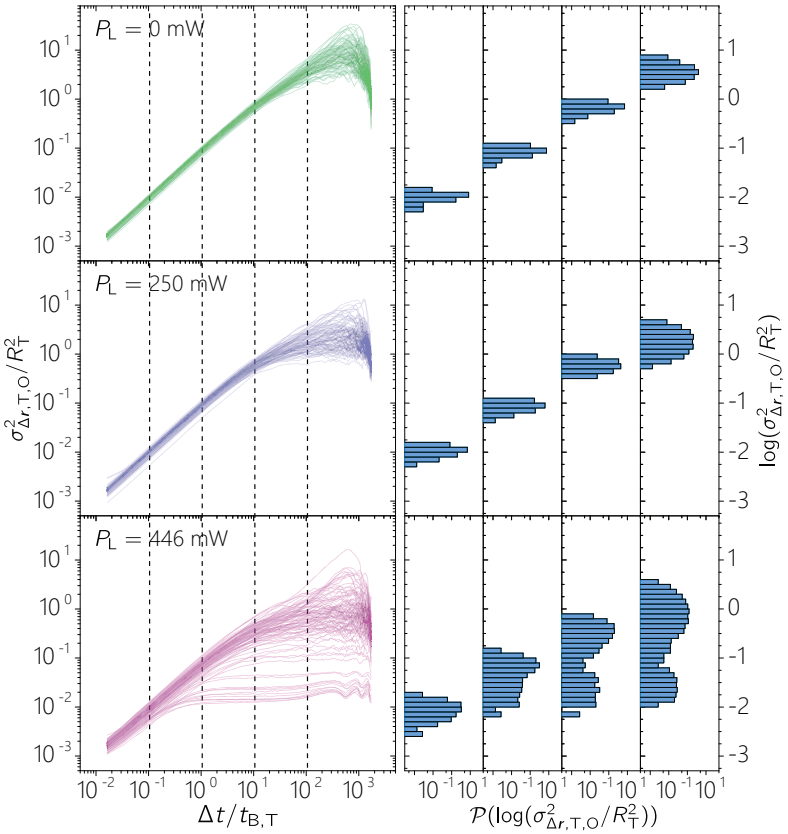

Figure VII.12: Time-averaged variances for single obstacle particle trajectories, each present the whole measurement, and the corresponding probability densities at times $\Delta t \approx 0.1$, 1, 10 and $100\,t_{B,T}$ for three different laser powers and $\varphi_{A,O} = 0.74$. For the sake of a better overview, 100 randomly chosen variances were plotted for each measurement.

stacles. A change of the previously found Lorentz gas-like behaviour, namely the localisation transition, to a rather transient subdiffusion takes place.

In Fig. VII.12 d) and f), the concentration lies above the localisation transition

with $\varphi_{A,O} = 0.74 > \varphi_{A,O,c}$. Still, tracer dynamics show the same reaction to a decreasing P_L that is found for the critical area fraction: instead of showing a localised diffusion indicated by $D_T(\Delta t)$ decreasing stronger than $\propto \Delta t^{2/3.036-1}$ as it is found for $P_L = 446$ mW, a plateau becomes apparent for long times. Accordingly, $\alpha_{D,T}(\Delta t)$ starts to rise for $\Delta t \gtrsim 50\, t_{B,T}$ similar to the case where P_L is decreased for $\varphi_{A,O} = \varphi_{A,O,c}$. Thus, independently of $\varphi_{A,O}$, the Lorentz gas-like system found for $P_L = 446$ mW is successively altered when laser powers are lowered. The formerly localised diffusion gives way to a transient subdiffusive behaviour. This stems from the obstacles no longer being trapped or highly restricted when $P_L < 446$ mW (cf. Fig. VII.12). Instead of obstacles forming a percolating void cluster at $\varphi_{A,O} = \varphi_{A,O,c}$, they diffuse up to an order of magnitude faster than they would at $P_L = 446$ mW. Consequently, void structures change more rapidly. Obstacles do not form a static, impermeable wall, but rather a diffusing layer that constantly changes its shape while it opens and closes holes through which tracers can diffuse. This does not resemble the situation of a Lorentz gas at the critical obstacle area fraction, but rather that of a freely diffusing binary mixture of small and big particles, which shows transient subdiffusion and Brownian motion for long times similar to what can be seen here [323]. The same argument works for $\varphi_{A,O} = 0.74$. There, no percolating void cluster but rather voids localising tracers are formed by the obstacles when $P_L = 446$ mW. For a lower laser power, these localising voids undergo steady structural change causing tracers to be delocalised. This leads to $D_T(\Delta t)$ exhibiting a plateau and $\alpha_{D,T}(\Delta t)$ returning to 1 for long times and implies long-time Brownian behaviour. The single-particle analysis of tracer motion, similar to the one for obstacle particles presented in Fig. VII.12, does not reveal any distinctive features other than the subdiffusive motion discussed in this paragraph and is therefore not shown here.

5.1 Discussion

In the previous section, it was found that, for long times, a transition from a Lorentz gas-like subdiffusive behaviour to normal diffusion occurs when obsta-

cles are mobilised. Such a transition has been described in the literature [314, 328, 333–335], albeit using slightly different approaches and systems.

Saxton [314, 333, 334] used point obstacles on lattices with point tracers conducting a random walk to non-occupied lattice points. For a system made up of immobile obstacles only, results agree with the diffusion in a percolating void presented in Sec. VII.1. He changed the ratio of immobile to mobile obstacles and also the rate with which mobile obstacles jump, i.e. the diffusion coefficient. Both lead to qualitatively the same result: the more mobile obstacles are present and the larger the diffusion coefficient of the obstacles, the sooner tracers tend to be diffusive and the faster their diffusion becomes. This agrees well with the findings discussed in this thesis, where a lower P_L leads to less-pronounced transient subdiffusion (cf. Fig. VII.11). Saxton emphasised the importance of obstacle motion-dependent time scales for the tracer dynamics [333], also in the context of measuring the obstructed motion in biological samples, where, depending on the technique, subdiffusion of tracers might be observed or not [314]. Applied to the results presented here, this raises the question of whether or not the continuous subdiffusive behaviour for $P_\mathrm{L} = 446$ mW is found to be diffusive at larger Δt. Longer observation times would, however, result in measurements taking days to weeks, which might not be feasible due to possible instabilities of the experimental setup.

Tremmel et al. [335] also found that mobile obstacles lead to a disappearance of the continuous subdiffusive tracer motion. Additionally, they extended Saxton's approach for different obstacle sizes and shapes. Bigger obstacles were found to yield an increased critical density. Thus spheres have to be concentrated higher than points to reach the localisation transition. Irregular shaped proteins as obstacles on the other hand were more efficient than spheres, resulting in a decreased critical area fraction.

Another simulation study by Berry et al. [328] was based on finite spherical tracers and obstacles, which could overlap. Although they used finite sized particles, they were said to be in the picometre range. Therefore, time scales cannot be compared to the results discussed here. For the case of immobile ob-

struction, they found results agreeing with [222], which is also close to the result found in Secs. VII.4.2 and discussed in Sec. VII.4.3. Furthermore, they extended their model to mobile Brownian, Ornstein-Uhlenbeck and polydisperse obstacles. Brownian obstacles were found to have the strongest effect on the localisation transition. Even for diffusion coefficients four orders of magnitude lower than that of the tracers, a change from the characteristic tracer subdiffusion, i.e. localisation, to a transient subdiffusive behaviour is found. Ornstein-Uhlenbeck particles are more effective obstacles. They also conduct Brownian motion but feature a feedback relaxation which restricts them to an area around their average position. When these obstacles are present, the Lorentz gas-like subdiffusive behaviour for tracers is found for obstacle diffusion coefficients more than an order of magnitude below the short-time tracer diffusion. This observation agrees well with the results shown in Fig. VII.11. As P_{L} is decreased, obstacle particles become more Brownian. This in turn leads to the diffusive tracer motion at long times, similar to [328]. Polydispersity of obstacles on the other hand is not found to have a strong influence in the simulations of Berry et al.. Thus, the particle size distribution does not seem to play an important role as long as the amount of void area stays the same.

Finally, obstructed motion with mobile obstacles is of great interest for biomolecules. Saxton [333] explained the motion of a lipid in a membrane with mobile obstacles hindering it. Tremmel et al. [335] used the idea to describe the diffusion of molecules hindered by proteins in a chloroplast membrane. Protein lateral movements in lipid bilayers are said to be diffusive for long times due to mobile obstacles [336]. Similarly, the unique subdiffusive behaviour of molecular motion on cells [337, 338] could be explained by mobile, not immobile obstacles [328].

VIII Conclusions

In this thesis, a set of examples of driven and obstructed dynamics of colloidal particles in one- and two-dimensional random potentials have been discussed. In Chapter IV, particles quenched by a one-dimensional random potential were in focus. It was found that the quench led to a temporarily enhanced diffusion coefficient while the particles relaxed into the potential minima and subsequently showed subdiffusion. The obtained experimental results agree well with simulations. The characteristics of the transient superdiffusion depends on the roughness of the external potential, σ_U, where the maximum of the diffusion coefficient showed a linear increase and the time at which the maximum was reached a logarithmic decrease with increasing σ_U. Furthermore, the normalised excess kurtosis transiently showed negative values indicating a broadening of the shoulders in the van-Hove function. Similar observations were made for simulated random, periodic and quasicrystalline potentials.

Building on those findings, particles were periodically quenched by similar one-dimensional potentials in Chapter V. Depending on the frequency with which the realisations of the external potential were changed, the long-time diffusion coefficient of the colloids was reduced, enhanced or unaffected resembling a resonance curve-like behaviour. For very large periods, a behaviour similar to that discussed in Chapter IV was found. Intermediate periods led to a strong enhancement with particles being constantly driven by the change of potentials with the optimum period, τ_0, showing the strongest enhancement. For small periods, the realisation of the random potential was changed too fast for the colloids to react. Thus, they showed Brownian motion. The shape of the oscillations of the time-dependent diffusion coefficient revealed whether the potential they were exposed to varied with a period above or below the optimum. Convex oscilla-

tions indicated periods lower than τ_0 while concave oscillations were caused by periods larger than the optimum. Again, the experimental results showed good agreement with simulations. The dynamics in this system showed similarities to resonance phenomena like stochastic resonance and resonant activation, where the latter showed the closest relations to the characteristics found here.

After a couple of one-dimensional problems had been discussed, Chapter VI concerned the exertion of a two-dimensional random potential on driven colloidal particles. Both the force with which the particles were dragged and the roughness of the random potential were changed. The particle dynamics was separately analysed for the direction parallel to the drag force (x-direction) and that perpendicular to it (y-direction). Independent of the absolute values of drag force and potential roughness, five different regimes could be found for the motion in x-direction. When no drag force was present, the particles showed the same dynamics that was discussed in the literature for diffusion in one- and two-dimensional random potentials. For small forces, only a few particles were dragged out of the local potential minima and thus the van-Hove function exhibited asymmetry with a leading tail. Intermediate drag forces led on average to a compensation of this very force and forces due to the random potential. The van-Hove function was stretched resulting in a strong enhancement of the diffusion coefficient and a negative normalised excess kurtosis. When drag forces were large, most particles were dragged out of the local potential minima and the van-Hove function showed asymmetry with a trailing tail. For even larger forces, the external potential was weaker than the drag force resulting in Brownian motion with a mean displacement reflecting the drag velocity. The drag force-dependent enhancement of the diffusion coefficient was compared to the case of giant diffusion which exhibits similar results. In the y-direction, the subdiffusive behaviour found without a drag force was successively mitigated when drag forces became larger. For the largest drag force, the dynamics in x- and y-direction became similar. Additionally, the first-passage times were discussed showing strong deviations from theory with the long-time tail decaying successively slower for larger potential roughnesses.

The last experiment in this thesis is discussed in Chapter VII and is based on the same setup used in Chapter VI. This time, a sample made up of two particle species with different sizes is placed inside the two-dimensional random potential. The bigger particles, also referred to as obstacles, reacted more strongly to the external potential than the smaller ones, called tracers, and were thus restricted in their motion while the tracers almost diffused as if they were free. Depending on the concentration of the obstacles, they formed random labyrinth-like structures with voids in which the tracers could diffuse. For small obstacle concentrations, the long-time tracer dynamics was diffusive while for large concentrations, it became subdiffusive. In between these two extremes there was a critical concentration that resembled a localisation transition of the network formed by the obstacles. Thus the findings were similar to the dynamics of tracers diffusing inside a Lorentz gas. Furthermore, the obstacle motion could be tuned by the roughness of the external potential. By lowering σ_U, the obstacles became more mobile. This resulted in a mitigation of the localisation transition and in the tracers showing long-time diffusion instead of subdiffusion.

References

[1] G. M. Cooper and R. E. Hausman. **The Cell: A Molecular Approach**. 4. ed. Washington DC: ASM Press, 2007.

[2] H. Terashima, S. Kojima, and M. Homma. **Chapter 2: Flagellar Motility in Bacteria**. In: *Volume 270*. Vol. 270. International Review of Cell and Molecular Biology. Elsevier, 2008, pp. 39–85. DOI: 10.1016/S1937-6448(08)01402-0.

[3] C. Di Rienzo et al. **Probing short-range protein Brownian motion in the cytoplasm of living cells**. In: Nature communications 5 (2014), p. 5891. DOI: 10.1038/ncomms6891.

[4] B. J. Sung and A. Yethiraj. **Lateral diffusion and percolation in membranes**. In: Physical review letters 96.22 (2006), p. 228103. DOI: 10.1103/PhysRevLett.96.228103.

[5] F. Höfling and T. Franosch. **Anomalous transport in the crowded world of biological cells**. In: Reports on progress in physics. Physical Society (Great Britain) 76.4 (2013), p. 046602. DOI: 10.1088/0034-4885/76/4/046602.

[6] P. Polanowski and A. Sikorski. **Simulation of Molecular Transport in Systems Containing Mobile Obstacles**. In: The journal of physical chemistry. B 120.30 (2016), pp. 7529–7537. DOI: 10.1021/acs.jpcb.6b02682.

[7] K. Norregaard et al. **Manipulation and Motion of Organelles and Single Molecules in Living Cells**. In: Chemical reviews 117.5 (2017), pp. 4342–4375. DOI: 10.1021/acs.chemrev.6b00638.

[8] C. Bechinger et al. **Active Particles in Complex and Crowded Environments**. In: Reviews of Modern Physics 88.4 (2016), p. 1. DOI: 10.1103/RevModPhys.88.045006.

[9] H. Khalilian and H. Fazli. **Obstruction enhances the diffusivity of self-propelled rod-like particles**. In: The Journal of chemical physics 145.16 (2016), p. 164909. DOI: 10.1063/1.4966188.

[10] H. L. Peng, D. M. Herlach, and Th. Voigtmann. **Crystal growth in fluid flow: Nonlinear response effects**. In: Physical Review Materials 1.3 (2017). DOI: 10.1103/PhysRevMaterials.1.030401.

[11] T. Sentjabrskaja, M. Laurati, and S. U. Egelhaaf. **One- and two-component colloidal glasses under transient shear**. In: The European Physical Journal Special Topics 226.14 (2017), pp. 3023–3037. DOI: 10.1140/epjst/e2017-70076-0.

[12] H. Vandebroek and C. Vanderzande. **The effect of active fluctuations on the dynamics of particles, motors and DNA-hairpins**. In: Soft Matter 13.11 (2017), pp. 2181–2191. DOI: 10.1039/c6sm02568d.

[13] J. Horbach, N. H. Siboni, and S. K. Schnyder. **Anomalous transport in heterogeneous media**. In: The European Physical Journal Special Topics 226.14 (2017), pp. 3113–3128. DOI: 10.1140/epjst/e2017-70081-3.

[14] A. Yethiraj and A. van Blaaderen. **A colloidal model system with an interaction tunable from hard sphere to soft and dipolar**. In: Nature 421.6922 (2003), pp. 513–517. DOI: 10.1038/nature01328.

[15] W. C. K. Poon. **Colloids as big atoms**. In: Science (New York, N.Y.) 304.5672 (2004), pp. 830–831. DOI: 10.1126/science.1097964.

[16] V. N. Manoharan. **Colloidal matter: Packing, geometry, and entropy**. In: Science (New York, N.Y.) 349.6251 (2015), p. 1253751. DOI: 10.1126/science.1253751.

[17] J. Perrin. **Mouvement Brownien et réalité moléculaire**. In: Annales de Chimie et de Physique 18 (1909), pp. 5–114.

[18] T. Bohlein, J. Mikhael, and C. Bechinger. **Observation of kinks and antikinks in colloidal monolayers driven across ordered surfaces**. In: Nature Materials 11.2 (2011), pp. 126–130. DOI: 10.1038/NMAT3204.

[19] G. Boniello et al. **Brownian diffusion of a partially wetted colloid**. In: Nature Materials 14.9 (2015), pp. 908–911. DOI: 10.1038/nmat4348.

[20] T. Sentjabrskaja et al. **Anomalous dynamics of intruders in a crowded environment of mobile obstacles**. In: Nature communications 7 (2016), p. 11133. DOI: 10.1038/ncomms11133.

[21] I. Williams et al. **Direct measurement of osmotic pressure via adaptive confinement of quasi hard disc colloids**. In: Nature communications 4 (2013), p. 2555. DOI: 10.1038/ncomms3555.

[22] T. Dabroś and T. G. M. van de Ven. **A direct method for studying particle deposition onto solid surfaces**. In: Colloid and Polymer Science 261.8 (1983), pp. 694–707. DOI: 10.1007/BF01415042.

[23] E. Allahyarov et al. **Crystallization seeds favour crystallization only during initial growth**. In: Nature communications 6 (2015), p. 7110. DOI: 10.1038/ncomms8110.

[24] Y. Han et al. **Brownian motion of an ellipsoid**. In: Science (New York, N.Y.) 314.5799 (2006), pp. 626–630. DOI: 10.1126/science.1130146.

[25] V. Meester and D. J. Kraft. **Spherical, Dimpled, and Crumpled Hybrid Colloids with Tunable Surface Morphology**. In: Langmuir : the ACS journal of surfaces and colloids (2016). DOI: 10.1021/acs.langmuir.6b02952.

[26] E. Bianchi, R. Blaak, and C. N. Likos. **Patchy colloids: State of the art and perspectives**. In: Physical chemistry chemical physics : PCCP 13.14 (2011), pp. 6397–6410. DOI: 10.1039/C0CP02296A.

[27] M. N. Juniper et al. **Acousto-optically generated potential energy landscapes: Potential mapping using colloids under flow**. In: Optics Express 20.27 (2012), p. 28707. DOI: 10.1364/OE.20.028707.

[28] S. Das et al. **Boundaries can steer active Janus spheres**. In: Nature communications 6 (2015), p. 8999. DOI: 10.1038/ncomms9999.

[29] X.-g. Ma et al. **Colloidal transport and diffusion over a tilted periodic potential: dynamics of individual particles**. In: Soft Matter 11.6 (2015), pp. 1182–1196. DOI: 10.1039/c4sm02387k.

[30] P. Tierno. **Depinning and Collective Dynamics of Magnetically Driven Colloidal Monolayers**. In: Physical Review Letters 109.19 (2012). DOI: 10.1103/PhysRevLett.109.198304.

[31] J. E. Molloy and M. J. Padgett. **Lights, action: Optical tweezers**. In: Contemporary Physics 43.4 (2002), pp. 241–258. DOI: 10.1080/00107510110116051.

[32] A. Gopinathan and D. G. Grier. **Statistically Locked-In Transport through Periodic Potential Landscapes**. In: Physical Review Letters 92.13 (2004). DOI: 10.1103/PhysRevLett.92.130602.

[33] M. Evstigneev et al. **Diffusion of colloidal particles in a tilted periodic potential: Theory versus experiment**. In: Physical Review E 77.4 (2008). DOI: 10.1103/PhysRevE.77.041107.

[34] C. Dalle-Ferrier et al. **Dynamics of dilute colloidal suspensions in modulated potentials**. In: Soft Matter 7.5 (2011), p. 2064. DOI: 10.1039/c0sm01051k.

[35] M. Slutsky and L. A. Mirny. **Kinetics of protein-DNA interaction: facilitated target location in sequence-dependent potential**. In: Biophysical Journal 87.6 (2004), pp. 4021–4035. DOI: 10.1529/biophysj.104.050765.

[36] F. U. Hartl and M. Hayer-Hartl. **Converging concepts of protein folding in vitro and in vivo**. In: Nature structural & molecular biology 16.6 (2009), pp. 574–581. DOI: 10.1038/nsmb.1591.

[37] A. Heuer. **Exploring the potential energy landscape of glass-forming systems: from inherent structures via metabasins to macroscopic transport**. In: Journal of Physics: Condensed Matter 20.37 (2008), p. 373101. DOI: 10.1088/0953-8984/20/37/373101.

[38] M. Sahimi. **Flow phenomena in rocks: From continuum models to fractals, percolation, cellular automata, and simulated annealing**. In: Reviews of Modern Physics 65.4 (1993), pp. 1393–1534. DOI: 10.1103/RevModPhys.65.1393.

[39] B. Jamtveit and B. W. D. Yardley. **Fluid Flow and Transport in Rocks**. Dordrecht: Springer Netherlands, 1996. DOI: 10.1007/978-94-009-1533-6.

[40] I. W. Hamley. **Introduction to Soft Matter: Synthetic and Biological Self-Assembling Materials**. Rev. ed. Chichester et al.: John Wiley & Sons, 2007.

[41] S. U. Egelhaaf. **Experimental Soft Matter Physics**. Skript. Düsseldorf: Heinrich-Heine-Universität, 2011.

[42] R. A. L. Jones. **Soft condensed matter**. Reprinted. Vol. 6. Oxford master series in condensed matter physics. Oxford: Oxford Univ. Press, 2002.

[43] OCAL. **Double Helix clip art**. Website. URL: http://www.clker.com/clipart-3261.html (visited on 10/02/2017).

[44] Wikimedia Foundation Inc. **Water molecule**. Website. URL: https://commons.wikimedia.org/wiki/File:Water_molecule.svg (visited on 10/02/2017).

[45] Wikimedia Foundation Inc. **Main protein structure levels en**. Website. URL: https://commons.wikimedia.org/wiki/File:Main_protein_structure_levels_en.svg (visited on 10/02/2017).

[46] Shawn Hagenes. **Ink Splat Clipart**. Website. URL: https://clipartfest.com/download/9FyhtVm (visited on 10/02/2017).

[47] WPClipart. **Glass of beer**. Website. URL: https://www.wpclipart.com/food/beverages/alcohol/beer/more_beer/glass_of_beer.png.html (visited on 10/02/2017).

[48] Simple Icon. **Wifi Signal**. Website. URL: http://simpleicon.com/wifi-signal.html (visited on 10/02/2017).

[49] Wikimedia Foundation Inc. **Rubik's cube scrambled**. Website. URL: https://commons.wikimedia.org/wiki/File:Rubik%27s_cube_scrambled.svg (visited on 10/02/2017).

[50] Universität Wien Wiki der Fakultät für Physik. **Einfuehrung Optik Arndt Glasfaser**. Website. URL: https://www.univie.ac.at/physikwiki/index.php?title=Datei:Einfuehrung_Optik_Arndt_Glasfaser.svg&limit=500 (visited on 10/02/2017).

[51] M. Doi. **Soft matter physics**. 1. ed. Oxford u.a.: Oxford Univ. Press, 2013.

[52] T. A. Witten and P. A. Pincus. **Structured fluids: Polymers, colloids, surfactants**. Oxford: Oxford University Press, 2010. URL: http://search.ebscohost.com/login.aspx?direct=true&scope=site&db=nlebk&db=nlabk&AN=330476.

[53] R. M. Pashley and M. E. Karaman. **Applied colloid and surface chemistry**. Chichester: Wiley, 2004.

[54] D. H. Everett. **Basic Principles of Colloid Science**. Royal Society of Chemistry paperbacks. London: Royal Soc. of Chemistry, 1988.

[55] J. W. Goodwin. **Colloids and interfaces with surfactants and polymers**. 2nd ed. Chichester, U.K: Wiley, 2009. URL: http://site.ebrary.com/lib/alltitles/docDetail.action?docID=10325849.

[56] Chemistry World. **The impact of colloid science**. Website. URL: http://www.rsc.org/chemistryworld/Issues/2003/February/science.asp (visited on 05/02/2015).

[57] J. R. Howse et al. **Self-motile colloidal particles: from directed propulsion to random walk**. In: Physical Review Letters 99.4 (2007), p. 048102. DOI: 10.1103/PhysRevLett.99.048102.

[58] G. H. Koenderink et al. **An active biopolymer network controlled by molecular motors**. In: Proceedings of the National Academy of Sciences of the United States of America 106.36 (2009), pp. 15192–15197. DOI: 10.1073/pnas.0903974106.

[59] S. J. Ebbens and J. R. Howse. **In pursuit of propulsion at the nanoscale**. In: Soft Matter 6.4 (2010), p. 726. DOI: 10.1039/b918598d.

[60] I. Buttinoni et al. **Active Brownian motion tunable by light**. In: Journal of physics. Condensed matter : an Institute of Physics journal 24.28 (2012), p. 284129. DOI: 10.1088/0953-8984/24/28/284129.

[61] J. Prost, F. Jülicher, and J.-F. Joanny. **Active gel physics**. In: Nature Physics 11.2 (2015), pp. 111–117. DOI: 10.1038/NPHYS3224.

[62] W. Gao et al. **Bioinspired helical microswimmers based on vascular plants**. In: Nano letters 14.1 (2014), pp. 305–310. DOI: 10.1021/nl404044d.

[63] D. J. Shaw. **Introduction to colloid and surface chemistry**. 4. ed., repr. Oxford u.a.: Butterworth-Heinemann, 1997.

[64] Jacob N. Israelachvili. **Intermolecular and surface forces**. 2. ed., [corr. repr.] Amsterdam u.a.: Elsevier, 1998.

[65] L. Dong and D. Johnson. **Surface Tension of Charge-Stabilized Colloidal Suspensions at the Water-Air Interface**. In: Langmuir 19.24 (2003), pp. 10205–10209. DOI: 10.1021/la035128j.

[66] M. Karg et al. **Multiresponsive hybrid colloids based on gold nanorods and poly(NIPAM-co-allylacetic acid) microgels: temperature- and pH-tunable plasmon resonance**. In: Langmuir : the ACS journal of surfaces and colloids 25.5 (2009), pp. 3163–3167. DOI: 10.1021/la803458j.

[67] W. B. Rogers and J. C. Crocker. **Direct measurements of DNA-mediated colloidal interactions and their quantitative modeling**. In: Proceedings of the National Academy of Sciences of the United States of America 108.38 (2011), pp. 15687–15692. DOI: 10.1073/pnas.1109853108.

[68] Atextures. **Smoke Abstract Background Thirty Two**. Website. URL: http://atextures.com/smoke-abstract-background-thirty-two/ (visited on 05/03/2015).

[69] Eskipaper. **Paint 3**. Website. URL: http://eskipaper.com/paint-3.html#gal_post_65936_paint-3.jpg (visited on 05/03/2015).

[70] Magic 4 Walls. **Close up of milk splashing out of glass on black background photo**. Website. URL: http://www.magic4walls.com/wallpaper/close-up-of-milk-splashing-out-of-glass-on-black-background-photo-241.html (visited on 05/03/2015).

[71] M. A. Rutgers et al. **Measurement of the hard-sphere equation of state using screened charged polystyrene colloids**. In: Physical Review B 53.9 (1996), pp. 5043–5046. DOI: 10.1103/PhysRevB.53.5043.

[72] A. D. Dinsmore, A. G. Yodh, and D. J. Pine. **Phase diagrams of nearly-hard-sphere binary colloids**. In: Physical Review E 52.4 (1995), pp. 4045–4057. DOI: 10.1103/PhysRevE.52.4045.

[73] R. Brown. **Microscopical Observations On The Particles Contained In The Pollen of Plants**. In: Edinburgh new Philosophical Journal (1828), pp. 358–371.

[74] A. Einstein. **Über die von der molekularkinetischen Theorie der Wärme geforderte Bewegung von in ruhenden Flüssigkeiten suspendierten Teilchen**. In: Annalen der Physik 322.8 (1905), pp. 549–560. DOI: 10.1002/andp.19053220806.

[75] D. S. Lemons. **Paul Langevin's 1908 paper "On the Theory of Brownian Motion" ["Sur la théorie du mouvement brownien," C. R. Acad. Sci. (Paris) 146, 530–533 (1908)]**. In: American Journal of Physics 65.11 (1997), p. 1079. DOI: 10.1119/1.18725.

[76] F. Reif. **Fundamentals of statistical and thermal physics**. McGraw-Hill series in fundamentals of physics. New York u.a: McGraw-Hill, 1965.

[77] P. H. Westfall and K. S. S. Henning. **Understanding Advanced Statistical Methods**. Chapman & Hall / CRC Texts in Statistical Science. Hoboken: CRC Press, 2013. URL: http://gbv.eblib.com/patron/FullRecord.aspx?p=1438156.

[78] A. R. Dinner and S. A. Rice. **Advances in Chemical Physics: Volume 148**. Vol. 148. Advances in Chemical Physics. Hoboken, NJ: Wiley, 2012.

[79] Yu. P. Syrnikov. **Current concepts on thermal motion in liquids and the concepts of positive and negative hydration**. In: Journal of Structural Chemistry 25.2 (1984), pp. 215–219. DOI: 10.1007/BF00747340.

[80] E. R. Weeks and D.A Weitz. **Subdiffusion and the cage effect studied near the colloidal glass transition**. In: Chemical Physics 284.1-2 (2002), pp. 361–367. DOI: 10.1016/S0301-0104(02)00667-5.

[81] E. Kepten et al. **Guidelines for the fitting of anomalous diffusion mean square displacement graphs from single particle tracking experiments**. In: PloS one 10.2 (2015), e0117722. DOI: 10.1371/journal.pone.0117722.

[82] I. M. Sokolov. **Models of anomalous diffusion in crowded environments**. In: Soft Matter 8.35 (2012), p. 9043. DOI: 10.1039/c2sm25701g.

[83] E. W. Montroll and G. H. Weiss. **Random walks on lattices. II**. In: Journal of Mathematical Physics 6.2 (1965), pp. 167–181. DOI: 10.1063/1.1704269.

[84] J.-H. Jeon et al. **In vivo anomalous diffusion and weak ergodicity breaking of lipid granules**. In: Physical review letters 106.4 (2011), p. 048103. DOI: 10.1103/PhysRevLett.106.048103.

[85] S. M. A. Tabei et al. **Intracellular transport of insulin granules is a subordinated random walk**. In: Proceedings of the National Academy of Sciences of the United States of America 110.13 (2013), pp. 4911–4916. DOI: 10.1073/pnas.1221962110.

[86] J. Klafter and I. M. Sokolov. **First Steps in Random Walks: From Tools to Applications**. Oxford: OUP Oxford, 2011. URL: http://site.ebrary.com/lib/alltitles/docDetail.action?docID=10691670.

[87] S. Redner. **A Guide to First-Passage Processes**. 1. publ. Cambridge: Cambridge Univ. Pr, 2001.

[88] R. Metzler et al. **Anomalous diffusion models and their properties: non-stationarity, non-ergodicity, and ageing at the centenary of single particle tracking**. In: Physical chemistry chemical physics : PCCP 16.44 (2014), pp. 24128–24164. DOI: 10.1039/C4CP03465A.

[89] B. Dybiec et al. **Lévy flights versus Lévy walks in bounded domains**. In: Physical review. E 95.5-1 (2017), p. 052102. DOI: 10.1103/PhysRevE.95.052102.

[90] K. Burnecki et al. **Universal algorithm for identification of fractional Brownian motion. A case of telomere subdiffusion**. In: Biophysical Journal 103.9 (2012), pp. 1839–1847. DOI: 10.1016/j.bpj.2012.09.040.

[91] B. B. Mandelbrot and J. W. van Ness. **Fractional Brownian Motions, Fractional Noises and Applications**. In: SIAM Review 10.4 (1968), pp. 422–437. DOI: 10.1137/1010093.

[92] N. Enriquez. **A simple construction of the fractional Brownian motion**. In: Stochastic Processes and their Applications 109.2 (2004), pp. 203–223. DOI: 10.1016/j.spa.2003.10.008.

[93] C. C. Bernido et al., eds. **Stochastic and Infinite Dimensional Analysis**. Switzerland: Birkhäuser, 2016. URL: http://lib.myilibrary.com/detail.asp?ID=947581.

[94] J. Kursawe, J. Schulz, and R. Metzler. **Transient aging in fractional Brownian and Langevin-equation motion**. In: Physical review. E, Statistical, nonlinear, and soft matter physics 88.6 (2013), p. 062124. DOI: 10.1103/PhysRevE.88.062124.

[95] L. P. Sanders and T. Ambjörnsson. **First passage times for a tracer particle in single file diffusion and fractional Brownian motion**. In: The Journal of chemical physics 136.17 (2012), p. 175103. DOI: 10.1063/1.4707349.

[96] Q. Wei, C. Bechinger, and P. Leiderer. **Single-file diffusion of colloids in one-dimensional channels**. In: Science 287.5453 (2000), pp. 625–627. DOI: 10.1126/science.287.5453.625.

[97] M. Magdziarz et al. **Fractional brownian motion versus the continuous-time random walk: a simple test for subdiffusive dynamics**. In: Physical review letters 103.18 (2009), p. 180602. DOI: 10.1103/PhysRevLett.103.180602.

[98] R. Metzler. **Weak ergodicity breaking and ageing in anomalous diffusion**. In: International Journal of Modern Physics: Conference Series 36 (2015), p. 1560007. DOI: 10.1142/S2010194515600071.

[99] D. ben-Avraham and S. Havlin. **Diffusion and Reactions in Fractals and Disordered Systems**. 1. publ. Cambridge: Cambridge Univ. Press, 2000.

[100] A. G. Cherstvy, A. V. Chechkin, and R. Metzler. **Particle invasion, survival, and non-ergodicity in 2D diffusion processes with space-dependent diffusivity**. In: Soft Matter 10.10 (2014), pp. 1591–1601. DOI: 10.1039/C3SM52846D.

[101] A. G. Cherstvy and R. Metzler. **Population splitting, trapping, and non-ergodicity in heterogeneous diffusion processes**. In: Physical chemistry chemical physics : PCCP 15.46 (2013), pp. 20220–20235. DOI: 10.1039/c3cp53056f.

[102] Timo A. Nieminen et al. **Optical tweezers: Theory and modelling**. In: Journal of Quantitative Spectroscopy and Radiative Transfer 146 (2014), pp. 59–80. DOI: 10.1016/j.jqsrt.2014.04.003.

[103] K. Dholakia, P. Reece, and M. Gu. **Optical micromanipulation**. In: Chemical Society Reviews 37.1 (2007), p. 42. DOI: 10.1039/b512471a.

[104] A. Ashkin. **Acceleration and trapping of particles by radiation pressure**. In: Physical Review Letters 24.4 (1970), pp. 156–159. DOI: 10.1103/PhysRevLett.24.156.

[105] A. Ashkin et al. **Observation of a single-beam gradient force optical trap for dielectric particles**. In: Optics Letters 11.5 (1986), p. 288. DOI: 10.1364/OL.11.000288.

[106] S. Chu et al. **Three-dimensional viscous confinement and cooling of atoms by resonance radiation pressure**. In: Physical review letters 55.1 (1985), pp. 48–51. DOI: 10.1103/PhysRevLett.55.48.

[107] S. Chu et al. **Experimental observation of optically trapped atoms**. In: Physical review letters 57.3 (1986), pp. 314–317. DOI: 10.1103/PhysRevLett.57.314.

[108] Nobelprize.org. **The Nobel Prize in Physics 1997**. Website. URL: http://www.nobelprize.org/nobel_prizes/physics/laureates/1997/illpres/ (visited on 05/09/2015).

[109] T. Čižmár et al. **Multiple optical trapping and binding: new routes to self-assembly**. In: Journal of Physics B: Atomic, Molecular and Optical Physics 43.10 (2010), p. 102001. DOI: 10.1088/0953-4075/43/10/102001.

[110] David G. Grier. **A revolution in optical manipulation**. In: Nature 424.6950 (2003), pp. 810–816. DOI: 10.1038/nature01935.

[111] P. C. Ke and M. Gu. **Characterization of trapping force in the presence of spherical aberration**. In: Journal of Modern Optics 45.10 (1998), pp. 2159–2168. DOI: 10.1080/09500349808231752.

[112] H. Kim et al. **Dependence of the Optical Trapping Efficiency on the Ratio of the Beam Radius-to-the Aperture Radius**. In: Journal of the Korean Physical Society, 43.3 (2003), pp. 348–351.

[113] N. Malagnino et al. **Measurements of trapping efficiency and stiffness in optical tweezers**. In: Optics Communications 214.1-6 (2002), pp. 15–24. DOI: 10.1016/S0030-4018(02)02119-3.

[114] V. Kahl et al. **Microelectrophoresis in a laser trap: A platform for measuring electrokinetic interactions and flow properties within microstructures**. In: Review of Scientific Instruments 80.7 (2009), p. 073704. DOI: 10.1063/1.3169511.

[115] K. Dholakia and T. Čižmár. **Shaping the future of manipulation**. In: Nature Photonics 5.6 (2011), pp. 335–342. DOI: 10.1038/nphoton.2011.80.

[116] A. Rohrbach. **Stiffness of optical traps: quantitative agreement between experiment and electromagnetic theory**. In: Physical review letters 95.16 (2005), p. 168102. DOI: 10.1103/PhysRevLett.95.168102.

[117] G. Roosen. **La lévitation optique de sphères**. In: Canadian Journal of Physics 57.9 (1979), pp. 1260–1279. DOI: 10.1139/p79-175.

[118] A. Ashkin. **Forces of a single-beam gradient laser trap on a dielectric sphere in the ray optics regime**. In: Biophysical Journal 61.2 (1992), pp. 569–582. DOI: 10.1016/S0006-3495(92)81860-X.

[119] J. P. Gordon. **Radiation Forces and Momenta in Dielectric Media**. In: Physical Review A 8.1 (1973), pp. 14–21. DOI: 10.1103/PhysRevA.8.14.

[120] Y. Harada and T. Asakura. **Radiation forces on a dielectric sphere in the Rayleigh scattering regime**. In: Optics Communications 124.5-6 (1996), pp. 529–541. DOI: 10.1016/0030-4018(95)00753-9.

[121] J. D. Jackson. **Klassische Elektrodynamik**. Berlin u.a: de Gruyter, 2006.

[122] K. Svoboda and S. M. Block. **Biological Applications of Optical Forces**. In: Annual Review of Biophysics and Biomolecular Structure 23.1 (1994), pp. 247–285. DOI: 10.1146/annurev.bb.23.060194.001335.

[123] H. Furukawa and I. Yamaguchi. **Optical trapping of metallic particles by a fixed Gaussian beam**. In: Optics Letters 23.3 (1998), p. 216. DOI: 10.1364/OL.23.000216.

[124] P. M. Hansen et al. **Expanding the optical trapping range of gold nanoparticles**. In: Nano letters 5.10 (2005), pp. 1937–1942. DOI: 10.1021/nl051289r.

[125] F. Hajizadeh and S. Nader S. Reihani. **Optimized optical trapping of gold nanoparticles**. In: Optics express 18.2 (2010), pp. 551–559. DOI: 10.1364/OE.18.000551.

[126] T. Bohlein and C. Bechinger. **Experimental Observation of Directional Locking and Dynamical Ordering of Colloidal Monolayers Driven across Quasiperiodic Substrates**. In: Physical Review Letters 109.5 (2012). DOI: 10.1103/PhysRevLett.109.058301.

[127] G. Mie. **Beiträge zur Optik trüber Medien, speziell kolloidaler Metallösungen**. In: Annalen der Physik 330.3 (1908), pp. 377–445. DOI: 10.1002/andp.19083300302.

[128] G. Gouesbet and G. Grehan. **On the scattering of light by a Mie scatter center located on the axis of an axisymmetric light profile**. In: Journal of Optics 13.2 (1982), pp. 97–103. DOI: 10.1088/0150-536X/13/2/006.

[129] K. C. Neuman and S. M. Block. **Optical trapping**. In: Review of Scientific Instruments 75.9 (2004), p. 2787. DOI: 10.1063/1.1785844.

[130] T. A. Nieminen et al. **Optical tweezers computational toolbox**. In: Journal of Optics A: Pure and Applied Optics 9.8 (2007), S196–S203. DOI: 10.1088/1464-4258/9/8/S12.

[131] R. D. L. Hanes et al. **Colloids in one dimensional random energy landscapes**. In: Soft Matter 8.9 (2012), p. 2714. DOI: 10.1039/c2sm07102a.

[132] C. Lutz et al. **Diffusion of colloids in one-dimensional light channels**. In: Journal of Physics: Condensed Matter 16.38 (2004), S4075–S4083. DOI: 10.1088/0953-8984/16/38/022.

[133] C. Lutz, M. Kollmann, and C. Bechinger. **Single-file diffusion of colloids in one-dimensional channels**. In: Physical Review Letters 93.2 (2004). DOI: 10.1103/PhysRevLett.93.026001.

[134] M. P. N. Juniper et al. **Microscopic dynamics of synchronization in driven colloids**. In: Nature communications 6 (2015), p. 7187. DOI: 10.1038/ncomms8187.

[135] F. Evers et al. **Particle dynamics in two-dimensional random-energy landscapes: Experiments and simulations**. In: Physical Review E 88.2 (2013). DOI: 10.1103/PhysRevE.88.022125.

[136] G. Volpe, G. Volpe, and Sylvain Gigan. **Brownian Motion in a Speckle Light Field: Tunable Anomalous Diffusion and Selective Optical Manipulation**. In: Scientific Reports 4 (2014). DOI: 10.1038/srep03936.

[137] M. C. Jenkins and S. U. Egelhaaf. **Colloidal suspensions in modulated light fields**. In: Journal of Physics: Condensed Matter 20.40 (2008), p. 404220. DOI: 10.1088/0953-8984/20/40/404220.

[138] J. Bewerunge and S. U. Egelhaaf. **Experimental creation and characterization of random potential-energy landscapes exploiting speckle patterns**. In: Physical Review A 93.1 (2016). DOI: 10.1103/PhysRevA.93.013806.

[139] K. M. Douglass, S. Sukhov, and A. Dogariu. **Superdiffusion in optically controlled active media**. In: Nature Photonics (2012). DOI: 10.1038/nphoton.2012.278.

[140] U. Efron, ed. **Spatial light modulator technology: Materials, devices and application**. New York, Basel, and Hong Kong: M. Dekker, 1995.

[141] W. J. Hossack. **Modern Optics**. Script. Edinburgh: University of Edinburgh, 1998.

[142] A. M. Ruiz. **Accurate predictive model for twisted nematic liquid crystal devices. Application for generating programmable apodizers and Fresnel lenses**. PhD Thesis. Faculatat de Ciènces: Universitat Autònoma de Barcelona, 2001.

[143] M. Knapczyk et al. **High-resolution pulse shaper based on arrays of digital micromirrors**. In: IEEE Photonics Technology Letters 17.10 (2005), pp. 2200–2202. DOI: 10.1109/LPT.2005.854411.

[144] G. J. Evans et al. **Development and application of a ray-based model of light propagation through a spherical acousto-optic lens**. In: Optics express 23.18 (2015), pp. 23493–23510. DOI: 10.1364/OE.23.023493.

[145] H. Kawamoto. **The history of liquid-crystal displays**. In: Proceedings of the IEEE 90.4 (2002), pp. 460–500. DOI: 10.1109/JPROC.2002.1002521.

[146] W. Demtröder. **Atome, Moleküle und Festkörper: Mit 48 Tabellen, zahlreichen durchgerechneten Beispielen und 149 Übungsaufgaben mit ausführlichen Lösungen**. Vol. 3,3. 2005.

[147] Meadowlark Optics Inc. **High Contrast Optical Shutter**. Website. URL: http://www.meadowlark.com/images/products_large/twisted_nematic_shutter_diagram__for_tom__2_14659.jpg (visited on 08/17/2016).

[148] V. G. Chigrinov. **Liquid crystal devices: Physics and applications**. Boston: Artech House, 1999.

[149] M. Schadt and W. Helfrich. **Voltage-dependent Optical Activity of a Twisted Nematic Liquid Crystal**. In: Applied Physics Letters 18.4 (1971), p. 127. DOI: 10.1063/1.1653593.

[150] Hamamatsu Photonics K.K. **LCOS-SLM (Liquid Crystal on Silicon – Spatial Light Modulator)**. Website. URL: http://www.hamamatsu.com/resources/pdf/ssd/x10468_series_etc_kacc1172e.pdf (visited on 08/17/2016).

[151] J. W. Goodman. **Introduction to Fourier Optics**. second edition. Englewood and Colo: Roberts, 1996.

[152] R. W. Gerchberg and W. O. Saxton. **A Practical Algorithm for the Determination of Phase from Image and Diffraction Plane Pictures**. In: Optik 35.2 (1972), pp. 237–246.

[153] A. L. Gaunt and Z. Hadzibabic. **Robust digital holography for ultracold atom trapping**. In: Scientific reports 2 (2012), p. 721. DOI: 10.1038/srep00721.

[154] Wikimedia Foundation Inc. **GS-diagram**. Website. URL: https://en.wikipedia.org/wiki/File:GS-diagram.png (visited on 08/18/2016).

[155] T. R. M. Sales et al. **Light Tamers: Engineered microlens arrays provide new control for display and lighting applications.** Ed. by RPC Photonics Inc. 2004. URL: http://www.rpcphotonics.com/pdfs/Light_Tamers.pdf (visited on 08/24/2016).

[156] T. R. M. Sales. **Structured microlens arrays for beam shaping**. In: Optical Engineering 42.11 (2003), p. 3084. DOI: 10.1117/1.1618817.

[157] C. Gu et al. **Diffraction properties of volume holographic diffusers**. In: Journal of the Optical Society of America A 13.8 (1996), p. 1704. DOI: 10.1364/JOSAA.13.001704.

[158] L. E. Helseth and I. Singstad. **Diffusers for holographic stereography**. In: Optics Communications 193.1-6 (2001), pp. 81–86. DOI: 10.1016/S0030-4018(01)01246-9.

[159] RPC Photonics Inc. **Optical Diffuser Technologies**. Ed. by RPC Photonics Inc. White Paper. 2015. URL: http://www.rpcphotonics.com/pdfs/Optical_Diffuser_Technologies_Final_030215.pdf (visited on 08/24/2016).

[160] F. M. Dickey. **Laser Beam Shaping: Theory and Techniques, Second Edition**. 1st ed. Hoboken: Taylor and Francis, 2000. URL: http://gbv.eblib.com/patron/FullRecord.aspx?p=1589030.

[161] RPC Photonics Inc. **Fact Sheet: EDC-1-07108**. Ed. by RPC Photonics Inc. URL: http://www.rpcphotonics.com/wp-content/uploads/2015/01/Fact-Sheet-EDC-1-07108-A.pdf (visited on 08/22/2016).

[162] RCP Photonics Inc. **Engineered Diffusors**. Website. URL: http://www.rpcphotonics.com/engineered-diffusers-information/ (visited on 08/24/2016).

[163] D. H. Raguin, G. M. Morris, and P. M. Emmel. **Method for Making Optical Microstructures Having Profile Heights Exceeding Fifteen Microns**. Pat. US6410213 B1. 2002.

[164] G. M. Morris and T. R. M. Sales. **Structured Screens for Controlled Spreading of Light**. Pat. US7033736 B2. 2006.

[165] RPC Photonics Inc. **How to Use Engineered Diffusers**. White Paper. URL: http://www.rpcphotonics.com/pdfs/How_to_use_Engineered_Diffusers.pdf (visited on 08/25/2016).

[166] J. Palacci et al. **Sedimentation and effective temperature of active colloidal suspensions**. In: Physical review letters 105.8 (2010), p. 088304. DOI: 10.1103/PhysRevLett.105.088304.

[167] V. Chikkadi and P. Schall. **Nonaffine measures of particle displacements in sheared colloidal glasses**. In: Physical review. E, Statistical, nonlinear, and soft matter physics 85.3 Pt 1 (2012), p. 031402. DOI: 10.1103/PhysRevE.85.031402.

[168] Thomas Voigtmann. **Nonlinear glassy rheology**. In: Current Opinion in Colloid & Interface Science 19.6 (2014), pp. 549–560. DOI: 10.1016/j.cocis.2014.11.001.

[169] S.-H. Lee and D. G. Grier. **Giant colloidal diffusivity on corrugated optical vortices**. In: Physical review letters 96.19 (2006), p. 190601. DOI: 10.1103/PhysRevLett.96.190601.

[170] M. H. G. Duits, S. Ghosh, and F. Mugele. **Measuring advection and diffusion of colloids in shear flow**. In: Langmuir : the ACS journal of surfaces and colloids 31.21 (2015), pp. 5689–5700. DOI: 10.1021/acs.langmuir.5b01369.

[171] M. P. N. Juniper et al. **Colloidal particles driven across periodic optical-potential-energy landscapes**. In: Physical Review E 93.1 (2016), p. 012608. DOI: 10.1103/PhysRevE.93.012608.

[172] A. J. Moulson and J. M. Herbert. **Electroceramics: Materials, properties, applications**. 2. ed. Chichester u.a.: Wiley, 2003.

[173] J. L. Pons. **Emerging actuator technologies: A micromechatronic approach**. Chichester, England and Hoboken, NJ: Wiley, 2005. DOI: 10.1002/0470091991. URL: http://site.ebrary.com/lib/alltitles/docDetail.action?docID=10307853.

[174] Mad City Labs Inc. **Piezoactuator Information**. Website. URL: http://www.madcitylabs.com/pactuators.html (visited on 08/29/2016).

[175] Mad City Labs Inc. **Nano-BioS Series**. Ed. by Mad City Labs Inc. URL: http://www.madcitylabs.com/catalog/nanobiosseries.pdf (visited on 08/29/2016).

[176] R. C. Hardy and R. L. Cottington. **Viscosity of deuterium oxide and water in the range 5 to 125 C**. In: Journal of Research of the National Bureau of Standards 42.6 (1949), p. 573. DOI: 10.6028/jres.042.049.

[177] J. Happel and H. Brenner. **Low Reynolds number hydrodynamics: With special applications to particulate media**. 5. printing. Mechanics of fluids and transport processes. Dordrecht: Kluwer Acad. Publ, 1991.

[178] B. Lin, J. Yu, and S. A. Rice. **Direct measurements of constrained Brownian motion of an isolated sphere between two walls**. In: Physical Review E 62.3 (2000), pp. 3909–3919. DOI: 10.1103/PhysRevE.62.3909.

[179] Norland Products Inc. **Norland Optical Adhesive 61**. Ed. by Norland Products Inc. URL: https://www.norlandprod.com/adhesives/NOA%2061.html (visited on 09/02/2016).

[180] A. L. Thorneywork et al. **Effect of Hydrodynamic Interactions on Self-Diffusion of Quasi-Two-Dimensional Colloidal Hard Spheres**. In: Physical review letters 115.26 (2015), p. 268301. DOI: 10.1103/PhysRevLett.115.268301.

[181] A. L. Thorneywork et al. **On the Gaussian approximation in colloidal hard sphere fluids**. In: Soft Matter 12.18 (2016), pp. 4129–4134. DOI: 10.1039/c5sm03049h.

[182] R. D. L. Hanes, M. C. Jenkins, and S. U. Egelhaaf. **Combined holographic-mechanical optical tweezers: Construction, optimization, and calibration**. In: Review of Scientific Instruments 80.8 (2009), p. 083703. DOI: 10.1063/1.3196181.

[183] J. Nicolás, J. Campos, and M. J. Yzuel. **Phase and amplitude modulation of elliptic polarization states by nonabsorbing anisotropic elements: application to liquid-crystal devices**. In: Journal of the Optical Society of America A 19.5 (2002), p. 1013. DOI: 10.1364/JOSAA.19.001013.

[184] I. Moreno et al. **Jones matrix method for predicting and optimizing the optical modulation properties of a liquid-crystal display**. In: Journal of Applied Physics 94.6 (2003), p. 3697. DOI: 10.1063/1.1601688.

[185] R. D. L. Hanes. **Colloids in controlled energy landscapes**. PhD Thesis. Düsseldorf: Heinrich-Heine-Universität, 2012.

[186] J. W. Goodman. **Speckle Phenomena in Optics**. Roberts & Co, 2010.

[187] J. Bewerunge. **Colloids in random potentials: Optical realization and characterization of rough laser light fields**. PhD Thesis. Düsseldorf: Heinrich-Heine-Universität, 2016.

[188] E. Wolf. **Progress in Optics**. Vol. v. 14. Progress in Optics. Amsterdam and New York: North-Holland Pub. Co, 1976.

[189] S. E. Skipetrov et al. **Noise in laser speckle correlation and imaging techniques**. In: Optics express 18.14 (2010), pp. 14519–14534. DOI: 10.1364/OE.18.014519.

[190] J. Bewerunge et al. **Time- and ensemble-averages in evolving systems: the case of Brownian particles in random potentials**. In: Physical chemistry chemical physics : PCCP 18.28 (2016), pp. 18887–18895. DOI: 10.1039/c6cp02559e.

[191] J. Crocker and D. G. Grier. **Methods of Digital Video Microscopy for Colloidal Studies**. In: Journal of Colloid and Interface Science 179.1 (1996), pp. 298–310. DOI: 10.1006/jcis.1996.0217.

[192] J. C. Crocker and E. R. Weeks. **Particle tracking using IDL**. URL: http://www.physics.emory.edu/faculty/weeks//idl/ (visited on 11/29/2016).

[193] D. Blair and E. Dufresne. **The Matlab Particle Tracking Code Repository**. URL: http://site.physics.georgetown.edu/matlab/ (visited on 11/29/2016).

[194] D. Allan et al. **Trackpy: Fast, Flexible Particle-Tracking Toolkit**. URL: http://soft-matter.github.io/trackpy/v0.3.2/ (visited on 11/29/2016).

[195] M. C. Jenkins and S. U. Egelhaaf. **Confocal microscopy of colloidal particles: Towards reliable, optimum coordinates**. In: Advances in Colloid and Interface Science 136.1-2 (2008), pp. 65–92. DOI: 10.1016/j.cis.2007.07.006.

[196] A. A. Michelson. **Studies in Optics**. Dover ed. New York: Dover Publications, 1995.

[197] L. van Hove. **Correlations in Space and Time and Born Approximation Scattering in Systems of Interacting Particles**. In: Physical Review 95.1 (1954), pp. 249–262. DOI: 10.1103/PhysRev.95.249.

[198] J.-P. Hansen and I. R. McDonald. **Theory of Simple Liquids: With Applications to Soft Matter**. 4th ed. Amsterdam and Boston: Academic Press, 2013. URL: http://search.ebscohost.com/login.aspx?direct=true&scope=site&db=nlebk&db=nlabk&AN=501312.

[199] P. Hopkins et al. **The van Hove distribution function for Brownian hard spheres: Dynamical test particle theory and computer simulations for bulk dynamics**. In: The Journal of Chemical Physics 133.22 (2010), p. 224505. DOI: 10.1063/1.3511719.

[200] C. Holmes. **The Jamming of Dense Suspensions Under Imposed Stress**. Ph. D. Thesis. Edinburgh: University of Edinburgh, 2004. URL: https://www.era.lib.ed.ac.uk/bitstream/handle/1842/14086/Holmes2004.Pdf?sequence=1.

[201] A. G. Cherstvy and R. Metzler. **Anomalous diffusion in time-fluctuating non-stationary diffusivity landscapes**. In: Physical chemistry chemical physics : PCCP 18.34 (2016), pp. 23840–23852. DOI: 10.1039/c6cp03101c.

[202] J. P. Mithen. **Molecular dynamics simulations of the equilibrium dynamics of non-ideal plasmas**. Ph. D. Thesis. Oxford: University of Oxford, 2012.

[203] A. V. Ivlev et al. **Complex Plasmas and Colloidal Dispersions: Particle-Resolved Studies of Classical Liquids and Solids**. Vol. 5. $aSeries in soft condensed matter. Hackensack, NJ u.a.: World Scientific, 2012.

[204] B. J. Berne and R. Pecora. **Dynamic Light Scattering: With Applications to Chemistry, Biology, and Physics**. Dover Books on Physics. Newburyport: Dover Publications, 2013. URL: http://gbv.eblib.com/patron/FullRecord.aspx?p=1893216.

[205] S. Kotz et al., eds. **Encyclopedia of statistical sciences**. [2. ed. ff.] Hoboken, NJ: Wiley, 2006.

[206] W. C. K. Poon and D. Andelman, eds. **Soft Condensed Matter Physics in Molecular and Cell Biology**. Scottish graduate series. New York: Taylor & Francis, 2006. URL: http://site.ebrary.com/lib/alltitles/docDetail.action?docID=10143493.

[207] J. W. R. Mellnik et al. **Maximum likelihood estimation for single particle, passive microrheology data with drift**. In: Journal of Rheology 60.3 (2016), pp. 379–392. DOI: 10.1122/1.4943988.

[208] J. Dangaria, S. Yang, and P. Butler. **Improved nanometer-scale particle tracking in optical microscopy using microfabricated fiduciary posts**. In: BioTechniques 42.4 (2007), pp. 437–440. DOI: 10.2144/000112427.

[209] H. Deschout et al. **Precisely and accurately localizing single emitters in fluorescence microscopy**. In: Nature methods 11.3 (2014), pp. 253–266. DOI: 10.1038/nmeth.2843.

[210] J. Gelles, B. J. Schnapp, and M. P. Sheetz. **Tracking kinesin-driven movements with nanometre-scale precision**. In: Nature 331.6155 (1988), pp. 450–453. DOI: 10.1038/331450a0.

[211] D. Chakraborty and D. Chaudhuri. **Stochastic ratcheting of two-dimensional colloids: Directed current and dynamical transitions**. In: Physical review. E, Statistical, nonlinear, and soft matter physics 91.5 (2015), p. 050301. DOI: 10.1103/PhysRevE.91.050301.

[212] M. S. Simon, J. M. Sancho, and K. Lindenberg. **Transport and diffusion of overdamped Brownian particles in random potentials**. In: Physical Review E 88.6 (2013). DOI: 10.1103/PhysRevE.88.062105.

[213] R. Salgado-García. **Effective diffusion coefficient in tilted disordered potentials: Optimal relative diffusivity at a finite temperature**. In: Physical Review E 90.3 (2014). DOI: 10.1103/PhysRevE.90.032105.

[214] J. M. Sancho and A. M. Lacasta. **The rich phenomenology of Brownian particles in nonlinear potential landscapes**. In: The European Physical Journal Special Topics 187.1 (2010), pp. 49–62. DOI: 10.1140/epjst/e2010-01270-7.

[215] William H. Press et al. **Numerical recipes in C: The art of scientific computing**. 2. ed., reprinted with corr. to software version 2.10. Cambridge: Univ. Press, 2002.

[216] T. F. Chan, G. H. Golub, and R. J. LeVeque. **Algorithms for Computing the Sample Variance: Analysis and Recommendations**. In: The American Statistician 37.3 (1983), p. 242. DOI: 10.2307/2683386.

[217] Inc. Exelis Visual Information Solutions. **MOMENT**. URL: http://www.harrisgeospatial.com/docs/MOMENT.html (visited on 12/20/2016).

[218] K. Ahnert and M. Abel. **Numerical differentiation of experimental data: Local versus global methods**. In: Computer Physics Communications 177.10 (2007), pp. 764–774. DOI: 10.1016/j.cpc.2007.03.009.

[219] F. Jauberteau and J. L. Jauberteau. **Numerical differentiation with noisy signal**. In: Applied Mathematics and Computation 215.6 (2009), pp. 2283–2297. DOI: 10.1016/j.amc.2009.08.042.

[220] OriginLab Corp. **Help Online - Origin Help - Algorithms (Smooth)**. URL: http://www.originlab.com/doc/Origin-Help/Smooth-Algorithm (visited on 04/06/2017).

[221] F. Evers et al. **Colloids in light fields: Particle dynamics in random and periodic energy landscapes**. In: The European Physical Journal Special Topics 222.11 (2013), pp. 2995–3009. DOI: 10.1140/epjst/e2013-02071-2.

[222] T. Bauer et al. **The localization transition of the two-dimensional Lorentz model**. In: The European Physical Journal Special Topics 189.1 (2010), pp. 103–118. DOI: 10.1140/epjst/e2010-01313-1.

[223] H. H. Wensink et al. **Long-time self-diffusion for Brownian Gaussian-core particles**. In: Computer Physics Communications 179.1-3 (2008), pp. 77–81. DOI: 10.1016/j.cpc.2008.01.009.

[224] A. Imhof and J. K. G. Dhont. **Long-time self-diffusion in binary colloidal hard-sphere dispersions**. In: Physical Review E 52.6 (1995), pp. 6344–6357. DOI: 10.1103/PhysRevE.52.6344.

[225] E. Dickinson, ed. **Food Colloids: Interactions, Microstructure and Processing**. Vol. 298. Special publication / Royal Society of Chemistry. Cambridge: Royal Society of Chemistry, 2005. URL: http://www.loc.gov/catdir/enhancements/fy0625/2006494198-d.html.

[226] D. M. Heyes and A. C. Brańka. **Molecular and Brownian Dynamics Simulations of Self-Diffusion in Inverse Power Fluids**. In: Physics and Chemistry of Liquids 28.2 (1994), pp. 95–115. DOI: 10.1080/00319109408029546.

[227] R. D. L. Hanes, M. Schmiedeberg, and S. U. Egelhaaf. **Brownian particles on rough substrates: Relation between intermediate subdiffusion and asymptotic long-time diffusion**. In: Physical Review E 88.6 (2013). DOI: 10.1103/PhysRevE.88.062133.

[228] H. Cramér. **Mathematical methods of statistics**. 19. printing. Princeton paperbacks. Princeton: Princeton Univ. Press, 1999.

[229] D. N. Joanes and C. A. Gill. **Comparing measures of sample skewness and kurtosis**. In: Journal of the Royal Statistical Society: Series D (The Statistician) 47.1 (1998), pp. 183–189. DOI: 10.1111/1467-9884.00122.

[230] M. Abramowitz and I. A. Stegun, eds. **Handbook of mathematical functions with formulas, graphs, and**. Washington: U S Dept Of Commerce, 1970.

[231] B. Rönz and H. G. Strohe, eds. **Lexikon Statistik**. Wiesbaden: Gabler Verlag, 1994. DOI: 10.1007/978-3-322-91144-5. URL: http://dx.doi.org/10.1007/978-3-322-91144-5.

[232] K. Pearson. **Contributions to the Mathematical Theory of Evolution. II. Skew Variation in Homogeneous Material**. In: Philosophical Transactions of the Royal Society A: Mathematical, Physical and Engineering Sciences 186.0 (1895), pp. 343–414. DOI: 10.1098/rsta.1895.0010.

[233] K. Pearson. **Mathematical Contributions to the Theory of Evolution. XIX. Second Supplement to a Memoir on Skew Variation**. In: Philosophical Transactions of the Royal Society A: Mathematical, Physical and Engineering Sciences 216.538-548 (1916), pp. 429–457. DOI: 10.1098/rsta.1916.0009.

[234] J. E. Wilkins. **A Note on Skewness and Kurtosis**. In: The Annals of Mathematical Statistics 15.3 (1944), pp. 333–335. DOI: 10.1214/aoms/1177731243.

[235] K. Pearson. **Das Fehlergesetz und seine Verallgemeinerungen durch Fechner und Pearson. A Rejoinder**. In: Biometrika 4.1-2 (1905), pp. 169–212. DOI: 10.1093/biomet/4.1-2.169.

[236] P. H. Westfall. **Kurtosis as Peakedness, 1905 - 2014. R.I.P**. In: The American Statistician 68.3 (2014), pp. 191–195. DOI: 10.1080/00031305.2014.917055.

[237] K. P. Balanda and H. L. Macgillivray. **Kurtosis: A Critical Review**. In: The American Statistician 42.2 (1988), pp. 111–119. DOI: 10.1080/00031305.1988.10475539.

[238] T. F. Crack. **Foundations for Scientific Investing: Capital Market Intuition and Critical Thinking Skills**. Revised Sixth edition. 2016.

[239] B. Vorselaars et al. **Non-Gaussian nature of glassy dynamics by cage to cage motion**. In: Physical Review E 75.1 (2007). DOI: 10.1103/PhysRevE.75.011504.

[240] A. Rahman. **Correlations in the Motion of Atoms in Liquid Argon**. In: Physical Review 136.2A (1964), A405–A411. DOI: 10.1103/PhysRev.136.A405.

[241] B.R.A. Nijboer and A. Rahman. **Time expansion of correlation functions and the theory of slow neutron scattering**. In: Physica 32.2 (1966), pp. 415–432. DOI: 10.1016/0031-8914(66)90068-1.

[242] K. V. Mardia. **Measures of Multivariate Skewness and Kurtosis with Applications**. In: Biometrika 57.3 (1970), p. 519. DOI: 10.2307/2334770.

[243] M. Guo et al. **Probing the stochastic, motor-driven properties of the cytoplasm using force spectrum microscopy**. In: Cell 158.4 (2014), pp. 822–832. DOI: 10.1016/j.cell.2014.06.051.

[244] M. Khantha and V. Balakrishnan. **First passage time distributions for finite one-dimensional random walks**. In: Pramana 21.2 (1983), pp. 111–122. DOI: 10.1007/BF02894735.

[245] A. Molini et al. **First passage time statistics of Brownian motion with purely time dependent drift and diffusion**. In: Physica A: Statistical Mechanics and its Applications 390.11 (2011), pp. 1841–1852. DOI: 10.1016/j.physa.2011.01.024.

[246] A. Godec and R. Metzler. **First passage time distribution in heterogeneity controlled kinetics: Going beyond the mean first passage time**. In: Scientific Reports 6 (2016), p. 20349. DOI: 10.1038/srep20349.

[247] R. Zwanzig. **Diffusion in a Rough Potential**. In: Proceedings of the National Academy of Sciences 85.7 (1988), pp. 2029–2030. DOI: 10.1073/pnas.85.7.2029.

[248] M. Khoury et al. **Diffusion coefficient in periodic and random potentials**. In: Physical Review E 80.2 (2009). DOI: 10.1103/PhysRevE.80.021123.

[249] Richard D. L. Hanes and Stefan U. Egelhaaf. **Dynamics of individual colloidal particles in one-dimensional random potentials: a simulation study**. In: Journal of Physics: Condensed Matter 24.46 (2012), p. 464116. DOI: 10.1088/0953-8984/24/46/464116.

[250] M. Slutsky, M. Kardar, and L. Mirny. **Diffusion in correlated random potentials, with applications to DNA**. In: Physical Review E 69.6 (2004). DOI: 10.1103/PhysRevE.69.061903.

[251] A. N. Bloch, R. B. Weisman, and C. M. Varma. **Identification of a Class of Disordered One-Dimensional Conductors**. In: Physical Review Letters 28.12 (1972), pp. 753–756. DOI: 10.1103/PhysRevLett.28.753.

[252] Z. Zhou et al. **One-dimensional electron transport in Cu-tetracyanoquinodimethane organic nanowires**. In: Applied Physics Letters 90.19 (2007), p. 193115. DOI: 10.1063/1.2738380.

[253] M. Schmiedeberg and H. Löwen. Personal Communication.

[254] E. M. Purcell. **Life at low Reynolds number**. In: American Journal of Physics 45.1 (1977), p. 3. DOI: 10.1119/1.10903.

[255] D. L. Ermak and J. A. McCammon. **Brownian dynamics with hydrodynamic interactions**. In: The Journal of Chemical Physics 69.4 (1978), pp. 1352–1360. DOI: 10.1063/1.436761.

[256] L. Golan and S. Shoham. **Speckle elimination using shift-averaging in high-rate holographic projection**. In: Optics Express 17.3 (2009), p. 1330. DOI: 10.1364/OE.17.001330.

[257] M. Schmiedeberg, J. Roth, and H. Stark. **Brownian particles in random and quasicrystalline potentials: How they approach the equilibrium**. In: The European Physical Journal E 24.4 (2007), pp. 367–377. DOI: 10.1140/epje/i2007-10247-7.

[258] A. Bodrova et al. **Intermediate regimes in granular Brownian motion: Superdiffusion and subdiffusion**. In: Physical review letters 109.17 (2012), p. 178001. DOI: 10.1103/PhysRevLett.109.178001.

[259] N. Koumakis et al. **Start-up shear of concentrated colloidal hard spheres: Stresses, dynamics, and structure**. In: Journal of Rheology 60.4 (2016), pp. 603–623. DOI: 10.1122/1.4949340.

[260] J. Spiechowicz, J. Łuczka, and P. Hänggi. **Transient anomalous diffusion in periodic systems: Ergodicity, symmetry breaking and velocity relaxation**. In: Scientific Reports 6 (2016), p. 30948. DOI: 10.1038/srep30948.

[261] E. Najafi et al. **Super-diffusion of excited carriers in semiconductors**. In: Nature communications 8 (2017), p. 15177. DOI: 10.1038/ncomms15177.

[262] R. Benzi, A. Sutera, and A. Vulpiani. **The mechanism of stochastic resonance**. In: Journal of Physics A: Mathematical and General 14.11 (1981), pp. L453–L457. DOI: 10.1088/0305-4470/14/11/006.

[263] C. R. Doering and J. C. Gadoua. **Resonant activation over a fluctuating barrier**. In: Physical review letters 69.16 (1992), pp. 2318–2321. DOI: 10.1103/PhysRevLett.69.2318.

[264] A. A. Dubkov and B. Spagnolo. **Acceleration of diffusion in randomly switching potential with supersymmetry**. In: Physical Review E 72.4 (2005). DOI: 10.1103/PhysRevE.72.041104.

[265] B. J. Lopez et al. **Realization of a feedback controlled flashing ratchet**. In: Physical Review Letters 101.22 (2008), p. 220601. DOI: 10.1103/PhysRevLett.101.220601.

[266] S. Santer et al. **Dynamically Reconfigurable Polymer Films: Impact on Nanomotion**. In: Advanced Materials 18.18 (2006), pp. 2359–2362. DOI: 10.1002/adma.200601270.

[267] A. Fiasconaro et al. **Monitoring noise-resonant effects in cancer growth influenced by external fluctuations and periodic treatment**. In: The European Physical Journal B 65.3 (2008), pp. 435–442. DOI: 10.1140/epjb/e2008-00246-2.

[268] C. Pan et al. **Resonant activation through effective temperature oscillation in a Josephson tunnel junction**. In: Physical review. E, Statistical, nonlinear, and soft matter physics 79.3 Pt 1 (2009), p. 030104. DOI: 10.1103/PhysRevE.79.030104.

[269] S. M. Ross. **Introduction to probability models**. 11. ed. Amsterdam: Elsevier Acad. Press, 2014.

[270] P. Reimann et al. **Giant Acceleration of Free Diffusion by Use of Tilted Periodic Potentials**. In: Physical Review Letters 87.1 (2001). DOI: 10.1103/PhysRevLett.87.010602.

[271] P. Reimann and R. Eichhorn. **Weak Disorder Strongly Improves the Selective Enhancement of Diffusion in a Tilted Periodic Potential**. In: Physical Review Letters 101.18 (2008). DOI: 10.1103/PhysRevLett.101.180601.

[272] P. Reimann. **Brownian motors: Noisy transport far from equilibrium**. In: Physics Reports 361.2-4 (2002), pp. 57–265. DOI: 10.1016/S0370-1573(01)00081-3.

[273] P. Tierno et al. **Giant Transversal Particle Diffusion in a Longitudinal Magnetic Ratchet**. In: Physical Review Letters 105.23 (2010). DOI: 10.1103/PhysRevLett.105.230602.

[274] J. Spiechowicz and J. Łuczka. **Diffusion anomalies in ac-driven Brownian ratchets**. In: Physical review. E, Statistical, nonlinear, and soft matter physics 91.6 (2015), p. 062104. DOI: 10.1103/PhysRevE.91.062104.

[275] P. Hänggi and F. Marchesoni. **Artificial Brownian motors: Controlling transport on the nanoscale**. In: Reviews of Modern Physics 81.1 (2009), pp. 387–442. DOI: 10.1103/RevModPhys.81.387.

[276] R. Gernert and Klapp, S. H. L. **Enhancement of mobility in an interacting colloidal system under feedback control**. In: Physical review. E, Statistical, nonlinear, and soft matter physics 92.2 (2015), p. 022132. DOI: 10.1103/PhysRevE.92.022132.

[277] C. Schmitt et al. **Stochastic resonance vs. resonant activation**. In: Europhysics Letters (EPL) 74.6 (2006), pp. 937–943. DOI: 10.1209/epl/i2006-10052-6.

[278] R. Benzi et al. **Stochastic resonance in climatic change**. In: Tellus 34.1 (1982), pp. 10–16. DOI: 10.1111/j.2153-3490.1982.tb01787.x.

[279] P. Reimann et al. **Diffusion in tilted periodic potentials: Enhancement, universality, and scaling**. In: Physical review. E, Statistical, nonlinear, and soft matter physics 65.3 Pt 1 (2002), p. 031104. DOI: 10.1103/PhysRevE.65.031104.

[280] R. Benzi. **Stochastic resonance: From climate to biology**. In: Nonlinear Processes in Geophysics 17.5 (2010), pp. 431–441. DOI: 10.5194/npg-17-431-2010.

[281] M. Perc, M. Gosak, and S. Kralj. **Stochastic resonance in soft matter systems: Combined effects of static and dynamic disorder**. In: Soft Matter 4.9 (2008), p. 1861. DOI: 10.1039/b804566f.

[282] L. Gammaitoni, F. Marchesoni, and S. Santucci. **Stochastic resonance as a bona fide resonance**. In: Physical review letters 74.7 (1995), pp. 1052–1055. DOI: 10.1103/PhysRevLett.74.1052.

[283] P. Reimann. **Thermally driven escape with fluctuating potentials: A new type of resonant activation**. In: Physical review letters 74.23 (1995), pp. 4576–4579. DOI: 10.1103/PhysRevLett.74.4576.

[284] A. Fiasconaro and B. Spagnolo. **Resonant activation in piecewise linear asymmetric potentials**. In: Physical review. E, Statistical, nonlinear, and soft matter physics 83.4 Pt 1 (2011), p. 041122. DOI: 10.1103/PhysRevE.83.041122.

[285] D. Beece et al. **Solvent viscosity and protein dynamics**. In: Biochemistry 19.23 (1980), pp. 5147–5157. DOI: 10.1021/bi00564a001.

[286] B. Spagnolo and A. Dubkov. **Diffusion in flashing periodic potentials**. In: The European Physical Journal B 50.1-2 (2006), pp. 299–303. DOI: 10.1140/epjb/e2006-00108-y.

[287] S. Bleil, P. Reimann, and C. Bechinger. **Directing Brownian motion by oscillating barriers**. In: Physical Review E 75.3 (2007). DOI: 10.1103/PhysRevE.75.031117.

[288] S. Bianchi et al. **Active dynamics of colloidal particles in time-varying laser speckle patterns**. In: Scientific reports 6 (2016), p. 27681. DOI: 10.1038/srep27681.

[289] Y. Su et al. **Colloidal diffusion over a quenched two-dimensional random potential**. In: Soft Matter (2017). DOI: 10.1039/c7sm01056g.

[290] E. Helfer et al. **Microrheology of biopolymer-membrane complexes**. In: Physical review letters 85.2 (2000), pp. 457–460. DOI: 10.1103/PhysRevLett.85.457.

[291] D. Winter et al. **Active nonlinear microrheology in a glass-forming Yukawa fluid**. In: Physical review letters 108.2 (2012), p. 028303. DOI: 10.1103/PhysRevLett.108.028303.

[292] J. R. Gomez-Solano and C. Bechinger. **Transient dynamics of a colloidal particle driven through a viscoelastic fluid**. In: New Journal of Physics 17.10 (2015), p. 103032. DOI: 10.1088/1367-2630/17/10/103032.

[293] R. Dasgupta, S. Ahlawat, and P. K. Gupta. **Microfluidic sorting with a moving array of optical traps**. In: Applied Optics 51.19 (2012), pp. 4377–4387. DOI: 10.1364/AO.51.004377.

[294] K. Xiao and D. G. Grier. **Sorting colloidal particles into multiple channels with optical forces: Prismatic optical fractionation**. In: Physical Review E 82.5 (2010). DOI: 10.1103/PhysRevE.82.051407.

[295] J. R. Gomez-Solano et al. **Non-equilibrium work distribution for interacting colloidal particles under friction**. In: New Journal of Physics 17.4 (2015), p. 045026. DOI: 10.1088/1367-2630/17/4/045026.

[296] D. S. Dean, I. T. Drummond, and R. R. Horgan. **Effective transport properties for diffusion in random media**. In: Journal of Statistical Mechanics: Theory and Experiment 2007.07 (2007), P07013. DOI: 10.1088/1742-5468/2007/07/P07013.

[297] R. J. Hunter. **Foundations of Colloid Science**. 2. ed., 1. publ. Oxford: Oxford Univ. Press, 2001.

[298] R. Wittkowski and H. Löwen. **Self-propelled Brownian spinning top: Dynamics of a biaxial swimmer at low Reynolds numbers**. In: Physical review. E, Statistical, nonlinear, and soft matter physics 85.2 Pt 1 (2012), p. 021406. DOI: 10.1103/PhysRevE.85.021406.

[299] Paul C. Bressloff. **Stochastic Processes in Cell Biology**. Vol. 41. Cham: Springer International Publishing, 2014. DOI: 10.1007/978-3-319-08488-6.

[300] G. Costantini and F. Marchesoni. **Threshold diffusion in a tilted washboard potential**. In: Europhysics Letters (EPL) 48.5 (1999), pp. 491–497. DOI: 10.1209/epl/i1999-00510-7.

[301] B. Lindner and I. M. Sokolov. **Giant diffusion of underdamped particles in a biased periodic potential**. In: Physical review. E 93 (2016), p. 042106. DOI: 10.1103/PhysRevE.93.042106.

[302] V. Blickle et al. **Characterizing potentials by a generalized Boltzmann factor**. In: Physical review. E, Statistical, nonlinear, and soft matter physics 75.6 Pt 1 (2007), p. 060101. DOI: 10.1103/PhysRevE.75.060101.

[303] R. Hayashi et al. **Giant Acceleration of Diffusion Observed in a Single-Molecule Experiment on F(1)-ATPase**. In: Physical review letters 114.24 (2015), p. 248101. DOI: 10.1103/PhysRevLett.114.248101.

[304] M. Schreier et al. **Giant enhancement of diffusion and particle selection in rocked periodic potentials**. In: Europhysics Letters (EPL) 44.4 (1998), pp. 416–422. DOI: 10.1209/epl/i1998-00488-0.

[305] P. K. Ghosh et al. **Driven Brownian transport through arrays of symmetric obstacles**. In: Physical Review E 85.1 (2012). DOI: 10.1103/PhysRevE.85.011101.

[306] A. M. Berezhkovskii and S. M. Bezrukov. **Effective drift and diffusion of a particle jumping between mobile and immobile states**. In: Journal of electroanalytical chemistry (Lausanne, Switzerland) 660.2 (2011), pp. 352–355. DOI: 10.1016/j.jelechem.2010.08.017.

[307] M. S. Simon, J. M. Sancho, and K. Lindenberg. **Transport and diffusion of underdamped Brownian particles in random potentials**. In: The European Physical Journal B 87.9 (2014). DOI: 10.1140/epjb/e2014-50295-9.

[308] T. Voigtmann and J. Horbach. **Slow dynamics in ion-conducting sodium silicate melts: Simulation and mode-coupling theory**. In: Europhysics Letters (EPL) 74.3 (2006), pp. 459–465. DOI: 10.1209/epl/i2006-10012-2.

[309] B. J. Sung and A. Yethiraj. **Lateral diffusion of proteins in the plasma membrane: spatial tessellation and percolation theory**. In: The journal of physical chemistry. B 112.1 (2008), pp. 143–149. DOI: 10.1021/jp0772068.

[310] M. J. Saxton. **Wanted**. In: Biophysical Journal 103.12 (2012), pp. 2411–2422. DOI: 10.1016/j.bpj.2012.10.038.

[311] H. A. Lorentz. **The Motion of Electrons in Metallic Bodies I**. In: KNAW, Proceedings 7 (1905), pp. 438–453.

[312] C. P. Dettmann. **Diffusion in the Lorentz Gas**. In: Communications in Theoretical Physics 62.4 (2014), pp. 521–540. DOI: 10.1088/0253-6102/62/4/10.

[313] P. Grassberger. **Conductivity exponent and backbone dimension in 2-d percolation**. In: Physica A: Statistical Mechanics and its Applications 262.3-4 (1999), pp. 251–263. DOI: 10.1016/S0378-4371(98)00435-X.

[314] M. J. Saxton. **Anomalous diffusion due to obstacles: A Monte Carlo study**. In: Biophysical Journal 66.2 (1994), pp. 394–401. DOI: 10.1016/S0006-3495(94)80789-1.

[315] J. C. Dyre et al. **Fundamental questions relating to ion conduction in disordered solids**. In: Reports on Progress in Physics 72.4 (2009), p. 046501. DOI: 10.1088/0034-4885/72/4/046501.

[316] J. Horbach, W. Kob, and K. Binder. **Dynamics of sodium in sodium disilicate: channel relaxation and sodium diffusion**. In: Physical review letters 88.12 (2002), p. 125502. DOI: 10.1103/PhysRevLett.88.125502.

[317] N. Borghini and C. Gombeaud. **Anisotropic collective flow of a Lorentz gas**. In: Journal of Physics G: Nuclear and Particle Physics 38.12 (2011), p. 124172. DOI: 10.1088/0954-3899/38/12/124172.

[318] T. O. E. Skinner et al. **Localization dynamics of fluids in random confinement**. In: Physical review letters 111.12 (2013), p. 128301. DOI: 10.1103/PhysRevLett.111.128301.

[319] R. Castaneda-Priego. Personal Communication. Mar. 2017.

[320] D. Magatti et al. **Dynamic heterodyne near field scattering**. In: Applied Physics Letters 92.24 (2008), p. 241101. DOI: 10.1063/1.2937841.

[321] M. D. Alaimo et al. **Heterodyne speckle velocimetry of Poiseuille flow**. In: Journal of Applied Physics 102.7 (2007), p. 073113. DOI: 10.1063/1.2786905.

[322] J. A. Perera-Burgos et al. **Assessment of the micro-structure and depletion potentials in two-dimensional binary mixtures of additive hard-disks**. In: The Journal of chemical physics 145.10 (2016), p. 104905. DOI: 10.1063/1.4962423.

[323] A. L. Thorneywork et al. **Self-diffusion in two-dimensional binary colloidal hard-sphere fluids**. In: Physical review. E 95.1-1 (2017), p. 012614. DOI: 10.1103/PhysRevE.95.012614.

[324] M. Spanner et al. **Anomalous transport of a tracer on percolating clusters**. In: Journal of physics. Condensed matter : an Institute of Physics journal 23.23 (2011), p. 234120. DOI: 10.1088/0953-8984/23/23/234120.

[325] S. K. Schnyder et al. **Rounding of the localization transition in model porous media**. In: Soft Matter 11.4 (2015), pp. 701–711. DOI: 10.1039/c4sm02334j.

[326] Markus Spanner et al. **Splitting of the Universality Class of Anomalous Transport in Crowded Media**. In: Physical review letters 116.6 (2016), p. 060601. DOI: 10.1103/PhysRevLett.116.060601.

[327] F. Höfling et al. **Critical dynamics of ballistic and Brownian particles in a heterogeneous environment**. In: The Journal of chemical physics 128.16 (2008), p. 164517. DOI: 10.1063/1.2901170.

[328] H. Berry and H. Chaté. **Anomalous diffusion due to hindering by mobile obstacles undergoing Brownian motion or Orstein-Ulhenbeck processes**. In: Physical review. E, Statistical, nonlinear, and soft matter physics 89.2 (2014), p. 022708. DOI: 10.1103/PhysRevE.89.022708.

[329] S. Torquato. **Bulk properties of two–phase disordered media. I. Cluster expansion for the effective dielectric constant of dispersions of penetrable spheres**. In: The Journal of Chemical Physics 81.11 (1984), pp. 5079–5088. DOI: 10.1063/1.447497.

[330] S. Torquato. **Random Heterogeneous Materials: Microstructure and Macroscopic Properties**. Vol. 16. Interdisciplinary Applied Mathematics. New York, NY: Springer, 2002. DOI: 10.1007/978-1-4757-6355-3.

[331] B. I. Halperin, S. Feng, and P. N. Sen. **Differences between lattice and continuum percolation transport exponents**. In: Physical review letters 54.22 (1985), pp. 2391–2394. DOI: 10.1103/PhysRevLett.54.2391.

[332] M. Zeitz, K. Wolff, and H. Stark. **Active Brownian particles moving in a random Lorentz gas**. In: The European Physical Journal E 40.2 (2017), p. 23. DOI: 10.1140/epje/i2017-11510-0.

[333] M. J. Saxton. **Lateral diffusion in an archipelago. The effect of mobile obstacles**. In: Biophysical Journal 52.6 (1987), pp. 989–997. DOI: 10.1016/S0006-3495(87)83291-5.

[334] M. J. Saxton. **Lateral diffusion in a mixture of mobile and immobile particles. A Monte Carlo study**. In: Biophysical Journal 58.5 (1990), pp. 1303–1306. DOI: 10.1016/S0006-3495(90)82470-X.

[335] I.G Tremmel et al. **Dependence of plastoquinol diffusion on the shape, size, and density of integral thylakoid proteins**. In: Biochimica et Biophysica Acta (BBA) - Bioenergetics 1607.2-3 (2003), pp. 97–109. DOI: 10.1016/j.bbabio.2003.09.004.

[336] D. A. Pink. **Protein lateral movement in lipid bilayers. Stimulation studies of its dependence upon protein concentration**. In: Biochimica et Biophysica Acta (BBA) - Biomembranes 818.2 (1985), pp. 200–204. DOI: 10.1016/0005-2736(85)90562-0.

[337] P. R. Smith et al. **Anomalous Diffusion of Major Histocompatibility Complex Class I Molecules on HeLa Cells Determined by Single Particle Tracking**. In: Biophysical Journal 76.6 (1999), pp. 3331–3344. DOI: 10.1016/S0006-3495(99)77486-2.

[338] K. Murase et al. **Ultrafine membrane compartments for molecular diffusion as revealed by single molecule techniques**. In: Biophysical Journal 86.6 (2004), pp. 4075–4093. DOI: 10.1529/biophysj.103.035717.